MACHINES. TECHNOLOGIES. MATERIALS 2015

16-19.09.2015 Varna, Bulgaria

• МЕЖДУНАРОДЕН КОНГРЕС – МАШИНИ, ТЕХНОЛОГИИ И МАТЕРИАЛИ •

2015

• INTERNATIONAL CONGRESS – MACHINES, TECHNOLOGIES, MATERIALS •

PROCEEDINGS

VOLUME 1

SCIENTIFIC TECHNICAL UNION OF MECHANICAL ENGINEERING

108 RAKOVSKI STR, SOFIA, BULGARIA

S C I E N T I F I C
P R O C E E D I N G S

OF THE SCIENTIFIC-TECHNICAL UNION
OF MECHANICAL ENGINEERING

Year XXIII **Volume 21/184** **SEPTEMBER 2015**

XII INTERNATIONAL CONGRESS

MACHINES, TECHNOLOGIES, MATERIALS 2015

September 16-19.09.2015, VARNA, BULGARIA

SECTION “MACHINES”

SECTION “TECHNOLOGIES”

ISSN 1310-3946

C O N T E N T S

CAST EQUIPMENT FOR HEAT TREATMENT FURNACES

ЛИТЕЙНОЕ ОБОРУДОВАНИЕ ТЕРМИЧЕСКИХ ПЕЧЕЙ

Dr. Eng. Drotlew A., Dr. Eng. Garbiak M., Prof. DSc. Piekarski B.*
West Pomeranian University of Technology – Szczecin, Poland
*E-mail: bogdan.piekarski@zut.edu.pl

***Abstract**: Various designs of equipment used in heat treatment furnaces are presented. The equipment is assembled from components varying in shape and size. In this case study it is composed of castings only. Castings are made from creep-resistant alloys, mainly cast austenitic steel and nickel alloys, using gravity poured sand molds. The design should allow for the simultaneous solidification of all thin-walled cast parts. The study focuses on the equipment for the heat treatment of parts of uncommon shape and size, or parts that require special heat treatment conditions. It is used for the charge formation in furnace and transport of this charge inside and outside the furnace. Different designs are illustrated. Their shape and size depends on the type of furnace, production volume, and the number and shape of heat-treated parts.*
KEYWORDS: CASTINGS FOR HEAT TREATMENT PLANTS, TECHNOLOGICAL EQUIPMENT, GRATES, BASKETS

1. Introduction

A part of tooling in most heat treatment furnaces is the technological equipment used for the formation of charge and its transport inside and outside the furnace. The performance life of this equipment often determines the reliability and durability of the furnace [1–3]. There are three procedures commonly adopted in the design of this equipment, each of them depending on the type of furnace, production volume, and the number and shape of heat-treated products. Future user of the equipment must decide on the choice of one of the following solutions [3]:

1. Use standard furnace equipment provided by the manufacturer, and then, depending on current production needs, add to this equipment, within his own capacity, other complementary elements for handling of the heat treated parts.
2. Use in standard furnace the equipment of his own non-standard design.
3. Order at a manufacturer a nonstandard furnace and install in this furnace the pre-designed equipment of nonstandard shape and size.

This study describes a user-tailored type of technological equipment, designed for the heat treatment of selected parts of machinery in a furnace of uncommon design. The need to take a "special approach" to the design of the equipment was dictated by:

- the shape and size of heat-treated parts,
- the need to increase the durability of the equipment,
- specific heat treatment parameters,
- other requirements essential for the required quality of heat-treated parts and reduced cost of their production.

The presented equipment has been made from cast components only, using creep-resistant alloys, mainly cast austenitic chromium-nickel / nickel-chromium steel and nickel alloys [3–5].

2. Design of the equipment

In designing of the equipment, the engineer is guided by the following principles [1, 3, 6–9]:

1. As far as possible, both the equipment and the heat treated parts should form a compact whole.
2. The mate components of the equipment should be joined together in a loose way. Loose fit allows free heat distortion of connected components in the range of operating temperatures. It also makes the replacement of worn out parts much easier.
3. Different components of the equipment should have the same wall thickness and the walls should be as thin as possible. It is recommended to avoid heavy build up of material separated by thin walls from other components.

The equipment shown in Figures 1–10 has been designed in accordance with the requirements formulated earlier. The individual components are connected with pins.

The equipment for the heat treatment of shafts of a wind turbine (Fig. 1) is designed for use in a pit furnace. The heat-treated batch consists of three shafts, each weighing 920 kg (Fig. 1a). The weight of the equipment alone is 1280 kg and the whole is composed of 72 pieces (Fig. 1b).

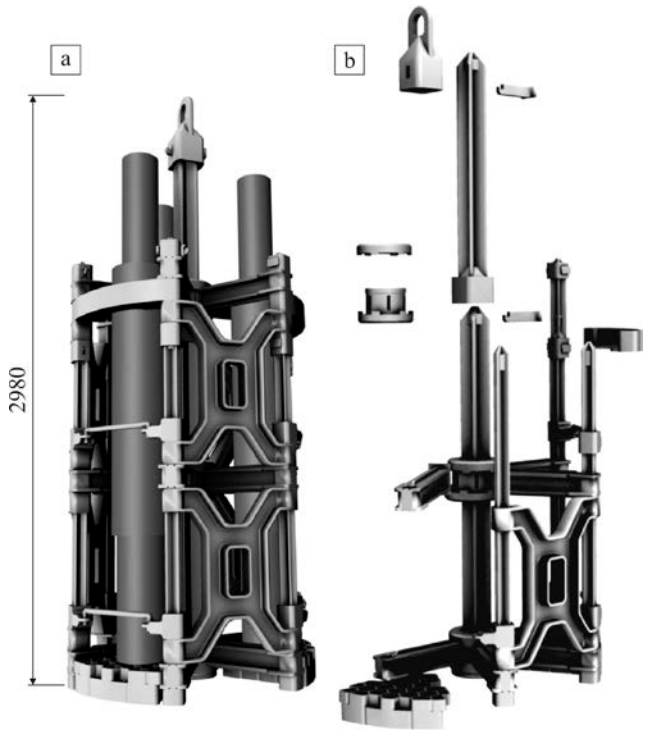

***Fig. 1.** The equipment for the heat treatment of shafts of a wind turbine: a) general view [3, 9], b) single components*

The equipment shown in Figure 2 is used for the heat treatment of turbojet engine gas guide vanes. The process of heat treatment is the last one in the refurbishment cycle of these vanes. The user request was to set the guide vanes in a vertical position in the equipment using base elements, for which the additional design was made (Fig. 2a). However, with this setting of the treated parts, any change in the equipment position during transport would have to be done with utmost care, since the gravity center of heat-treated parts would be located at a considerable height. Changing the setting of heat-treated parts (Fig. 2b) eliminated this inconvenience, bringing additionally a number of other advantages, to mention as an example the loading capacity of the equipment increased from 18 to 20 parts, the overall weight of the equipment reduced by 150 kg, and the manufacturing cost reduced by 12%. Then the total weight of the equipment (Fig. 2b) was 414 kg, and it consisted of 42 items, this including 29 pins.

The equipment for the heat treatment of turbojet engine rotor blades (Fig. 3) is a good example of how the conversion from a welded structure to a structure composed entirely of castings can increase the life of the elements [3, 10].

This equipment is to be used in a hood furnace. The weight of the modified structure (Fig. 3a) is 280 kg. The equipment is composed of 261 parts (Fig. 3b), of which 192 are hooks for hanging the individual heat-treated blades (Fig. 3a).

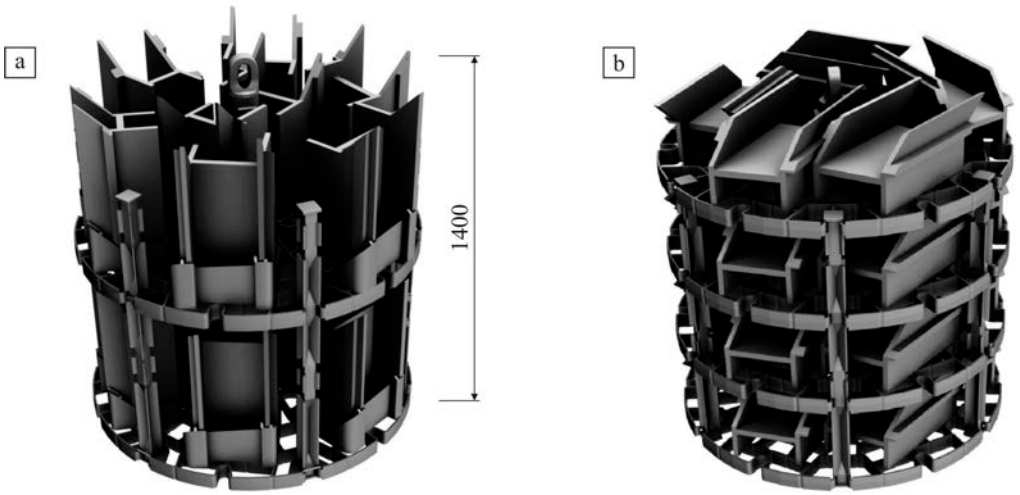

Fig. 2. *The equipment for the heat treatment of turbojet engine gas guide vanes [9]: a) initial design, b) modified design*

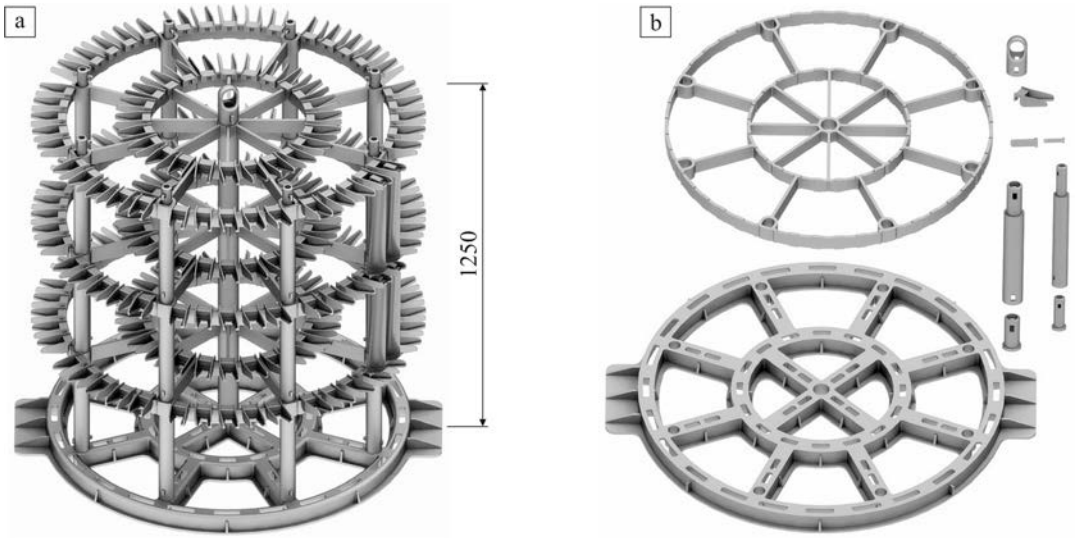

Fig. 3. *The equipment for the heat treatment of turbojet engine rotor blades [3, 9]: a) general view, b) single components*

In the next step of the modification of the equipment design (Fig. 3a), also the hook, on which the blades are hung, was modified (Fig. 4). This change significantly increased the number of blades heat treated in a single cycle.

Fig. 4. *Increased capacity of the equipment shown in Fig. 3a by the use of double hook [9]*

The equipment shown in Figure 5 was designed for the heat treatment of tension springs for railway electric traction. It was to be used in the pusher furnace. The design of the equipment shown in Figure 5 was tailored to the user specific needs; hooks were introduced to facilitate transport outside the furnace.

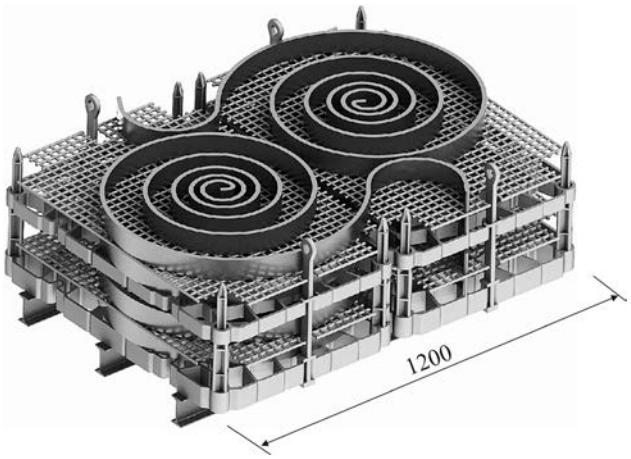

Fig. 5. *The equipment for heat treatment of springs [9]*

Baskets are commonly used in the heat treatment process, especially when the process of annealing is done on small parts. The use of baskets allows maximum utilization of the furnace working space and facilitates work organization. The equipment shown in Figures 6 and 8 has been designed with a view to encouraging the users of baskets welded from the wrought semi-products to switch over to the use of baskets made of cast components.

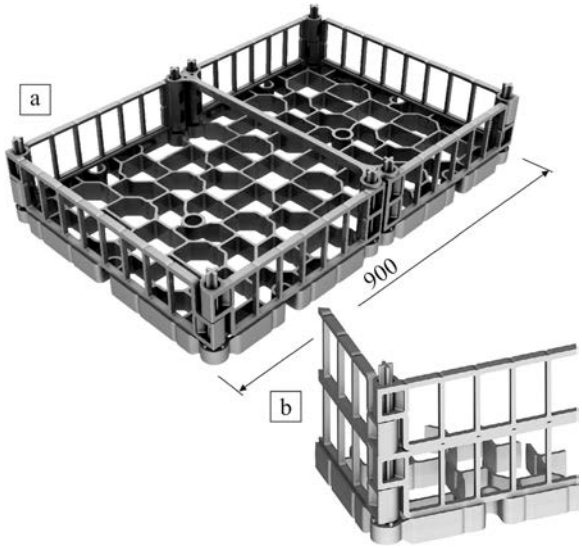

Fig. 6. *Basket: a) general view, b) high capacity design with additional side walls [9]*

Basket (Fig. 6a) is a sort of container designed for the heat treatment of small parts in the chamber furnace. Parts are placed in a basket in bulk. Long columns allow increasing the loading capacity of the basket, since a number of extra side walls can be added (Fig. 6b).

Welded baskets (Fig. 7) for annealing of the cast gearbox bodies are used in the roller pusher furnace. The one shown in the drawing has been replaced with a basket made of cast components (Fig. 8a). The basket has a weight of 440 kg and consists of 32 castings.

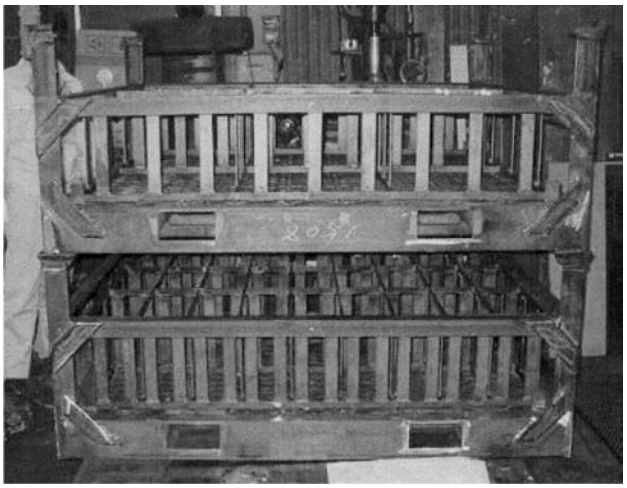

Fig. 7. *Welded basket for annealing of gearbox bodies [3, 10]; the gearbox bodies are placed in separate compartments of the basket*

Some fragments (or the entire surface) of the ceramic lining of the furnace for heat treatment may require shielding or other means of protection to prevent them from getting damaged during operation.

The equipment shown in Figure 9 illustrates the method of protecting the ceramic hearth of a bogie hearth furnace from mechanical damage during loading / unloading of charge.

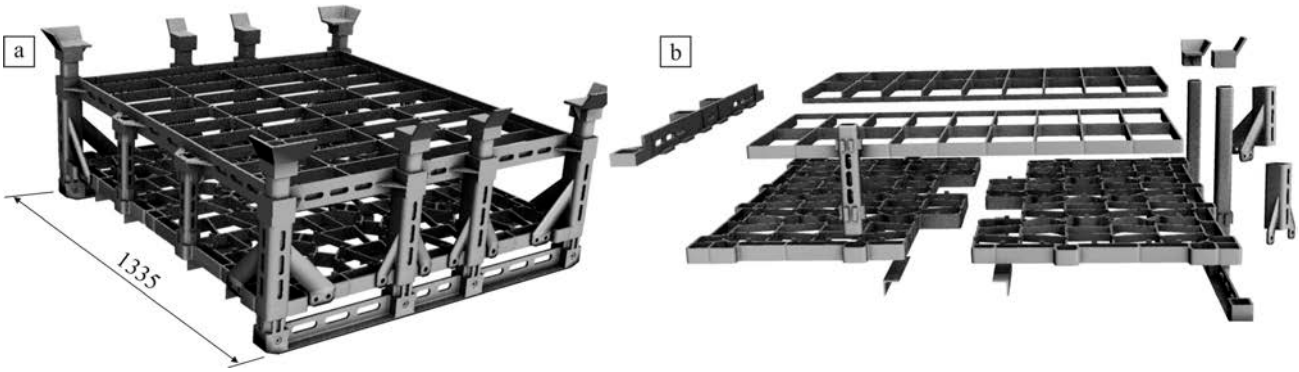

Fig. 8. *Modified design of basket shown in Figure 7 [3, 9]: a) general view, b) single components*

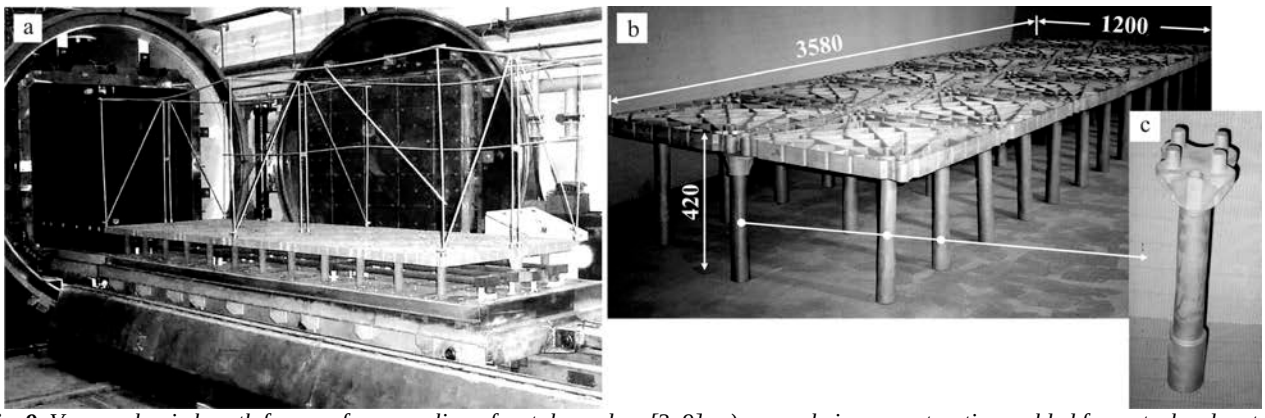

Fig. 9. *Vacuum bogie hearth furnace for annealing of metal powders [3, 9]: a) general view; construction welded from steel rods set on a stem indicates the space occupied by the containers in which the charge is placed, b) the core made from pallets and racks set on the furnace hearth*

The hearth of the furnace is provided with an electrical heating system arranged on a ceramic substrate (Fig. 9a). The equipment, in addition to protecting the hearth of the furnace, has also another task, namely that of maintaining a stable position of the heavy charge above the heaters without constituting a significant barrier to heat flow in this area. To ensure that these requirements are met, a base was designed that consists of 12 openwork pallets and 30 columns (Fig. 9b, c). The columns with heads ending in bolts (Fig. 9c) join palettes together. Loose connection of these elements enables them (and the equipment) to undergo free heat distortion in the range of operating temperatures.

In the process of hardening products made of titanium alloys it is necessary to cool them very rapidly in a cooling liquid. Additionally, the heat treatment process is difficult to carry out if products are heavy and intricate. The equipment for the heat treatment of parts made from titanium alloys is shown in Figure 10.

The equipment (Fig. 10) is designed for the heat treatment of parts of the aircraft chassis. It consists of 55 components with a total weight of 450 kg. The main components of the equipment are: a body with a transport hook, a latch (Fig. 10–1, 2) and a sling (Fig. 10–3). The charge of up to 2500 kg is hung on sling hooks (Fig. 10–4). The equipment with the charge is suspended under a crane and introduced into the furnace chamber. In the furnace it is held at a predetermined temperature for a predetermined lapse of time. Then, together with the furnace, it is placed above the liquid coolant reservoir and lowered into the reservoir under its own weight.

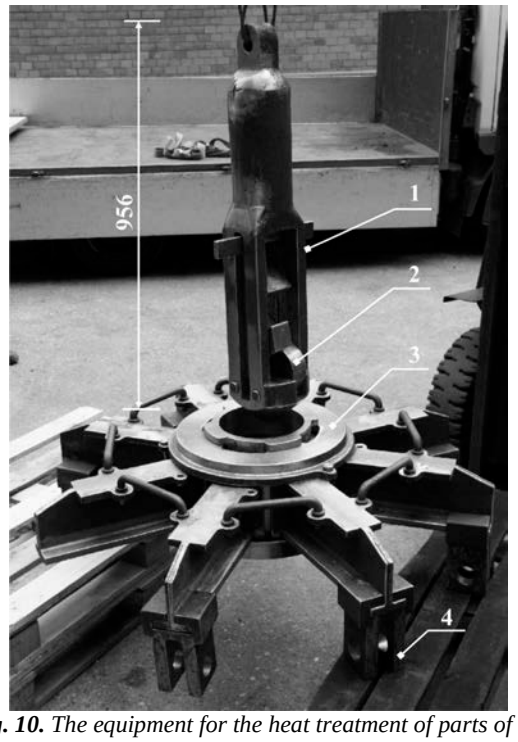

Fig. 10. *The equipment for the heat treatment of parts of the aircraft chassis [3]: 1 – body with transport hook, 2 – latch, 3 – sling, 4 – clip for fastening of heat treated parts*

3. Final remarks

When the described components of the technological equipment were designed, three groups of factors that determine the reliability and durability of this type of construction were examined [3]. These factors include:

1. Construction – operating conditions (temperature changing in a wide range of the operating values) and the expected parameters of the heat-treated charge (size, shape, weight).
2. Material – chemical and phase composition, as well as the morphology of microstructure providing the required creep properties during operation.
3. Casting – the use of technological solutions in the manufacture of castings, which guarantee low level or complete elimination of defects, both external and internal.

When decisions are made jointly by the manufacturer and foundry process engineer as to the selected material, design and technology, it should be remembered that the results of the operation of these three factors overlap and together affect the life and stability of the equipment considered as one integral whole.

All variants of the equipment shown in Figures 1–9 were designed by the authors of this study. Most of the types have already been used in industrial practice, in whole or in part. In the case of the equipment shown in Figure 10, the authors participated in the process of its manufacture. All designs are protected by intellectual property laws.

4. References

[1] Steinkusch, W., „Verbesserte Werkstoff und Konstruktionen verringern Betriebskosten bei der Wärme-Behandlung". Fachberichte Hütten. Metall. 23(1985)746-749.

[2] Lai, G. Y., „Heat-Resistant Materials for Furnace Parts, Trays, and Fixtures". In ASM Handbook 4 – Heat Treating (pp. 510-518). ASM International 1991.

[3] Piekarski B., „Creep-resistant castings used in heat treatment furnaces". Wydawnictwo Zachodniopomorskiego Uniwersytetu Technologicznego w Szczecinie, Szczecin 2012 (in Polish).

[4] Lai, G. Y. High-Temperature Corrosion and Materials Applications. ASM International 2007.

[5] Davis, J. R. (Ed.), Industrial Applications of Heat-Resistant Materials. In Heat Resistant Materials ASM International 1997, 67-85.

[6] Piekarski, B., Drotlew A., „Cast functional accessories for heat treatment furnaces". Archives of Foundry Engineering 4(2010)183-190.

[7] Drotlew A., Garbiak M., Kubicki J., Piekarski B., Siluk P. „Structure of guide grate in heat treatment technological equipment". Prace Instytutu Odlewnictwa 3(2013) 59-71 (in Polish).

[8] Drotlew A., Garbiak M., Piekarski B., „Technological equipment for heat treatment". Mechanik 5-6(2013)398-403 (in Polish).

[9] Drotlew A., Piekarski B.: Technological equipment for heat treatment furnaces. POLCAST, Szczecin 2010-2014 (unpublished; in Polish).

A MULTINOMIAL APPROACH TO THE MACHINE INTERFERENCE PROBLEM

Prof. Gurevich G., Prof. Hadad Y., Dr. Keren B.
Department of Industrial Engineering and Management – SCE-Shamoon College of Engineering, Beer Sheva, Israel

gregoryg@sce.ac.il, yossi@sce.ac.il, baruchke@sce.ac.il

Abstract: *This paper presents a multinomial model for a special case of the machine interference problem (MIP), where each of N identical machines randomly requests several different service types. The model allows the calculation of the expected interference time in the queue for each service type. The extended version of the model allows calculation of the exact distribution function of the steady state waiting time and total service time for each type of requested service. In addition, the model can be adjusted for the case where the service is provided by a group of K identical operators, each operator is capable to handle all types of service, but each service type has a different priority.*

Keywords: MULTINOMIAL MODEL, QUEUING, MACHINE INTERFERENCE PROBLEM, MULTIPLE SERVICE TYPES, PRIORITY.

1. Introduction

The presented multinomial approach to the machine interference problem was recently developed by Hadad et al. [1], Gurevich et al. [2]-[3] and Keren et al. [4]. The proposed models are applicable for a production system with *N* identical machines that produce the same product in parallel and independently of each other. Each of N identical machines randomly requests several different service types. Each request for a service type is fulfilled by an operator who can provide only one service type. Firstly, we shortly outline the basic model proposed by Hadad et al. [1] that allows the calculation of the expected interference time in the queue for each service type. The advantages of this model are that it is much easier to apply compared to the Markovian models and it does not need any restrictive assumptions about failure rate and service distribution, as those of the Markovian models. Afterward, we present the extended version of the model that allows calculation of the exact distribution function of the steady state waiting time and total service time (waiting time + service time) for each type of requested service. These distributions functions are useful for the case in which there is a time limit for one service (or more), such that it must be accomplished within a certain time from the moment of the request. A delay in the service above a given time spoils the product and makes it useless for its intended purpose. Finally, we adjust the basic model for the case where the service is provided by a group of K identical operators, each operator is capable to handle all types of service, but each service type has a different priority. The presented models enable practitioners to determine the optimal number of operators in order to minimize the cost per unit of product or maximize the total profit, or to set other performance measures.

2. The basic model

The model is suitable for MIP with multiple service type requests. Each request can be handled by a qualified operator that assigned to only one service type. At least one operator is assigned for each service type, but the number of operators may not exceed the number of machines, *N*.

2.1. The model assumptions

The following list sets forth the assumptions used in creating the model:

1) There are *N* identical machines.

2) Each machine can be in one of the following positions, where the probabilities for each position are constant in a steady state situation and identical for all machines:

   a. running (producing items),

   b. having a type j service, $j=1,...,J$,

   c. waiting for type j service (interference).

3) Machine failures are independent.

4) Service time is random.

5) Each service request transfers immediately to the operators assigned to handle that specific service request type.

6) An available operator handles a service request immediately.

7) Each service request is handled by only one operator.

8) Walking time from one machine to another is negligible.

9) A machine is idle while waiting for a service or while getting a service.

2.2. Notations

This section presents the notations that are used for the model definition.

T - Runtime**.** The length of time needed for a machine to process one unit of a product.

t_j - Average time of a type j service, $j=1,...,J$. The average length of time that a type j operator invests in one unit of a product during a cycle time.

H_1 - Cycle time. The length of time needed for one machine and one operator for each service type to produce one unit of the product. This cycle time is calculated as follows:

$$H_1 = T + \sum_{j=1}^{J} t_j \ . \qquad (1)$$

The parameters T, t_j and H_1 are not dependent upon the number of machines (N).

N - Number of machines. The number of identical machines in the production line.

H_N - Adjusted cycle time. The expected length of time needed for a production line with N identical machines that are operated by a given number of operators for each service type to

produce N units of the product. (During H_N each machine produces an average of one unit.)

t_{I_j} - Interference time. The average time during a production cycle (H_N) during which a machine is idle because it is waiting for a type j operator, $j=1,...,J$.

i_j - Interference rate. The ratio between the interference time t_{I_j} and the adjusted cycle time H_N , that is, $i_j = {t_{I_j}}/{H_N}$.

S_j - Service rate. The ratio between the average time of a type j service t_j and the adjusted cycle time H_N , that is, $S_j = {t_j}/{H_N}$.

K_j - Number of operators assigned to type j service, $1 \le K_j \le N$.

The adjusted cycle time H_N is calculated as follows:

$$H_N = T + \sum_{j=1}^{J} t_j + \sum_{j=1}^{J} t_{I_j} \qquad (2)$$

$$= H_1 + \sum_{j=1}^{J} t_{I_j} = H_1 + \sum_{j=1}^{J} i_j \times H_N$$

$$= \frac{H_1}{\left(1 - \sum_{j=1}^{J} i_j\right)} .$$

p_0 - Probability that a machine is running. This probability is calculated as follows:

$$p_0 = \frac{T}{H_N} = \frac{T\left(1 - \sum_{j=1}^{J} i_j\right)}{H_1}.$$

p_j - Probability that a machine is getting or requiring a type j service, $j=1,...,J$. This probability is calculated as follows: $p_j = S_j + i_j,\ j=1,...,J$.

Each machine can be in one of two states-running or idle. The idle state has J sub-states for each service type request. A machine in sub-state j can be in one of two positions-getting a service j or waiting for this service. Because all these states are mutually exclusive, it is clear that $p_0 + \sum_{j=1}^{J} p_j = 1$.

X_0 - Number of running machines (a random variable).

X_j - Number of machines that are getting or requiring a type j service (a random variable), $j=1,...,J$. It is clear that $X_0 + \sum_{j=1}^{J} X_j = N$, where the number of running machines and the number of idle machines is equal to the number of machines in production line N .

A group with *N* machines and *J* types of service has $\binom{N+J}{J}$ states. A state is a vector $\left(X_0 = x_0, X_1 = x_1, ..., X_J = x_J\right)$, where X_0 is the number of running machines and X_j, $j=1,2,...,J$, is the number of idle machines that are getting or requiring a type j service. The probability of each state can be calculated using the multinomial distribution as shown in equation (3):

$$P\left(X_0 = x_0, X_1 = x_1, ..., X_J = x_J\right)$$

$$= \begin{cases} \dfrac{N!}{\prod_{j=0}^{J} x_j!} \prod_{j=0}^{J} \left(p_j\right)^{x_j} & \text{where } \sum_{j=0}^{J} x_j = N \\ 0 & \text{otherwise} \end{cases} . \qquad (3)$$

2.3. An interference calculation

This section presents the interference rate calculation derived directly from the multinomial distribution properties.

Step 1- Perform time study/work measurement to measure and to determine the running time T and the time for each service type t_j $(j=1,2,...,J)$. Use the measured data and equation (1) to calculate H_1.

Step 2 – Calculate $E\left(L_j\right)$, the expected number of machines waiting for type j service, $j=1,...,J$. According to the model assumptions, the number of machines requiring a type j service has a binomial distribution with expected value computed by:

$$E(X_j) = \sum_{m=0}^{N} P\left(X_j = m\right) \times m = N \times p_j .$$

Then, $E\left(L_j\right)$ has the form

$$E\left(L_j\right) = \sum_{m=K_j+1}^{N} P\left(X_j = m\right) \times \left(m - K_j\right) \qquad (4)$$

$$= N \times p_j - K_j$$

$$+ \sum_{m=0}^{K_j} \binom{N}{m} \left(p_j\right)^m \left(1 - p_j\right)^{N-m} \times \left(K_j - m\right) .$$

(see [1]).

Step 3 – Calculate i_j, the interference rate, as follows:

$$i_j = \frac{E\left(L_j\right)}{N}.$$

Since $p_j = i_j + S_j = i_j + t_j\left(1-\sum_{j=1}^{J} i_j\right)/H_1$, by (4), the previous equation has the following form:

$$i_j = \left(i_j + \frac{t_j}{H_1}\left(1-\sum_{j=1}^{J} i_j\right)\right) - \frac{K_j}{N} \qquad (5)$$
$$+ \sum_{m=0}^{K_j}\binom{N}{m}\left(\left(i_j + \frac{t_j}{H_1}\left(1-\sum_{j=1}^{J} i_j\right)\right)\right)^m$$
$$\times\left(1-\left(i_j + \frac{t_j}{H_1}\left(1-\sum_{j=1}^{J} i_j\right)\right)\right)^{N-m} \times\left(K_j - m\right)$$
$$\frac{}{N}.$$

Equation (5) produces a system of J equations, one for each service type. The solution of these J equations is the interference rate. This system of J equations has a uniquely feasible solution as derived from the multinomial distribution properties (see [1]). The solution can be obtained by "trial and error" or by software tools such as Excel-Solver.

3 Distribution of the steady state waiting time and total service time

This section considers a production line with N identical machines, as was presented in Section 2. An additional assumption here is that the service time of a specific service type j has an exponential distribution with the parameter λ_j. For all service types other than j, the additional assumption related to the exact service time distribution is not needed. The section presents exact CDFs for the steady state waiting time and total service time for service type j, $j=1,...,J$, in the context of FCFS queue discipline.

The first step in deriving these distributions is evaluation of the inputs of the model described in section 2 (the machine runtime and the average time of each service type) by work study (Hadad et al. [5]). The second step is to use the model described in section 2 to calculate the probability that a machine is getting or requiring a type j service, p_j. Let us define the following random variables:

W_j - the steady state waiting time of a machine for a type j service, $j=1,...,J$, (the waiting time from the moment of the request for this service until the moment the requested service is commenced.)

TS_j - the steady state total service time (waiting time + service time) of a machine for a type j service, $j=1,...,J$, from the moment of the request for this service until completion of the requested service.

The following Proposition 1 provides the CDF of the steady state waiting time W_j and total service time TS_j of a machine for service type j, $j=1,...,J$, in the context of the FCFS queue discipline.

Proposition 1. Given that the queue discipline is FCFS, for any value of time $y>0$, the probability that the steady state waiting time W_j is longer than y is:

$$P\left(W_j > y\right) \qquad (6)$$
$$= \sum_{r=1}^{N-K_j}\left(\binom{N}{r+K_j}\times\left(p_j\right)^{r+K_j}\times\left(1-p_j\right)^{N-r-K_j}\right.$$
$$\left.\times\left(\sum_{n=0}^{r-1} e^{-\lambda_j\times K_j\times y}\times\frac{\left(\lambda_j\times K_j\times y\right)^n}{n!}\right)\right).$$

The probability that the steady state total service time TS_j is longer than y is:

$$P\left(TS_j > y\right) = e^{-\lambda_j\times y}\times\left(\sum_{m=0}^{K_j}\binom{N}{m}\times\left(p_j\right)^m\times\left(1-p_j\right)^{N-m}\right) \qquad (7)$$
$$+\sum_{r=1}^{N-K_j}\left(\binom{N}{r+K_j}\times\left(p_j\right)^{r+K_j}\times\left(1-p_j\right)^{N-r-K_j}\right.$$
$$\left.\times\left(\int_0^y\left(\sum_{n=0}^{r-1} e^{-\lambda_j\times K_j\times(y-x)}\times\frac{\left(\lambda_j\times K_j\times(y-x)\right)^n}{n!}\right)\times\lambda_j e^{-\lambda_j\times x}dx + e^{-\lambda_j\times y}\right)\right).$$

Note that the integral in Equation (7) can be easily calculated numerically.

4. Different priorities of service types

This Section presents an adjusted model for the case where the service is provided by a group of K identical operators, each operator is capable to handle all types of service, but each service type has a different priority. The service types are ranked according to their priorities. The operators serve the machines (handling the requests) according to these priorities. For example, if two machines are waiting for different service types and only one operator is available, the operator will serve the machine that requests the service type with the higher priority. The machines are served according to the absolute priority policy (a preemptive priority). When all the operators are busy and an additional machine requests a service with a higher priority than one of the machines currently being served, the lowest priority service type that is provided ceases immediately and the operator serves the machine with the higher priority service type. When a ceased service is resumed, this service is accomplished from the point where it was preempted without loss of the prior work. If there are several machines with the same priority, and there are not enough operators available to service all of them, machines are randomly selected to be served. The probability of each state of the production system $\left(X_0 = x_0, X_1 = x_1, ..., X_J = x_J\right)$ can be calculated using the multinomial distribution as shown in equation (3). According to the model assumptions, the expected number of machines that are getting or requiring a type 1 service (with the highest priority) has a binomial distribution with an expected value computed by:

$$E(X_1) = \sum_{m=0}^{N} P\left(X_1 = m\right)\times m = N\times p_1.$$

Hence, for $K=1,...,N-1$, $E\left(L_1\right)$ (the expected number of

machines that are waiting for a type 1 service) is calculated as:

$$E(L_1) = \sum_{m=K+1}^{N} P(X_1 = m) \times (m-K) = \sum_{m=K+1}^{N} \binom{N}{m} (p_1)^m (1-p_1)^{N-m} \times (m-K) \ . \quad (8)$$

It is obvious that for $K = N$, $E(L_1) = 0$. The ratio between the expected number of machines that are waiting for a type 1 service and the total number of the machine is the interference rate for type 1 service, $i_1 = E(L_1) / N$ (see [6]).

Under the model assumptions, the machines are served according to the absolute priority policy. Therefore, the number of machines waiting for the type 1 service does not depend on the number of machines requiring or getting service types with lower priority. The number of machines that are waiting for type j, $2 \le j \le J$, service depends on the number of machines requiring or getting service types with higher priority. The expected number of machines that are waiting for type j service is calculated as follows for any $2 \le j \le J$:

$$E(L_j) = \sum_{n=0}^{N} E\left(L_j \left| \sum_{i=1}^{j-1} X_i = n \right. \right) \times P\left(\sum_{i=1}^{j-1} X_i = n \right), \quad (9)$$

where

$$P\left(\sum_{i=1}^{j-1} X_i = n \right) = \binom{N}{n} \left(\sum_{i=1}^{j-1} p_i \right)^n \left(1 - \sum_{i=1}^{j-1} p_i \right)^{N-n} \quad (10)$$
$$n = 0,1,...,N,$$

because according to the model assumptions $\sum_{i=1}^{j-1} X_i \sim Bin\left(N, \sum_{i=1}^{j-1} p_i \right)$. Thus, straightforwardly we have for any $1 \le K \le N-1, 2 \le j \le J$, the expected number of machines that are waiting for type j service is presented by the following equation:

$$E(L_j) = \sum_{n=0}^{N} \left(\left(\sum_{m=\max(0,K-n+1)}^{N-n} \left[\left(\binom{N-n}{m} \left(\frac{p_j}{1-\sum_{i=1}^{j-1} p_i} \right)^m \left(1 - \frac{p_j}{1-\sum_{i=1}^{j-1} p_i} \right)^{N-n-m} \right) \times (m - \max(0, K-n)) \right] \right) \times \binom{N}{n} \left(\sum_{i=1}^{j-1} p_i \right)^n \left(1 - \sum_{i=1}^{j-1} p_i \right)^{N-n} \right) . \quad (11)$$

The interference rates i_j are calculated as follows:

$$i_j = \frac{E(L_j)}{N}, \ j = 1,...,J . \quad (12)$$

By substitution of $p_j = i_j + S_j = i_j + t_j \left(1 - \sum_{j=1}^{J} i_j \right) / H_1$, and by calculating $E(L_j)$ as defined by equation (8) and equation (11), equation (12) produces a system of J equations, one for each service type. This system of J equations has a unique feasible solution (see [4]). The solution of these J equations is the interference rate. The solution can be obtained by "trial and error" or by software tools such as Excel-Solver.

5. Conclusions

This paper outlines the multinomial approach to a special case of the machine interference problem where each of N identical machines randomly requests several different service types. The presented models derived by this approach allow the calculation of the expected interference time in the queue for each service type and the exact distribution function of the steady state waiting time and total service time for each type of requested service. The interference times enable practitioners to calculate the adjusted cycle time, the expected number of machines that are waiting for each service type, the workload, the utilization of the machines, and the outputs for any given number of operators and priority.

6. References

1. Hadad Y., Keren, B. and Gurevich, G. (2013). A multinomial model for the machine interference problem with different service types and multiple operators. *Computers & Industrial Engineering*, 66(2), pp: 264-273.
2. Gurevich, G., Hadad, Y. and Keren, B. (2015a). Calculation of the steady state waiting time distribution in the context of the machine interference problem. *International Journal of Operational Research*, in press.
3. Gurevich, G., Keren, B. & Hadad, Y. (2015b). The economic number of operators for the machine interference problem with heterogeneous machines and preemptive priority. *International Journal of Logistics Systems and Management*, in press.
4. Keren, B., Gurevich, G. and Hadad, Y. (2015). Machines interference problem with several operators and several service types that have different priority. *International Journal of Operational Research*, in press.
5. Hadad, Y., Keren, B. and Hanani, Z.M. (2014). The number of measurements to be performed for time study analysis. *European Journal of Industrial Engineering*, 8(2): 222-243.
6. Jones, D.W. (1971) Work measurement of multi machine assignments, 3.92-3.112 of Maynard HB., *Industrial Engineering Handbook*, McGraw-Hill: New-York.

STRUCTURAL AND KINEMATIC ASPECTS OF A NEW ANKLE REHABILITATION DEVICE

PhD. Stud. Eng. Racu (Cazacu) C.[1], Prof. Dr. Eng. Doroftei I.[2]
Faculty of Mechanical Engineering – "Gheorghe Asachi" Tehnical University of Iasi, Romania [1,2]

[1]cristina.racu@tuiasi.ro , [2]idorofte@mail.tuiasi.ro

Abstract: *The goal of this paper is to propose a new ankle rehabilitation platform, which can realize a large range of ankle related foot movements. In designing the rehabilitation system, we assume that the device must provide dorsiflexion/plantar flexion and inversion/eversion movements, necessary for complete recovery of the ankle joint. Therefore the system must be spatial oriented (rotations around two perpendicular axes, hence two degrees of freedom). The device should aim to achieve low cost, low weight and ease of practical realization of the device. We present structural and kinematic aspects of the proposed device for ankle rehabilitation.*

Keywords: ANKLE REHABILITATION, KINEMATICS, ROBOTIC DEVICE

1. Introduction

The ankle joint forms a junction between the leg and the foot, turned into a horizontal mobile platform, adaptable to irregularities of the surface. Due to its important role in human locomotion, the ankle is the most injured segment of the lower limb. Ankle injuries can be divided into ligament tears, fractures and sprains (last one is the most encountered). Higher rates of ankle sprain appear to men between 15 and 24 years old, and also woman over 30 have higher rates than men [1]. Most ankle injuries occur either during sports activities or while walking on an uneven surface that forces the foot and ankle into an unnatural position.

The treatment of any injury of this articulation consists in three phases:

- treating swelling with ice, rest and anti-inflammatory drugs;
- starting the recovery through exercises that aim to restore joint mobility;
- resumption of sports activities and continuing the recovery exercises.

Several mechanisms have been developed for helping the therapists in the recovery of the ankle. In some recuperations centers, patients still use primitive mechanisms such as elastic bands and foam shapes for balance exercises. There is a tendency of using a programmable robotic system to provide a wide range of exercises, and also to reduce the physical effort due to their repetitive nature and, furthermore, to store the patient's evolution. To meet this need several various rehabilitation systems were developed, that can be divided into: robotic systems (under the form of parallel mechanisms), orthoses and exoskeletons.

Most encountered rehabilitation parallel mechanisms are Stewart platforms [2]. Some devices use two platforms, one fixed and one mobile, providing three degrees of freedom [3] with various types of actuators, from artificial muscles to brush DC motors. Most common and used rehabilitation devices for ankle injuries are ankle-foot orthosis. The main purpose of these devices is to achieve low weight and ease of operation. They can be powered by a wide range of actuators [4,5]. Powered exoskeletons are mainly used for learning gait, but also can be used in recovery, especially for the ankle joint, which supports all human body's weight.

For a healthy ankle, normal movements are presented in figure 1. For most people, the angle range of ankle movements varies as following: plantar flexion, 25 to 50 degrees; dorsiflexion, 20 to 25 degrees; inversion, 35 to 40 degrees; eversion, 0 to 25 degrees; adduction, 25 to 30 degrees; abduction, 25 to 30 degrees [6].

Starting from the basic ankle movements, we propose a 2 DOF mechanism, which could recover the plantar flexion/dorsiflexion and inversion/eversion movements.

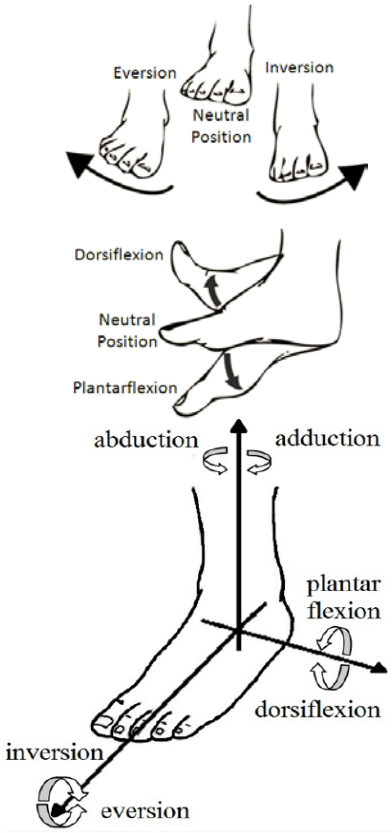

Fig. 1. *Normal ankle movements*

2. Structural aspects

Our goal is to find light weight, low cost and easy to manufacture solutions for ankle rehabilitation platforms. The proposed solution should consider offering the two movements (flexion-extension and inversion-eversion) necessary for a complete recovering of the injured ankle, resulting in two degrees of freedom.

We propose a solution, based on simple four bars mechanism, presented in Fig. 2. This device has a fixed frame (link 0) connected to the ground and also to the shank. The foot will be placed on the plate 4 and the ankle joint will be forced to be recovered for the two mentioned movements. The actuated links are 1 and 1' and the plate 4 is the driven link. If we rotate links 1 and 1' with same angle, $\theta_1 = \theta_1'$ (both in clockwise or counterclockwise direction), the plate 4 will be driven with θ_4' angle, producing the flexion-extension of the ankle joint.

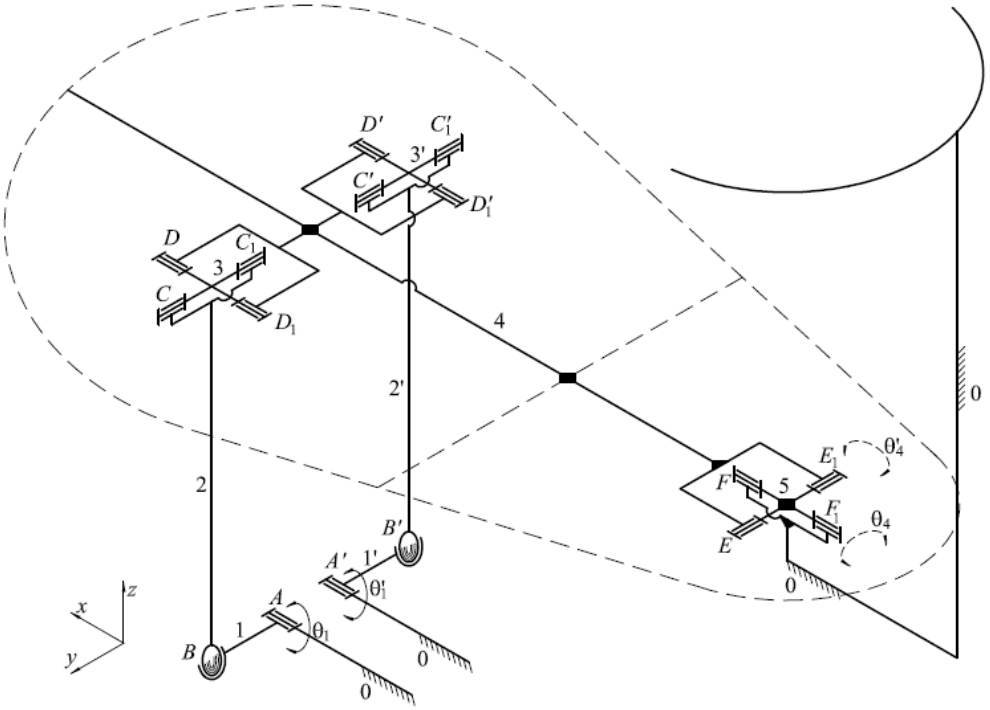

Fig. 2. *Kinematics of the proposed mechanism, for a platform-based version*

If these mentioned links are rotated with the same angle but in opposite direction, $\theta_1 = -\theta'_1$ the plate 4 will be driven with θ_4 angle, producing the eversion-inversion movement.

To compute the degree of mobility, we use Kutzbach formula for a spatial mechanism:

$$M = 6(n-1-j)+\sum_{i=1}^{j} f_i\,, \tag{1}$$

where: n is the number of links (including the frame); j is the number of kinematic pairs (joints); f_i represents the degrees-of-freedom of the i^{th} kinematic pair. For our mechanism, n = 9, j = 10 (8 rotational joins with f = 1 and two spherical joints with f = 3). It means,

$$M = 6(9-1-10)+8\cdot 1+2\cdot 3 = 2\ \ DOF\,, \tag{2}$$

which means that we need two actuators to drive the mechanism (*A* and *A'* joints in Fig. 2).

3. Kinematic aspects

The link 4 from our mechanism will support the sole, which has to be fixed (through some belts) on it. As we mention before, if the links 1 and 1' are rotating with the same angle, $\theta_1 = \theta'_1$, the link 4 will be driven with θ_4 angle, around *x* axis, producing inversion-eversion movement of the ankle joint. If these links are rotating with the same angle but in opposite direction, $\theta_1 = -\theta'_1$, the link 4 will be driven with θ'_4 angle, around *y* axis, producing plantar flexion-dorsiflexion movement [7].

In figure 3 we present the equivalent decoupled mechanisms for both inversion-eversion movement (a) and flexion-dorsiflexion movement (b).

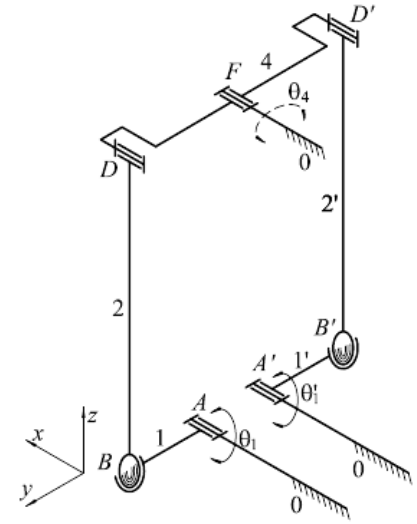

(a)

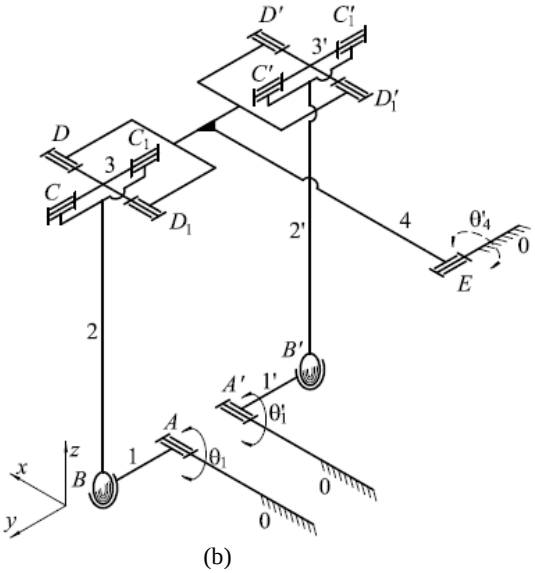

(b)

Fig. 3. *Equivalent decoupled mechanisms: a) for inversion-eversion movement; b) for flexion-dorsiflexion movement*

For the inversion-eversion movement (Fig 3.a) the simplified mechanism has two actuated links, but it could work using a single motor, the second one being redundant. The main condition for the correct operation of this mechanism is to impose the control of the motors as $\theta_1 = \theta_1^{'}$, or else the mechanism will be blocked.

To write inverse kinematics, an equivalent mechanism, using a single motor, will be considered (see Fig. 4). The position loop closure equation can be written as following

$$\overline{l_1} + \overline{l_2} + \overline{l_4} + \overline{l_2} + \overline{a} = \overline{0}\,, \tag{3}$$

or

$$\begin{cases} l_1 \cdot \cos\theta_1 + l_2 \cdot \cos\theta_2 - l_4 \cdot \cos\theta_4 + a = 0 \\ l_1 \cdot \sin\theta_1 + l_2 \cdot \sin\theta_2 - l_4 \cdot \sin\theta_4 - l_2 = 0 \end{cases}, \tag{4}$$

where θ_i is the angle measured from *y* axis direction to the *i* link axis, being positive if the rotation of this link is clockwise.

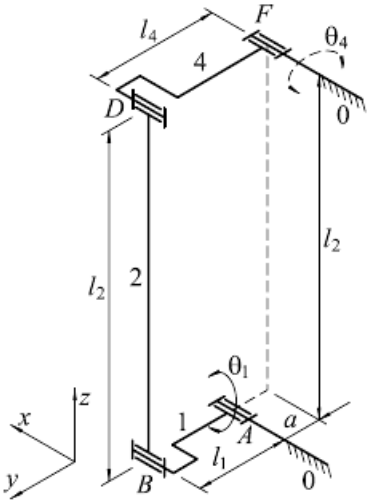

Fig. 4. *Equivalent mechanism with one DOF for inversion-eversion movement*

Solving equations (4) we will get

$$\theta_1 = \operatorname{atan2}\left(\frac{-u}{\sqrt{t^2+u^2}}, \frac{-t}{\sqrt{t^2+u^2}}\right) \pm \arccos\left(\frac{-l_1^2 + l_4^2 - t^2 - u^2}{2l_1\sqrt{t^2+u^2}}\right), \tag{5}$$

with $t = -l_4\cos\theta_4 + a,\ \ u = -l_4\sin\theta_4 - l_2$.

Let now consider a mechanism with one DOF for plantar flexion-dorsiflexion movement (see Fig. 5). Spherical joint, in this case, may be replaced by an universal joint (see Fig. 6). First, if we apply standard Denavit - Hartenberg convention to this closed-loop mechanism, we get the parameters presented in Table 1. Based on these, we will write the transition homogeneous transformation matrixes that express the position and orientation of the current frame with respect to the previous one. Multiplying all these matrixes we will get the total homogeneous transformation matrix of the mechanism that expresses the position and orientation of the last frame with respect to the referential frame.
The orientation loop closure equation for our mechanism can be written as following

$${}_5^0R = {}_1^0R \cdot {}_2^1R \cdot {}_{2'}^2R \cdot {}_3^{2'}R \cdot {}_4^3R \cdot {}_5^4R = I\,, \tag{6}$$

where ${}_i^{i-1}R$ is the transition orientation matrix that expresses the orientation of the $\{i\}$ frame with respect to the $\{i-1\}$ frame.

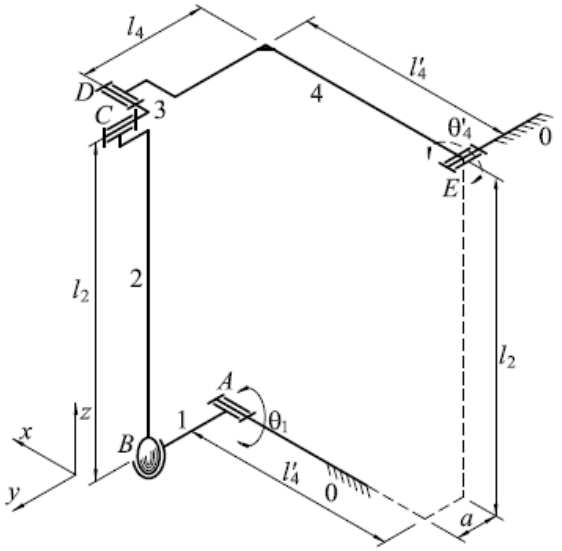

Fig. 5. *Real mechanism for flexion-dorsiflexion movement*

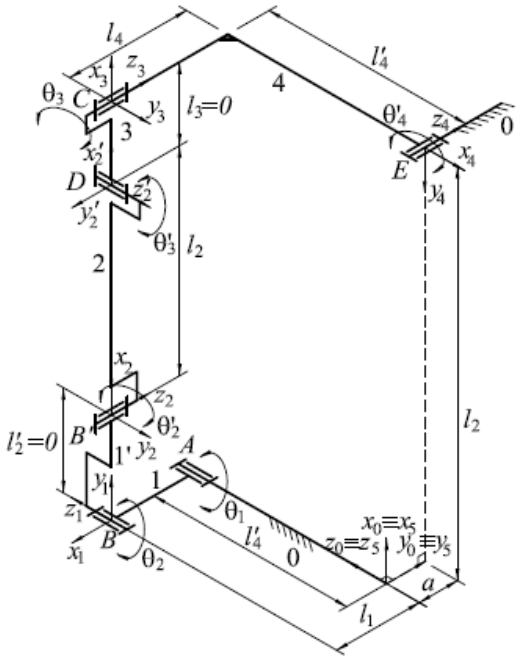

(b)

Fig. 6. *Equivalent mechanism with one DOF for flexion-dorsiflexion movement*

Table 1. *Standard Denavit-Hartenberg parameters*

Link	a_i	α_i	d_i	θ_i
1	l_1	0	$l_4^{'}$	$\theta_1 - \pi/2$
2	0	$-\pi/2$	0	$\theta_2 + \pi/2$
2’	l_2	$-\pi/2$	0	$\theta_2^{'}$
3	0	$\pi/2$	0	$\theta_3^{'}$
4	$l_4^{'}$	0	l_4	$\theta_3 + \pi/2$
5	$-l_2$	$\pi/2$	$-a$	$\theta_4^{'} - \pi/2$

The position loop closure equation can be written as following

$$\overline{r_1} + \overline{r_2} + \overline{r_3} + \ldots + \overline{r_n} = \overline{0}\,, \tag{7}$$

where $\overline{r_i}$ is a vector drawn from the origin of the frame $\{i-1\}$ to the origin of the $\{i\}$ frame.

The following equation is obtained according to standard Denavit - Hartenberg convention,

$$^{0}\overline{r_i} = d_i \cdot {}_{i-1}^{0}R \cdot \overline{z} + a_i \cdot {}_{i}^{0}R \cdot \overline{x}\,, \tag{8}$$

where $^{0}\overline{r_i}$ represents the column matrixes form of $\overline{r_i}$ defined in $\{0\}$ referential.

Thus equation (7) can be written in the following form,

$$\begin{matrix} d_1 \cdot \overline{z} + a_1 \cdot {}_{1}^{0}R \cdot \overline{x} + d_2 \cdot {}_{1}^{0}R \cdot \overline{z} + a_2 \cdot {}_{2}^{0}R \cdot \overline{x} + ... \\ ... + d_n \cdot {}_{n-1}^{0}R \cdot \overline{z} + a_n \cdot {}_{n}^{0}R \cdot \overline{x} = \overline{0} \end{matrix}\,, \tag{9}$$

The loop closure equations written above are two fundamental matrix equations by which the general displacement equation of any spatial linkage is obtained. According to equation (7), the next equation can be written for our mechanism

$$\begin{matrix} l_4^{'} \cdot \overline{z} + l_1 \cdot {}_{1}^{0}R \cdot \overline{x} + l_2 \cdot {}_{2'}^{0}R \cdot \overline{x} + l_4 \cdot {}_{3}^{0}R \cdot \overline{z} + l_4^{'} \cdot {}_{4}^{0}R \cdot \overline{x} - \\ - a \cdot {}_{4}^{0}R \cdot \overline{z} - l_2 \cdot {}_{5}^{0}R \cdot \overline{x} = \overline{0} \end{matrix}\,, \tag{10}$$

Considering equation (6), next equations are obtained,

$${}_{1}^{0}R = \begin{bmatrix} \sin\theta_1 & \cos\theta_1 & 0 \\ -\cos\theta_1 & \sin\theta_1 & 0 \\ 0 & 0 & 1 \end{bmatrix}, \tag{11}$$

$${}_{2'}^{0}R = \begin{bmatrix} \cos(\theta_1+\theta_2)\cos\theta_2^{'} & \sin(\theta_1+\theta_2) & -\cos(\theta_1+\theta_2)\sin\theta_2^{'} \\ \sin(\theta_1+\theta_2)\cos\theta_2^{'} & -\cos(\theta_1+\theta_2) & -\sin(\theta_1+\theta_2)\sin\theta_2^{'} \\ -\sin\theta_2^{'} & 0 & -\cos\theta_2^{'} \end{bmatrix}, \tag{12}$$

$$\begin{matrix} {}_{3}^{0}R = \left({}_{5}^{3}R\right)^{-1} = \left({}_{4}^{3}R \cdot {}_{5}^{4}R\right)^{-1} = \\ = \begin{bmatrix} \cos\left(\theta_3+\theta_4^{'}\right) & -\sin\left(\theta_3+\theta_4^{'}\right) & 0 \\ 0 & 0 & -1 \\ \sin\left(\theta_3+\theta_4^{'}\right) & \cos\left(\theta_3+\theta_4^{'}\right) & 0 \end{bmatrix}, \end{matrix} \tag{13}$$

$${}_{4}^{0}R = {}_{5}^{4}R^{-1} = \begin{bmatrix} \sin\theta_4^{'} & \cos\theta_4^{'} & 0 \\ 0 & 0 & -1 \\ -\cos\theta_4^{'} & \sin\theta_4^{'} & 0 \end{bmatrix}, \tag{14}$$

$${}_{5}^{0}R = \begin{bmatrix} 1 & 0 & 0 \\ 0 & 1 & 0 \\ 0 & 0 & 1 \end{bmatrix}. \tag{15}$$

Substituting from (11)-(15) into equation (10), we get:

$$\begin{matrix} l_4^{'} \cdot \overline{z} + l_1 \cdot \sin\theta_1 \cdot \overline{x} - l_1 \cdot \cos\theta_1 \cdot \overline{y} + l_2 \cdot \cos(\theta_1+\theta_2) \cdot \cos\theta_2^{'} \cdot \overline{x} + \\ + l_2 \cdot \sin(\theta_1+\theta_2) \cdot \cos\theta_2^{'} \cdot \overline{y} - l_2 \cdot \sin\theta_2^{'} \cdot \overline{z} - l_4 \cdot \overline{y} + l_4^{'} \cdot \sin\theta_4^{'} \cdot \overline{x} - \\ - l_4^{'} \cdot \cos\theta_4^{'} \cdot \overline{z} + a \cdot \overline{y} - l_2 \cdot \overline{x} = \overline{0} \end{matrix} \tag{16}$$

This results in the following equations,

$$\begin{cases} l_1 \cdot \sin\theta_1 + l_2 \cdot \cos(\theta_1+\theta_2) \cdot \cos\theta_2^{'} + l_4^{'} \cdot \sin\theta_4^{'} - l_2 = 0 \\ -l_1 \cdot \cos\theta_1 + l_2 \cdot \sin(\theta_1+\theta_2) \cdot \cos\theta_2^{'} - l_4 + a = 0 \\ l_4^{'} - l_2 \cdot \sin\theta_2^{'} - l_4^{'} \cdot \cos\theta_4^{'} = 0 \end{cases}. \tag{17}$$

From this equations we obtain the inverse kinematics solution, $\theta_1 = f\left(\theta_4\right)$ for the flexion-dorsiflexion movement.

4. Conclusion

In this paper a simple solution of ankle rehabilitation platform has been proposed, based on the four bar mechanism. The solution has two degrees of freedom, in order to offer the two required movements for a complete recovery of the injured ankle. Some structural and kinematic aspects are presented in this paper. It's 3D design, some simulations, control aspects and experimental results will be presented in future papers.

Acknowledgement

This work was supported by the strategic grant POSDRU/159/1.5/S/133652, co-financed by the European Social Fund within the Sectorial Operational Program Human Resources Development 2007 – 2013.

References

[1]http://www.webmd.com/fitness-exercise/ankle-injuries-causes-and-treatments , june 2015;

[2] Racu (Cazacu), C.M., I. Doroftei, An overview on ankle rehabilitation devices, Advanced Materials Research vol. 1036, 2014, p. 781-786 ;

[3] Jamwal, P.K., S. Xie, K.C. Aw, Kinematic design optimization of a parallel ankle rehabilitation robot using modified genetic algorithm, Robotics and Autonomous Systems vol.57, 2009, p. 1018- 1027;

[4] Pittaccio, S., S. Viscuso, An EMG- Controlled SMA device for the rehabilitation of the ankle joint in post-acute stroke, Journal of materials engineering and performance vol.20, 2011, p. 666-670;

[5] Ferris, D.P., K.E. Gordon, G.S. Sawicki, A. Peethambaran, An improved powered ankle-foot orthosis using proportional myoelectric control, Gait&Posture, vol.23, 2006, p. 425-428;

[6] Parenteau, C.S., D.C. Viano and P.Y. Petit, Biomechanical Properties of Human Cadaveric Ankle-subtalar Joints in Quasi-static Loading. Journal of Biomechanical Engineering, 120(1):105-110, 1998.

[7] Racu (Cazacu), C.M., I. Doroftei, Structural and Kinematic Aspects of a New Ankle Rehabilitation Device, Applied Mechanics and Materials, vol. 658, 2014, p. 507-512.

STUDY OF A TRIAXIAL SPECIMEN AND A REVIEW FOR THE TRIAXIAL MACHINES

PhD Student Eng. Comanici A. M., Prof. Dr. Eng. Goanta V., Prof. Dr. Eng. Barsanescu P. D.
Faculty of Mechanical Engineering – "Gheorghe Asachi" Technical University of Iaşi, Iasi, Romania
E-mail: ana.comanici@yahoo.com, vgoanta@tuiasi.ro, paulbarsanescu@yahoo.com

Abstract: *The paper presents a review of the most important triaxial testing machines and triaxial specimens from literature. It also includes a finite element analysis of a triaxial specimen. The main feature that is studied refers to the geometry of the specimen so that it is obtained a state of stress as favourable as possible for the fracture to occur.*

KEYWORDS: TRIAXIAL TENSILE TEST, STRESS STATE, FINITE ELEMENT ANALYSIS, SPECIMEN

1. Introduction

In engineering applications, ductile behavior of solid materials is preferred [2]. Reaching the limit stress state of a material signifies in the broad sense, lost of its load bearing capacity. It can occur for example by fracture at brittle materials or appearance of the yield field for materials that shows ductile behavior. Predicting the limit stress state of the material subjected to multiaxial stress is very difficult. Ductile materials under triaxial tests are still insufficiently investigated, but the existing results describe two phenomena:

a) failure cannot take place under the equi-triaxial stress compression state [4];

b) failure of the specimen under triaxial tensile tension is always having a fragile character [3].

2.1 Triaxial testing machines

These machines are based on hydraulic actuators to apply forces to the tested specimens. Active-controlled hydraulic system configurations allows variation ratio of forces acting on the specimen on the desired direction so as to obtain a complete failure envelope.

Calloch and *Marquis* describe their machine as being able to load a cube of material in tension or compression along three perpendicular directions. The machine has been developed by LMT-Cachan and Schenck AG, Darmstadt, Germany and it has six servo hydraulic actuators that actually apply the loads up to 250kN. In front of each actuator there are additional hydrostatic bearings and along each axis the two actuators are coupled together to maintain the loadings. The central point of the specimen is motionless thus avoiding coupling between the different axes of the specimen [1].

A complex electromechanical system for testing, able to apply any combination of loads: tension and / or compression on the three mutual orthogonal axes on a cruciform specimen with its central area thickness reduced compared to the thickness of the arms was designed, manufactured, assembled and evaluated by *Welsh* and *Adams* [8]. *Welsh* triaxial machine is formed from three subsystems: the reaction frame, the test fixture and the computer control system. The main structural component is the reaction frame which provides precise alignment of the six for actuators, of the test fixture in relation with the force actuators and a surface that holds the test fixture. The machine was designed for maximum forces of ±133 kN, but the six force actuators can generate forces up to ±94 kN because of undersized drive motors [6].

A similar system was developed at the University of Castilla – La Mancha –Ciudad Real, Spain [9]. There, the machine has six actuators, six pneumatic grips and six electric gear motor for each actuator. In order to control the displacement or the loads applied to the specimen, the machine has specific software. The measurement of the loads is made with loading cells and the displacements of the actuator are regulated by encoder. The machine has a maximum load of 50 kN/axis and 50 mm/actuator displacement.

The University of Sheffield from United Kingdom also has a triaxial testing machine [5]. Their mac^{2T} machine was designed to satisfy some of the following criteria: multiaxial compression of 100 mm cubic specimens up to 400 MPa at any Lode angle, ability to test in the post-peak range because by monitoring post-peak response the information about ductility and fracture can be obtained, multiaxial compression at temperatures up to 300ºC, complex multi stage experiments following arbitrary pre-programmed loading paths with simultaneous temperature cycling, to minimize the friction on the platen specimen interface, to ensure that the three stresses are delivered centrally on the six faces of the specimen [5]. The load in mac^{2T} is delivered by three 4 MN hydraulic actuators installed in independent, diagonally interlaced loading frames.

3.2 Triaxial specimens

Calloch specimen has the form of a cube. The specimen was subjected to a heat treatment of 1 hour at 1050ºC and in order to ensure initial isotropy of the material the specimen went through a process of annealing in water. This cube was made of 316 austenitic stainless steel, with an edge of 80 mm. Each face of the cube has drilled four 3 mm diameter holes and saw cuttings, which results in a center small cube with 9 mm edge [1].

Welsh specimen is cruciform made out of composite materials with its central area thickness reduced compared to the thickness of the arms [7]. The triaxial specimen has an extension glued on third direction which makes the results difficult to validate. It is 161 mm long across posing 24.8 mm wide loading arms, each of which contain two 4.76 mm diameter holes used to align each set of wedge grips assume a specimen thickness of 4.06 mm and a gage section thickness-taper fillet radius of 12.7 mm [6].

4.3 Geometric parameters of triaxial specimen

The specimens used for spatial state of stress (Fig.1) present some important features that have to be taken into consideration when a finite element analysis is going to be made or if the actual experiments take place.

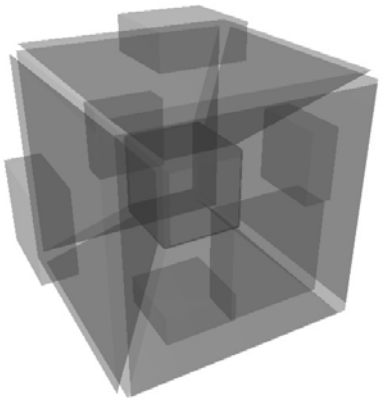

Fig. 1 *Triaxial specimen – spatial view*

Some of those characteristics are: the existence of stress concentrators in the section of the specimen due to how the connection is made (corner region or plain region), a surface where the triaxial testing machine applies the force, a intermediary segment of the specimen which submit to the stress but it only

makes the connection between the surface and the center of specimen. Another important aspect is the calculus method to determinate the stresses from the forces applied on the central cube. For this paper the specimen was considered cubic recreating the Calloch specimen with an edge of 80 mm, 3 mm diameter holes and cuttings, 400 mm2 the surface to apply the loadings (Fig. 2).

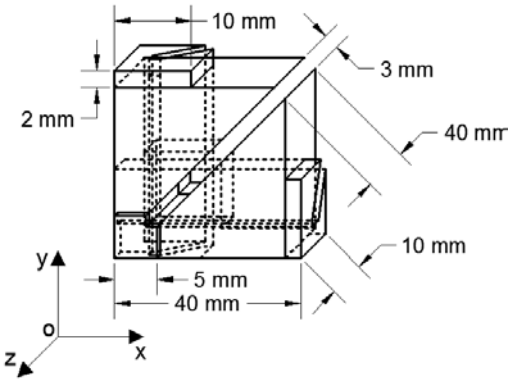

Fig. 2 *The scheme of one eighth of the specimen and dimensions of elements*

5. Finite element analysis

The specimen was tested for triaxial tension with a load of 12 MPa distributed on a surface of 109.3 mm^2 to determine the evolution in plasticity domain. We analyzed one eighth of the initial cube (Fig. 3) due to geometry and loadings symmetry conditions.

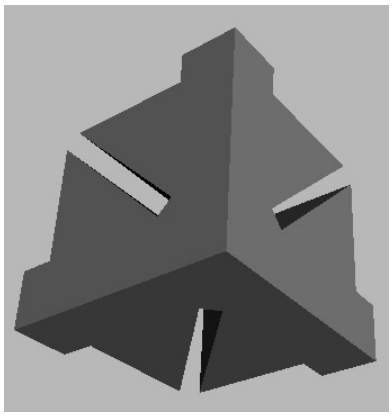

Fig. 3 *One eighth of the specimen*

Boundary conditions imposed to the specimen: no translation on perpendicular plans in relation with symmetry ones, no rotation on the symmetry plans (Fig. 4).

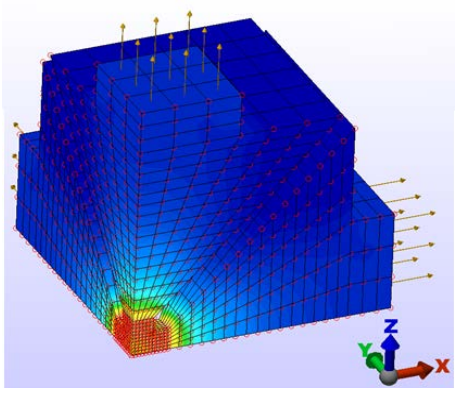

Fig. 4 *Loading and symmetry conditions for the specimen*

The material adopted to perform FEA was AISI 1010 Steel from program's library that has strain hardening modulus of 302.248 MPa, yield strength of 305 MPa and *Young* modulus of 205000 MPa. Simulation was made in ALGOR program, analysis type being "MES with Nonlinear Material Models" and the elements type was "brick". FEA were conducted on two versions of the specimen as they are presented in the following figures.

This study is preliminary in order to validate the finite element analysis of the triaxial specimen and to achieve an optimisation of the geometry so that a state of stress as favourable as possible is obtained. In this paper we have two geometries of the specimen that come from the execution of the canals. The canals diameter is 3 mm on both cases, but first geometry has a canal made with a cutter with sharp tip referred as ***g***eometry 1 and the second geometry is made with a cutter without the angle tip referred as geometry 2. Requirements in composed solicitations are high stress state in failure volume, more uniform stress distribution and stress ratio to be constant till failure.

2.1 Geometry 1

The specimen's canals have been extruded using a cutter with a sharp tip that has an angle of 90º so from a initial cube we would have the gripping parts with a trapezoidal shape, canals of 3 mm and in center would be a full cube that has a side of 10 mm.

Fig. 5, Fig. 6 and Fig 7 are the maps of the stresses and strains in the specimen in the plastic-elastic simulation.

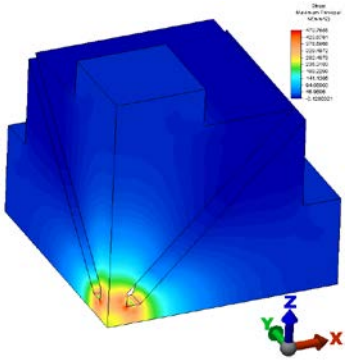

Fig.5 *Maximum principal stress distribution*

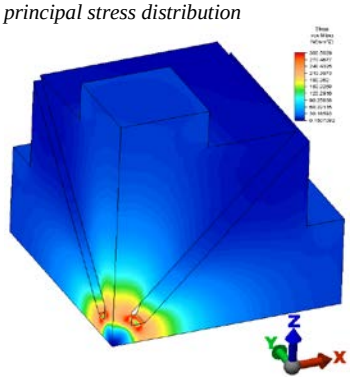

Fig.6 *von Mises stress distribution*

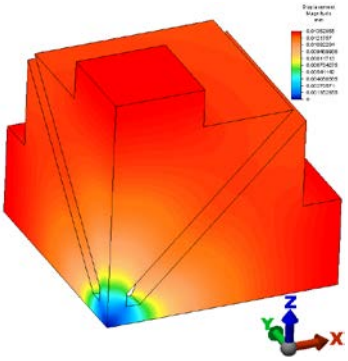

Fig.7 *Displacement magnitude evolution*

Maximum principal stress and *von Mises* stress have a distribution more constant and higher value at the periphery cube which means that the objective of having higher stresses in failure volume is achieved. Even though the maximum principal stresses has a higher value up to 470MPa, the *von Mises* stress is more concentrated with a high end value of 300MPa.

Fig. 8, Fig. 9 and Fig. 10 are the maps for the middle cube of 10mm that was mentioned before. Here we can observe better the stress and displacement that takes place after the loading takes place.

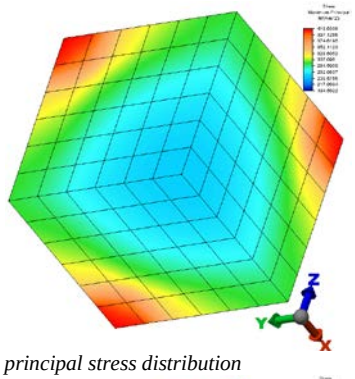

Fig.8 *Maximum principal stress distribution*

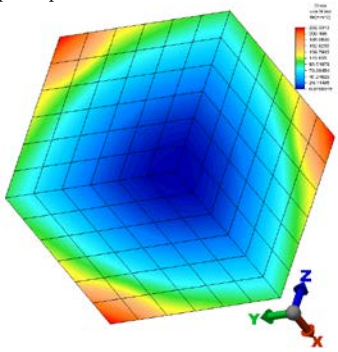

Fig.9 *von Mises stress distribution*

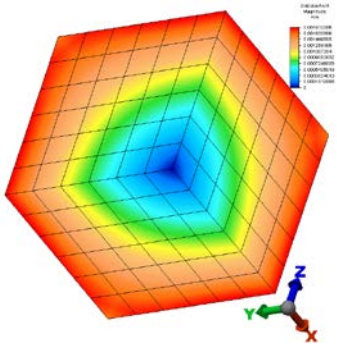

Fig.10 *Displacement magnitude evolution*

2.2 Geometry 2

On the second geometry that has been studied the canals were made with a disk in order to not have any angles in the middle cube.

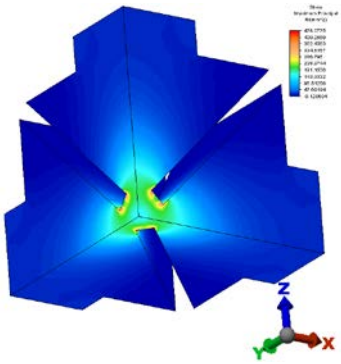

Fig.11 *Maximum principal stress distribution*

The failure will appear at the corners of the periphery cube and will advance towards interior. From Fig. 11 to Fig. 16 it is seen the simmetry of both the stresses and the deformations in relation to planes of symmetry. As a result, the symmetrical loading and support conditions are well defined. On the other hand, it appears that the movement pattern (Fig. 14, 15 and 16) confirms the correct application of boundary condition.

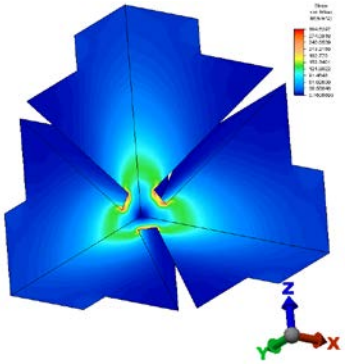

Fig.12 *von Mises stress distribution*

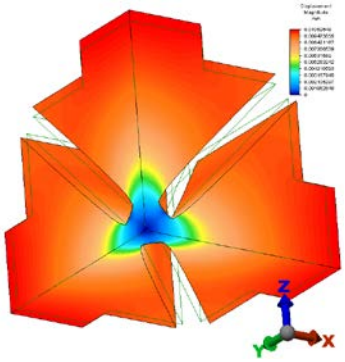

Fig.13 *Displacement magnitude evolution*

In the center of the specimen *von Mises* stresses are equal to zero and the value is obtained in triaxial state of stress using Eq. 2.

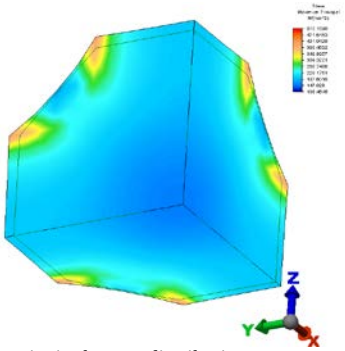

Fig.14 *Maximum principal stress distribution*

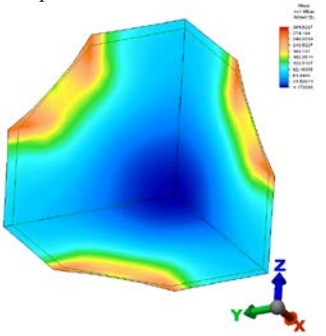

Fig.15 *von Mises stress distribution*

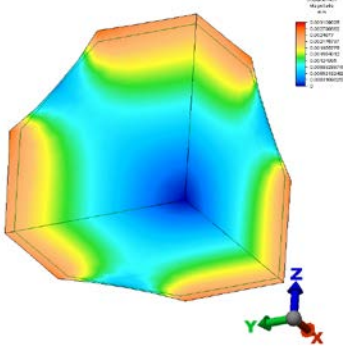

Fig.16 *Displacement magnitude evolution*

3. Results and discussion

Maximum principal stress has higher values in geometry 1 compared with geometry 2, case which is also seen for *von Mises* stress (Fig. 17 and Fig. 18).

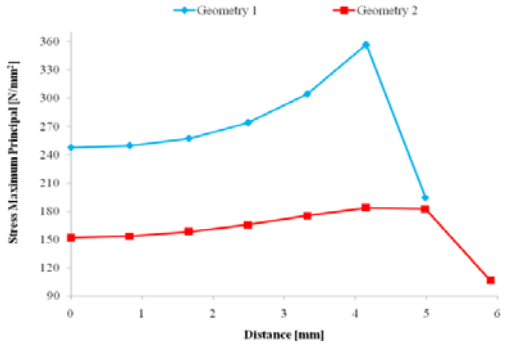

Fig. 17 *Graphic representation of maximum principal stress*

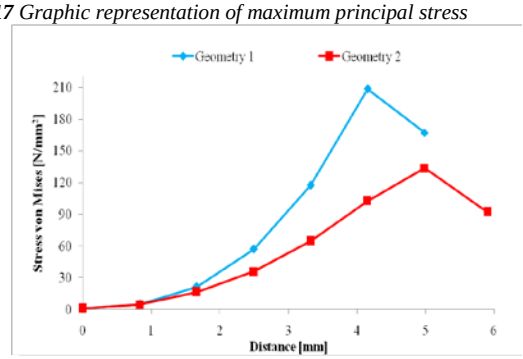

Fig. 18 *Graphic representation for von Mises stress*

According to actual failure theories the yielding stress can be wrote:

i. *Tresca* theory:

(1) $\sigma_y = \sigma_1 - \sigma_3$

ii. *von Mises* theory:

(2) $(\sigma_1 - \sigma_2)^2 + (\sigma_2 - \sigma_3)^2 + (\sigma_3 - \sigma_1)^2 = 2\sigma_y^2$

iii. in case of hydrostatic stress:

(3) $\sigma_1 = \sigma_2 = \sigma_3$

hence the Eq. 1, respectively Eq. 2 will become:

(4) $\sigma_1 = 0$ where σ_1, σ_2, and σ_3 are the maximum principal stresses and σ_v is the yielding stress.

Due to Eq. 4 it shows that the well known failure theories can not be applied on the triaxial state of stress as yielding stress will be all the time at a higher value then zero in order to have the yielding process start within the specimen. It is important to specify that von Mises stress is dangerous even if its value is zero or almost zero in all specimen volume (Fig. 18).

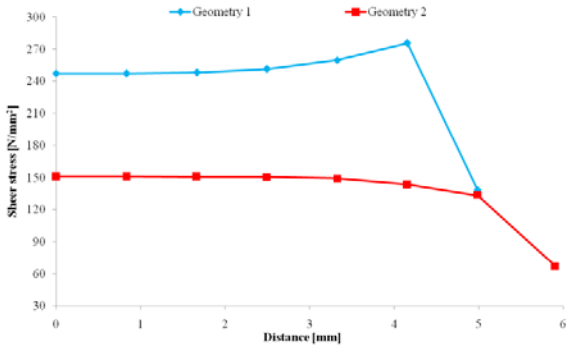

Fig. 19 *Graphic representation of shear stress*

The shear stress describes the fracture zone (Fig. 19) and the displacements magnitude represents the absolute value of the displacements (strain) of the specimen (Fig. 20).

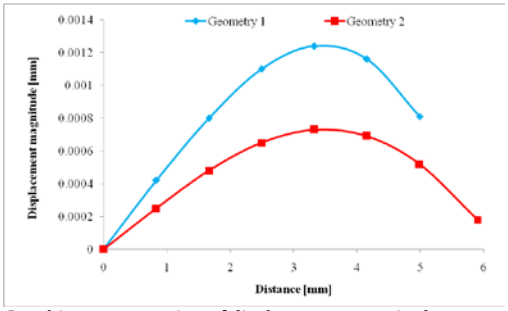

Fig.20 *Graphic representation of displacement magnitude*

4. Conclusions

One of the hypothesis of this paper was the schematization of the stress-strain curve using two lines that give the elasticity modulus (*Young*'s modulus) and plasticity modulus.

Because the triaxial machine are very difficult to make and requires a dedicated data system and considerable resources, with the finite element analysis we want to optimize the shape of the specimen, to obtain a more favorable state of stress or closer to the ideal. This study was made to emphasize the need of a new equi-triaxial state of stress theory because even if *von Mises* stress is zero in the center of the specimen, this happens due to the fact that *von Mises* theory can not be applied for equi-triaxial state of stress and does not mean that the state of stress is not dangerous.

It was obtained a relatively uniform state of stress, with higher value in geometry 1 case, both for sheer stress and maximum principal stress. Those high stresses are describing the failure section and the shear stress predicts fracture mode and so it is recommended the use of geometry 1.

5. Acknowledgement

This work was supported by the strategic grant POSDRU/159/1.5/S/133652, co-financed by the European Social Fund within the Sectorial Operational Program Human Resources Development 2007 – 2013.

6. References

[1] Calloch, S., D. Marquis: Triaxial tension compression tests for multiaxial cyclic plasticity, International Journal of Plasticity 15 (1999), pp. 521-549 (1998).

[2] Christensen R.M.: Failure Theory for Materials Science and Engineering, Chapter VII, The Ductile/Brittle Transition, Gaging Ductility Levels, http://www.failurecriteria.com/Media/Ductile_Brittle_Transition_Gaging_Ductility_Levels.pdf Accessed 15 September 2013.

[3] Christensen R.M.: The Theory of Materials Failure. Oxford Univ. Press, ISBN 978-0-19-966211-1, 2013.

[4] Yu Mao-hong: Advances in strength theories for materials under complex stress state in the 20th Century. Appl. Mech. Rev. 55, no 3, 2002, pp. 169-218.

[5] Petkovski, M., R.S. Crouch, P. Waldron: Apparatus for Testing Concrete under Multiaxial Compressionat Elevated Temperature (mac^{2T}), Experimental Mechanics (2006), 46:387–398.

[6] Welsh J.S., D.F. Adams: Development of a True Triaxial Testing Facility for Composite Materials, Multiaxial Fatigue and Deformation: Testing and Prediction, ASTM STP 1387, S. Kalluri and P.J. Bonacuse, Eds., American Society for Testing and Materials, West Conshohocken, PA, 2000, pp 423-437.

[7] J.S. Welsh and D.F. Adams: Development of an Electromechanical Triaxial Test Facility for Composite Materials, Experimental Mechanics (2000); 40(3): 312-320.

[8] J.S. Welsh, J.S. Mayes, and A. Biskner: 2-D biaxial testing and failure prediction of IM77/977-2 carbon/epoxy quasi-isotropic laminates, Composite Structures (2006); 75(1-4): 60-66.

[9] M.C. Serna Moreno, J.L. Martínez Vicente, J.J. López Cela: Failure strain and stress fields of a chopped glass-reinforced polyester under biaxial loading, Composite Structures 103 (2013), pp.27–33.

THE INFLUENCE OF ILLUMINATION PARAMETERS ON THE PERFOMANCES OF COLOR SORTING MACHINES

M.Sc. Markovic Ivana[1], Prof. PhD. Ilic Jelena[1], Prof. PhD. Markovic Dragan, M.Sc. Simonovic Vojislav [1]
Faculty of Mechanical Engineering – University of Belgrade, Serbia [1]

imarkovic@mas.bg.ac.rs

Abstract: The color recorded in the image is not an inherent value of observed object, because it is also influenced by the illumination properties, as well as geometry and surfaces of neighboring objects. Numerous studies have developed and investigated image processing procedures in color sorting machines, where as not many of them have considered the influence of illumination on numerical values related to the colors. In this paper, parameters related to the color of corn have been examined. In each image, the corn has been illuminated by one of four different types of light sources. And different luminous intensities of each type of light source have been applied. The processing of obtained images has been performed in MATLAB, and parameters of images in RGB, CIE L*a*b* and HSV color space have been analyzed. Further descriptive statistics analysis has been performed by IBM SPSS. The variations of parameters with the change of light intensity, showed no statistical significance. The change of the type of the light source has a significant impact on all analyzed features.

Keywords: SORTING, CORN, COLOR SPACE, ILLUMINATION

1. Introduction

In qualitative evaluation of agricultural products, many methods, based on evaluation of their main physical properties, has been developed. The morphological, optical and image texture features are useful in quality inspection, identification, classification, discrimination and differentiation between cultivars, varieties, etc. [1- 4]. Francis [5] found that human perception could be easily fooled. Together with the high labor costs, inconsistency and variability associated with human inspection, accentuates the need for objective measurements systems. The most successful and most widely utilized methods are the optical methods which incorporate high-speed optical sensing and data processing techniques to facilitate high-speed quality evaluation and sorting of many agricultural products with a high degree of accuracy [6].

The color is an important quality factor in differentiating between the acceptable and unacceptable agricultural product, and it has been widely studied [7 - 11]. Human eye perceives three colors: red, green and blue, and others synthesizes by mixing these three colors. Different papers presented methods and researches performed in different color spaces such as RGB, HIS, HSV, CIELAB and many others. Many researches were comparing effectiveness of some of these color spaces in color sorting and came to different results. Bianconi [12] has shown that the basic statistical methods, applied on RGB color space parameters, can be the best practice in approaching the color sorting problem. In regard to the problem of automatic classification of materials such as ceramic tiles, based on color, Lopez [13] has got satisfactory results using RGB and CIELAB color space.

Corn is one of the leading products in agriculture production in Serbia and has a yield of 7.951.583 t in 2014. [14]. Since the sorting is one of the fundamental operations during industrial processing, many researchers is trying to find appropriate, non-destructive, simple and cheap method based on good color recognition.

When capturing color images, proper light source is important since the color of the food sample depends on the part of spectrum reflected from it [15]. The perception of color of any object depends on illumination which is utilized. The idea of this paper is to examine the influence several types of illuminations on color of the image of the product. This paper also presents the attempt to investigate the impact of the intensity of illumination on agricultural product image parameters. Of many image parameters, the parameters of RGB, Lab and HSV color spaces were chosen to be evaluated.

2. Materials and methods

In this paper, the color of defrosted corn, which had been frozen to -18℃, has been investigated. The products were put in black chamber, of dimensions 50x50x50 cm. Olympus VG-110 camera was used. As the illumination Philips bulbs, of color rendering index (CRI) Ra8, and color temperature 2700K were used. Table 1 shows other primary characteristics of illuminations, as well as abbreviated notification of used illumination. The snapshots was taken at the distance of 40 cm from products, in dark room, on temperature 15℃. Total measurements were performed within 10 minutes.

Table 1: *Main features of the applied illumination*

Types of illuminatio n	Power (W)	Luminous flux (lm)	Luminous intensity (cd)	Notification of illumination	
				1 bulb	2 bulbs
Clear	60W	655		c1	c2
Reflector	60W		750	r1	r2
Soft White	60W	630		sw1	sw2
Warm White	14W=68W	856		ww1	ww2

Once the color images of the corn samples were captured, pictures were cropped to form the same portions of each image of dimensions 50x50 pixels using Adobe Photoshop® 7.0. Thus, the obtained images are further processed in the program Matlab®, where the color was analyzed qualitatively and quantitatively. A digital color image is represented in RGB form with three components per pixel in the range 0 to 225 and conventionally stored using eight bits per color component. Each parameter of color: red, green and blue is presented in the form of 50x50 matrix. Further statistical analysis where performed in IBM SPSS® 21.0. It was necessary to switch square matrix to column matrix, which has been performed in Matlab and then matrix extracted in Office Excel 2007, because SPSS have possibility for uploading data from Office Excel. Schematic presentation of algorithm is shown in figure 1.

By subsequent transformation of the images into CIELAB color space, values of *L, a*, b** parameters for each pixel were obtained. L* defines lightness, a* denotes the red/green value and b* the yellow/blue value. These values were used to calculate chroma and hue angle from equations 1 and 2.

(1) $$C^* = \sqrt{a^{*2} + b^{*2}}$$

(2) $$h^\circ = arctg(b^*/a^*)$$

The *c** represents *Chroma* or 'saturation'. It ranges from 0 at the centre of the circle, which is completely unsaturated (i.e. a neutral grey, black or white) to 100% at the edge of the circle for very high Chroma (saturation) or 'color purity'. The *h** axis represents *Hue*.

The units for h^* are degrees (angular), ranging from 0° (red) through 90° (yellow), 180° (green), 270° (blue) and back to 0° [15].

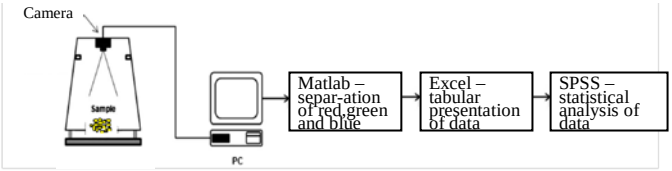

Fig. 1. *Shematic view of procedure*

The first step in this research was to examine whether the data for each of parameters deviate from normality, because many statistical analyses are based on assumption that the distribution of the values of dependent variables is normal. Normality can be evaluated partly based on the calculated values of indicators like skewness and kurtosis. According to Garson [17], distributions are normal if their skewness is in range [-2,+2], although some authors use the more stringent requirement that a narrower interval [-1,+1]. Also according to Garson, normal distribution characterized kurtosis in range [-2,+2] (some authors use more lenient criteria [-3,+3], and others authors use stricter criteria [-1,+1]). The resulting an non-normal distribution is usually obtained when it comes to a large number of samples such as this case. Within the first analysis, descriptive analysis of values was performed. In further analyzes, two non-parametric test were used: Wilcoxon signed-rank test and Friedman test. Both tests are appropriate for determining whether or not there is a significant association between a dichotomous variable and a continuous variable with independent samples data.

3. Results and discussion

In table 2, taken images of examined corn in format 50x50 pixels under different illumination are shown. With visual method we can see differences between illuminations, while differences between the illuminations by one or two bulbs are unclear.

Table 2. *Display samples of corn captured under different illumination*

Type of illumination	1 bulb	2 bulbs	Resolution
Clear			50x50
Reflector			50x50
Soft White			50x50
Warm White			50x50

Figure 2 gives a perspective view of L, a^*, b^*, c and h values associated with basic colors.

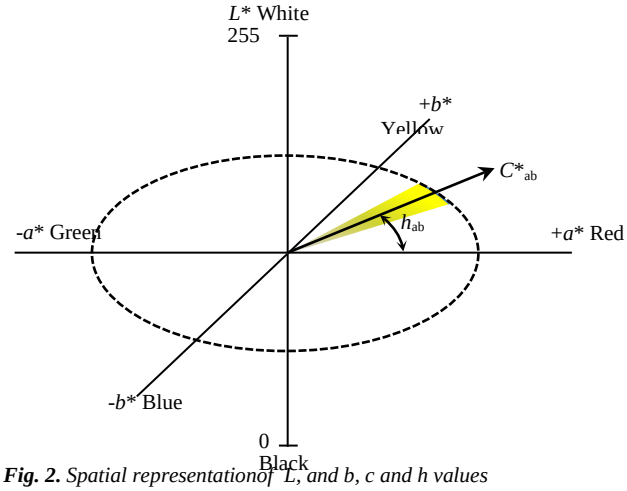

Fig. 2. *Spatial representationof L, and b, c and h values*

After analyses of data using descriptive analysis, based on skweness and kurtosis in range [-1, +1], we came to conclusion that distribution is not normal for all test color values. Weather the distribution is normal or not, we can see on histograms and some other diagrams which we can obtain from descriptive analysis Explore in IMB SPSS. All normal distributions are symmetric and have bell-shaped density curves with a single peak and a lower number of results towards to the ends (tails) bell [18] and with Normal Q-Q Plot, higher the bar of observed results closer to a straight line, it is closer to a normal distribution. For example, figure 3 and 4 show histogram and Normal Q-Q Plot of blue value when reflector light was used with single bulb, where we conclude that the distribution is not normal.

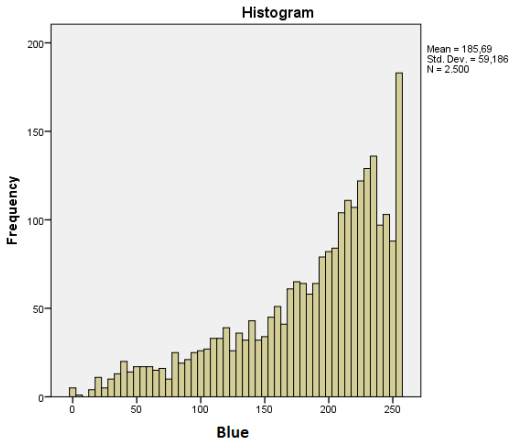

Fig. 3. Histogram for blue value under reflector light with single bulb

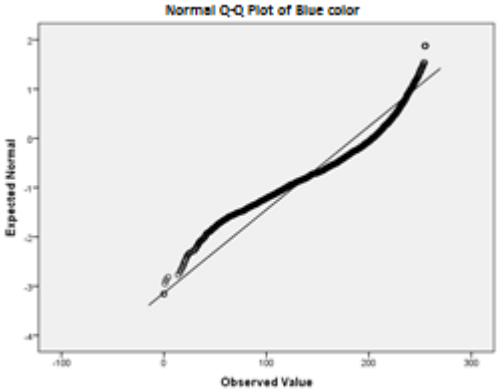

Fig. 4. *Normal Q-Q plot for blue value under reflector light with single bulb*

Results of descriptive statistics are summarized in table 3 for RGB values, and in table 4 for CIELAB values and in table 5 for Chroma and Hue angle.

Table 3. *Descriptive Statistics for RGB value*

	Min	Max	Mean	Std. Dev.
Red c1	173	255	240,63	11,231
Red c2	179	255	240,60	10,732
Red r1	175	255	243,01	10,847
Red r2	184	255	243,21	10,491
Red sw1	181	255	240,19	10,614
Red sw2	173	255	240,51	11,148
Red ww1	172	255	236,63	9,198
Red ww2	179	255	236,33	9,798
Green c1	139	255	243,73	15,405
Green c2	148	255	243,30	14,400
Green r1	145	255	245,95	13,023
Green r2	142	255	246,12	12,836
Green sw1	124	255	242,46	14,441
Green sw2	140	255	243,61	14,476
Green ww1	126	255	239,06	14,004
Green ww2	141	255	238,95	15,279
Blue c1	2	255	134,62	47,457
Blue c2	0	255	130,48	44,003
Blue r1	11	255	161,87	45,191
Blue r2	23	255	162,16	45,028
Blue sw1	0	255	122,32	39,095
Blue sw2	0	255	130,48	44,585
Blue ww1	0	219	69,89	25,059
Blue ww2	0	216	72,06	25,257

Table 4. *Descriptive Statistics for CIELab value*

	Min	Max	Mean	Std. Dev.
L c1	156	255	240,30	12,886
L c2	167	255	239,88	12,025
L r1	161	255	243,01	11,428
L r2	159	255	243,17	11,228
L sw1	148	255	239,01	11,940
L sw2	156	255	240,07	12,186
L ww1	143	253	235,04	11,002
L ww2	162	252	234,93	11,970
a* c1	102	144	116,46	5,021
a* c2	101	147	116,30	4,828
a* r1	104	140	118,36	4,746
a* r2	103	139	118,38	4,588
a* sw1	102	150	115,90	4,510
a* sw2	102	148	116,13	4,825
a* ww1	101	140	113,37	4,513
a* ww2	102	146	113,38	4,893
b* c1	126	216	178,84	17,672
b* c2	123	216	180,66	16,513
b* r1	123	215	167,71	17,718
b* r2	124	214	167,66	17,603
b* sw1	124	214	184,09	14,311
b* sw2	126	213	180,72	16,608
b* ww1	145	216	203,34	7,745
b* ww2	146	215	202,58	7,588

Table 5. *Descriptive Statistics for chroma and hue angle*

	Min	Max	Mean	Std. Dev.
chroma c* c1	178	245	213,78	13,291
chroma c* c2	179	243	215,18	12,411
chroma c* r1	179	242	205,70	12,509
chroma c* r2	179	243	205,65	12,566
chroma c* sw1	181	246	217,77	10,996
chroma c* sw2	180	244	215,14	12,453
chroma c* ww1	191	244	232,87	6,492
chroma c* ww2	189	245	232,23	6,394
Hue angle h c1	44	64	56,73	3,494
Hue angle h c2	43	65	57,05	3,270
Hue angle h r1	42	63	54,56	3,799
Hue angle h r2	43	63	54,56	3,737
Hue angle h sw1	43	64	57,68	2,771
Hue angle h sw2	44	64	57,09	3,279
Hue angle h ww1	49	64	60,83	1,609
Hue angle h ww2	51	64	60,73	1,632

Since the surface color of a corn is highly heterogeneous due the complex distribution of water, starch, reducing sugars, etc., principally, it is generally important to compute the average color which is representative of the complete surface. Also, it is useful to know standard deviation of investigated parameters. Since standard deviation is a measure that is used to quantify the amount of variation or dispersion of a set of data values, the illumination and the color parameter that gives the smallest standard deviation of parameters are those that offer the best definition of a color. A standard deviation close to 0, indicating that the data points tend to be very close to the mean value, is preferable, concerning the definition of color, while a high standard deviation indicates that the data points are spread out over a wider range of values, making it harder to define unacceptable color.

In tables 3, 4 and 5, maximum value are marked. There it can be concluded that the light reflector gives the most intense RGB values and the *chroma* and *hue angle* most pronounced in warm white light, and that the standard deviation is the lowest for *a** value that represents the yellow color.

Since the studied product is corn, it is required more specific values of yellow color. According to *r, g, b* values it is harder to get the exact values of acceptable color, while using *b*, c* i *h* we can define optimal range aceptable values and a visual display in the spatial diagram. Based on average values and standard deviation, the most intensive yelow color give warm white illuminant, where the standard deviation are lowest. Taking into account table 1, and with visual method lead to the same conclusion. The illumination gives a warm tone and therefore the more intensive experience of color, so that *b** value that defines the yellow are the largest, like it is expected. However, based on small standard deviations, we can conclude that the warm white illumination is the most appropriate to define the optimal range of hue values of yellow.

After descriptive analysis, test of Frequency was performed, where it can bee seen which values are the most frequent and with minimum deviations. Data analysis and histogram shows that the most of invesigated data gave large range and large deviations of values. Minimum range clustered values give *Hue angle*, *Chroma* and *b** values for warm white illuminations. Example of histograms are given in figures 5, 6 and 7.

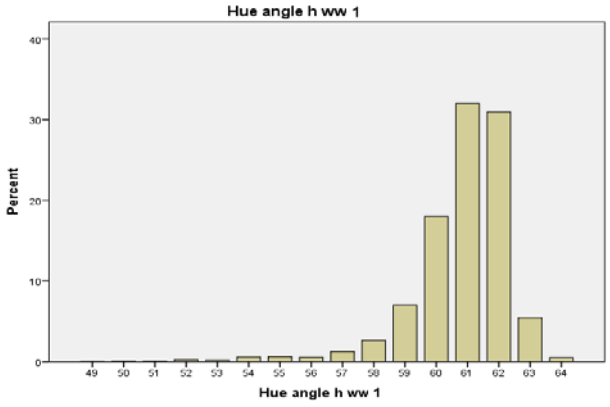

Fig. 5. *Hue angle of warm white illumination with one bulb*

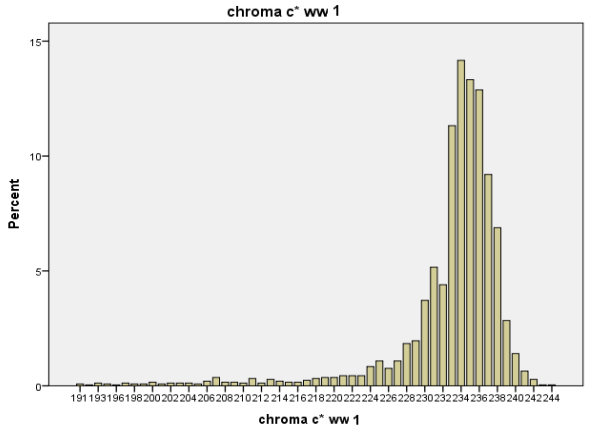

Fig. 6. *Chroma of warm white illumination with one bulb*

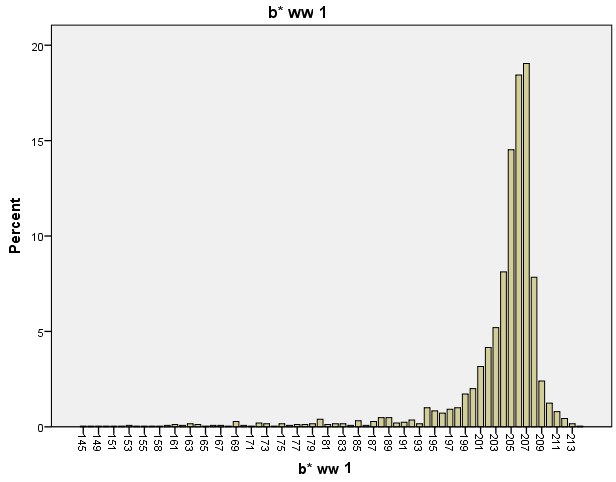

Fig. 7. *b* value of warm white illumination with one bulb*

Based on histograms of *hue angle*, *chroma* and *b** values, it can be defined range of color values and then based on that range in the further research, we can define good color of product.

As it has already been mentioned, with visual method it cannot be seen difference between pictures with one bulb and two bulbs. In order to examine it using statistics, color parameters were evaluated with Wilcoxon signed-rank test and showed a statically significant change in some cases. The results of this test are presented in tables 6, 7, and 8.

Table 6. *Wilcoxon signed-rank test for R,G,B values*

	Red c2 - Red c1	Green c2 - Green c1	Blue c2 - Blue c1
Z	-0,838[b]	-4,008[b]	-7,702[b]
Asymp. Sig. (2-tailed)	0,402	0,000	0,000
r	-	0,06	0,11
	Red r2 - Red rs1	Green r2 - Green r1	Blue r2 - Blue r1
Z	-0,697[c]	-1,886[c]	-0,846[c]
Asymp. Sig. (2-tailed)	0,486	0,059	0,398
r	-	-	-
	Red sw2 - Red sw1	Green sw2 - Green sw1	Blue sw2 - Blue sw1
Z	-2,586[c]	-7,837[c]	-17,614[c]
Asymp. Sig. (2-tailed)	0,010	0,000	0,000
r	0,04	0,11	0,25
	Red ww2 - Red ww1	Green ww2 - Green ww1	Blue ww2 - Blue ww1
Z	-1,402[b]	-1,214[c]	-8,113[c]
Asymp. Sig. (2-tailed)	0,161	0,225	0,000
r	-	-	0,11

a. Wilcoxon Signed Ranks Test
b. Based on positive ranks.
c. Based on negative ranks.

Table 7. *Wilcoxon signed-rank test for L, a*b* values*

	L c2 – L c1	a* c2 - a* c1	b* c2 - b* c1
Z	-4,677[b]	-1,931[b]	-8,155[c]
Asymp. Sig. (2-tailed)	0,000	0,053	0,000
r	0,07	-	0,11
	L r2 – L r1	a* r2 - a* r1	b* r2 - b* r1
Z	-1,798[c]	-0,309[c]	-0,373[b]
Asymp. Sig. (2-tailed)	0,072	0,757	0,709
r	-	-	-
	L sw2 - L sw1	a* sw2 - a* sw1	b* sw2 - b* sw1
Z	-9,084[c]	-3,117[c]	-17,845[b]
Asymp. Sig. (2-tailed)	0,000	0,002	0,000
r	0,13	0,04	0,25
	L ww2 - L ww1	a* ww2 - a* ww1	b* ww2 - b* ww1
Z	-0,934[c]	-0,083[b]	-11,642[b]
Asymp. Sig. (2-tailed)	0,350	0,934	0,000
r	-	-	0,16

Table 8. *Wilcoxon signed-rank test for Chroma and Hue angle*

	chroma c* c2 – chroma c* c1	Hue angle h c2 - Hue angle h c1
Z	-8,761[c]	-6,569[c]
Asymp. Sig. (2-tailed)	0,000	0,000
r	0,12	0,09
	chroma c* r2 – chrom c* r1	Hue angle h r2 – Hue angle h r1
Z	-0,524[b]	-0,112[b]
Asymp. Sig. (2-tailed)	0,600	0,910
r	-	-
	chroma c* sw2 - chroma c* sw1	Hue angle h sw2 - Hue angle h sw1
Z	-19,232[b]	-14,221[b]
Asymp. Sig. (2-tailed)	0,000	0,000
r	0,27	0,2
	chroma c* ww2 - chroma c* ww1	Hue angle h ww2 - Hue angle h ww1
Z	-10,440[b]	-4,701[b]
Asymp. Sig. (2-tailed)	0,000	0,000
r	0,15	0,07

Significant difference is present when Asymp. Sig. (2-tailed) – is below p<0,005 (red cells) and the degree of the difference is determined by the value of r which is defined by equation 4. According to Cohen (1988) [19] criteria, the differences does not have influence, if r is close to 0,1 or it is is less than 0,1. This is the case for almost all types of illumination and color parameters except in three cases where there is a medium impact when r approaches to the value of r=*0,3* and that is the case in the following cases: blue sw1-sw2, b*ww1-ww2 i chroma c*sw1-sw2, as it is marked as green cells in tables 6, 7 and 8.

(4) $$r = \frac{Z}{\sqrt{N}}$$

Next analysis, related to the examination with Friedman test, gives the answer on question whether there is difference between the images made with different illuminations. This test is appropriate to test the significance of the association between a categorical variable (k≥ 2). The statistically significant for all values (Asymp. Sig. (2-tailed) is below 0,005, according to which concludes that there is statistically significant difference between values of applied illuminations. The example was given in table 9 for L* value when the clear illuminations with one bulb applied.

Table 9. **Example for L value using Friedman test**

Test Statistics[a]

N	2500
Chi-Square	1990,415
df	3
Asymp. Sig.	0,000

a. Friedman Test

Friedman test shows differences in calculated values but it does not show exactly between which types of illumination and in what extent. The answers to these questions are obtained by applying Wilcoxon signed-rank test.

Of all the results of Wilcoxon signed-rank test, only the values where effect size are $r \geq 0{,}2$, which represents medium effect size, and $r \geq 0{,}5$ which represents a large effect size (red cells), are shown in tables 9, 10 and 11.

Table 9. **Wilcoxon signed-rank test and level of significance for red, green and blue values**

Red	r	Green	r	Blue	r
wwb1 - r1	0,39	ww1 - c1	0,27	r1 - c1	0,31
wwb1 - sw1	0,35	ww1 - r1	0,4	sw1 - c1	0,25
ww2 - c2	0,29	ww1 - sw1	0,33	ww1 - c1	0,59
ww2 - r2	0,38	ww2 - c2	0,29	sw1 - r1	0,53
ww2 - sw2	0,33	ww2 - r2	0,37	ww1 - r1	0,61
		ww2 - sw2	0,37	ww1 -sw1	0,61
				r2 - c2	0,39
				ww2 - c2	0,41
				sw2 - r2	0,41
				ww2 - r2	0,61
				ww2 - sw2	0,61

Table 10. **Wilcoxon signed-rank test and level of significance for L, a* and b* values**

L	r	a*	r	b*	r
ww1 - c1	0,33	ww1 - c1	0,34	r1 - c1	0,34
sw1 - r1	0,29	sw1 - r1	0,32	sw1 - c1	0,27
ww1 - r1	0,47	ww1 - r1	0,48	ww1 - c1	0,6
ww1 - sw1	0,43	ww1 - sw1	0,38	sw1 - r1	0,55
ww2 - c2	0,33	ww2 - c2	0,36	ww1 - r1	0,61
ww2 - r2	0,45	sw2 - r2	0,27	ww1 - sw1	0,6
ww2 - sw2	0,45	ww2 - r2	0,47	r2 - c2	0,41
		ww2 - sw2	0,36	ww2 - c2	0,6
				sw2 - r2	0,44
				ww2 - r2	0,61
				ww2 - sw2	0,6

Table 11. **Wilcoxon signed-rank test and level of significance for chroma c* and hue angle h* values**

c*	r	h*	r
r1 - c1	0,34	r1 - c1	0,32
sw1 - c1	0,28	ww1 - c1	0,56
ww1 - c1	0,6	sw1 - r1	0,52
sw1 - r1	0,55	ww1 - r1	0,6
ww1 - r1	0,61	ww1 - sw1	0,57
ww1 - sw1	0,61	r2 - c2	0,38
r2 - c2	0,41	ww2 - c2	0,56
ww2 - c2	0,61	sw2 - r2	0,41
sw2 - r2	0,44	ww2 - r2	0,6
ww2 - r2	0,61	ww2 - sw2	0,57
ww2 - sw2	0,61		

4. Conclusion

Sample images were processed in MATLAB by implementing the explained algorithm. In this algorithm for color analysis of samples, different combinations of color spaces and intensity transformation functions were applied on the images. The digital imaging method allows measurements and analyses of the color of food surfaces that are adequate for food engineering research. While it is not yet a adequate substitute for sophisticated color measurement instruments, it is an attractive alternative due to its simplicity, versatility, and low cost. In IBM SPSS all the approaches achieved factory compliance exceeding 95% minimum accuracy. The preliminary results of this study are useful information for future development of the quality control technique in practical usage.

5. References

[1] Majumdar, S., Jayas, D.S. Classification of cereal grains using machine vision. I. Morphology models. T. ASAE 43 (6). 2000a. pp. 1669–1675.

[2] Majumdar, S., Jayas, D.S. Classification of cereal grains using machine vision. II. Colour models. T. ASAE 43 (6). 2000b. pp. 1677–1680.

[3] Majumdar, S., Jayas, D.S. Classification of cereal grains using machine vision. III. Texture models. T. ASAE 43 (6). 2000c. pp. 1681–1687.

[4] Majumdar, S., Jayas, D.S. Classification of cereal grains using machine vision. IV. Combined morphology, colour, and texture models. T. ASAE 43 (6). 2000d. pp. 1689–1694.

[5] Francis, F. J. Colour quality evaluation of horticultural crops, HortScience, 15(1). 1980. pp. 14-15.

[6] Chen, P. and Sun, Z. A review of non-destructive methods for quality evaluate and sorting of agriculture products. Journal of Agriculture Engineering research, 49. 1991. pp:85-89.

[7] Dobrzanski B; Rybczynski R. Colour change of apple as a result of storage, shelf-life, and bruising. International Agrophysics, 16. 2002. pp. 261–268

[8] Hahn, F. Multispectral prediction of unripe tomatoes. Biosystems Engineering, 81(2), 2002. pp. 147–155, doi:10.1006/ bioe.2001.0035

[9] Lee, D., Archibald, K. J., Chang, Yu-Chou, Greco, R.C. Robust color space conversion and color distribution analysis techniques for date maturity evaluations. Journal of Food Engineering, 88. 2008. pp:364-372.

[10] Singh N; Delwiche M J; Johnson R S. Image analysis methods for real-time color grading of stonefruit. Computers and Electronics in Agriculture, 9. (1993). pp. 71–84

[11] Singh N; Delwiche M J; Johnson R S; Thompson J. Peach maturity grading with color computer vision. ASAE Paper No. 92-3029. (1992).

[12] Bianconi, F., Fernandez, A., Gonzalez, E., Saetta A.S. Performance analysis of colour descriptors for parquet sorting. Expert systems with applications, 40. 2013. pp. 1636-1644.

[13] López, F., Valiente, J. M., Prats, J. M., Ferrer A. Performance evaluation of soft color texture descriptors for surface grading using experimental design and logistic regression. Pattern Recognition, 41. 2008. pp. 1744-1755.

[14] Statisticki zavod Srbije: http://webrzs.stat.gov.rs/WebSite/Public/ReportResultView.aspx?rptKey=indId%3d1301IND01%2635%3d6%262%3d201400%2639%3d03000%266%3d2%26sAreaId%3d1301%26dType%3dName%26lType%3dSerbianCyrillic (Pristupljeno 22.06.2015)

[15] Francis, F. J., and Clydesdale, F. M. Food colorimetry: theory and applications. 1975. Westport, CT: AVI Publishing.

[16] Garson, D. Testing statistical assumption. 2012. eBook, Statistical Publishing Assosiates, Asheboro USA

[17] McGuire, R.G.. Reporting of objective color measurements. HortScience 27. 1992. pp. 1254–1255.

[18] Gravetter, F. J. and Wallnau, L.B. Statistics for the behavioral sciences (6th edn.). 2004. Belmont, CA: Wadsworth.

[19] Cohen J. Statistical power analysis for the behavioral science. Lawerence Erlbaum Associates Publishers, New Jersey. 1988.

INVESTIGATION OF THE PARAMETERS OF THE QUALITY AT AN AXISYMETRIC DRAWING

ИССЛЕДОВАНИЕ ПАРАМЕТРОВ КАЧЕСТВА ПРИ ОСЕСИММЕТРИЧНОЙ ВЫТЯЖКЕ

Doctor of engineering, Prof. Nazaryan E. A., Candidate of physicist of mathematical sciences Arakelyan M. M.
PHD student Simonyan A.S. Facullty of Physics-Yerevan State University, Armenia

Abstract : *Based on the analysis of the initial equations of the plastic state,established the distribution of strains in the initial and final stages of axisymmetric drawing. The dependencies to assess the accuracy of linear and diametrical sizes taking into account volumetric of strain state.*

Keywords**:** stress, strain, deep drawing, hardening, sheet blank.

1. Introduction.

One poorly developed theoretical problems of the drawing process is to assess the impact of amount and distribution of stress and strain on parameters and strength of precision manufactured parts. The scientific-technical handbooks no calculated based, allowing to determine the maximum possible deviations of linear and diametrical dimensions and strength values at different degrees of deformation and technological characteristics of the materials used [1, 2].

This state is due to the fact that the existing theoretical approaches to the creation of science-based methods for the analysis of the stress-strain state built, as a rule, based on simplifying assumptions, the most important of which are the adoption of the plane scheme strain state, the analysis methods of deformation theory with the approximate conditions of plasticity adoption perfectly rigid-plastic model deformable material.

The decisions derived from such approaches are very approximate and provide a idea of the stress-strain state of the blank. Besides this, the theoretical analysis methods developed in many respects depend also on the interests of authors of scientific studies and carry to some extent subjective.

An essential feature of the drawing process is that initially the same material elements sheet blank, plastically deformed acquire certain identity, characterized by changing the thickness of the accumulated value of deformation due to hardening effects, the change indicator of resistance to deformation.

Obviously, the performance precision linear and diametrical sizes of cylindrical parts of an isotropic material, manufactured by drawing, without the influence of the he elastic aftereffect must be due to the value and distribution of finite deformation and strength parameters under the same conditions - the total and the distribution of the index of deformation resistance.

In the present paper the process of drawing cylindrical parts sets the following tasks:

- *Establishment of settlement dependences allowing to define the dimensions of workpieces with volume strain state;*
- *Determination of the distribution of finite quantities and component deformation and deformation resistance index.*

2.An analysis of the initial stage of the drawing process.

Numerous studies have established that the drawing process starts with plastic deformation of the uncompressed part annular portion of the blank located between the contact zones deforming tools[3,4].At this stage, as you move the deforming tool is increasing stress deformation and plastic deformation of the flange cover the entire piece. Set a balance between effort and drawing resistance to plastic deformation of the flange and the second stage of the process - the retraction flange blank into a die.

At the initial stage of the outer boundary of the plastic material and the field elements are moved radially in opposite directions, and the second stage - in the same direction. In both phases of the size of the plastic zone are continuously changing, so that the process of forming the blank is transient in nature. Therefore, scientifically based methods of analysis of drawing should be based on the theory of plastic flow with the hardening material and of volumestrain state.

Given the complexity of the analysis of the processes occurring in the initial stage of drawing, first consider an axially symmetric tension thin plate with a low-cut, limited radius circular contour r_0 along which the specified uniformly distributed normal stresses σ_ρ .Existing solutions such tasks usually carried out either for a plate of constant thickness, or for perfectly rigid-plastic model deformable material with plasticity condition for the hypothesis of constant maximum shear stress, thus cannot be used for the task [5].

In [6,7] that the stress-strain state in the process of forming an axially symmetric parts from sheet metal appropriate and convenient to represent the deviatory plane Mises plasticity cylinder in oblique two-dimensional coordinate system. The possibility of such a representation should be the condition on which the incompressible materials for three linear strain are interdependent and have only two degrees of freedom, as well as the assumption that the deformation of the blank with the flange stretching occurs under conditions close to the plane stress[3].

In these studies found that the module current vector magnitude equivalent strain is numerically equal to the value of accumulated deformation (strains rate), the current value of the linear strains are the projections of the vector equivalent strain in the oblique coordinate axes, and the pattern of accumulation of strains in this material element describes the nature of the change in the vector equivalent strain in time.

Consequently, the problem of assessing the performance precision linear and diametrical sizes, as well as the final value of the index of deformation resistance is reduced to the analysis of time-dependent vector fields equivalent deformations.

The [6,7] initial equations of plastic flow under plane stress deformation and axial symmetry, namely the equilibrium equation for the changes in thickness of the material condition of plasticity Mises condition of constant volume equation relating voltage and increment (speed) of strains are shown in single structure and displayed in the deviatoric plane plasticity cylinder as the differential between the radial dependence of tensile stress and strain accumulate $d\sigma_\rho = \sigma_s d\varepsilon_i$.

Acceptance of the power law strain hardening $\sigma_s = A\varepsilon_i^n$ allowed to integrate said differential dependence and dependence to obtain and a component of accumulated strains on a parameter φ ωin the form of:

$$\left.\begin{aligned} &|\vec{\varepsilon}|_1 = \varepsilon_i = (\ln K + n)\frac{2}{\sqrt{3}}\cos(\varphi + \pi/6); \\ &\varepsilon_\rho = \frac{\ln K + n}{2}\left(1 + \cos 2\varphi - \frac{\sqrt{3}}{3}\sin 2\varphi\right); \\ &\varepsilon_\theta = -\frac{\ln K + n}{2}\left(\cos 2\varphi + \frac{\sqrt{3}}{3}\sin 2\varphi\right); \\ &\varepsilon_z = -\frac{\ln K + n}{2}\left(1 - \frac{2\sqrt{3}}{3}\sin 2\varphi\right). \end{aligned}\right\} \quad (1)$$

where $|\vec{\varepsilon}|_1$ - the magnitude of equivalent strain in the initial stage of the drawing process, $n = \ln(1+\delta)$ - in the received exponent law strain hardening , δ - relative uniform deformation of the material when tested in uniaxial tension, φ - the angle between the polar axis and the radial strain vector equivalent strain varying within $0 \le \varphi \le \pi/3$ (Fig. 1), $\varepsilon_\rho, \varepsilon_\theta, \varepsilon_z$ - linear deformations, respectively, in the radial and circumferential directions, as well as perpendicular to the workpiece surface, the coefficient of drawing $K = R_0/r_0$ (R_0 and r_0 - respectively outer radius of the workpiece and the radius of the point of the die).

Dependence $\varepsilon_i(\varphi)$ on deviatoric plane is a circle of radius $(\ln K + n)/\sqrt{3}$ $(\ln K + n)/\sqrt{3}$, centered on the line $\varepsilon_\theta = 0$ and passes through the origin [6].

The possibility of integrating the differential above depending based on the assumptions made about the same for the considered material element of the vector direction of the increment equivalent strain in the deviatoric plane, which is equivalent to the assumption of proportional relationships change over time component strains $(\varepsilon_\rho/\varepsilon_\theta = const)$.

Upon receipt of (1) the following dependence for the radial and circumferential stress

$$\sigma_\rho = \sigma_s\frac{2}{\sqrt{3}}\cos(\varphi + \pi/6); \quad \sigma_\theta = -\sigma_s\frac{2}{\sqrt{3}}\sin\varphi \ , \qquad (2)$$

satisfying Mises plasticity plane stress condition and set of joint solution of the equations of stress and communication increments (speeds) strains with the condition that the volume [7] .

From the analysis of (1) that the resulting solution can be represented as the sum of two deformed states. The first term describes the initial plastic state for ideal rigid-plastic model deformable material ($n = 0$) is the largest size of the plastic zone $(K = e)$ and characterizes the distribution of strains in the parameter φ . The second term linearly superimposed on the first, describes the increment of strains at a given index in the received power-law strain hardening.

Such an interpretation of the results based on the fact that the oblique axes in the deviatoric plane are logarithmic dimension, whereby it becomes possible additive sum strains.

Dependencies (1) and (2), describing the stress-strain state are closed parametric solution of axially symmetric stretching thin plate with a low-cut, limited circular contour, taking into account the interdependent changes in the thickness of the material and work hardening.

From (1) it also follows that as the indicator, the relative magnitude of the plastic region increases in the direction of the inner contour (reduced radius of the inner contour). This result follows from the condition, according to which the external contour of the workpiece is realized the stress state of the linear compression, regardless of the relative magnitude of the field of plastic and technological characteristics of the deformable material.

In between these kinds of deformed states is a smooth transition from one type to another strain state. The schedule of dependence (1) and (2) as well as the main characteristics of the distribution of stresses and strains in detail in [7,8].

(1) is determined by the highest relative value of the plastic region $R_0/r = \exp(1+n)$ (R_0, r - respectively the radii of the outer and inner contours of the plate in a deformed state). Obviously, when $n = 0, r = r_0$, the relative value $K = R_0/r_0 = e(\approx 2{,}718)$ and coincides with the results of the prior art for a plate of constant thickness at an ideal rigid-plastic model deformable material [3,5].

3. An analysis of the second stage of the drawing process.

The main problem of analysis of the second step drawing process is obtained for mapping the initial stage parametric solutions (1) and (2) into the material of the deformable medium of the preform. To do this, first consider the process of being drawn into the die blank flange, excluding the effect of hardening $(n = 0)$ and bending effects on the stress-strain state.

With the reduction of the outer radius of the blank flange material elements moving radially coordinates $R_0 \le \rho \le r_0$, accumulate a certain deformation and radius reaching further move vertically without deforming. At the end of this process for forming cylindrical parts set a specific variable distribution of accumulated strain, the values of which can be determined by the well-known relationship between the parameter φ in the deviatoric plane and relative coordinates ρ/r_0 in a material medium deformable billet.

The previous section established that for a perfectly rigid-plastic model deformable material nature of the distribution of the accumulated deformation in (1) and radial stresses in relative units (2) are similar in the deviatoric plane and described the same functional dependence $F(\varphi) = (2/\sqrt{3})\cos(\varphi + \pi/6)$. From (1) and (2) it also follows that the initial stage of drawing $(\sigma_s = \sigma_{0,2}; \varepsilon_i = 0{,}2\%; n = 0)$ blank thickness remains constant,

the distribution of radial stresses in relative units of well-known solution has the form $\sigma_\rho/\sigma_s = \ln R/\rho$ [3] on the basis of which (2)

$$\frac{\rho}{r_0} = K^{\left[1 - \frac{2}{\sqrt{3}}\cos\left(\varphi + \frac{\pi}{6}\right)\right]}. \qquad (3)$$

For (1) and (3) it is possible to find the distribution of the accumulated strain in the deviatoric plane and forming the cylindrical member. Different range φ of fixed K and (3) defines the relationship ρ/r_0 $0 \le \varphi \le \pi/3$ and the value calculated by the formula $\varepsilon_\theta = \ln(r_0/\rho)$ district deformations. Among the relevant points of the negative direction of the axis ε_θ drop a perpendicular to the intersection with radial rays φ . Connect the start of oblique coordinate the points of intersection is set equivalent to the vector

field strains for all material elements.Based on the generality of the methodical approach and to simplify the numerical calculations, the outer radius of the plastic zone R_0 is adopted when changing K is the fixed and variable radius of the die is considered r_0.

From trigonometric representation strains in the deviatoric plane (Figure 1) shows $\varepsilon_\rho/|\varepsilon_\theta| = \cos\varphi/cos(\pi/3-\varphi)$ where the absolute value of the components of the district, according to (3) shall be determined from the equation $\varepsilon_\theta = \ln(\rho/r_0)$. On the basis of the established relationship between φ the parameter and the relative coordinate ρ/r_0 in a material medium deformable billet it becomes possible to install the distribution component of finite deformations and appropriate equivalent deformations of the vector field

$$\left.\begin{aligned} |\vec{\varepsilon}|_2 &= \frac{|\varepsilon_\theta|}{\cos(\pi/3-\varphi)};\\ \varepsilon_\rho &= \left[1-F(\varphi)\right]\frac{\cos\varphi}{\cos(\pi/3-\varphi)}\ln K;\\ \varepsilon_\theta &= -\left[1-F(\varphi)\right]\ln K;\\ \varepsilon_z &= \left[1-F(\varphi)\right]\left[1-\frac{\cos\varphi}{\cos(\pi/3-\varphi)}\right]\ln K \end{aligned}\right\}, \qquad (4)$$

where $|\vec{\varepsilon}|_2$ - the magnitude of equivalent strain (cumulative strain) in the second stage of the drawing process.

Figure 1 shows a plot of the component deformation and deformation resistance index at the end of the second stage drawing at K = 2 assigned in accordance with (3), to the original plastic state. From the analysis of (4) and provided graphs implies that the radial component of the outer contour near the blank (at a certain distance from the end of the extended parts (ρ/r_0 = 1.76) reached the highest value (0.36), and the strain in the thickness achieves the lowest (-0.047) values near the points of the matrix (at some distance from the bottom of the elongated parts ρ/r_0 = 1.13). On the basis of (3) and (4) it is possible to define the size of blanks on the set sizes detail and thickness distribution of the generator with volume strain state.

The current value for a given height K and $h(\varphi)$ can be determined by comparing the width $d\rho$ of the ring members on the initial preparation and the increment dh in the cylindrical part, according to the expression $\varepsilon_\rho = \ln(dh/d\rho)$, which, after transformation, taking into account (3) and (4) leads to the following differential equation

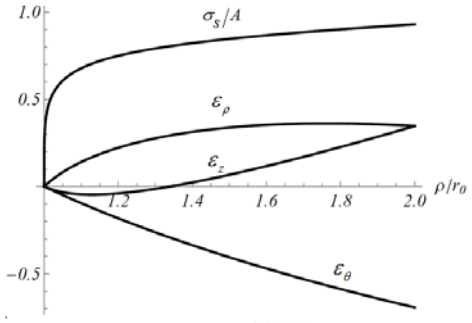

Figure 1. *The distribution of the components of deformation and deformation resistance index at the end of the second stage drawing*

$$d\left(\frac{h}{r_0}\right) = K^{\left[1-F(\varphi)\right]\left[\frac{\cos\varphi}{\cos(\pi/3-\varphi)}+1\right]}\frac{2}{\sqrt{3}}\sin(\varphi+\pi/6)\ln K d\varphi. \qquad (5)$$

Integrals $\int_0^\varphi \Phi(\varphi;K)\ln K d\varphi$ allow us to determine the current value of the relative height of the cylindrical part $h/r_0(\varphi)$ of the annular portion of the blank $\rho - r_0$, as well as the distribution of thickness in a volume strain state.

The main difference between the stated and the actual drawing process is that when drawing deforming tool in a region close to the inner contour of the blank has the effect of limiting the radial movement of certain material elements. Material element initially located at a radius r_0 moves vertically in the absence of circumferential strain $(\varepsilon_\theta = 0)$ and, according to the equation $\varepsilon_\rho = |\varepsilon_z|$, it is deformed in a shear plane $(\rho; z)$.

The vector equivalent strain characterizing the deformation of the element, the deviatoric plane is shifted to the left and becomes perpendicular to the axis ε_θ, and the parameter φ has values in the range $-\pi/6 \le \varphi \le \pi/3$. Absence of circumferential deformation at constant unit vector equivalent strain offset by increased strain thinning.

4. Results and discussion. Let us compare the results of studies with similar results obtained by making assumptions about the constancy of the thickness of the material in the process of drawing cylindrical parts with a diameter $2r_0$ and height h, excluding the radius of curvature [2]:

$$\frac{h}{r_0} = \frac{1}{2}\left(K^2-1\right). \qquad (6)$$

For the same K values h/r_0, taking into account the volume of strain state, is smaller than the corresponding values calculated by (6) $(2{,}72 \to h/r_0 = 2{,}66;\ 2 \to h/r_0 = 1{,}34;\ 1{,}5 \to h/r_0 = 0{,}59)$. In expressing this difference as a quadratic trinomial, after determining the relevant standing, we obtain the expression $\Delta(h/r_0) = 1/3\left[(2/3)K^2 - (5/3)K + 1\right]$, from which it follows that the relative height of the cylindrical part, with the of volume strain state $1{,}5 \le K \le e$ it can be written as:

$$\frac{h}{r_0} = \frac{1}{2}\left(K^2-1\right) - \frac{1}{3}\left(\frac{2}{3}K^2 - \frac{5}{3}K + 1\right). \qquad (7)$$

From a comparison of (6) and (7) it follows that the relative error of the height of the cylindrical part, without changing the thickness reaches 20%.

Despite some arbitrariness of the analysis obtained calculated dependences allow to determine the relative error of linear and diametrical sizes, as well as indicators of resistance to deformation and to evaluate the quality of cylindrical parts.

5. Conclusion

1. Is given the theoretical accuracyestimateof linear and diametrical sizes and index of resistance to deformation of cylindrical parts in drawing.
2. Set vector fields equivalent deformations for the initial and final stages of the drawing process.
3. Based on the display of finite strains in deformed blank material environment identified characteristic features of the distribution of the radial deformation and deformation in thickness.

6. References

1. Metal *Forming Handbook/Shuler (c) Springer-Verlag, Heidelberg, 1998. 2013, N12,p.23-27*
2. *Forging and* Stamping, Handbook in 4 volumes, ed. E. I. Semenov Volume 4 (Stamping), M., Mechanical engineering, 2010, 544 p.
3. Technology and automation of sheet metal forming, Popov E.A.,Kovalev V.G.,Shubin I.N., , Ed. Bauman MSTU, 2000, 480 p.
4. Electronic handbook of cold forming. Omsk State University, Department of TMF 2006.
5. Hill R. The Mathematical Theory of Plasticity, Oxford Classic Texts in the Physical Sciences, 1998, p.362.
6. Nazaryan E.A., V.F.Konstantinov, Kinematics of deformation in the forming operations of sheet metal stamping // Bulletin engineering. 1999, N 2, S.35-41.
7. Nazaryan E.A., Arakelyan M.M. et al., Mechanics of forming thin ring plates, Izv. NAS RA, Mechanics, 2009, v.62, N4, S.80-88.
8. Nazaryan E.A., Arakelyan M.M., Analytic model of axisymmetric drawing // Blank production in mechanical engineering.

INDUCTIVE ENERGY INPUT IN FLUIDIZED BEDS

Dipl.-Ing. Vesselin V. Idakiev, Jun.-Prof. Dr.-Ing. Andreas Bück, Prof. Dr.-Ing. habil. Evangelos Tsotsas, Prof. Dr.-Ing. habil. Dr. h. c. Lothar Mörl
Thermal Process Engineering / NaWiTec, Otto von Guericke University Magdeburg, Germany

Vesselin.Idakiev@ovgu.de

Abstract: *The energy input in fluidized beds is usually performed by convection. In this case, the fluid stream is heated through a heater before entering the fluidized bed chamber. This method has long heating and cooling time. Therefore the purpose of this work is to find out other energy input options in fluidized beds. Such as, the induction heating is suggested. In this case, the fluidizing gas is not the source of energy, but the electrically conductive inert particles (like iron hollow spheres) into the fluidized bed, in which an induction electromagnetic field is transferred. On the surface of these particles, the heat is released directly into the fluidized bed. Here, since the heat is emitted via a large overall surface of the bed material, a very high energy density and, finally, highly efficient heat transfer can be achieved. In this way, the energy efficiency of fluidized bed processes can be significantly increased.*

Keywords: FLUIDIZED BED, INDUCTIVE HEATING, DRYING, SPRAY LAYERING GRANULATION

1. Introduction

A fluidized bed is a state of a two-phase mixture of particulate solid material and fluid, which has various procedural advantages and is widely used in various applications like drying, granulation and coating. Furthermore, the fluidized beds have a very good heat and mass transfer, which play an important role in many industrial processes. Usually, the fluidized beds are heated by the hot fluidizing gas. In this case, the energy input is realized by convection. Due to the long heating and cooling time of this method and thus resulting energy losses, other energy input methods should be suggested for increasing the energy efficiency of fluidized bed processes. The inductive heating is a possible way to achieve this objective.

Here, the energy input is transmitted directly by non-contact heating of electrically conductive but chemically inert particles in the fluidized bed. For this purpose, an induction electromagnetic field is transferred in this particles leading to their heating, and thereby, the heat is released on the surface of these particles directly into the fluidized bed. This results in large heat transfer surface areas and very quick heating and cooling.

By induction, the energy conversion occurs mainly at the edge zones (surface) of the particle due to the skin effect. The term " skin effect" refers to the tendency for alternating current to flow mostly near the outer surface of an electrical conductor, e.g. iron balls. It takes place with high frequency alternating current and describes the appearance of the current density. Due to the fact that the electric current flows mainly at the "skin" of the conductor, the current density decreases towards the center and it is largest near the surface of the conductor. The higher the frequency is, the greater the skin effect. This is a positive characteristic of the inductive energy input. In this way, only the particle surface must be heated for heat transfer (Filtz and Birenbaum 1987, Rudnev et al. 2003).

The inductive heating is applied in various processes including annealing, bonding, brazing, forging, hardening, melting, plasma production etc.. The heating by induction offers very clear benefits in terms of reducing heat loss and energy consumption in comparison to conventional convective heating. Moreover, induction transfers more energy per square meter than the open flame, which leads to faster heating. Ultimately this improves both the throughput and the quality (EFD 2010).

These considerable advantages of induction can also be transferred to fluidized bed processes. By using induction, the bed material will be faster heated and faster cooled, resulting in high efficiency and better product quality. Therefore, the research strategy pursued here focuses on the application of induction technology in fluidized beds in order to lower energy costs and thus enhance the complete production profitability.

In previos own research studies it was shown how induction influensses the fluidization behavior (Idakiev et al. submitted). The presented contribution describes therefore the heating behavior. Both methods of energy input in fluidized beds (induction and convection) are shown and compared. In addition, the application possibilities of the inductive energy input are presented, e.g. drying of suspensions in inductively heated fluidized beds and fluidized bed granulation with conventional and inductive heating. The ultimate goal of this work is to reduce the energy consumption during particle formulation processes in fluidized bed apparatus.

2. Experimental setup

In this study, two cylindrical fluidized bed apparatus are used for experimental purposes. One is heated by induction. Therefore, the plant is equipped with an inductor with 9 windings, which generate the electromagnetic field in the fluidized bed, leading to heating of the electrically conductive particles in the fluidized bed chamber. The inductor is electrically powered by a generator from Hüttinger Elektrik GmbH + Co. KG (TruHeat MF 3040). It can transmit electrical power up to 40 kW and is made from copper of high purity and has a good electrical conductivity. In order to avoid heating of the copper, the inductor is cooled with water during the trials. In this manner, the electrical conductivity is kept stable. The schematic representation of this experimental plant and the illustration of the inductor surrounding the fluidized bed chamber are given in Figure 1. The 2nd plant used in this study is heated by convection, thus via the fluidizing gas, in which the benchmark experiments are conducted. It is electrically heated and has the same fluid bed distributor plate as the inductive fluidized bed apparatus. Also, the fluidized bed chambers of both experimental plants have the same inner diameter of 300 mm permiting reproducibility of the tests carried out.

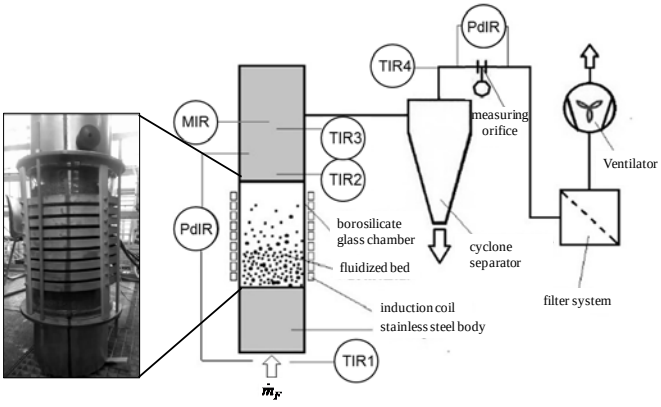

Fig. 1 *Schematic design and picture of the inductive experimental plans*

As an experimental material electrically conductive iron hollow balls (IHB) are used. Based on the production process of the

company Hollomet GmbH nearly monodisperse particles of defined diameter with varying the particle layer thickness can be produced (Hollomet 2014). This allows to create particles with defined fluidization properties. Therefore, hollow balls of conductive material with wide-ranging properties can be manufactured enabling a broad range of possible fluidization of solid material.

The iron hollow balls used in this work exhibit a sauter mean diameter of 3.22 mm, an iron layer thickness of 120 µm, and an apparent density of 1774 kg/m³. In addition, the experimental material can be coated with kaolin to insulate the iron hollow balls in order to prevent possible electricity flows at higher energy input between the individual particles leading to local overheating and sparks on particle surface. The kaolin coated and non-coated iron hollow balls are shown in Figure 2.

Fig. 2 *Iron hollow balls (kaolin coated and non-coated)*

As an experimental material electrically non-conductive glass beads (GB) in diameter of 2.66 mm and with an apparent density of 2615 kg/m³ are used to study the heating behavior of mixtures of conductive and non-conductive materials. They have similar fluid dynamic properties (determined by similar Archimedes number, minimum fluidization and elutriation Reynolds numbers) as the iron hollow balls. The glass beads are meant to represent the product of a real process, e.g. moist bulk materials for drying processes or carriers cores for spray layering granulation processes. In this study, they are used as model substance for carriers cores, too.

In order to determine the impact of individual process parameters on the efficiency of the inductive energy input and the behavior of the fluidized bed, various parameters such as applied electrical power, air velocity, kaolin coating, ratio of iron hollow balls to non-conductive material were systematically varied. In the presented study, only the influence of the applied electrical power and the ratio of conductive to non-conductive material on the heating behavior will be discussed. The impact of the other parameters can be gathered from our previous research studies (Idakiev et al. 2015, Idakiev et al. submitted).

In further experiments, the drying of suspensions in inductive heated fluidized beds is investigated. Here, limestone powder as raw material for the preparation of suspension to be dried by induction is used. The solids content in the tested suspension is 20 % m/m. After reaching the desired process temperature, the suspension is sprayed for 2 hours on the surface of the inert particles (IHB) forming solid layers on their surface, which break by collision resulting in finely-dispersed particles.

Subsequently, the fluidized bed spray layering granulation with inductive energy input is studied. In these experiments, 30 % m/m sodium benzoate solution is sprayed for 2 hours after reaching the desired process temperature. The spraying takes place from below in the form of a bottom spray. As carriers cores for build-up of granules, glass beads in diameter of 2.66 mm and with an apparent density of 2615 kg/m³, having a good thorough mixing and fluidization with the IHB are used in this study.

3. Results and Discussion

In this section, the temperature response under inductive energy input are presented and discussed. The evaluation of fluidized bed processes such as drying of suspensions and spray layering granulation in inductive heated fluidized beds is given in this section, too.

3.1 Heating behavior

Figure 3 shows the effect of the induction heating on the temperature increase and decrease, respectively. In the induction trials, after a few seconds the gas outlet temperature has already achieved a steady-state value while in the convective one the achieving of the steady-state value takes significantly longer. This also applies for the cooling process. The figure 3 proves that the induction technology massively reduces heating and cooling times. Therefore, temperature gradients are much more controllable. This allows the treatment of heat sensitive materials or biological substances demanding quick heating and cooling.

Moreover, all conducted experiments show a similar time response of the temperature. Even at different induction powers, the heating and cooling occurs equally quick. The gas outlet temperature increases with the increasing energy supplied to the system. It is to be noted that not all of the supplied electrical power is transferred to the iron hollow balls, but a part of the energy is consumed by the water cooling of the inductor as well as heat losses to the environment. This is the reason, why in the induction experiment more electrical power (5.5 kW) should be applied to achieve the same steady-state gas outlet temperature than the experiment with convective heating (4.0 kW).

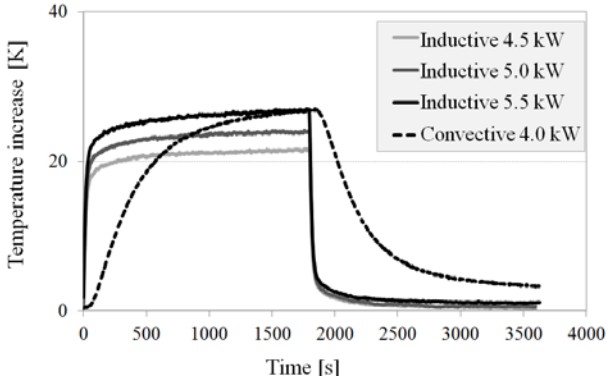

Fig. 3 *Influence of the energy input on the heating behavior*

Since the mixture ratio is an important parameter from the point of view of heating behavior, the necessary ratio of electrically conductive particles to bed material for efficient and uniform heating is investigated. The results thereof are presented in the Figure 4.

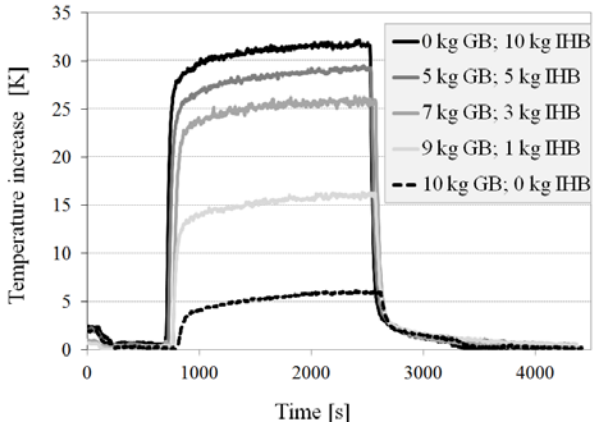

Fig. 4 *Influence of the mixing ratio on the heating behavior*

It can be seen an increase in temperature with the increasing proportion of iron balls. The greater number of electrically conductive balls is, the higher the surface of the particle collective on which the air can be heated. In the experiment, where the bed consist only of glass beads, therefore there are no conductive particles for the heat transfer, the slight increase in temperature can

be attributed to the fact that the steel flanges of the fluidized bed chamber are heated under influence of the electromagnetic field and they release the heat to their surroundings. Figure 4 illustrates that even with a small mass fraction of iron hollow balls (30 %), a high temperature increase similar to that of bed consisting only of iron hollow balls can be achieved. Therefore, the mixing ratio of 1:0.43 GB:IHB is selected for the spray layering granulation experiments (10 kg bed mass consisting of 7 kg GB and 3 kg IHB).

3.2 Drying of suspensions with inductive energy input

The temperature curves during the heat-up and spraying phases of the drying process with inductive and convective energy input are illustrated in the Figure 5. The heat-up phase designates the time difference between the switching on the heating and reaching the steady state temperature, at which the temperature deviation from the average is less than 0.25 K.

The heat-up phase of inductive heating is several times shorter than that of convective heating. Furthermore, the gas temperature or the operating temperature can be controlled very well with the induction heating method, since with switching on the heating the heat is available immediately for the drying process and with switching off the heating the process temperature immediately sinks. Although the steady state temperature is reached in a few seconds, the spraying is conducted after 1 hour to ensure comparability of the both experiments.

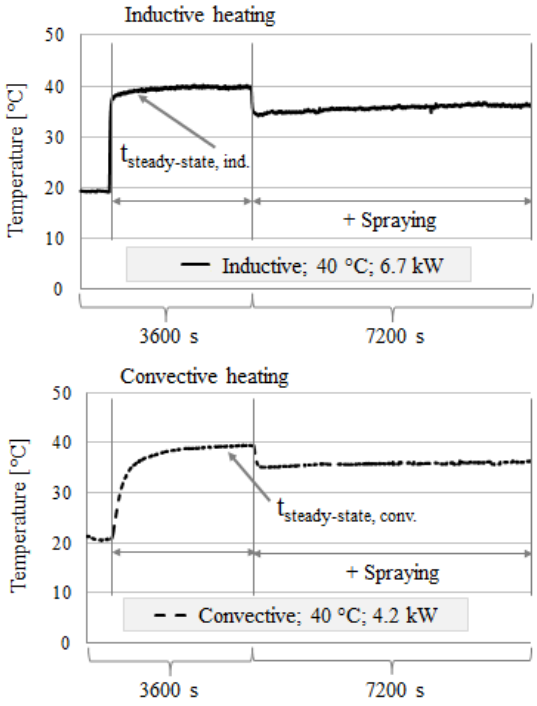

Fig. 5 *Temperature profile of suspension drying process*

Since the sprayed suspension is dried on the surface of the inert particles (IHB), it is important to know if some of solids adhere on the surface of IHB. As shown in Figure 6, no coating of the inert particles is observed, so that they are directly reusable. The scanning-electron-microscope (SEM) studies reveal that almost no differences exist in the surface structure of untreated IHB and IHB after the drying process (see Figure 6). Some pores are covered with limestone dust, but no homogeneous coating has been formed during the drying process.

Fig. 6 *SEM images of iron hollow balls before and after drying*

To clarify the possible changes in the product quality through the drying process, the surface structure and the particle size distribution of the untreated and dried product are investigated. The SEM images and the graphical presentation of the particle size distribution are provided in Figures 7 and 8.

The SEM images clearly show that no marked differences between the individual samples can be identified. The particle structure of all products is characterized by angular, irregular but smooth surfaces (Figure 7). But the particle size is clearly influenced by the drying process. The convective drying yields a product with wide particle size distribution. In comparison, the inductive drying results in formation of particles with a very narrow size distribution (Figure 8), which is especially preferred in pharmaceutical applications, e.g. pharmaceutical powders for use in inhalation.

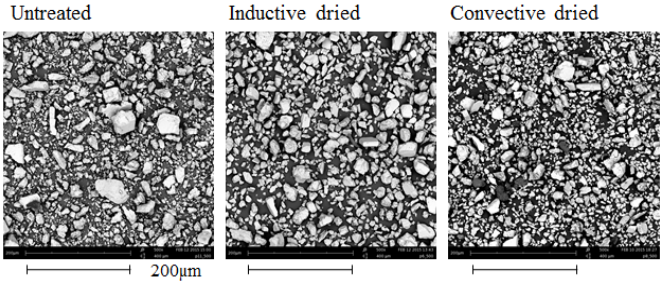

Fig. 7 *SEM images of limestone powder before and after drying*

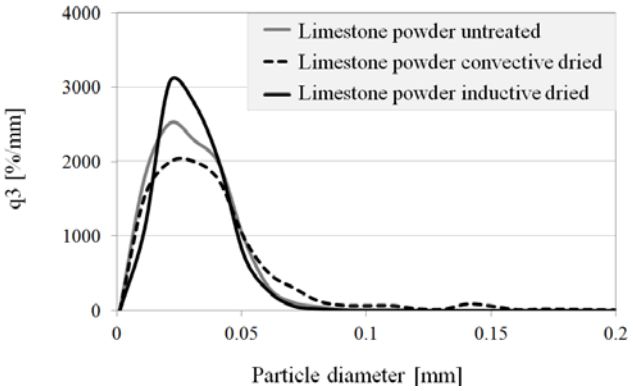

Fig. 8 *Particle size distribution of limestone powder before and after drying*

3.3 Spray layering granulation with inductive energy input

A comparison between the particle size of the untreated particles (IHB and GB) and that of the formed granules is given in Figure 9. The conductive particles as well as the carriers cores are simultaneously coated as illustrated by the SEM images in Figure 10 resulting in particle growth of both materials. It is important to note that the type of fluidized bed heating does not affect the particle growth. No differences between the inductive heating and convective one are observed.

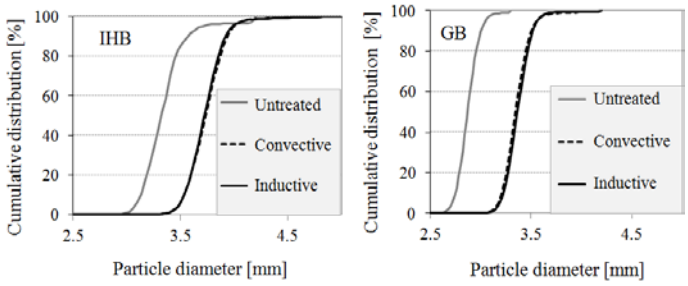

Fig. 9 *Cumulative distribution of IHB (left) and GB (right) before and after drying*

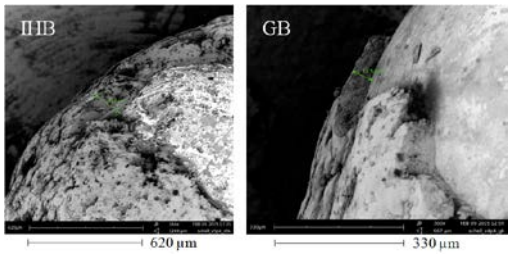

Fig. 10 *SEM images of coated IHB (left) and coated GB (right)*

To make a clear statement about the product quality of the produced granules, the morphology of the formed layer was investigated. For this purpose, the coating layer thickness and porosity of the obtained granules are measured using micro-computed X-ray tomography according to the method reported by Sondej et al. (2015). The 3D reconstruction of granule shells of glass beads is given in Figure 11. It was determined that by rising spray rate from 3.1 to 5.4 kg/h and constant temperature (55 °C) the coating layer thickness of granules is increased having a value ranging from 130 to 212 µm by inductive heating and from 169 to 243 µm by convective heating, respectively. By convective heating, the coating layer porosity also increases with increasing spray rate, so that it is 9.3 µm at 3.1 kg/h and 11.6 µm at 5.4 kg/h spray rate. Conversely, by inductive heating it decrease from 12.2 to 7.3 µm. Despite this difference, it could be concluded that the granules obtained from inductive and convective spray layering granulation do not differ essentially with respect to the product quality.

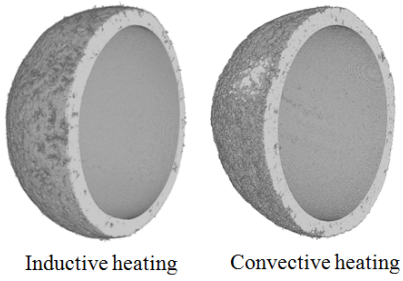

Fig. 11 *3D reconstruction of granule shells using micro-computed X-ray tomography*

4. Summary

In the presented study, the inductive heating is tested as an alternative to the convective heating in fluidized beds. In essence, this is attributable to the advantages that inductive energy input demonstrates, most notably in comparison with convective one. For example: very high heat transfer surfaces and energy densities due to the fact that the heat exchanger is the electrically conductive particles in the fluidized bed. Also invaluable here is the very quick time response, minimizing time and energy consuming heating and cooling times, and giving the possibility to precisely control the process. It is therefore the objective of the present study to apply the inductive energy input in fluidized beds in order to improve efficiency and enhance product quality.

From the investigation carried out, it can be concluded that the induction heating massively reduces heating and cooling times. The heating and cooling process is very fast, which is favourable for processing of heat sensitive materials or biological substances demanding quick heat treatment and short residence times.

Special attention was put on ways to find application of the inductive energy input in fluidized bed processes. Therefore, drying of suspensions and spray layering granulation are evaluated as possible application of inductive energy input in fluidized beds.

The inductive drying is characterized by a shorter heat-up phase in comparison with convective heating. The surface of the inert particles (IHB) is not affected by the inductive drying process. No undesired coating takes place during the drying, so that the iron hollow balls can be directly reused. From the point of view of product quality, the inductive and the convective drying can not be differentiated from each other. The inductive drying appears to be even more promising in regard to the narrow particle size distribution of the resulting product.

In view of spray layering granulation process, no differences between particle growth by inductive and convective heating are recognizable. The granules made by means of spray granulation with inductive and convective energy input show similar product properties like surface structure and layer morphology.

In summary, the results of the presented study clearly demonstrate the enormous potential of inductive energy input in fluidized beds. However, to use it in industrial applications as well as to bring fluidized bed apparatus with inductive heating to a marketable stage, further research effort is needed.

Acknowledgements

The project is funded by the Federal Ministry of Education and Research (BMBF) under the funding program “InnoProfile-Transfer”. The authors thank BMBF for the financial support as well as the master's degree students Ludger Schmidt and Stefan Helmeke for their experimental support. The authors would also like to convey thanks to Franziska Sondej for performing the micro-computed X-ray tomography measurements.

References

EFD, 2010. Induction heating applications. Brochure.

Filtz, M., Birenbaum, G., 1987. Der Skineffekt in Bandleitern bei aufgeprägtem Wechselstrom. Archiv für Elektrotechnik, 205-212.

Hollomet®, 2014. Hollomet Brochure.

Idakiev, V. V., Mörl, L., Bück, A., Tsotsas, E., 2015. Induktiver Energieeintrag in Wirbelschichten, Schriftenreihe zum 16. IFF-Forschungskolloquium am Fraunhofer IFF (Nov. 2014), XX–XX, Ed. M. Schenk, ISSN 2191-8783, docupoint.

Idakiev, V. V., Marx, S., Roßau, A., Bück, A., Tsotsas, E., Mörl, L., submitted. Inductive heating of fluidized beds: Influence on fluidization behavior. Powder Technology.

Rudnev, V., Loveless, D., Cook, R., Black., M., 2003. Handbook of Induction Heating. New York: Marcel Dekker Inc.

Sondej, F., Bück, A., Koslowsky, K., Bachmann, P., Jacob, M., Tsotsas, E., 2015. Investigation of coating layer morphology by micro-computed X-ray tomography. Powder technology 273, 165-175.

MICROSTRUCTURE AND MECHANICAL BEHAVIOR OF TIG BIMETALLIC JOINTS

M.F. Benlamnouar, R. Badji, M. Hadji, A. Boutaghane, N. Bensaid
Welding and NDT Research Center (CSC), PB 64, Chéraga, Algiers, Algeria
E-mail: csc.farid@yahoo.fr

Abstract: *Bimetallic weld techniques have progressed a great deal in the last decade. In this work, the effect of the filler metal composition on microstructure and mechanical behavior of dissimilar HSLA-X70/304L stainless steels weld joint is investigated. The dissimilar weld joints are fabricated using austenitic, duplex and low Carbone filler metal. The mechanical behavior is investigated through microhardness, charpy impact and tensile test.*

The results show that, the weld metal composition has a great influence on mechanical properties and microstructure of weldments, in particular the grain size and phases nature, changes with filler metal composition. In addition presence of martensitic slats in the FZ when using the low Carbone filler metal, detailed microstructure examination is carried out and related to the mechanical behavior of the dissimilar joints.

KEYWORDS: TIG WELDING, BIMETALLIC WELD, HSLA, DSS, HAZ, MICROSTRUCTURE, MICROHARDNESS.

Nomenclature: *HAZ: heat affected zone, I: average intensity (A), FZ: fusion zone, MV: medium voltage (V), TIG: tungsten inert gas, D: Argon flowrate (l/min),* Φ : electrode diameter(mm), *K: Charpy impact energy (J), V: weld speed (mm/min) HV0.2: Microhardness (load of 0.2 kg),* σ_m *(MPa): maximum stress,* ε_m *(%): maximum strain, S: Sample (S3: third sample)*

Elément(%)	C	Si	Mn	P	S	Al	Cu
X70	0.08	0.7	2.39	0.01	0.001	0.06	0.01
304L	0.07	0.75	1.85	0.045	0.03	-	-
Elément(%)	**Cr**	**Mo**	**V**	**Nb**	**Ti**	**N**	**Ni**
X70	0.04	0.1	0.05	0.4	0.09	-	0.02
304L	18.5	-	-	0.08	-	0.08	-

Table 1: *Chemical composition of base materials*

1. Introduction

High strength low alloys (HSLA) and Austenitic stainless steels have been used widely by the fabrication industry owing to their high resistance to corrosion combined to excellent mechanical properties. Some of the typical applications of these steel include their use as pipelines, oil refining, pressure vessels, chemical and process industries ….etc.

Homogeneous weld applications require the use of filler metal which contains the same chemical composition with base metal in order to get more mechanical resistance of welded material, this resistance depending on a number of factors like mechanical properties, wear and friction characteristic... ... etc. In this regards There are numerous investigations on the characterization austenitic or HSLA steel using arc welding regardless of any assembly between them [1, 2]; however, there are little data on the evaluation of mechanical properties to weld together HSLA/Stainless steel.

At present, some Studies have been conducted on welding of stainless steel with HSLA steel, almost all common fusion welding techniques can be used to weld duplex stainless steel through selecting appropriate welding parameters, corrosion resistance... or residual stresses condition, in this study we interest to filler metal selection.

Filler metal composition has a great influence on the solder properties. Mechanical properties and toughness of weldment depend of microstructure of weld metal and heat affected zone.

The welding process used was Tungsten arc welding (TIG). These were chosen because each process is one of the most commonly used welding techniques in industry.

2. Experimental Procedure

Bases material used in present work is austenitic (304L) and ferrite-perlitic (X70) steels. Their chemical composition and mechanical properties are given in Table 1. The steel is welded by semi-automatic tungsten arc welding (TIG), According to moved table in order to set welding speed.

Based on partial plates of base materials, TIG welding was carried with three filler metal, namely, austenitic stainless steel 308, (Sample 1:S1), duplex stainless steel 2209 (S2), low Carbon E7018 (S3), and the fourth sample (S3) is intended to cover welding process without filler metal.

Filler metal selection is based on the homogeneity of chemical composition with each base metal: for X70 we take and for E7018 we take 304L.

In order to maintain similar welding parameters conditions, the weld cou- pon dimensions were fixed at 100 mm X 60m X 2mm (Fig. 1) and the electrodes diameter fixed at 1.5 mm.

Fig.1. *Plates of Sample number two (S2)*

Our welding has one pass based on TIG welding with to avoid cracking, supercooling and excessive penetration. Before welding, Pairs of plate were welded together (edge to edge) width-wise at each filler metal (Fig. 2).

Chemical composition of filler metal is given in Table 2. The welding is carried out with fixed parameters (Table 3).

Table 2: *Chemical composition of filler materials*

Elément (%)	C	Si	Mn	Cr	Ni	Mo
E308L	0.19	0.46	1.72	20.80	10.10	
E2209	0.03	0.46	0.9	22.5	9.3	2.8
E7018	0.12	0.80	0.90	-	-	0.5

Table 3: *Welding parameters*

I (A)	MV (V)	V (mm/min)	Φ (mm)	Temps (s)	D (L /min)
72	11.68	2.515	1.5	53	8

The tensile specimens were tested on a servo hydraulically controlled digital tensile testing machine. Three specimens per each filler metal were machined out from the weld plate. Each tensile specimen size was prepared in accordance with ASTM E08 standards [5] as illustrated schematically in Figure 2.

The Charpy test was performed according to standard test methods for notch bar impact testing of metallic materials [6]. The total length of the specimen is 55mm and the rectangular cross-section area is 5mm×2mm. Specimen has a V-shaped notch with a flank angle of 45° and depth of 2mm (Fig. 3) in the HAZ and FZ.

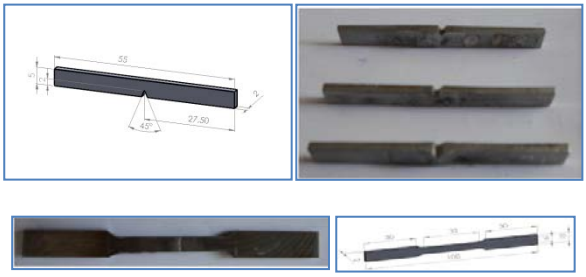

Fig.2 *Specifications of Charpy and tensile specimens [6-8].*

3. Metallography

For the observation of microstructural changes that take place during welding, corresponding to each filler metal; specimens were taken from the welded plates. The microstructures of the joints were captured with the help of optical microscopy. Standard polishing procedures were used for microstructural observations, Glycerine reactif was used with the conditions (20ml of nitric acid, 30 ml HCl acid and 30ml of glycerol) for 3min.

Table 4: *Morphology of solders*

S1	S2
	
S3	S4
	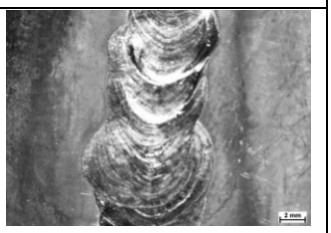

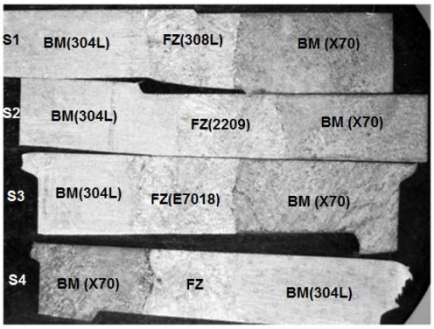

Fig.3 *Attacked samples*

These micrographs show that the weldments are free from welding defects like lack of penetration, undercut, cracks…etc.

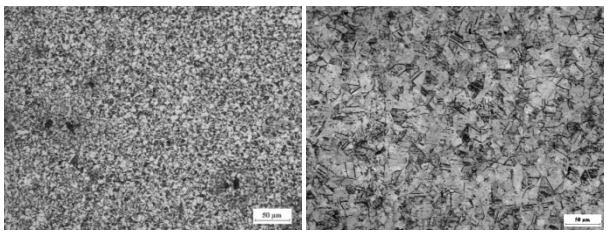

Fig.4 *Optical microstructure of the two materials (in the left HSLA-X70, 304L SS in the right)*

Micrograph of X70 base metal describes polygonal ferrite–pearlite containing about 70% ferrite, while the microstructure of 304L consists of polycrystal of single-phase which consists of equiaxed austenitic grains with an average diameter of 17µm.

Table.5: *Micrographs of weldments*

	FZ	HAZ
S1	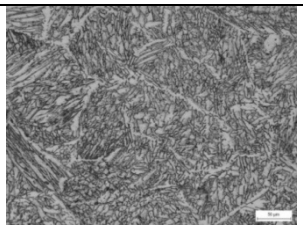	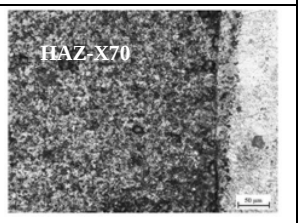
S2	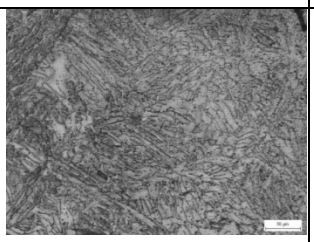	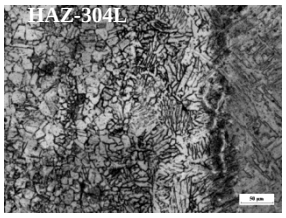
S3	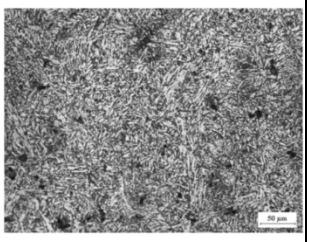	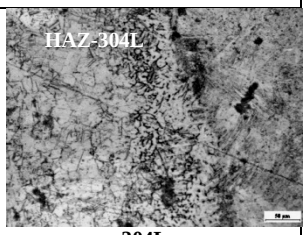 **304L**
S4	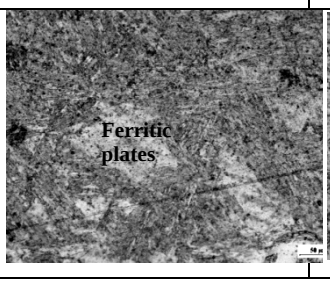	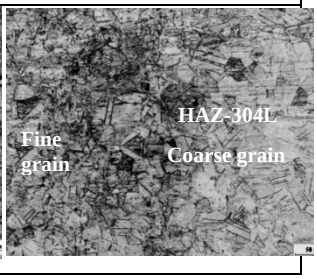

Polished samples were scanned on the optical microscope along the weldments zones of the fusion zone and the HAZ, and at a few places microphotographs were taken in the middle of fusion line (Fig.3). As a result, this study has many microstructures of dissimilar joints in accordance with various mechanical properties.

The microstructure of the (HAZ-X70) undergoes a decrease in grain size when it becomes close to the base metal, the latter is characterized by a ferritic-pearlitic structure with large ferrite content. it's also distinguished by the presence of acicular ferrite and the formation of martensitic slats, this presence is even greater in S4 with carbides formation in fusion line.

Microstructure of duplex fusion zone revealed that the principal constituents are austenite and columnar ferrite with fine intermetallic precipitation in ferritic phases. Moreover,

Microstructure evaluation of austenitic fusion zone reveals essentially a dendritic ferrite in austenitic matrix. With regard to the fourth sample, With regard to the fourth sample, fusion zone presents a continuous casting structure.

5. Mechanical behavior

Microhardness

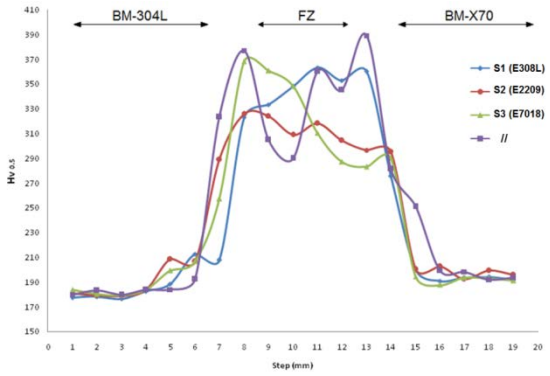

Fig.5 *Microhardness profiles*

The microhardness measurements are schematized relative to solder center of the four samples. For the S1 and S3, there was an increase in the microhardness of both the fusion lines and heat affected zones (HAZ). These higher microhardness values in fusion line are related to the higher Carbon content of 304L and X70 base materials (Table 2), which produced a large amount of Carbide precipitation.

In S4 fusion zone, Microhardness values is severly disrupted, this can be explained by the presence of ferrite plates and martensite lattices in this area.

As regards the austenitic HAZ of samples, Austenite grain growth increased from small ratio in S2, and S3 to big ratio in S4, this phenomenon can be explained by cooling rate and solubility modes of filler metals in 304L SS (Table 5).

The fuzion zone of S2 is characterized by balanced level of microhardness. Otherwise, In the other samples, microhardness is characterized by high level values.

A brittle microstructure was formed in FZ-S4, which contains primarily large ferritic plates (about 27µm) surrounded by lamellar martensite. This can be explained by the strong instability in microhardness values with the presence of intermetalic inclusions which were found in fusion zone (dark spots in FZ-S4, Table.5).

In fusion line of 304L SS, there is a similar properties of microhardness of duplex filler metal and austenitic filler metal, this is due to the presence of same nature of phases which formed during TIG welding, these phases consist principally of delta ferrite and Secondary austenite. The inclusions also were found on fusion line of 304L SS.

Tensile test

The tensile strength of joints has been evaluated. In each sample three specimens were tested, the tensile strength and their elongation are mentioned in Table 6.

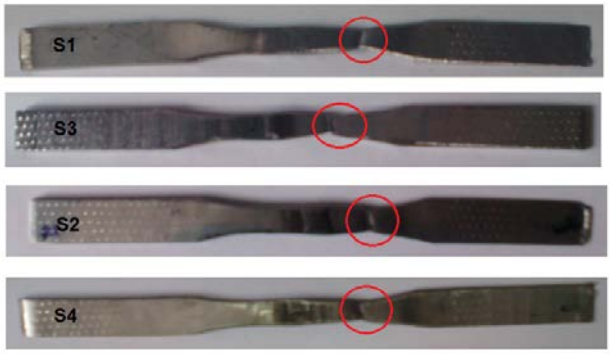

Fig.6 *Broken specimens*

The Ultimate strength and elongation of S1, S2, S3 and S4 specimen are shown in Table 2. therefore, the tensile properties change significantly with the filler metal nature, which can be attributed on one hand by the Difference between the four microstructures of fusion zones, and on the other hand by the joining zone, which is influenced, primarily by connection zone (FZ/HAZ), and in secondary consideration: by austenitic grain growth (in HAZ-304L) and ferritic grain growth (in HAZ-X70).

Among the different testes, a duplex filler metal clearly gives a better combination of strength, ductility compared to the other filler metals (Table.6).

Table.6: *Tensile properties of the weld joints*

Sample	S1	S2	S3	S4
σ_m (MPa)	522.40	642.02	671.77	487.13
ε_m (%)	15.1	14.8	11.8	9.3
Location of fracture	MB(X70)	MB(X70)	BM (304L)	BM(X70)

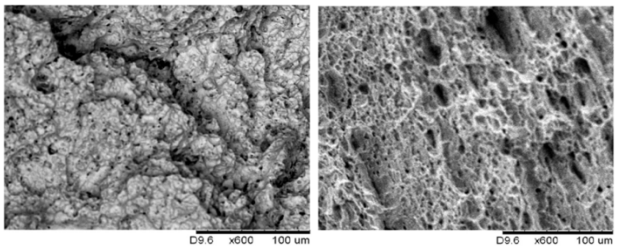

Fig.7 *SEM fractographs (X70 in the right)*

Examination of the fracture surfaces of the broken mechanical test specimens showed that Transgranular brittle failure and intergranular ductile failure occur in 304L-S3 specimen, which contains Clefts and river forms, with the presence of several crack arrest lines.

The fracture surface in X70 base metal indicated a ductile failure with granular aspect, which is consistent with significant ravelling of material. Therefore, ductile cleavage indicates that cracks growth phases were relatively slow compared to S3 specimen.

Charpy impact

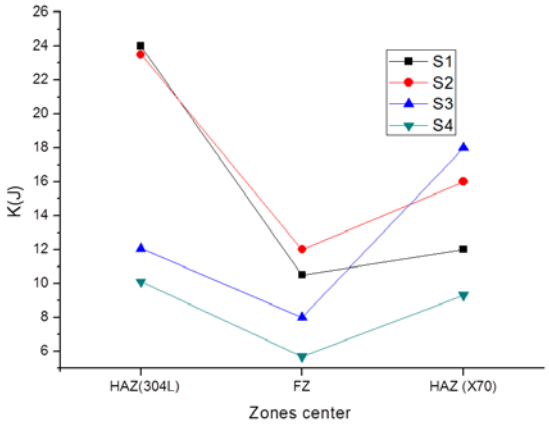

Fig.8 *Measurements of Charpy Impact*

The impact tests presented in figure 6 indicated that the combination of impact resistance (K) in second sample (S2) is better than the other samples. However the lower energy was found in S4 fusion zone. Furthermore, it is also apparent that homogeneous bimetallic joints have excellent impact properties (low Carbone fusion zone with X70 base materials and stainless fusion zones with 304L base material) compared to the heterogeneous joints.

6. Conclusion

Based on the results obtained, it was possible to conclude that:

Duplex filler have a good weldability with 304L SS/ HSLA-X70 dissimilar joints compared to austenitic low Carbone filler metal by medium energies of TIG process.

This study investigates the effects of filler metal composition on 304L SS/ HSLA dissimilar welds and the formation of microstructures at various weld zones of different filler metal composition, Variation in morphology of microstructures across the fusion zone and heat affected zone is evident within solder. Microhardness profiles charpy test tensile test are made and linked with the formation of the microstructures in different weld zones.

As regards the mechanical behavior, At Samples welded by filler metals, there was an increase in the hardness of both the FZ and the HAZ with the best characteristic given by duplex filler metal. This filler metal combines between improvement in maximum tensile and amelioration of impact resistance.

In welded sample without filler metal, we find a significant decrease in mechanical properties. That phenomenon can be explained mainly by existence of ferrite slabs and martensite lattices in fusion zone.

To understand more realistically the application of dissimilar weld joints in industry, electrochemical tests will be very important to evaluate the resistance of weldment against corrosion degradations.

References

[1] Subodh Kumar, A.S. Shahi. “Effect of heat input on the microstructure and mechanical properties of gas tungsten arc welded AISI 304 stainless steel joints” Materials and Design 32 (2011) 3617–3623

[2] S. Jana “Effect of heat input on the HAZ properties of two duplex stainless steels”, Journal of Materials Processing Technology, 33 (1992) 247-261

[3] V.S.R. Murti, Y.R. Sastry “Some studies on the service weldability of HSLA steels using 18Cr, 8Ni, 6Mn type austenitic electrodes”, Journal of Materials Processing Technology, 37 (1993) 759 765.

[4] Sindo Ko “Welding metallurgy”, Second Edition. ISBN: 0-471-43491-4 (2003).

[5] Rahul Unnikrishnan, K.S.N. Satish Idury. “Effect of heat input on the microstructure, residual stresses and corrosion resistance of 304L austenitic stainless steel weldments” materials characterization 93(2014)10–23

[6] ASME “Qualification Standard for Welding and Brazing”, An International Code of ASME Boiler and Pressure Vessel Committee on welding and Brazing, USA, 2010.

[7] ASTM International E08-03“Standard test methods for tension testing of metallic materials”.

[8] ISO 148 “teste d’impact sur échantillons iso en V”, NF EN ISO 148-2 (2009).

PRODUCTION AND CHARACTERIZATION OF Al - WC COMPOSITE POWDERS VIA MECHANICAL ALLOYING

M.Sc. Şelte A., Assoc. Prof. Dr. Özkal B.
Istanbul Technical University, Metallurgical and Materials Engineering Department, PML Laboratories,
34469, Maslak, Istanbul, Turkey
selte@itu.edu.tr, ozkal@itu.edu.tr

Abstract: *Mixtures of 10, 20 and 30 wt. % of tungsten carbide powder and aluminum powder were ball milled for 2, 4 and 8 hrs to investigate the effect of percentages of the reinforcement and mechanical alloying time on microstructural properties of the produced composite powders. Finer particles were tried to obtain in ductile matrix. The milled powders were analyzed using X-ray diffraction (XRD). Nano/micro particle size and distribution (PSD) technique was used to measure particle size and distribution. Scanning electron microscopy (SEM) was also performed to observe particle morphology.*

Keywords: NANO COMPOSITE POWDERS, Al-WC SYSTEM, MECHANICAL ALLOYING

1. Introduction

Despite of their poor friction and low wear resistance, aluminium alloys have been mostly preferred to use on automotive, aircraft and marine applications because of their low density and high specific strength, [1-5].

Aluminium-based metal matrix composites with small amount of particle size ordered as discontinuous hard phases as reinforcement have paid attention to remarkable research interest during recent years, [6]. Particularly, Al-based composites reinforced with ceramic particles are being demanded due to their high strength-to-weight ratios accompanied with high mechanical properties such as high strength, high modulus, high specific stiffness, fatigue resistance and wear resistance, [7]. These kind of metal matrix composites (MMCs) have been considered as the excellent candidates for automotive, aircraft and marine applications for a very long time, [8], [9]. Nevertheless, tungsten carbide (WC) is interesting reinforcing clearly leading very high hardness values and composite benefits [10-13].

In this respect, the aim of this study is to investigate the effects of particle size and amount of carbide addition on the production of Al-WC composite powders and to perform a detailed characterization of finer particles. The motivation of this study is related with the results of our previous findings during mechanical alloying of Cu-WC system [14].

2. Experimental Procedure

In this study, Al (Alfa Aesar, -325 mesh, 99.5% purity) and WC powders (Alfa Aesar, -325 mesh, 99.5% purity) were used. Powders were mechanically alloyed for 2, 4 and 8 hours. Elemental Al and WC powders were blended to constitute the composition of Al–10/20/30 wt% WC (hereafter called as Al10WC, Al20WC and Al30WC). Blended powders were mechanically alloyed (MA'd) for 2, 4 and 8h using a Spex™ Duo Mixer/Mill 8000D with a speed of 1200 rpm in a tungsten carbide (WC) vial with WC balls having a diameter of 6.35 mm (1 = 4 inches). The vials were sealed inside a Plaslabs™ glove box under purified Ar gas (99.995% purity) to prevent oxidation during MA. The ball-to-powder weight ratio (BPR) was 10:1. Powder particle size and distributions (PSD) were carried out in a Malvern™ Mastersizer Laser particle size analyser according to Mie's theory using ethanol as a dispersant. Finer particles were measured in Microtrac™ NanoFlex. All powders were dried at 100^{o}C to remove moisture for measuring true densities which were measured in Micromeritics™ AccuPyc II 1340 Gas Pycnometer under He atmosphere.

3. Results and Discussion

Particle size and distribution of initial powders were illustrated in the Figure 1.

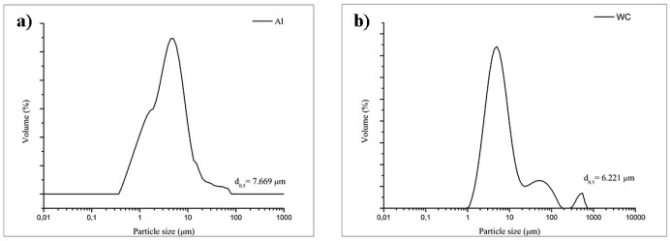

Figure 1. *Particle size and distribution of initial powders*

The d(0.5) value of particle sizes were found for initial Al and WC powders as 7.669 µm and 6.221 µm, respectively. As seen from the figures, WC powder particle size has a wide range of size distribution in coarse particle sizes. After performing mechanical alloying process, powder particle size and distribution of powders were described in Figure 2.

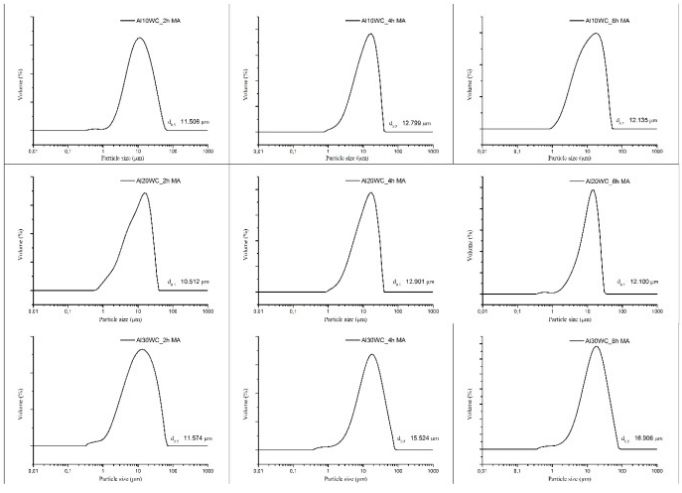

Figure 2. *Particle size and distribution of initial powders*

As seen from the figure, mean particle size of the powders changed slightly according to mechanical alloying (MA) time and hard phase amount. It is clearly seen that, MA time can be effective while the presence of high amount of hard phase. Otherwise, small amount of changes occurred by increasing milling time. It can be concluded from the figure that the agglomeration tendency increased even the mean particle size decreased.

True densities of the MA'ed powders were given in Table 1. And Table 2 summarizes the theoretical densities of the systems.

Table 1. *True densities of MA'ed powders*

Powder	Milling Time (h)	True Density (g/cm^3)
Al10WC	2	2,81
	4	2,86
	8	3,27
Al20WC	2	3,06
	4	3,28
	8	3,28
Al30WC	2	2,90
	4	2,96
	8	3,30

Table 2. *Theoretical densities of the powder compositions studied.*

Powder	Theoretical Density (g/cm^3)
Al10WC	2,94
Al20WC	3,24
Al30WC	3,59

The true densities values of MA'ed powders measured by gas pycnometer are considerably lower than theoretical densities for early milling times. This was occurred for Al10WC powder until 8 hours milling time, in where it was 4 hours for Al20WC. Besides, all measured densities for Al30WC were below the calculated value. This could have been existed by the high faults, misorientations of metal sublattice which is regulated by metal structural vacancies. Therefore, the imperfection in milling of Al-WC in high rate of WC is higher than Al-WC in low rate of WC can be deduced from these results.

Figure 3 shows the XRD patterns of the milled powders. All the detected peaks are characteristic of the Al (ICDD No: 04-0787) and WC (ICDD No: 89-2727).

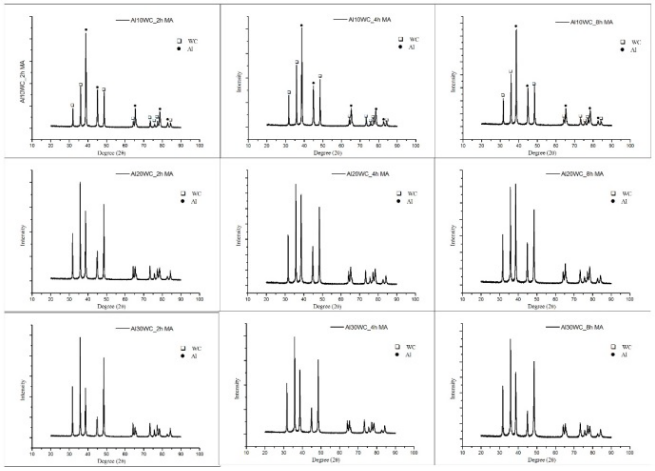

Figure 3. *XRD patterns of MA'ed powders*

Peaks belong to Al and WC powders can be seen clearly from the figure. It was observed that Al peak intensities increased and the peaks broadened by increasing milling time. Slight sliding in Al peaks was also detected. It was concluded that these attitudes appeared as a result of distortion and misorientation in lattice of Al owing to tensile and compressive loadings occurred by mechanical alloying. This situation was verified by calculating strain rates and changes in d spacings of Al peaks which were given in Table 3 and Table 4. However, the percentage of WC addition affected the broadening and intensities of Al peaks until 30 wt.% of WC. This can be a consequence of exceeding the maximum number of atoms which were needed for formation of hard-core solution. Therefore the increasing changes in intensity and peak broadening commenced to decline in the presence of high amount of WC addition.

Table 3. *Strain rate changes (%) in Al peaks against milling time.*

Powder	MA Time (h)	Strain Rate (%)
Al10WC	2	0.2123
	4	0.3911
	8	1.3226
Al20WC	2	0.3566
	4	0.6127
	8	1.6115
Al30WC	2	0.3324
	4	0.4469
	8	1.2901

Table 4. *Strain rate changes in d-spacings (%) in Al peaks against milling time.*

Powder	MA Time (h)	Change in d-spacings (%)
Al10WC	2	0.4155
	4	0.7101
	8	0.7088
Al20WC	2	0.6859
	4	0.9948
	8	0.8523
Al30WC	2	0.8523
	4	0.8367
	8	0.8107

Strain rates were determined by calculating the arithmetic mean of dominant three planes. D-spacings were estimated only by taking account of (111) plane of Al. As seen from the Table 3 and 4, strain rates increased by increasing milling time. After high percentage of reinforcement material, WC, this increase has become declining parabolic. Changes in d-spacings were determined on the same shifting direction. Hard core solid solution was considered to be a basis for this situation for high rate reinforcement existence.

Scanning electron microscope (SEM) micrographs were given in Figure 4.

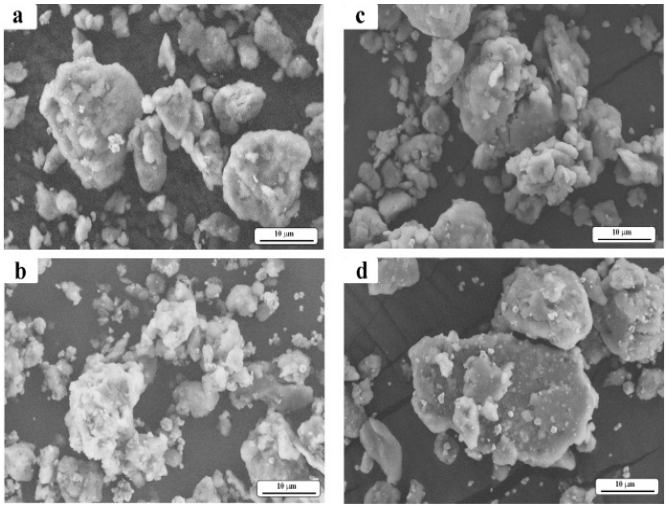

Figure 4. *SEM images of a) Al10WC 2h MA, b) Al10WC 8h MA, c) Al30WC 2h MA and d) Al30WC 8h MA at x2000 magnification.*

The effects of hard phase ratio and mechanical alloying time on the morphology of composite powders can be easily distinguished. The higher the hard phase rate, the more agglomeration tendency can be observed. In other respects, finer carbide particle existence increased by milling time and hard phase raise. WC particles were seems to be covered with Al particles and it was considered that the agglomeration tendency rate was multiplied as a result of increasing ductile Al milling time. Smaller and finer WC particles which were achieved via milling in the ductile Al matrix can also be seen in Figure 5.

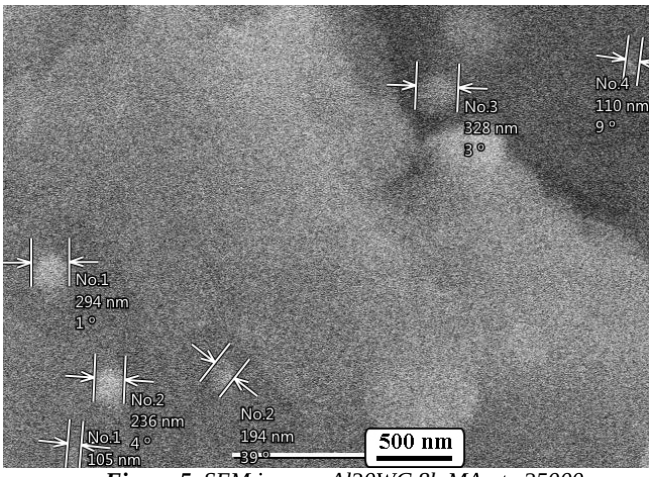

Figure 5. *SEM images Al30WC 8h MA at x25000 magnification.*

As seen from the Figure 5, it possible to obtain finer, submicron and nano particles. The presence of both phases provided suitable environment for production of nano structured powder composite despite the increasing tendency of agglomeration. It was clearly observed that obtaining finer/nano particles with increasing milling time by the existence of ductile matrix was convincingly possible.

4. Conclusions

In this study, the behaviors of WC and Al powders during mechanical alloying were investigated. According to results of the experiments these conclusions were obtained:

1. Although the mean particle size and the distributions of particle analysis applied to different mechanical alloyed powders does not show a significant difference, it was possible to observe finer hard particles inside of Al matrix during microstructural examinations.
2. Al peaks shifted slightly to the same direction. This was concluded as a result of distortion at crystal occurred by WC atoms which tried to constitute hard core solid solution.
3. It was observed that the strain value increases for longer mechanical alloying times.

References

[1]. C.L. He, Q. Zhou, J.T. Liu, X.W. Geng, Q.K. Cai, Effect of size of reinforcement on thickness of anodized coatings on SiC/Al matrix composites, Materials Letters, 62, 2008, 2441.

[2]. M. Yandouzi, P. Richer, B. Jodoin, SiC particulate reinforced Al–12Si alloy composite coatings produced by the pulsed gas dynamic spray process: Microstructure and properties, Surface and Coatings Technology, 203, 2009, 3260.

[3]. R.L. Sun, Y.W. Lei, Microstructure and hardness of laser clad SiCp–Al composite coatings on Al alloys, Materials Letters, 62, 2008, 3272.

[4]. S.O. Chwaa, D. Kleina, F.L. Tomaa, G. Bertranda, H. Liaoa, C. Coddeta, A. Ohmori, Microstructure and mechanical properties of plasma sprayed nanostructured TiO2–Al composite coatings, Surface and Coatings Technology, 194, 2005, 215.

[5]. S. Yang, N. Chena,W. Liua, M. Zhong, In situ formation of MoSi2/SiC composite coating on pure Al by laser cladding, Materials Letters, 57, 2003, 3412.

[6]. S.C. Tjong, Novel nanoparticle-reinforced metal matrix composites with enhanced mechanical properties, Advanced Engineering Materials, 9, 2007, 639.

[7]. A.A. El-Daly, M. Abdelhameed, M. Hashish, Walid M. Daoush, Fabrication of silicon carbide reinforced aluminum matrix nanocomposites and characterization of its mechanical properties using non-destructive technique, Materials Science & Engineering A, 559, 2013, 384.

[8]. S. Bathula, R.C. Anandani, A. Dhar, A.K. Srivastava, Microstructural features and mechanical properties of Al 5083/SiCp metal matrix nanocomposites produced by high energy ball milling and spark plasma sintering , Materials Science and Engineering: A, 545, 2012, 97.

[9]. H.R. Hafizpour, A. Simchi, S. Parvizi, Analysis of the compaction behaviour of Al–SiC nanocomposites using linear and non-linear compaction equations, Advanced Powder Technology, 21, 2010, 273.

[10]. H.C. Man, Y.Q. Yang,W.B. Lee, Laser induced reaction synthesis of TiC+WC reinforced metal matrix composites coatings on Al 6061, Surface and Coatings Technology, 185, 2004, 74.

[11]. G. Bolelli, L. Lusvarghi, M. Barletta, HVOF-sprayed WC–CoCr coatings on Al alloy: Effect of the coating thickness on the tribological properties, Wear, 267, 2009, 944.

[12]. R. Jendrzejewski, K. Van Acker, D. Vanhoyweghen, G. Śliwiński, Metal matrix composite production by means of laser dispersing of SiC and WC powder in Al alloy, Applied Surface Science, 255, 2009, 5584.

[13]. M.H. Staia, M. Cruz, N.B. Dahotre, Wear resistance of a laser alloyed A-356 aluminum/WC composite, Wear, 251, 2001, 1459.

[14]. A. Selte, B. Ozkal, Infiltration behavior of mechanical alloyed 75 wt.% Cu - 25 wt.% WC powders into porous WC compacts, Archives of Metallurgy and Materials, 60, 2015 1565.

PRESENTATION OF A NOVEL APPROACH TO RECYCLE METAL COATED PRODUCTS

Dipl.-Ing. Prumbohm M. F., Prof. Dr.-Ing. Lohrengel A., Dr.-Ing. Schaefer G.
Institute of Mechanical Engineering – Clausthal University of Technology, Germany

prumbohm@imw.tu-clausthal.de

Abstract: *By recycling old products mainly the elements, which are contained in large amounts in the product, are regained. Taking metal coated Waste Electrical and Electronic Equipment (WEEE) as an example, this is the plate of the component cover, which is made of steel or aluminum, the included plastic, the printed circuit board's material and copper. Those materials, which are contained on the printed circuit board belonging to the area of specialty metals such as tantalum, indium, palladium etc., cannot economically be extracted from a shredder plant's output mass flow. To solve this problem, a new approach for an automatic decomposition of metal coated components is introduced based on the process principle of the roll crusher. For finding a solution the systematic design approach and a first pilot plant's results are presented. Based on these results, conclusions for future developments are derived.*

Keywords: RECYCLING, DISASSEMBLING, WEEE, METAL COATED PRODUCTS, PRODUCT DEVELOPMENT

1. Introduction

With the increasing development of recycling technology the decomposition of metal coated products with valuable internal components is getting into the research focus. These products especially include WEEE. Those are for example hard drives, server and disk drives from desktop computers. In this context the automotive sector with its control units, entertainment units in high quantities and inverters from hybrid vehicles is quite important. The common WEEE recycling is structured into the detection of type and contaminants followed by sorting and extraction of the hazardous components. After this the shredding of the remaining products takes place in a machine (1). In this context it has to be pointed out that only for large parts or special units a manual disassembly is profitable.

As a result of the shredding process the outgoing mass flow, which contains small amounts of recyclable materials such as tantalum, indium, palladium etc., is highly mixed with all other materials. Large material fractions as plastic, ferrous metals and non-ferrous metals can be profitably separated from this mass flow and are reusable. This is not possible for small amounts of the previously named materials. They are getting lost for the recycling economy. Due to this effect the current recovery quota for these materials and some other important specialty metals from post-consumer-wastes is less than 1 % (2). Manual disassembly is the alternative to shredding as it is easier for the recycling of all the materials. However, as it enables on the one hand the separation of the circuit boards with only a few impurities and their use for another process, this procedure is on the other hand also very time-consuming and mostly not economically efficient. A third option for the preservation of all contained component materials, is the reuse of the whole component after some testing and repair work. This is done for instance by the Bosch company with components from the automobile sector (3).

2. Estimation of economics

Before a new approach is being developed, the needed time for the separation of components and the expected revenues are estimated by literature information. For this purpose a study on the content of recyclable materials such as circuit boards is used (4). Those circuit boards are taken from different car types. Within this study the revenue for the manual disassembly of the most profitable components is identified. In the following the revenue for the circuit boards is averaged over the different car types. For the manual disassembly the averaged revenue is 1.65 €/component. The gearbox control is with 7 €/component highly above this price (without considering the gearbox control price the averaged revenue amounts 0.96 €/component only). Comparing those values to german repair shop costs of 35 €/hour or approximately 0,58 €/minute, a maximum disassembly time of less than 3 minutes for a commercially profitable disassembly is required. Based on this assumption a revenue of 0.49 €/component is reachable, with a disassembly time of 2 minutes. This time target is difficult to reach even if impurities are neglected. A process, which separates at least 3 components/minute, increases the revenue by nine times up to 4.37 €/minute. Not considered in this calculation are the inverters in hybrid vehicles. Those reach a revenue up to 12.20 €/component, which improves the attraction of the manual disassembly as well as the attraction of an automatic separation process significantly. This rough analysis shows that an automatic component separation can be economically profitable.

3. current state of shredding processes

Components at the end of their life cycle are treated either by manual disassembly or more often by machines. The outgoing shredded fractions are sorted by type, decomposed and purified. Several well working first stage shredding processes exist for the shredding of components belonging to the WEEE-field. However, the recycling of elements, which are integrated only in small amounts in the component, cannot be regained afterwards, see chapter 1. It is looked upon the following existing shredding processes for metal coated components in more detail. They are the basis for the solution development, which is followed by an evaluation. In the brackets the main types of loads are listed (1); (5):

- profiled roll crusher (depending on the profile: pressure, shearing, impact),
- ripping machine (tension),
- rotary shear (combination of bending, tension, shearing and torsion lead to a complex stress state),
- Querstromzerspaner (impingement) (6) and
- pre-crushing machine SB² (impingement, shearing, bending) (6).

These listed existing shredding processes are compared with the following criteria of an ideal automatic separation process:

- complex stress states support separation with little deformation
- high stress speed supports separation with little deformation
- deformation of the component cover through pressure, impingement and impact by the process are rare or do not occur
- embedding of ductile elements of the component cover are avoided (double weighted)

An ideal solution fulfills the criteria entirely and is weighted with 100 %. It is used as a benchmark for the existing processes. The evaluation result shows that no existing process fulfills the majority

of the criteria. The profiled roll crusher achieves the best result with 54 % of an ideal solution. The main disadvantages of this process are the compaction of the components during the separation process and the cutting component due to the profiles.

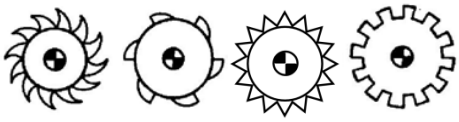

Fig. 1: *Considered roll crusher's profiles: toothed-, cam-, sting- und ripple-rolled crusher (5)*

The second-best result is achieved by the rotary shear with 42 %. Rotary shears have well suiting preconditions for the separation of metal coated components because of their complex stress states. However, the strong cutting component causes a good crushing of the electric and electronic components as well as a deformation of the component cover. The special application of the Querstromzerspaner and of the pre-crushing machine SB² from the manufacturer Andritz-MEWA are very well suited for electrical components with brittle component covers or components with metal elements and with high wall thickness such as die-cast cassis (6). Yet they are only limited suitable for the presented problem, see Fig. 2.

Fig. 2: *Querstromzerspaner's results. There are inclusions and compactions of the metal component cover.* ***(6)***

The evaluation results reveals that there is a high developing potential for a new process in comparison to the existing processes. The demand for the development of such a process is confirmed by the environmental authorities in Germany and Switzerland (3); (7); (8).

4. Solutions

Following the construction systematics by (9), the development of a new process for the automatic separation of metal coated components starts by developing a functional structure, which covers the main elements of the still unknown process. Root of this structure is the main function, which has to be fulfilled. The main function is described as follows:

Metal coated components, for instance from the WEEE-field, shell be opened due to energy input in a way that the inner components can be easily sorted and processed. Impurities of the inner elements in deformed cover components are avoided.

The main function shell be fulfilled by the part functions "component supply", "energy transfer" and "exit of the components". By using the constructing systematic tools "brainstorming", "synetics" and "morphological box" possible process principles are differentiated. As a result the tests for the principle of splitting, stripping and opening by sawing are carried out. Also the existing principle of the profiled roll crusher is tested. Desktop PC's CD-ROM-drives are used as testing components for all tests. For those a metal component cover with inner drive elements is typical. Due to their operating conditions they have a similar size and shape, which are independent of the manufacturer and the year of construction. Besides this CD-ROM-drives are easily available and have no data-protection related requirements like hard disks.

Splitting toll

In a first testing series the splitting of metal coated components is examined. The experimental setup allows examining different splitting tools as well as different heights respectively different velocities and energies of the fall. Considering a continuous process possible advantages of a drawing cut are tested. Furthermore the quality of component separation is regarded depending on the height of the fall, on the used energy input and on the component cover's deformation, which is depending on the tool's shape.

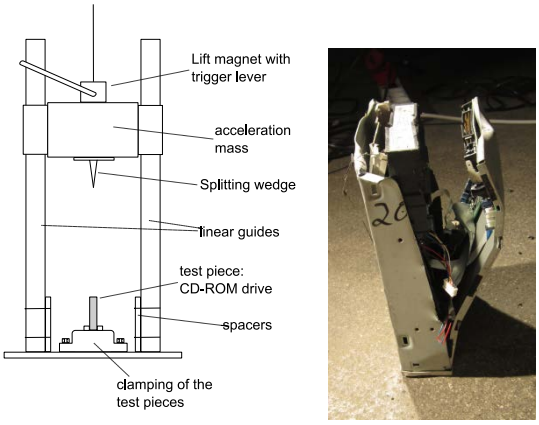

Fig. 3: *Left side: Schematic picture of the test series 1 to open the components. Right side: good result with little deformation but without a complete opening.*

No advantages of a drawing cut are discovered. Narrow and sharp tools penetrate the component's cover well at a minimum work of 880 J and a minimum velocity of 3 m/s, see Fig. 3. A reliable and complete component's opening has to be ensured trough a higher energy input per component. However, this endangers the process' economical implementation. With a high energy input per component the revenue decreases and by that the main advantage compared to a manual disassembly. Furthermore the cutting process turns out to be highly depending on the component's shape. With growing bending stiffness of the construction parallel to the cutting tool's direction of the fall, the deformation on the component's cover decreases, see Fig. 3. To use this circumstance effectively, an automatic component detection and orientation has to take place. Again this means a higher technical and economical effort. Due to the dependency of functionality on the component's shape the process of splitting is not persuade upon in more detail.

Profiled-roll crusher

After some further tests the best common process, the profiled roll crusher process principle, is modified and tested. The test bench is realized as shown in Fig. 4. As a special feature the adjustability of the roller gaps is emphasized. It should reduce or rather completely avoid a component's compaction. Only during deactivated test bench state the adjustment of the roller gabs is manually done. It is driven by two motors, each having 0.75 kW. The torque is transferred with rigid couplings to the roller axis. The tested roller speed varies from 6 – 36 rpm.

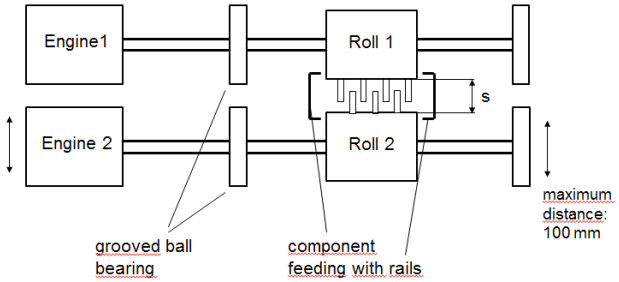

Fig. 4: *Schematic view from above the test bench, which is based on crushing with profiled rolls*

After the test run the evaluation of the test's is done depending on the component's opening degree. It is differentiated in

- 0 %: no opening, no main deformation of the component‘s cover, only perforation and grinding marks
- 25 %: no opening, only one cover side is highly deformed
- 50 %: partly component opening, one cover side open, other sides have only little deformation (this evaluation stage is declared as the minimum for an aceptable result)
- 75 %: partly component opening, one cover side is open, a second cover side is strongly deformed and almost open
- 100 %: complete opening, component is completely separated or at least two sides are completely open and on the inner component's elements are only a few cover rests.

5. Results and Discussion

As shown in Fig. 5, the results are promising. The component's cover is separated tidy and completely from the inner component's elements. This is done in one process step. At the moment components having a width of $s \leq 42$ mm can be fed to the system and are opened. For hard drives as well disk drives satisfying results are gained too.

Fig. 5: *Result with a 100 % - rating*

The best results are achieved with a roller gab, which is at a maximum the component's width. By that the component's compaction does not occur. The opening of only 21 % of the components does not satisfy the expectations. More than half of the used components with this parameter setting are completely opened, see Fig 6. This value meets the previously done theoretical evaluation.

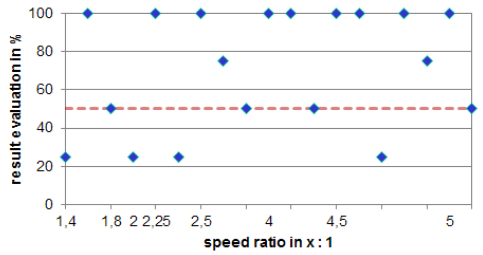

Fig. 6: *Result chart with distance between the rolls ≈ component width*

With the existing testing bench metal coated components are opened in an automatic and continuous process. Besides the automatically running main process, the accompanied processes such as supply, stripping of component rests and size setting are manually done in a deactivated state only. After the first step of process verification the further goal is to expand the process scope of performance in a second plant. For reaching market maturity the occurring stresses have to be documented and considered for the follow-up plant's construction which fulfills the stress requirements. The prospective goal is the separation of all kinds, shapes and sizes of metal coated components, which mainly come from the automotive sector.

Further steps will be

- more powerful motors
- flexible component guidance system
- flexible distance between the tool plate
- new tool design
- new solution for stripping of component rests
- maintenance suitable tool design

Including those changes, the process reliability of good and very good results should be increased up to over 80 %. Along with that the process evaluation improves compared to an ideal solution. Due to the changes a new concept for component separation is developed.

6. Conclusion

Within this article the need for developing a new concept for a continuous opening of metal coated components has been described. The carried out studies for possible solutions led to the redesign of the process principle of the profiled roll crusher. By changing the speed, the roll gab and the tools the first tests have shown remarkable results. Also some further possible improvements have been displayed. Those will be the basis for future research work at the Clausthal University of Technology.

7. References

1. **Martens, Hans.** *Recyclingtechnik.* Heidelberg : Spektrum Akademischer Verlag, 2011. ISBN 978-3-8274-2640-6.

2. **UNEP, et al., et al.** *Recycling Rates of Metals - A Status Report, A Report of the Working Group on the Global Metal Flows to the Internationel Resource Panel.* UNEP. Paris : s.n., 2011. ISBN 978-92-807-3161-3.

3. **Widmer, Rolf, et al., et al.** Seltene Metalle in Personenwagen und Fraktionen aus Autoshreddern. Berlin : EMPA, 2014.

4. **Groke, M., et al., et al.** Optimierung der Separation von Bauteilen und Materialien aus Altfahrzeugen zur Rückgewinnung kritischer Metalle (O.R.K.A.M.). *Abschlussbericht. Im Auftrag des Umweltbundesamtes. FKZ 371333337.* Ketzin : Umweltbundesamt, 2015.

5. **Höffl, Karl.** *Zerkleinerungs- und Klassiermaschinen.* Berlin Heidelberg New York Tokyo : Springer-Verlag, 1986. ISBN 3-540-16232-1.

6. **MeWa, ANDRITZ.** ANDRITZ MeWa - Machines. [Online] MeWa Recycling Anlagen, 2015. [Zitat vom: 31. Juli 2015.] http://www.mewa-recycling.de/maschinen.html.

7. **Kohlmeyer, Regina, et al., et al.** Perspektiven der zunehmenden Fahrzeugelektronik für das Altfahrzeugrecycling. [Hrsg.] Karl J. Thomé-Kozmiensky und Daniel Goldmann. 2015, Bd. 8, S. 183-205.

8. **Baudin, Isabelle und Schweizer Bundesamt für Umwelt (BAFU).** Erste Folgerungen aus dem Schweizer Autoelektronikprojekt. *Fachgespräch "Separation von Fahrzeugelektrik und -elektronik".* Berlin : Umweltbundesamt, 17. Juni 2014.

9. **Pahl, G., et al., et al.** *Konstruktionslehre.* Berlin Heidelberg New York : Springer, 2007. ISBN-10 3-540-34060-2.

MAGNETIC PULSE COMPACTION AND SUBSEQUENT SPARK PLASMA SINTERING OF NANOSTRUCTURED ALUMINA

МАГНИТНО-ИМПУЛЬСНОЕ ПРЕССОВАНИЕ И ПОСЛЕДУЮЩЕЕ СПАРК-ПЛАЗМЕННОЕ СПЕКАНИЕ НАНОСТРУКТУРНОГО ОКСИДА АЛЮМИНИЯ

Kovaleva I.[1], Zholnin A.[2], Grigoryev E.[3], Olevsky E.[4, 5]
NRNU MEPhI, Russia [1,2,3.4], San Diego State University, USA[5]

Abstract: *The purpose of this paper was to study the regularities of formation of ultrafine structure in alumina by magnetic pulse compaction (MPC) and spark plasma sintering, and the producing of nanostructured compacts having high density and microhardness. The combined application of two technologies magnetic pulse compaction and spark plasma sintering in the practice of compacting powders is very rare and unique. We have studied the microstructures of consolidated alumina samples. The anomalous zones present in volume of magnetic pulse compacted and spark plasma sintered samples of both types α and δ phases of alumina. The microstructure of the fracture surface between anomalous zones depends on the phase state of the particles of the initial powder. MPC of δ-alumina leads to a more uniform distribution of anomalous zones along diameter compact after SPS. MPC of α-alumina leads to an increase of the microhardness on the surface of compacts.*

***KEYWORDS**: MAGNETIC PULSE COMPACTION, SPARK PLASMA SINTERING, NANOSTRUCTURE, ALUMINA, MICROHARDNESS*

1. Introduction

The purpose was to study the regularities of formation of ultrafine structure in Al_2O_3 ceramics by magnetic - pulse compression and spark plasma sintering, and getting out of Al_2O_3 nanopowder compacts having high density and microhardness, observed experimentally in [1]. Overview magnetic pulse compaction and spark plasma sintering of powder materials [2] has showed that the combined application of these two technologies in the practice of compacting powders is very rare and unique.

The studies were conducted on the powder Al_2O_3, obtained by the explosion of aluminium wire in the oxygen-containing gas produced by "Advanced Powder Technology", Tomsk. The specific surface area is 35-40 m^2 / g. The mean particle size of 36 nm, an average size from the surface - 45 nm, a mass median size - 54 nanometers. Most of the powder was in a state of δ-phase. The part of the powder was heated in air to a temperature of 1300°C to transfer from unstable low temperature phases to stable α-phase.

2. Experimental results

Spark plasma sintering was performed in vacuum with LABOX-Sinter Land 625 in the graphite mold with an inside diameter of 10 mm at a pressure of 50 MPa. Temperature was determined by pyrometer. The mass of alumina powder was 0.4 g. The thickness of the resulting compacts was a little over 1 mm. Heating was performed at a rate of 100°C / min to 1400°C and staying10 minutes at this temperature.

In conventional pressure compaction was 185 MPa. Pressure at MPC was defined by high voltage discharge. For δ- Al2O3 we have used a single pulse with a discharge voltage of 1.8 kV, and for α- Al2O3 we have used five pulses with a discharge voltage of 2.0 kV. Selected compaction modes correspond to the boundary of the overpressing. If MCP compact was cracked, then it was ground in a mortar and this powder was loaded into a mold for SPS.

SPS results of α and δ phases alumina powders with four kinds of pre-treatment are shown in Figures 1 and 2.

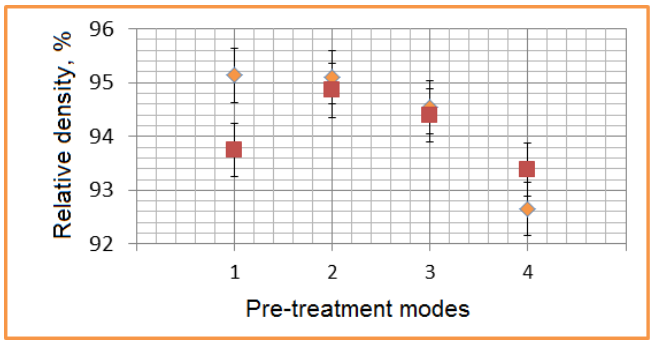

***Fig. 1.** Relative density of the SPS compact depending on the type of pre-treatment.*

The numbers on the x-axis correspond to: 1 − the initial powder material (without training), 2 − powder after the traditional pressing, 3 - after the MPC, 4 − milled powder after MPC. Rhombs correspond to the original δ-phase Al2O3 powder, quadrates correspond to the α-phase Al2O3 powder or powder compact before the SPS.

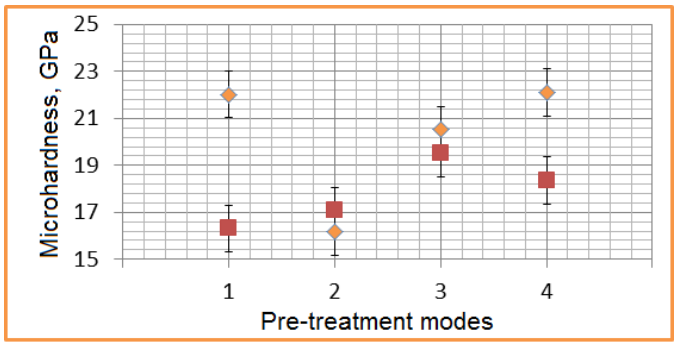

***Fig. 2.** Microhardness on the surface of SPS compacts depending on the type of pre-treatment.*

At the fracture surface of the sintered pellets for both types α and δ phases of alumina powders present anomalous zones (AZ) a bimodal structure with length of about 300 microns with a microhardness much higher than on the surface microhardness of compacts (Fig. 3).

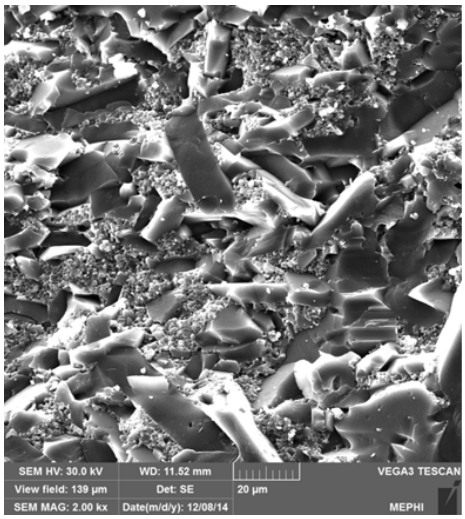

Fig. 3. *Microstructure zones bimodal structure.*

Dimensions of large crystallites in anomalous zones reach 40 microns. The proportion of fracture surface occupied by the anomalous zones increases from the edge to the center of the sample. In the center of the proportion of AZ is up to 40%. MPC leads to a more uniform distribution of AZ along the diameter of compact.

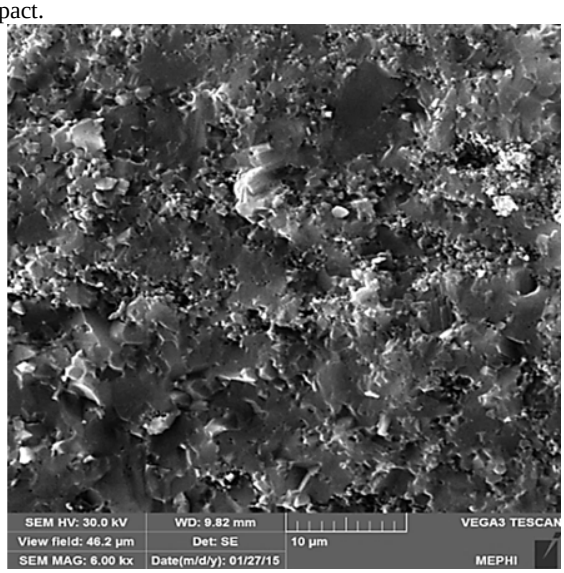

Fig. 4. *Microstructure with alternating coarse and fine-grained layers (mainly for compacts of α-phase Al_2O_3).*

The microstructure of the compact fracture surface between AZ depends on the phase state of the particles of the initial powder. The homogeneous microstructure of δ-Al2O3 powder regardless of the method of pre-treatment has an average grain size of 0.5-0.8 microns after SPS. Fine grains in anomalous zones have a similar size. The microstructure of α-Al2O3 samples between AZ is bilayer. It consists of layers of large and small grains (Fig. 4).

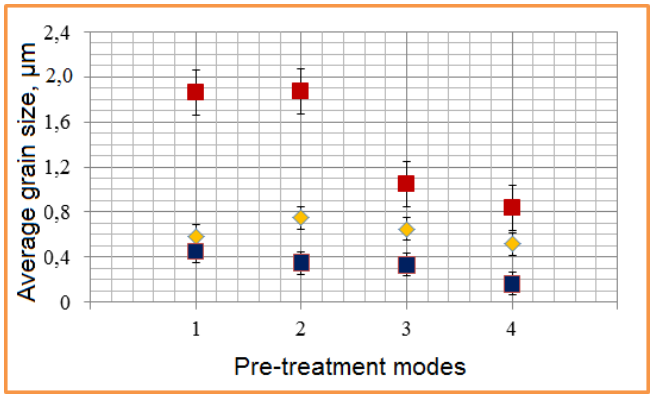

Fig. 5. *The average grain size alumina outside the zones with abnormal structure (coarse-grained layers - red quadrates; fine-grained layers - blue quadrates; original δ-phase Al_2O_3 - rhombs)*

Their dimensions are shown in Fig. 5.

3. Conclusion

Best results for the microhardness and density for all the studied options were obtained by SPS of initial nanopowder δ-Al_2O_3 without any pretreatment.

MPC of δ-alumina before SPS leads to a more uniform distribution of anomalous zones along diameter compact.

MPC of α-alumina before SPS leads to an increase of the microhardness on the surface of compacts, leads to equalize the distribution of anomalous zones along diameter compact and leads to reduce the size of the grains in a layered structure between AZ.

Acknowledgements

The support of the Department of Science and Education of Russian Federation (Grant Contract 11.G34.31.0051) is gratefully appreciated.

References

1. Lee J.K., Hong S.J., Lee M.K., Sung J.H., Lee C.G., You Y.Z. Fabrication of high-density nanostructured alumina by the combined processes of magnetic pulsed compaction (MPC) and spark plasma sintering (SPS), Solid State Phenomena, 118, 597-602 (2006).

2. Zholnin A.G., Yakushkin A.A., Rykovsky A.I., Grigoriev E.G. Olevsky E.Yu. The current state of technology magnetic pulse compression and its prospects, Nuclear Physics and Engineering, 5, 1, 62-76. (2014).

COMPARATIVE ANALYSIS OF THE ANALYTICAL METHODS FOR ASSESSING THE PRECISION OF THE MEASURING SYSTEM

Mr. Eng. Gjakovski I[1], Executive manager Dr.Eng. Brkovski D[2], Prof.Dr.Cvetkovski S[3]
Insurance Policy AD[1], RZ Inter-transsped AD Skopje[2] Macedonia, Faculty of Technology and Metallurgy[3] Skopje, Macedonia,
E-mail: ivan_gjakovski@yahoo.com, dean_brkovski@intertranssped.com.mk, sveto@tmf.ukim.edu.mk,

Abstract
The results of performed analysis and the study of analytical methods for assessing the precision of the measuring system are presented in this paper. Studies are related to the methods for assessing the precision based on the range calculation and the method of variances analysis (ANOVA).The importance of each factor in variation inducation in the measurement process is estimated by applying both methods in the analysis of the same measured sample. In order to assess the accuracy and efficiency of the applied methods, the obtained results are compared, which is the basis for obtaining specific conclusions.Reliability of the obtained results from the investigations are verified by applying the tools of programming package MINITAB.

KEYWORDS: PRECISION, ANALYTHICAL METHODS, MEASURING SYSTEM, VARIATIONS

1. Introduction

Modern measurement techniques has developed various measuring devices. Certain types of measuring devices have different specific properties, but also some common general characteristics that allow comparation. One of the basic metrological characteristics of the measuring device is its precision.

Measuring equipment precision - is the ability of the measuring device to show the similar measured values (Figure 1).

1) accurate and precise 2) inaccurate and precise

3) accurate and impreccise 4) inaccurate and imprecise

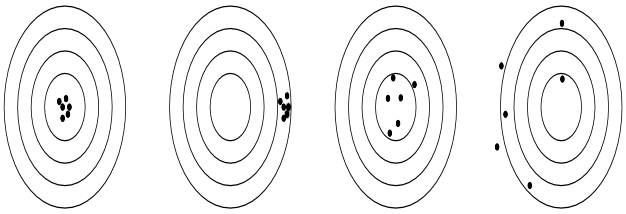

Figure 1: *Possibilities of accuracy and precision or inaccuracy and imprecision of a measurement [G1]*

The metrological charastheristics – measurement precission contains two typical aspects [G1] :

- repeatability of the measurement results, the degree of mutual overlapping of each measurement results obtained in mutually multiple repetition of the measuring operation over a measured value, which value is time-independent (constant), using the same measurement equipment, the same operator and the same ambient conditions.
- reproducibility of the measurement results, the variations that occur when multiple realization of the measurement process, using the same measurement equipment and different operators.

In practice, analytical and graphical procedures are used for assess the measurement systems accuracy. Analytical procedures for the determination of repeatability and reproducibility of the measuring system are aimed to determine (quantify) which part of the calculated variations of the observed measurement process are due to the variations of the measuring system, while graphical procedures allow analysis of the measurement process.

Analytical methods for repeatability and reproducibility calculation of the measuring system, which are subject of this paper can be:

• Method based on range, which assess the measurement variations by comparing the standard deviations of the factors in the measurement process. This "traditional" method divides the total variation in three categories: variations from product to product (variations induced in the manufacturing process), measurement repeatability and reproducibility (variations caused by the measuring system).

• ANOVA (Analysis of Variance) method - investigates the effects of one or more qualitative inputs (factors) on the quantitative outputs, that helps assessing which of the factors have the most significant impact on the output (answer). ANOVA Gauge R & R is a method which uses ANOVA random effects model for measurement systems analysis. This method calculates the level of variations induced in the measuring process of the measurement system and compares it with the total variation in order to determine the "quality" of the measuring system, i.e. its participation in the total variation. This method goes a step forward in terms of the first method and the component reproducibility is separated in two subcomponents: operator and operator - measured sample component in interaction.

Which analytical method will be applied depends on the measurement nature. If it is a non-destructive test (test sample after measuring retains all its properties), there is possibility to use both analytical methods.

In the case of a destructive test (test sample after measuring loses its characteristics, and repeated measurement is not possible) can be applied only ANOVA - method. The of homogeneity of the tested samples serie should be assumed, i.e. all samples in the tested

serie sufficiently identical to be able to consider operation with the same samples. Otherwise the variations of the process will "mask" the variations of the measuring system.

2. Preparation, planning and realization of then engineering experiment

In order to realize the analysis of the measuring system accuracy as a function of the measuring equipment and operator, it is necessary more operators to measure more samples on the same measurement equipment several times in reference conditions. Experiment is prepared from the measured samples. The aim is as much as possible sources of variation to be covered in the measurement process in order to be properly understood and assessed.

The aspect of measurement reproducibility to be covered, it is necessary the participation of more operators. Some standards [A1] require the participation of at least ten operators, but others require participation of only two or three operators for the same sample measuring.

To cover aspects of the measurement repeatability, the same samples are measured several times by the same operators. Each measurement cycle of each sample must include the whole set of required operations, including the complete handling, sampling and disposal of the measuring sample from the measuring system.

To include the interaction between the operator and the sample (eg some sample could be more difficult for measuring than the other samples), usually five till ten samples are measured.

Of course, this is not a universal criteria for the minimum samples recommended for R & R matrix. This is the question for the person which manage the experiment to establish a balance between the risks, measurements and laboratory ability. Model 10x2x2 (10 samples, two operators and two repetitions of measurements) is acceptable sample for certain studies, although there are little degrees of freedom for the component of the operator.

In order the measuring sample to be considered as relevant for further processing and carry out more valid conclusions it is necessary to check the existence of harsh errors and their elimination and verification of the fulfillment of the conditions of normality and homogenity of the measuring sample:

1) As a first step in the process of determining of the participation of measuring equipment and operator in the total level of variations from the set of measured values by applying the Grabs criteria [G2], harsh errors are identified and eliminated for measured values of each operator separately.
2) In the next step of the analysis, it is necessary to test the fulfillment of the conditions for normality of measured results and homogeneity of the variations. This is done through testing the hypothesis by applying more tests:

- for testing of normality: λ - test, λ- test, Anderson – Darling, Ryan – Joiner, Kolmogorov – Smirnov test, by using of probability diagram or by p - value analyze e.t.c.

- for testing of homogeneity: z – test, Student t – test, Fisher F – test e.t.c.

3. Results

Example number 1. *R&R Analisis of the mearuring system precision*

Table 1: *Measured values in the analysis of the components to the measuring system precision.*

Number	FIRST OPERATOR		SECOND OPERATOR	
Product	First measurement	Second measurement	First measurement	Second measurement
1	50,08	50,08	50,06	50,06
2	50,04	50,05	50,04	50,04
3	50,03	50,02	50,04	50,02
4	49,99	49,96	49,98	49,98
5	50,10	50,08	50,08	50,06
6	49,98	50,00	49,99	50,00
7	50,08	50,06	50,10	50,09
8	49,99	50,00	50,01	50,01
9	50,02	50,02	50,00	50,01
10	49,96	49,94	49,98	49,99

By the implementation of Grabs test for the series of measurements on the first and the second operator high values of p – indicator can be seen, significantly bigger than the level of trust α = 0.05 (p = 1.000 for the first operator, and p = 0.923 for the second operator) and can be concluded that in both series of measurements do not exist unusually measurements – harsh errors.

Although it is about series with a relatively small number of measurements (twenty measurements in serie), the two series of measurements (from the first and the second operator), show a high degree of compliance to normal distribution (p = 0.199 for the first operator, and p = 0.168 for the second operator),

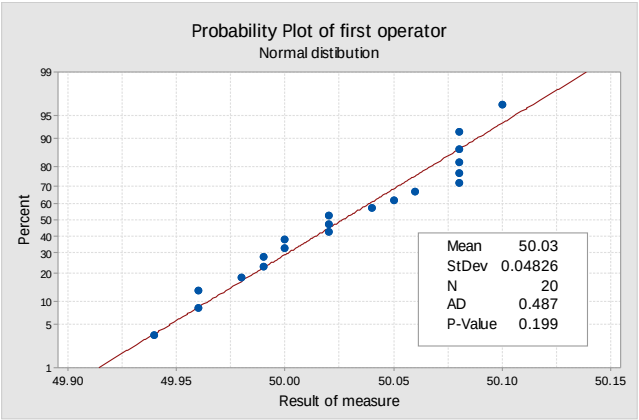

Figure. 2 *Analysisof the measurind results normality by using of probability diagram*

The existence of consistency of the variations and their uniformity can be determined by using of t – test for analysis of the homogeneity of the variations of whole measured sample.

Table 2: *Calculated values in the analysis of the components to the measuring system precision using a balanced ANOVA - method.*

Sources	Var. comp.	% Participation	Standard deviation	% Participation
Measuring system	0,0002381	12,58%	0,0154290	35,47%
Repeatibility	0,0001025	5,42%	0,0101242	23,27%
Reproducibility	0,0001356	7,16%	0,0116428	26,76%
Operator	0,0000000	0,00%	0,0000000	0,00%
Product*Operator	0,0001356	7,16%	0,0698570	26,76%
Product	0,0016544	87,42%	0,2440490	93,50%
Total variations	0,0018925	100,00%	0,2610170	100,00%

Table 3: *Calculated values in the analysis of the components to the measuring system precision using a method based on range*

Source	Var. Comp.	% Participation	Standard deviation.	% Participation
Measuring system	0,0001039	7,36%	0,0101950	27,13%
Repeatibility	0,0001039	7,36%	0,0101950	27,13%
Reproducibility	0,0000000	0,00%	0,0000000	0,00%
Product	0,0013078	92,64%	0,0361635	96,25%
Total variations	0,0014117	100,00%	0,0375731	100,00%

4. Conclusion

Both methods for assess the accuracy of the measuring system show that the manufacturing process is the most important factor that induces variations. Variations of the measuring system according to ANOVA – almost equally is due to the repeatability (variation of the measuring instrument) and reproducibility (variations induced by the interaction of the operator and the measuring sample). Because the method based on range did not detect variations from the interaction of the operator and the measuring sample, the whole measuring system variations are shown for repeatability.

• Procedure for analysis of the components on variation and procedure for standard deviation factors analysis are used in the analysis of the measuring system. The obtained results with both procedures are equally indicative. Which metrics will be used depends on the purpose of the research. If the measuring system is used in process for improvement, (reduction of variations in the manufacturing process), analysis of the components of variations is used, and if assessed the quality of the product in terms of meeting the specified values, then analysis of the standard deviations is used.

• Ability of ANOVA - Method to assess the variations caused by interaction of the operator and measuring sample makes this method more effective in detecting the sources of variation. Furthermore, only ANOVA – Method is applied in the realization of the analysis of the measuring system in the case of destructive test. The application of ANOVA method can significantly improve the view for measuring system precission by fulfillment of assumptions for realization of engineering experiment, by possession of mathematical, technical and practical experience of the operator and computer supported analytical process.

5. Literature

[A1] ASTM E 691 *Standard Practice for Conducting an Interlabaratories Study to Determine the Precision of a Test Method*

[G1] Ѓаковски Иван – Анализа на методите за дефинирање на метролошките карактеристики на мерните алати, Магистерска работа, Универзитет Свети Кирил и Методиј, Машински Факултет – Скопје, Јуни 2012.

[I1] ISO/IEC: GUIDE TO THE EXPRESSION OF UNCERTAINTY IN MEASUREMENTS 1995.

[M1] MINITAB RELEASE 17.0.1 – STATISTICAL SOFTWARE

[P1] Patki Mukul – Investigation, Improvement and Extension of Tecniques for Measurement System Analysis, Oklahoma State University Stillwater, Oklahoma.

OBTAINING OF ALUMINIUM FOAM BY INTRODUCING MECHANOCOMPOSITES INTO THE MELT

ПОЛУЧЕНИЕ ПЕНОАЛЮМИНИЯ ВВЕДЕНИЕМ В РАСПЛАВ МЕХАНОКОМПОЗИТОВ

Prof., Dr. Eng., Cor. Member of NAS of Belarus Ilyushchenko A.[1], Cand. Eng., Assoc. Prof. Kusin R.[2],
Cand. Eng., Assoc. Prof. Letsko A.I.[2], Charniak I.[3], Ilyukevich A.I.[2], Zhehzdryn D.[3], Haliakov M. [2]
State research and production powder metallurgy association, State Scientific Institution "Powder metallurgy institute" [1],
Belarusian state agriculture technical university [2], State Scientific Institution "Powder metallurgy institute"[3] - Minsk, Republic of Belarus
E-mail: nil23niipm@tut.by, irinacharniak@tut.by

Abstract *The report focuses on the process of obtaining closed cell aluminum foam by introducing a composite material obtained by high energy mechanical treatment in a planetary mill into the melt. In contrast to known methods, the paper describes the foaming performed by introducing compressed precursors based on aluminum into the melt. Air-atomized aluminum powder and titanium hydride were used as raw materials for the production of precursors, AK5M2 silumin melt was used for the basis. Implementation of these works does not require the creation of a protective atmosphere and equipment for hot pressing. Photographs of the samples' appearance and study results have been presented. It has been shown that the method of introducing mechanocomposites into the melt may be used for the manufacture of closed cell aluminum foam.*

KEYWORDS: ALUMINIUM FOAM, ALUMINIUM-BASED MELT, MECHANOCOMPOSITES, HIGH-ENERGY MECHANICAL TREATMENT, PROPERTIES

1. Introduction

Recently there has been a considerable interest in the development of new compounds and technologies for production of aluminum foam because the products from this material possess an unusual set of properties due to chemical and physical properties of aluminum and the anisotropic structure of the material.

Aluminum foam is a cellular aluminum-based material. There are two types of aluminum foam:

(a) close-cellular; and

(b) open-cellular.

Aluminum foam is widely used in various branches of engineering and construction. It is also applicable for manufacturing filters and heat exchangers, sound insulation material, etc.

The method for production of open-cellular foam aluminum is as follows: Liquid metal is cast into a mould with filler (water-soluble salt with the melting temperature which is higher than the liquidus of the implemented alloy) [1, 2]. After removal of the filler we have a solid with interconnected pores.

Basic methods for production of close-cellular foam aluminum [3, 4, 5]:

Gas purging through the molten Al-SiC or Al-Al_2O_3. It is the least expensive method which is used for production of foam aluminum with a relative density of 0.03-0.1 and pore diameter of 5-20 mm [3, 4].

Addition of titanium hydride (zirconium) into the melt followed by dynamic stirring, heating and pressure control during cooling of the resulting material [3, 4]. *Mixing of metal powder (mainly aluminum) with titanium hydride (TiH_2), followed by melting to a pasty consistency* [3, 4, 5].

Mixing of the charge components may occur as a result of either a direct mixing or simultaneous milling [3, 4], or mechanical alloying of the matrix material by a foaming agent [5]. This technique [3 - 6] involves four steps: preparing powder mixtures of a matrix alloy and foaming agent; compacting; heating to the foaming temperature and aging; cooling. This method is suitable for Al-, Zn-, Fe-, Pb-, and Au- alloys. Foaming occurs by introduction of solid mixed powders of different chemical substances into the metal.

The method of mechanical alloying is a promising method for producing foam aluminum. It involves handling of powder components and their mixtures of various compositions in high-energy mills and the subsequent consolidation of the newly-formed activated mixture for producing semi-finished or finished components [7]. The advantage of mechanical alloying is the use of production waste and scrap of aluminum alloys, which greatly reduces the cost of the process.

In this paper we suggest entering mechanocomposites into the silumin melt in order to obtain close-cellular foam aluminum. Foaming is achieved by introducing pressed mechanocomposites into the silumin melt (Grade AK5M2). The mechanocomposites are obtained from mechanically alloyed aluminum powder and titanium hydride, a foaming agent. The implementation of the process does not require additional machining (obtaining cuttings, grinding etc.) of the matrix alloy, supply of gas medium for foaming the melt, hot [8] or a two stage compacting of mechanocomposites [5].

The purpose of this work is to study the process of obtaining aluminum foam with closed porosity by means of introducing mechanocomposites (based on dispersed aluminum powder) into the melt.

2. Results and discussion

In order to investigate the process of producing aluminum foam with closed porosity we used aluminum powder obtained by spraying molten metal by the gas flow, titanium hydride TiH_2 and silumin alloy of Grade AK5M2. The content of the foaming agent TiH_2 in the charge of the mechanocomposite Al + TiH_2 was Al 99,25 - Ti 0,75 % wt, Al 99,0 - Ti 1,0 % wt, Al 98,5 - Ti 1,5 % wt, Al 98,25 - Ti 1,75 % wt, Al 98,0 - Ti 2,0 % wt; Al 97,75 - Ti 2,25 % wt. The process of preparation comprises the following steps: drying of initial powders, mixing, mechanical alloying, extrusion, foaming.

Drying of initial powders. The powders were dried on stainless steel trays. The depth of filling was not more than 30 mm. Drying was carried out in the oven SNVS 4,5.4,5.4/3I1 at 80 - 90 °C for two hours.

Mixing. In the creation of the mechanocomposite for producing aluminum foam we used the method of mechanical alloying which consists in intensive plastic deformation of the acquired charge in a high-energy mill. Initially suspended samples of dispersed aluminum powder fractions (-0.315 + 0.2) mm and 50 grams of the foaming agent (titanium hydride powder containing 1.5 % by weight of the powder) was placed in the mixer SMB-4 and stirred for four hours at the rotational speed of 60 min^{-1}. The photos describing the morphology of the powder particles of aluminum and titanium hydride are shown in Figure 1.

Mechanical alloying. Mechanical alloying of the powder mixture was carried out in a planetary ball mill RM400MA (Retsch, Germany) at the ratio of 10:1 (the weight of the balls to weight of the processed material). The rotational speed of the planetary disc was 400 rev/min (corresponding to an overload of 26 g) for 30 minutes.

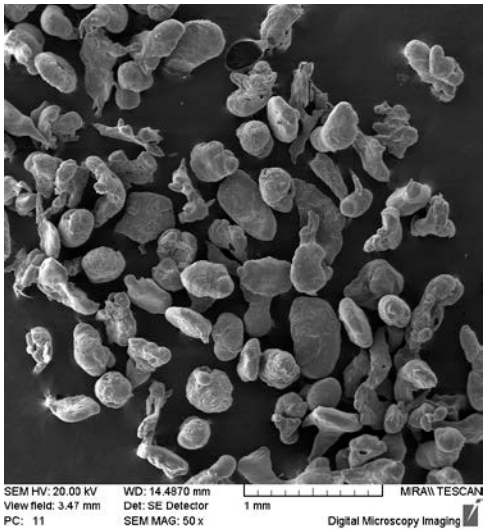

a)

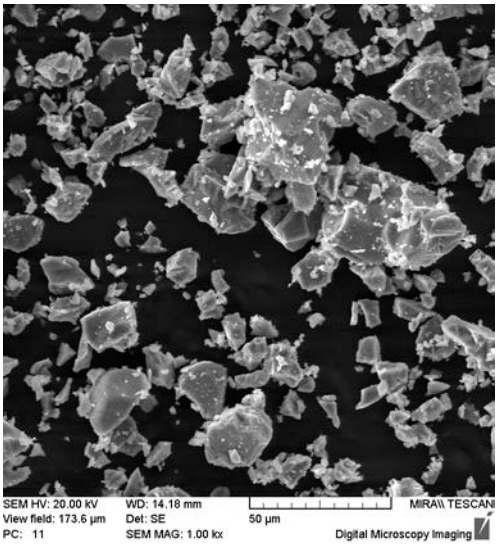

b)

Fig. 1 *Surface morphology of particles in the initial powders*
a) aluminum, atomization of molten metals by a gas flow (argon) × 50;
b) titanium hydride (TiH_2), × 1000

a)

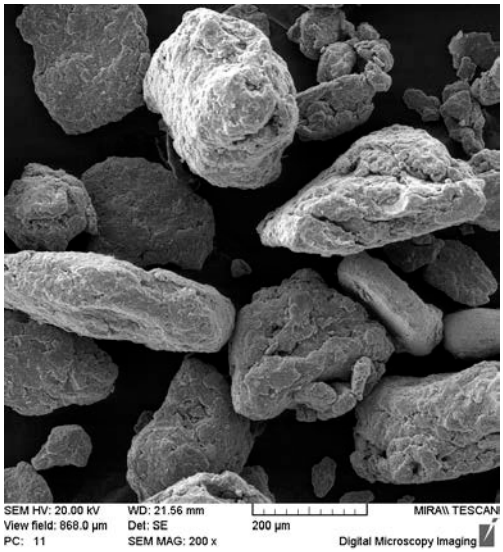

b)

Fig. 2 *Surface morphology of mechanocomposites Al – 1.5% TiH_2, for producing aluminum foam, 30 minutes after mechanical alloying in the planetary mill at different magnifications a) × 34; b) × 200*

We used steel balls (structural bearing steel) of 10 mm in diameter as grinding media. The surface morphology of the acquired mechanocomposites was performed using a scanning electron microscope MIRA from Tescan (Czech Republic) in the backscatter electron mode at accelerating voltage of 20 kW (Figure 2).
The phase composition study of the mechanocomposite Al + TiH_2 after mechanical alloying was performed in $Cu_{k\alpha}$ radiation using an x-ray diffractometer DRON-3. The analysis results show that the phase composition of the samples as follows: aluminum (Al), titanium hydride (TiH_2), aluminum hydride (AlH_3), titanium aluminide (Al_3Ti). The X-ray diffraction image of the sample mechanocomposite is shown in Figure 3.

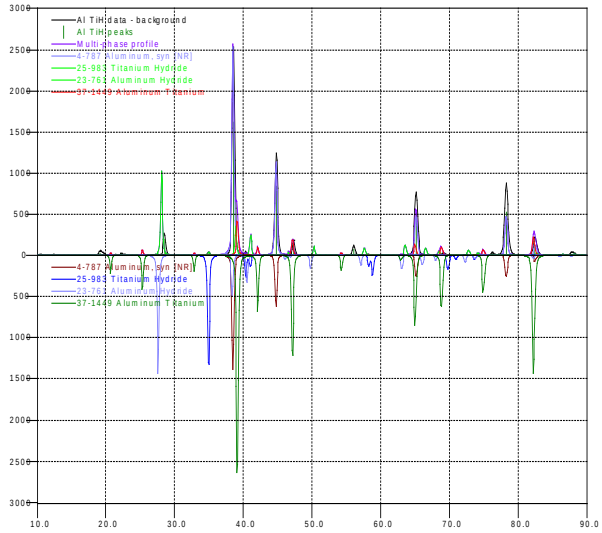

Fig. 3 *X-ray diffraction image of the sample mechanocomposite Al + TiH_2*

During the high-energy treatment a partial interaction of Al and TiH_2 takes place with formation of intermetallics Al_3Ti and AlH_3. Semi-quantitative analysis using the programs DRWIN (point-to-point X-ray processing) and Qual (comparison of the cards with processed X-ray images) is difficult due to the superposition of the main peaks of the identifiable phases.

Extrusion. The sample of mechanocomposite Al + TiH_2 was weighed on the scales VK-600 within the accuracy of 0.01 g. It was filled into the forming block with the diameter of 30 mm and then molded in a press type ZD40 at 425 MPa. After molding the preform is extruded from the die. Appearance of compacts is shown in Figure 4.

Fig. 4 *Appearance of a compact made of the mechanocomposite Al + TiH_2*

Foaming. Foaming was achieved by introducing compacts of the mechanocomposite Al + TiH2 into the silumin melt AK5M2. The silumin AK5M2 was melted at 700 °C in a muffle furnace SNOL 1.6 equipped with a pot for manufacturing test specimens of foam aluminum by mechanical alloying. The pot with the melt was removed from the furnace chamber and mechanocomposite compacts were added into the melt. While warming up the mechanocomposite to 350-400 °C, decomposition of the foaming agent intensified, together with evolution of hydrogen. During decomposition of the foaming agent the mechanocomposite was destroyed. Its particles were distributed in the melt, releasing hydrogen and foaming the silumin melt. Then the fixture was placed in the refrigerator for the final crystallization of the melt. After cooling, the experimental sample of aluminum foam was taken out. The structure of the aluminum foam is shown in Figure 5.

Fig. 5 *Structure of aluminum foam. The mechanocomposite Al + TiH_2 contains 1.5 % of the foaming agent (titanium hydride)*

The study of dependence of porosity on the content of the foaming agent showed the following results. When the charge contains less than 1.25 % of TiH_2 the porosity of the samples is uneven, some solid portions are not foamed and the close cell rate is low: (48 % or lower). The samples prepared using the charge with 1.25 – 1.5 % TiH_2 have a uniform structure, high close cell rate (56 and 63 %) and no cavities. The samples prepared using the charge with 1.75 % TiH_2 have uneven structure and contain unmelted inclusions of compacts. When the amount of TiH_2 exceeds 2 % the samples have open pore structure, cavities in the surface and a low close cell rate (lower than 55 %).

Based on the acquired data, the optimal composition of a workpiece for processing in a charge shall contain 1.5% of the foaming agent.

The results show that when the mechanocomposite Al + TiH_2 contains 1.5 % of TiH_2 there is a complete dissolution and uniform distribution of AK5M2 silumin in the melt. We observed a uniform distribution of closed pores without cavities. The porosity of the samples containing 1.5 % of the foaming agent TiH_2 was 63 %.

3. Conclusion

The study results show that when the mechanocomposite Al + TiH_2 contains 1.5% of TiH_2 there is a complete dissolution and uniform distribution of AK5M2 silumin in the melt. The porosity of the samples containing 1.5% of the foaming agent TiH_2 was 63%.

It is proved that the proposed method of manufacturing closed cell aluminum foam allows obtaining a uniform structure of closed pores. The method implies introduction of mechanically alloyed atomized aluminum-based powder into the melt.

The described works do not require additional mechanical treatment (shaving, grinding, etc.) of the matrix alloy, admission of gas environment for foaming the melt, hot [8], or a two stage compacting of mechanocomposites [5].

4. Literature

1. Kovtunov A., Khokhlov Y., Chernyshova Y. Technology of manufacturing products from foam aluminum. The proceedings of V All-Russian scientific conference "Problems and prospects of development of aviation, ground transportation and energy "ANTE-2009". 2009, vol. 2, pp. 320-322, (in Russian).

2. Pat. 2400552 Russian Federation, IPC C22C 1/08, C22B 21/00, B22D 21/04. Method for producing foam aluminum. Kovtunov A., Chermashentseva T., Semistenov D., Sidorov V. Applicant and patentee OOO Srednevolzhskij sertifikacionno-diagnosticheskij centr "Del'ta". No. 2008146788/0 dd 26.11.2008; publ. 27.09.2010, Bulletin No.27, 4 p. (in Russian).

3. Butarovich D. Aluminum foam as an energy absorbing material and its mechanical properties (eds. D. Butarovich, A. Smirnov, D. Ryabov) Izvestija vysshih uchebnyh zavedenij. Mashinostroenie, No. 7, pp. 53-58, 2011 (in Russian).

4. Ashby, M.F. Metal Foams: A Design Guide [Text] / MF Ashby, A.G. Evans, N.A. Fleck, L.J. Gibson, J.W. Hutchinson and H.N.G. Wadley, Butterworth-Heinemann, 2000.

5. Ivanov D. Research and modeling of aluminum foam produced by alloying from recycled aluminum raw materials (eds. O. Ivanov, A. Aksenov, I. Ivanov) Izvestija vuzov. Cvetnaja metallurgija. No. 6, pp. 56-61, 2007 (in Russian).

6. Ivanov D. Research and development of aluminum foam produced by mechanical alloying from secondary raw materials. Dissertator: Cand. Sc. Eng: Dmitry O. Ivanov. 05.16.01, Moscow, 2008 (in Russian).

7. Kuzmich Y. Mechanical alloying (eds. Y. Kuzmich, I. Kolesnikova V. Serba, B. Freidin; Executive Editor: E. Poliakov), Moscow: Nauka, 213 p., ISBN 5-02-033726-9, 2005 (in Russian).

8. Ersoy, Emrah. An experimental study on hot formability of closed cell metallic foams (eds. Emrah Ersoy, Yusuf Özçatalbaş, Ersin Bahçecı) The Proceedings of 1st International Symposium: Porous and Powder Materials (PPM 2013), 3-6 September 2013, Izmir Turkey, pp. 68-72; ISBN 978-975-6590-05-8.

ИЗСЛЕДВАНЕ НА ГРАНИЧНИТЕ ПРОЦЕСИ ПРИ ОБРАБОТКА НА ОТВОРИ

RESEARCH OF THE LIMIT PROCESSES IN MACHINING OF HOLES

доц. д-р инж. Евстати Лефтеров, ас. д-р инж. Таня Аврамова
Assoc. Prof. Dr. Eng. Evstati Lefterov, Assist. PhD. Eng. Eng. Tanya Avramova
Технически университет – Варна
Technical University of Varna

lefterov@tu-varna.bg, tanya_avramova@tu-varna.bg

Abstract: *In the article are researched combined tools for drilling (or boring) and smoothing holes. The behavior of equivalent cutting force at cut in and exit of the work surface, changing the diameter of the hole and quality after passing the smoothing elements are analyzed.*

It is also analyzed the effect of the cutting conditions on the aforementioned parameters.

Keywords: COMBINED TOOLS FOR DRILLING, SMOOTHING OF HOLES, CUTTING FORCE

1. Въведение

При обработка на отвори с инструменти, имащи две направляващи, които служат за опори и контактуващи посредством триене чрез плъзгане [1], се наблюдават изменения в качеството на обработваната повърхнина.

Тези изменения се изразяват в следното [3]:

- Отклонение в размера на обработвания отвор;
- Промяна в грапавостта в участъците на врязване и излизане на свредлото от заготовката;

Целта на разработката е да се открият и анализират причините за възникване на изброените проблеми, както и да се предложат мерки за отстраняването им.

2. Постановка на провежданите изследвания

За анализиране на процесите на врязване и излизане на инструмента от обработвания отвор е избран случай на разширяване на отвори при инструмент с две направляващи. Режещата част може да бъде изпълнена със стандартни сменяеми пластини с триъгълна или ромбоидна форма (тип CCMT и CPMT), с дължина на режещия ръб 6 mm и 9 mm (фиг.1) [5].

Изследванията са проведени при обработка на детайли от стомана S355 с диаметър D=40 mm.

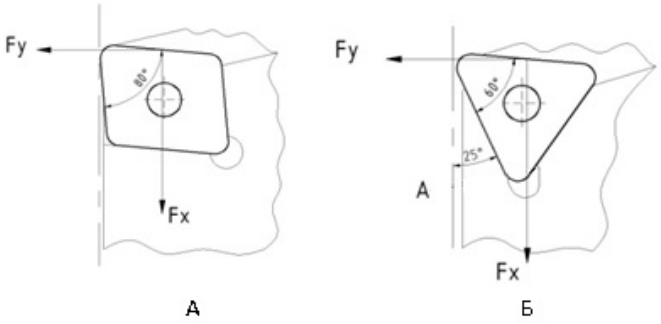

Фиг. 1 *Разположение на режещите пластини в тялото на инструмента и направление на съставляващите силата на рязане а – ромбоидна форма; б – триъгълна форма*

Таблица 1: *Схеми на натоварване на инструмент при разстъргване*

I Вариант - Една пластина периферно разположена	**Уравнения за равновесие - вариант I**
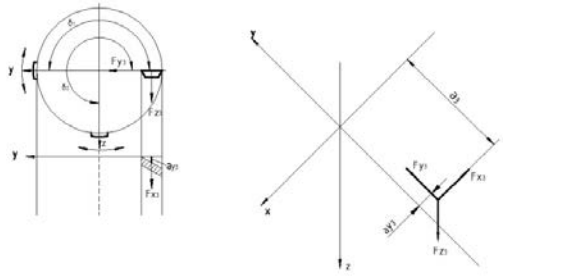	$R_x = -F_{x3}$ $R_y = F_{y3}$ $R_z = F_{z3}$ $M_x = -F_{z3}.a_3$ $M_y = F_{z3}.a_{y3}$ $M_z = -F_{x3}.a_3 - F_{y3}.a_{y3}$
II Вариант - Две пластини периферно разположени	**Уравнения за равновесие – вариант II**
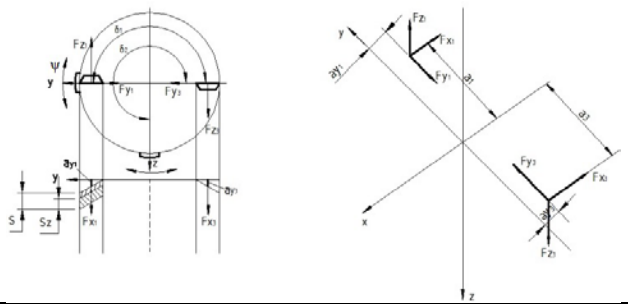	$R_x = -F_{x1} - F_{x3}$ $R_y = -F_{y1} + F_{y3}$ $R_z = -F_{z1} + F_{z3}$ $M_x = -F_{z1}.a_1 - F_{z3}.a_3$ $M_y = -F_{z1}.a_{y1} + F_{z3}.a_{y3}$ $M_z = F_{x1}.a_1 + F_{y1}.a_{y1} - F_{x3}.a_3 - F_{y3}.a_{y3}$

В табл.1 са показани схемите на натоварване и условията за равновесие на конструкцията. Възможните конструктивни варианти се разглеждат въз основа на различни стойности на ъглите на взаимно разположение на режещите пластини ψ за вариант 2 (табл.1) и ъглите δ_1 и δ_2, определящи положението на направляващите елементи [2].

Проведени са аналитични изследвания при условие на врязване от 1 до 6 mm активна част на режещия ръб (за вариант 1 от табл.1), подаване s=0,1 mm/rev, коефициент на триене μ=0,15 и установъчен ъгъл κ_r=87°.

Получените резултати са посочени в табл.2.

Таблица 2: *Резултати от аналитично изследвания при врязване на определена дължина на активната част на режещия ръб на пластината*

l, mm	1	2	3	4	5	6
Fx, N	428	542	650	753	851	943
Fy, N	168	301	424	537	640	733
Fz, N	533	824	1108	1383	1652	1913
δ_1/δ_2, °	180/270					
F1, N	243	415	577	728	868	998
F2, N	546	850	1145	1432	1710	1979

Анализирайки получените резултати, се оказва, че силите F_1 и F_2, действащи в направляващите се различават съществено. Това съществено нарушава работата на инструмента. До голяма степен това може да се компенсира ако тези сили биха били еднакви по стойност.

При определени условия това се постига при различни стойности на ъглите δ_1 и δ_2. Резултатите в този случай са показани в табл.3.

Таблица 3: *Резултати от аналитично изследвания при врязване на определена дължина на активната част на режещия ръб на пластината при различни стойности за ъглите δ_1 и δ_2*

l, mm	1	2	3	4	5	6
δ_1/δ_2, °	180/320					
F_1, N	835	1323	1794	2247	2682	3100
F_2, N	850	1323	1782	2228	2660	3078
δ_1/δ_2, °	180/310					
F_1, N	-	1055	1434	-	2145	2478
F_2, N	-	1110	1495	-	2242	2583
δ_1/δ_2, °	180/300					
F_1, N	-	-	-	-	1747	-
F_2, N	-	-	-	-	1974	-

В табл.3 са посочени само вариантите, при които силите F_1 и F_2 са приблизително еднакви и при които няма нарушаване на работата на инструмента.

Силите, действащи в направляващите при разгледаните конструктивни варианти са по-големи по стойност, но сравнително еднакви. Този подход позволява значително по-добра работа на инструмента, но не обяснява напълно причината за разликата в размера на диаметъра в преходния момент на врязване и излизане на инструмента. Предполага се, че това се дължи на момента, в който направляващите са все още извън контакт с обработвания отвор, тъй като при обработката не се използва кондукторна втулка. За да се изследва този момент, е необходимо да се направи измерване на силите на рязане, действащи радиално на инструмента преди навлизането на направляващите пластини.

3. Експериментални изследвания

Използва се динамометричен инструмент създаден на базата на конструкция [4] показана на фиг.2.

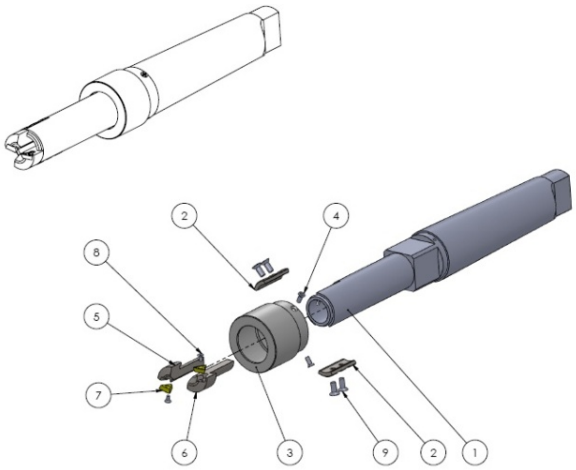

Фиг. 2 *Динамометричен инструмент*
1 – тяло; 2 – направляваща пластина; 3 – кожух; 4 – винт; 5 – модул за междинна пластина; 6 – модул за периферна пластина; 7 – режеща пластина; 8 – винт; 9 - винт

Показаният инструмент позволява да се променят ъглите δ_1 и δ_2 между направляващите пластини и да се фиксират в съответното положение [2]. При премахване на междинен модул 5 и използване на подходяща заготовка могат да се проверят радиалните съставляващи на силата на рязане, действаща на режещите пластини, огъваща тялото на инструмента и променяща диаметъра на отвора при врязване до пълната активна дължина на режещия ръб l. Максималната му дължина е 5 mm и отговаря на прибавката за отнемане.

Съставляващите Frz и Fry и сумарната деформация Wyz са показани в табл.4

Таблица 4: *Резултати за съставляващите Frz и Fry и сумарната деформация Wyz в зависимост от дължината на активния режещ ръб*

l, mm	1	2	3	4	5	6
Frz, N	170	310	430	540	635	730
Fry, N	550	818	1100	1375	1648	1900
Wyz, mm	0,001	0,012	0,018	0,021	0,031	0,036

Сложността на измерването се състои в малкия моментен участък, след който в работа се включват направляващите и заглаждащи елементи (позиция 2 от фиг.2).

Този участък е приблизително 1 mm и при него диаметъра на получавания отвор се получава по-голям с 0,072 mm, като за различни стомани този параметър е различен.

При излизане този ефект се наблюдава, но е в посока на намаляване на диаметъра на отвора. Излизащите направляващи заличават напълно този недостатък.

4. Изводи

1. В процеса на врязване по дължината на отвора приблизително 1 mm се получава увеличаване на диаметъра от 40 до 40,072 mm, което може да се избегне само с използване на кондукторно приспособление.

2. Причината за този недостатък е деформацията на тялото на инструмента под действието на силите Frz и Fry (табл.4).

3. Практически при работа с инструмент с една режеща пластина (табл.1, вариант 1) нормална работа се гарантира при снемане на прибавка до 3 mm, тъй като силите F_1 и F_2 в направляващите са по-големи от 2200 N и правят невъзможно осигуряването на хидродинамичното мазане в контакта на направляващите със стените на обработвания отвор.

4. При използването на разстъргващ инструмент с две режещи пластини (табл.1, вариант 2) силите F_1 и F_2 достигат максимум 900 N при $\delta_1=177°$ и $\delta_2=332°$, но постиганата грапавост Ra=1,2 μm е незадоволителна за детайли използвани в хидравлични съоръжения.

5. Посоченият в извод 4 недостатък се премахва посредством конструктивни варианти изградени чрез промяна на ъгъла между режещите пластини ψ и постигане на натоварване $F_1 \approx F_2 = 1500$ N.

Литература

1. Аврамова Т.Г., „Избор на направляващи елементи на инструменти за обработка на отвори с последователно въздействие ”, сп. „МТТ“, кн. 1, издание ТО на НТС – Варна и ТУ- Варна, 2012 г., ISSN 1312 – 0859, стр. 55-58

2. Аврамова Т., Управление на параметрите на качеството на обработени повърхнини, посредством приложение на комбинирани технологични въздействия, Автореферат на дисертация за получаване на образователна и научна степен „Доктор“, Варна, 2014, стр.40

3. Лефтеров Е.Л., Аврамова Т.Г., Заглаждане посредством триене при плъзгане чрез инструмент с два твърди и един подвижен елемент, III International Scientific Technical Conference, vol. 3 Mechanics, Dynamics, Strength and Reliability. Analysis of Elements, Issue 6, 2015, ISSN 1310-3946, p.33-35

4. Лефтеров Е., Аврамова Т., Комбиниран инструмент за обработка на отвори, Полезен модел, Република България, № BG 1913 U1, 01.07.2014

5. Лефтеров Е.Л., Аврамова Т.Г., „Подход за формиране на диаметъра на многоръбови пробивни инструменти”, сп. „МТТ“ кн. 1, издание ТО на НТС–Варна и ТУ- Варна, 2012 г., ISSN 1312 – 0859, стр.20-24

DETERMINING OF STRAIN RATIO IN TENSILE TEST USING BY IMAGE PROCESSING

Ass. Prof. Dr. Daei Sorkhabi A. H., Eng. Vahdat Panahi Shokouh V., Eng. Parsa Khanghah S.
Department of Mechanical Engineering, Tabriz Branch, Islamic Azad University, Tabriz, Iran.
Email: amirsorkhabi@iaut.ac.ir

Abstract: *In tensile machines to measure the change in length of the specimen during the stress, most time extensometer and various contact methods and tools, such as strain gauges are used, but these methods have limitations and low accuracy that cause unexpected and different results from the theoretical values for the strain. In this paper, to address this shortcoming and improve strain measurement, a non-contact method using image processing techniques in the MATLAB environment is introduced. for this purpose after capturing a move of tensile test and converting that in to some high quality pictures and using image processing we put some pattern in the first image and with using a special algorithm with name of Digital Image Correlation (DIC) detect that patterns until the last image then we can use of displacement algorithm and calculate change in the specimen's length and after that we can also have "Strain" with using these values.*

KEYWORDS: DIGITAL IMAGE CORRELATION, PATTERN RECOGNITION, STRAIN

Introduction: Nowadays we can see in order to perform strain test and record strain-stress changes, many of corporations or Academic Centers use of tensile machines. In these devices two different mechanisms measure the force and length change. For measure of the force they use of the change in length of the spring or use of force meters. Also the general mechanism for measuring the change in length of the specimen is using of strain gauge or Shaft encoder or Extensometer that all of these conventional instruments have special limitation for themselves. Therefore, in this study, to reducing these deficiencies in tensile testing machine we prepare a new and non-contact method that use of image processing to solve these problems. Fig 1)

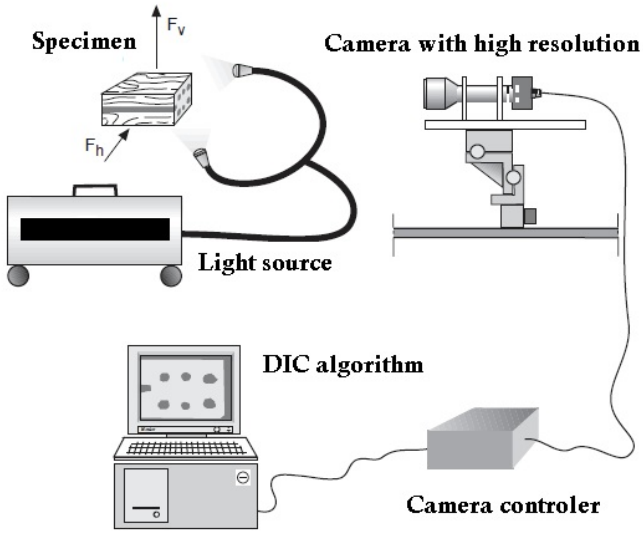

Fig. 1: *A schematic overview of research*

As you see tensile test specimen is connected to the machine and after that a camera with a high speed shooting capture movie as our specimen tolerate a force Then algorithms for image processing and digital image correlation function in MATLAB environment, measure variability of the sample. New method for detecting changes in the length is using of digital image correlation [1]. Image processing is a new and very powerful technique in computer science and electronics which has been implemented in several studies in various fields. For example, Shell and Nicola have used this method to achieve their goals [2,3].The use of image processing has many advantages, for one it is not difficult like conventional methods and also it has good accuracy. We can say there are several algorithms for computing the strain of an object that most common of them is based on image correlation. Correlation or cross-correlation between two images is a standard approach for the detection of object features which has also been widely used to measure the surface deformation. This method of analysis is called digital image correlation (DIC) which can detect form of shape and its movement. DIC is an optical metrology based on digital image processing and numerical computing. It was first developed by a group of researchers at the University of South Carolina in the 1980s [4–8] when digital image processing and numerical computing were still in their infancy [8]. In this technology some spot (like black and white points) will be selected in the surface of specimen and then we will take a picture. Now our pattern is ready. Many of these patterns will be prepared before deformation and also after deformation. These patterns will be then sent to the computer after digitization. In the next step digital images will be compared with each other. Generally a subset of pixels (30 × 30 or 40 × 40) from original picture will be selected. The algorithm works like this:

Position of the subset in the first picture will be searched in the second picture with matching of Gray Levels and for each point will be calculated a level of Gray light intensity and therefore we can find the closest match points in the second image with the original image subsets. Thus, the position of the points in the secondary image is obtained. After getting these subsets in the second picture we can have movement amount of specific points. Fig 2 can show an overall view of this topic:

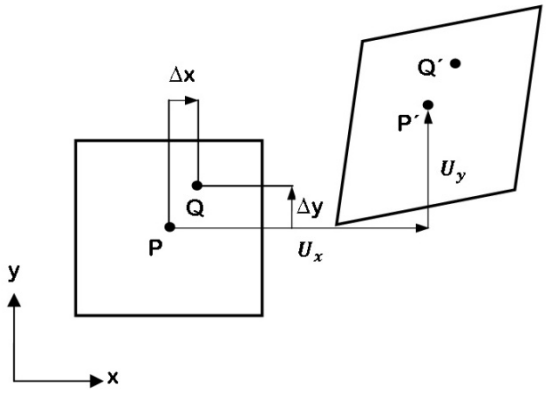

Fig 2. *Moving points in successive images*

In order to better estimate the displacement, one particular factor "S" is defined as the normalized cross-correlation:

$$(1) \qquad s\left(x,y,u_x,u_y,\frac{\partial u_x}{\partial x},\frac{\partial u_x}{\partial y},\frac{\partial u_y}{\partial x},\frac{\partial u_y}{\partial y}\right)=1-\frac{\sum I_u(x,y)I_d\left(x^*,y^*\right)}{\sqrt{\sum I_u(x,y)^2\sum I_d\left(x^*,y^*\right)^2}}$$

here u_x and u_y are movement parameters in the center of subset. I_u and I_u show Gray levels from Original image and the deformed image respectively. (x, y) and (x^*, y^*) are Coordinates of the point before and after deformation. So that the Coordinate of (x^*, y^*) after deformation is related to (x, y) before deformation.

$$(2) \qquad x^* = x + u_x + \frac{\partial u_x}{\partial x}\Delta x + \frac{\partial u_x}{\partial y}\Delta y$$

$$(3) \qquad y^* = y + u_y + \frac{\partial u_y}{\partial x}\Delta x + \frac{\partial u_y}{\partial y}\Delta y$$

We should also mention that all of this work can be performed in the MATLAB environment. In other words, we can advance our project with help of image processing toolbox functions and there is no need for the user to use more complex formulas.

The core of the correlation tool is based upon a Matlab routine which uses a normalized cross correlation to correlate a part of the source image with the target image (Fig 3). This routine uses the grey scale levels of the pixels in the area of interest. The routine returns for each pixel in the target image a correlation value between -1 and 1. The value 1 means that the part of the source image is exactly the same as the area in the target image, 0 means that no correlation exists and -1 means that the analysed area in the target image is a negative of the source image. Because DIC is an image based technology, a pixel based coordinate system is used. In this correlation tool the X and Y coordinate within an image are defined as shown in Fig. 3. The correlation square is always uneven with the pixel of interest exactly in the centre of this square. The size of the square must be such that enough detail of the specimen surface is included such that the square is unique. For instance if only one pixel is taken in the example, many locations exist in the target image which are the same. In the correlation tool the size of this square can be adapted.

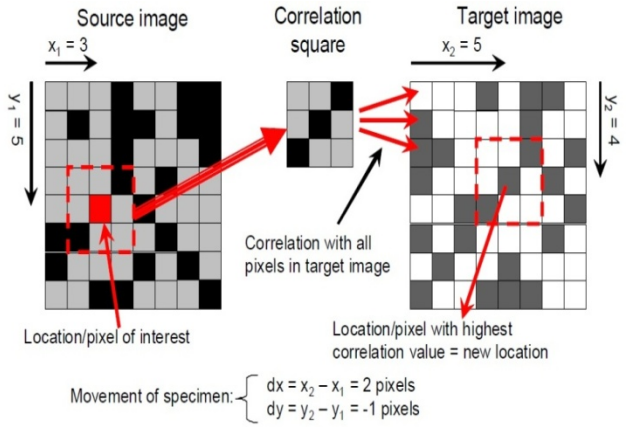

Fig 3. *Correlation process for one pixel*

The correlation square is compared with all the pixels in the target image, returning a correlation value for each pixel, resulting in a data set as illustrated by Fig 4. The location in the target image that corresponds best to the correlation square is clearly recognized by the peak with the highest correlation value. However, the new coordinate has an accuracy of 1 pixel which is not accurate enough for strain measurements. To get higher accuracy a method was developed which uses the correlation values around the peak to get sub pixel level accuracy. To obtain that a 6th degree polynomial surface is fitted through the correlation values of the pixels around the pixel with the highest correlation value, using a least squares approach. By filling a grid of sub pixel coordinates into the function of the fitted polynomial surface, a new maximum can be obtained at sub pixel level. In the correlation tool the resolution in which the coordinates are given is 0.01 pixels. It was found that a higher resolution did not further contribute to the accuracy of the measurement [19].

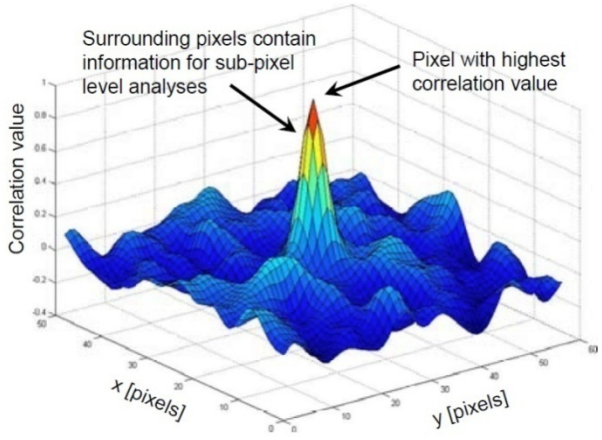

Fig 4. *Correlation values for an area in a target image*

Implementation:

The main processing in this test is defined like this:

For the first step we should prepare some pictures from our specimen before deformation. In this test, in order to remove possible vibrations, for example vibrations caused by the tensile test machine, we use of video camera. Finally, we can prepare some good pictures without any vibration. For this purpose we use a software that is suitable for video cameras (Fig 5). Other available software may be used for the purpose of this research.

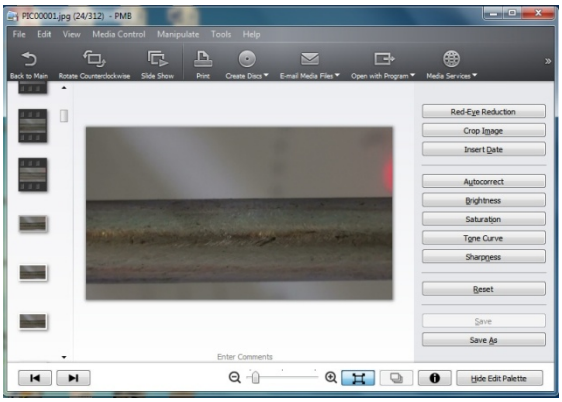

Fig 5. *PMB software from "SONY" corporation*

as we mentioned we have a video camera that its specifications is as follows(Fig 6):

Lens: Carl Zeiss® Vario-Tessar / 30m
Zoom Ratio (Optical) 25X
Zoom Ratio (Digital) 300X

In the next step the prepared images should be processed. For this purpose all pictures are sent to the MATLAB environment. After this the first image will be called for processing. With help of written codes we can select a desire region for processing. We will do that with making a rectangle region (Grid) that can be processed. In simple terms, the image processing code will only focus on these points. Fig7 and demonstrate an example of this way.

Fig 6. *Shoot picture with XR150E.*

.

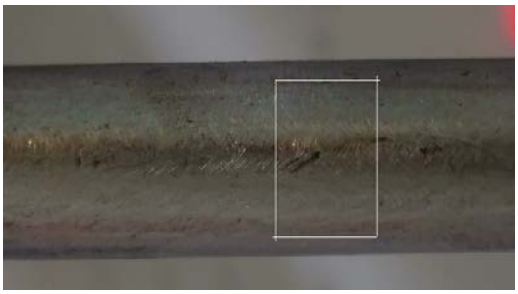

Fig 7. *Select the desired region for processing*

As it can be seen in Fig 8 we have some yellow points for processing although in this level we can increase a points density which will be more accurate. However, the processing time will increase. In fact we can say processing time relates both parameters. First number of pictures and second point density

In the third phase, correlation algorithm starts and searches points in the first image onto the second image. This is done using “Cpcorr” function in the MATLAB environment. This function using normalized image correlation algorithm and match its input arguments that they have acquired from both pictures first, before deformation and second, after deformation. As a result, coordinates of specified points in the first picture will be emerged in the second picture. (To learn more about this function refer to the MATLAB Help). Although it is noteworthy we should have image processing toolbox in MATLAB. After finding the location of specified points in the second picture they will save and process will be continued in the third picture and like this process will be gone until the final stage. It should also be noted that if “Cpcorr” function cannot detect the position of some points it will return points to its previous position. In this case some points that are static in their position during the processing will be demonstrated. Also we should say if we increase the points density in the first stage its probability will be less that “Cpcorr” function don’t be able to detect position of points or in other word Noises will decrease dramatically. However, processing some area like this will require a computer system with powerful processors. Two different phases of image processing are visible in Fig 8

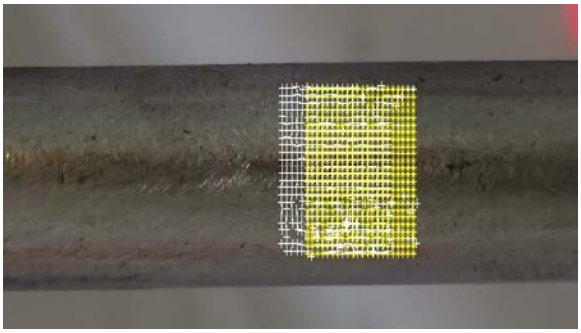

Fig 8. *Coordinates of the points in picture 32*

In the fourth phase we can get the desired amount of displacement or traction during the test using the coordinates of points obtained for each image and processing and mathematical calculations on them. The result of the process will have two matrices. A matrix for the x coordinates of the points in each image and also other matrix y coordinates for the points in the same image. (Fig 9)

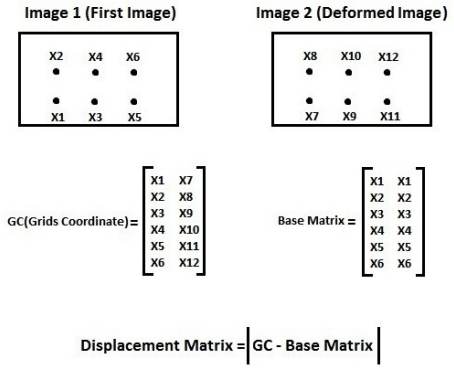

Fig 9. *Calculating displacement matrix in X dimension*

Now with caring that the displacement matrix is available, we can calculate strain. It can be said the core of this research at this stage will implement like this:

It uses "GC" matrix, Displacement Matrix, and also a function with name of "Lsqcurvefit" in "matlab" optimization toolbox to calculate optimal strain. Optimal strain for processed pictures will fit with a liner function and then strain amount for each picture will detect.

Result: With caring to image correlation Algorithm and also calculations the results will be presented like bellow: The plot (Fig 10) is related to the strain in the tensile direction. As shown, the strain is specified for each image.

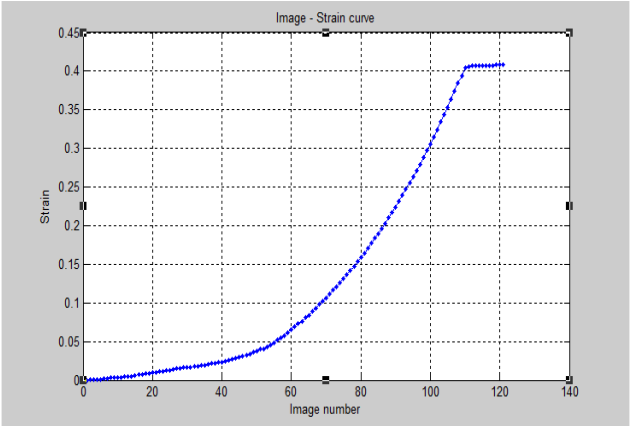

Fig 10. *Strain plot in a tensile direction*

Conclusions: With considering the results that are obtained through image correlation Algorithm and using of image processing techniques we can say although this method needs more accuracy during test but obtained results show our information after test can be reliable and even sometimes it can compete with conventional methods. So we can use of this method for an alternative ways for calculating Poisson's ratio.

References:

[1] Bing Pan, Kemao Qian, Huimin Xie and Anand Asundi. (2009), "Two-dimensional digital image correlation for in-plane displacement and strain measurement",Measurement Science and Technology., 20, 062001

[2] Nicolella D.P., Nicholls A.E, Lankford J.and, 2001,Davy D.T, Machine Vision Photogrammetry: a technique for measurement of microstructural strain in cortical bone, journal of Biomechanics, 34,135-139.

[3] G'Sell C., Hiver J.M. and Dahoun A.,2002, Experimental characterization of deformation damage in solid polymersunder tension, and its interrelation with necking, International journal of Solids and Structures 39,3857 3872.

[4] PetersWH and RansonWF 1981 Digital imaging techniques in experimental stress analysis Opt. Eng. 21 427–31

[5] Chu T C et al 1985 Applications of digital-image-correlation techniques to experimental mechanics Exp. Mech.25 232–44

[6] Sutton M A et al 1986 Application of an optimized digital correlation method to planar deformation analysis Image Vis. Comput 4 143–50

[7] Peters W H et al 1983 Application of digital correlation methods to rigid body mechanics Opt. Eng. 22 738–42

[8] Sutton M A, McNeill S R, Helm J D and Chao Y J 2000 Advances in two-dimensional and three-dimensional computer vision Topics in Applied Physics 77, 323–72

MODELING AND OPTIMIZATION OF ELECROCHEMICAL MACHINING OF 321-STAINLESS STEEL USING RESPONSE SURFACE METHODOLOGY

M.Sc. Mehrvar A. PhD Student.[1], Dr. Basti A. PhD.[1], Dr. Jamali A. PhD. [1]
Faculty of Engineering, University of Guilan, Rasht, Iran [1]
mehrvar@phd.guilan.ac.ir, basti@guilan.ac.ir, ali.jamali@guilan.ac.ir

Abstract: *This paper demonstrates a systematic approach for achieving comprehensive mathematical models for electrochemical machining (ECM) of 321-stainless steel based on the response surface methodology (RSM). Machining voltage, tool feed rate, electrolyte flow rate and concentration of NaNO3 solution were considered as the machining parameters while material removal rate (MRR) and surface roughness (Ra) were considered as the process responses. Experimental plan was performed by a central composite design (CCD). The proposed mathematical models statistically have been evaluated by analysis of variance (ANOVA). Analysis shows that the RSM method has been appointed properly as the design of experiments (DOE) method for resolving curvature in ECM process responses. Also, the optimal machining parameter for single optimization of MRR and Ra is determined by desirability function. The results showed that the proposed approach is an effective and suitable way for modeling and optimization of the ECM machining process.*

Keywords: ELCTROCHEMICAL MACHINING, MODELING, OPTIMIZATION, RESPONSE SURFACE METHODOLOGY, DESIRABILITY FUNCTION

1. Introduction

ECM is a modern and non-traditional machining contributing significantly in various industries from consumer product to more sophisticated, high-tech applications and to produce micro to macro scale products. Moreover, ECM gives advantages over other conventional and non-conventional machining processes. As a case in point, conductive materials regardless of their hardness and toughness can be machined with a tool which is not harder than workpiece; there is especially no tool wear. In view of the fact that in this cold process there is no contact between cathode and anode, products without any residual stress and heat affected zone (HAZ) can be machined (Rumyantsev and Davydov, 1989; Rajurkar et al., 2006; Huang and Liu, 2014).

Even though traditional methods for conducting experiments such as trial-and-error, best-guest approach and one variable at a time (OVAT) still common (Neto et al., 2006; Bhattacharyya and Munda, 2003), these methods are time consuming and incapable of detecting the interactions between variables (Montgomery, 2009). Thus, implementation of design-of-experiments (DOE) method has increased in various manufacturing processes (El-Taweel 2008; Haridy et al. 2011). Response surface methodology, RMS, is capable of resolving curvature in the output associated with each input, detecting interactions effects and establishing mathematical models with suitable sets of experiments (Bhattacharyya and Sorkhel, 1999; Malapati and Bhattacharyya, 2011; Munda and Bhattacharyya, 2008; Munda et al., 2007).

However, the ECM process involves several physical and chemical phenomena and a number of process parameters that make it difficult to model the process (Hinduja and Kunieda, 2013). Consequently, experimental investigations, DOE, statistical and optimization approaches play a vital part in selection of proper selection of parameters setting which influence the machining performance considerably (Venkata Rao and Kalyankar, 2014).

There are researches that had been investigated this process experimentally and offer some excellent results and approaches for modeling and predicting machining conditions; still, much more experimental studies must be conducted to cover wide range of materials and methods for optimization and improving machining performance. The purpose of this research is mathematically modeling ECM process parameters, i.e. machining voltage (x_1), tool feed rate (x_2), electrolyte flow rate (x_3) and electrolyte concentration (x_4) on machining criteria, i.e. MRR and Ra of 321stainless steel. This kind of steel contains titanium which making it an excellent choice for prolonged high temperature applications such as aircraft exhaust stacks, manifolds, welded equipment, jet engine parts and so on. Response surface methodology (RSM) is also used for correlating and analyzing the various machining parameters on the response; therefore, mathematical models develop through RSM. In addition, the adequacy of the developed mathematical models has also been tested by the analysis of variance (ANOVA). Finally, optimal machining parameters for achieving maximum MRR and minimum Ra are determined.

2. Experimental procedure and details

2.1. Set-up and machine

The experiments were carried out on home-developed machine. This machine was set up in this investigation shows in Fig. 1 consists of four well-designed units, i.e. machine, electrolyte, control and power supply unit. The tool feeds forwards and backwards using the AC servo motor through a ground precision ballscrew with pitch of 2.5 mm and precision linear guides. Machining place was built by Plexiglas with a door provided more convenience for changing the workpiece. All used connectors, valves and hose made of 316 stainless steel, PVC and polyethylene; thus, the electrolyte composition does not change moving through these parts. Two PVC tanks have duty for supplying and storing electrolyte. Main pump with 3-ph AC motor and inverter provide setting electrolyte flow rate with help of ultrasonic flowmeter. Another magnetic pump used for draining electrolyte form storing tank to main supplying tank through filters. Output of power supply is 30 volt and 100 ampere.

Fig. 1 *The ECM machine.*

2.2. Materials and measurements

Fig. 2 displays workpiece and tool with their fixtures in the machining chamber. Thirty-one 321stainless steel bars 8 mm in diameter specimens were used as workpiece for runs and Table 1 presents the weight percentage of chemical composition for the workpiece material. Commercial cylindrical copper with the same diameter as workpiece were also employed as tool. As long as experiments conducted in stable conditions and with uniform initial gap distance, workpiece and tool were grinded and deburred to remove any possible surface irregularities to guarantee an even and parallel surfaces.

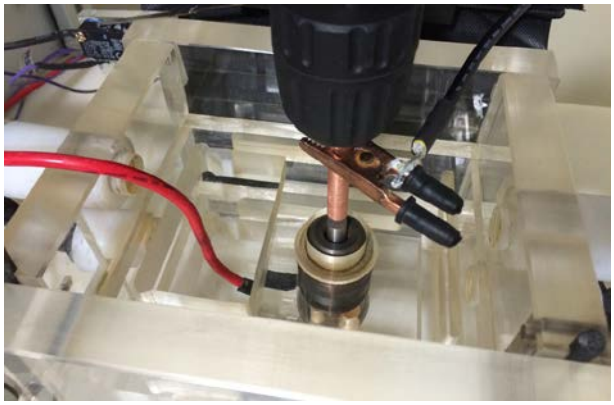

Fig. 2 *machining chamber with workpiece and tool.*

The experiments were carried out in NaNO3 solution electrolyte with various concentrations. The electrolyte flow system used in cross and planning method to ensure an effective flushing during machining. The weight of workpiece was measured before and after machining by a precision weighing machine (0.0001g) for calculating the material removal rate (MRR). The arithmetic mean roughness (Ra) was employed to evaluate surface roughness of specimens. This measurement was performed with the help of surface tester SJ-210-MITUTOYO. The cut-off length and measuring speed were set as 0.8 mm and 0.5mm/s respectively.

Table 1: *Chemical composition (%wt) of the 321 stainless steel*

Fe	**C**	**Mn**	**Si**	**S**	**P**
Rem	0.045	1.66	0.479	0.014	0.034
Cr	**Ni**	**Cu**	**Mo**	**Co**	**Ti**
18.05	8.81	0.59	0.64	0.169	0.227

3. Design of experiments (DOE)

3.1. Experimental plan and conditions

The machining was carried out for a fixed time interval of 2 min and an initial gap distance was 0.6 mm. In the present study, the experimentation strategy was considered based on central composite second order rotatable design (CCD) for the purpose that the higher-order input parameters effects and their interactions on machining responses were determined. The values of four process inputs and their levels are shown in Table 2. Therefore, the design consists of 31 runs, in which 16 factorial points, 8 axial points, 7 center points for estimating the experimental error and the central composite parameter α was considered 2 to ensure a rotatable design Table 3 presents the values of machining responses, i.e. MRR and Ra according to experimentation plan with various sets of machining parameters, i.e. voltage (x1), tool feed rate (x2), electrolyte flow rate (x3) and electrolyte concentration (x4).

3.2. Response Surface Methodology (RSM)

In this research, Response Surface Methodology (RSM) was applied, as one of DOE methods, for determining how the machining parameters influence machining responses. RSM is a powerful way for building the relationship between machining parameters and responses that are useful for the modeling and analysis of the problems; accordingly, the relationship mathematically and statistically could be developed by second-order polynomial as follows:

$$y = b_0 + \sum_{i}^{k} b_i x_i + \sum_{i}^{k} b_{ii} x_i^2 + \sum_{i} \sum_{j} b_{ij} x_i x_j + \varepsilon \qquad (1)$$

Where y is the desired response, e.g. MRR and Ra in this paper, xi is the uncoded or coded levels of the independent variables, and ε is the fitting error. Also, the coefficient b0 is the constant value or intercept and the coefficients bi, bii and bij represent the linear, quadratic and interaction terms respectively (Myers and Montgomery, 1995).

Table 2: *The independent ECM process factors and their levels*

Factors	**Symbol**	**Unit**	**Levels**				
			-2	**-1**	**0**	**1**	**2**
Voltage	x_1	**V**	**10**	**15**	**20**	**25**	**30**
Tool feed rate	x_2	**mm/min**	**0.2**	**0.3**	**0.4**	**0.5**	**0.6**
Electrolyte flow rate	x_3	**l/min**	**5**	**6**	**7**	**8**	**9**
Electrolyte concentration	x_4	**g/l**	**50**	**100**	**150**	**200**	**250**

4. Design of experiments (DOE) Validation and analysis of models

Adequate and suitable measures, tests and analyses were examined the models, so the fitness of the models to the experimental data, significant and insignificant parameters and adequacy of models were analyzed; that is, the analysis of variance (ANOVA) and the F-ratio test have been executed to check the goodness of the mathematically modeled fittings. Moreover, the R-squared (R-Sq) and adjusted R-squared (R-Sq(adj)) is used for assessing the modeling goodness of fit, as more the R2 approaches unity, the better the model fits the experimental data. Indeed, the best condition of analysis of effective models happens as the lack-of-fit is insignificant. Then, a student's t-test has also been performed for determining the significance of each parameter in the models. Accordingly, insignificant terms have been eliminated from the models, and ANOVA has been done again through the available significant terms. In addition, a complete residual analysis has been done through normal probability plot of residuals, plot of residuals versus fitted values and plot of residuals against the order of experimentations in order that the quality of fit for the responses and adequacy of models have been examined.

5. Results and discussion

5.1. Mathematical modeling of MRR

According to the model explained by Eq. 1, Table 4 details the ANOVA and F-ratio test information about MRR response. On the grounds that the p-value of the quadratic model is greatly less than 0.05, the model is statistically significant in the 95% of confidence interval. Besides, the p-value of the lack-of-fit is more than 0.05, so this term is insignificant which is desired. Through the ANOVA result, the MRR model is developed with coded variables as follows:

$$\begin{aligned} MRR = & -0.3374 + 0.0055x_1 - 0.0496x_2 + 0.0755x_3 + 0.00072x_4 \\ & - 1.4494E-05x_1^2 + 0.2275x_2^2 - 0.00551x_3^2 - 2.50494E-06x_4^2 \\ & + 0.00049x_1x_2 + 5.875E-05x_1x_3 + 3.4875E-05x_1x_4 + 0.0073x_2x_3 \\ & - 2.0875E-04x_2x_4 + 9.125E-06x_3x_4 \end{aligned} \qquad (2)$$

The R2 (R-Sq) and adjusted R2 (R-Sq(adj)) are respectively 99.45% and 99.25% for the above MRR model which ensuring an excellent fitting for the model.

Table 3: *Central composite design plan matrix and results*

Exp No.	Factors				Responses	
	x_1	x_2	x_3	x_4	MRR (g/min)	Ra(μm)
1	-1	-1	-1	-1	0.1253	0.76
2	1	-1	-1	-1	0.2134	1.08
3	-1	1	-1	-1	0.1547	0.89
4	1	1	-1	-1	0.2361	1.13
5	-1	-1	1	-1	0.1246	0.84
6	1	-1	1	-1	0.2107	1.16
7	-1	1	1	-1	0.1569	0.96
8	1	1	1	-1	0.2525	1.31
9	-1	-1	-1	1	0.1673	1.29
10	1	-1	-1	1	0.2921	1.94
11	-1	1	-1	1	0.1975	1.63
12	1	1	-1	1	0.3218	2.21
13	-1	-1	1	1	0.1779	1.47
14	1	-1	1	1	0.2979	2.15
15	-1	1	1	1	0.2019	1.78
16	1	1	1	1	0.3235	2.49
17	-2	0	0	0	0.1154	1.22
18	2	0	0	0	0.3379	2.17
19	0	-2	0	0	0.1989	1.12
20	0	2	0	0	0.2755	1.51
21	0	0	-2	0	0.1927	1.12
22	0	0	2	0	0.2194	1.35
23	0	0	0	-2	0.1365	0.72
24	0	0	0	2	0.2696	2.45
25	0	0	0	0	0.2351	1.00
26	0	0	0	0	0.2291	0.98
27	0	0	0	0	0.2250	1.02
28	0	0	0	0	0.2238	0.96
29	0	0	0	0	0.2220	1.04
30	0	0	0	0	0.2275	0.95
31	0	0	0	0	0.2232	1.02

Table 4: *The ANOVA results for MRR response using the Minitab software*

Source of variation	**DF**	**Sum of Squares**	**Mean Squares**	**F value**	**P value**
Regression	14	0.103873	0.007419	219.16	0.000
Linear	4	0.100478	0.025120	742.00	0.000
Square	4	0.002148	0.000537	15.85	0.000
Interaction	6	0.001216	0.000208	6.14	0.002
Residual Error	16	0.000542	0.000034		
Lack-of-Fit	10	0.000419	0.000042	2.06	0.195
Pure Error	6	0.000122	0.000020		
Total	30	0.104414			
R-Sq = 99.45%, R-Sq(adj) = 99.25%					

A student's t-test has also been performed for determination of significant terms in the model. Based on the t values and their p values shown in Table 5, it is concluded that all the linear terms (input parameters, i.e. x_1: voltage, x_2: feed rate, x_3: flow rate and x_4: electrolyte concentration), quadratic terms of input factors x_2, x_3 and x_4, and interaction effect of factors x_1 and x_4 are significant and other terms are insignificant. The insignificant terms have been eliminated, and the ANOVA has again been done to significant terms. As a result, the final reduced model of MRR based on significant parameters in terms of coded factors is developed as follows:

$$MRR = -0.35879 + 0.00549x_1 - 0.02305x_2 + 0.08043x_3 + 0.00069x_4 + 0.23137x_2^2 - 0.00547x_3^3 - 2.48952E\text{-}06x_4^4 + 3.48750E\text{-}05x_1x_4 \quad (3)$$

Table 5: *The T-test results for MRR response including all parameters using the Minitab software*

All Term	**Coefficient**	**SE coefficient**	**T value**	**P-value**
x_1	0.053621	0.001188	45.148	0.000
x_2	0.016204	0.001188	13.644	0.000
x_3	0.003796	0.001188	3.196	0.006
x_4	0.032163	0.001188	27.080	0.000
$x_1 * x_1$	-0.000362	0.001188	-0.333	0.743
$x_2 * x_2$	0.002275	0.001188	2.091	0.053
$x_3 * x_3$	-0.005512	0.001188	-5.066	0.000
$x_4 * x_4$	-0.006262	0.001188	-5.755	0.000
$x_1 * x_2$	0.000244	0.001455	0.168	0.869
$x_1 * x_3$	0.000294	0.001455	0.202	0.843
$x_1 * x_4$	0.008719	0.001455	5.994	0.000
$x_2 * x_3$	0.000731	0.001455	0.503	0.622
$x_2 * x_4$	-0.001044	0.001455	-0.718	0.483
$x_3 * x_4$	0.000456	0.001455	0.314	0.758

Next, a complete residual analysis has been performed for evaluating the quality of fit for the yielded MRR response. Normal probability plot of residuals in Fig. 3 shows that experimental data are located approximately along a straight line; that is, the experimental values correlate closely with the predicted values for the response.

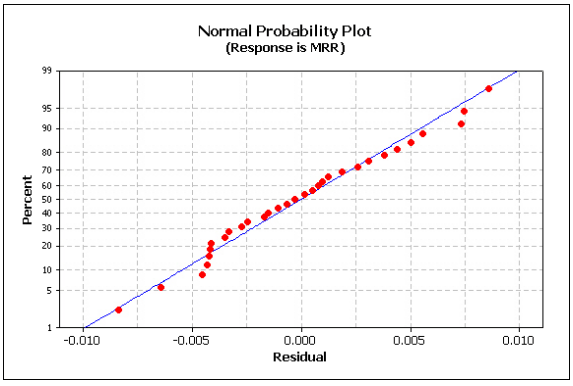

Fig. 3 *Normal probability plot of Residuals for MRR*

The plot of residuals versus fitted values is shown in Fig. 4 indicates that only small variations can be seen. Also, it is clearly observed form the plot of residual versus order of the experimentation, Fig. 5, that residuals are independent of one another and both negative and positive residuals exist in this plot indicate no special tendency. Hence, the presented discussion implies that the above MRR model does not show any inadequacy.

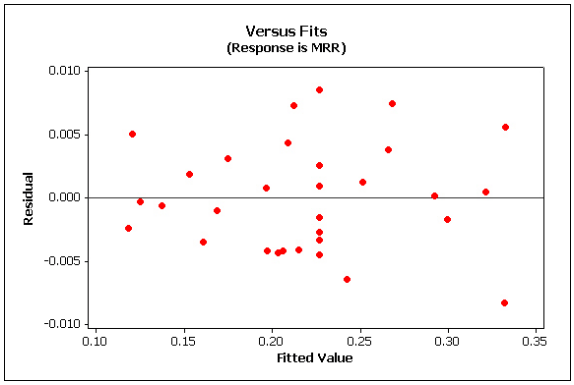

Fig. 4 *Residuals versus Fits for MRR*

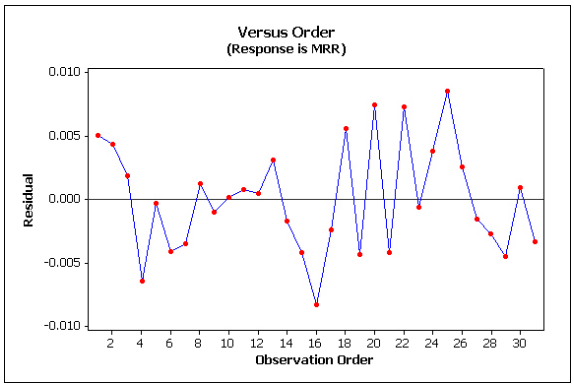

Fig. 5 *Residuals versus Observation Order for MRR*

5.2. Mathematical modeling of Ra

The same procedure is used to deal with the Ra and the ANOVA details of quadratic model are shown in Table 6. The results of the table points out that the model is significant and the lack-of-fit is insignificant according to the p-values. Based on the ANOVA result, the developed mathematical model for Ra with coded variables as follows:

$$Ra = 8.75714 - 0.29921x_1 - 7.01905x_2 - 0.91042x_3 - 0.0234x_4 + 0.0069x_1^2 + 7.74256x_2^2 + 0.05743x_3^2 + 5.79702E-05x_4^2 - 0.01125x_1x_2 + 0.00338x_1x_3 + 0.00035x_1x_4 + 0.08125x_2x_3 + 0.01013x_2x_4 + 0.00051x_3x_4 \quad (4)$$

Table 6: *The ANOVA results for Ra response using the Minitab software*

Source of variation	**DF**	**Sum of Squares**	**Mean Squares**	**F value**	**P Value**
Regression	14	7.73831	0.55274	648.07	0.000
Linear	4	6.16678	1.54170	1807.59	0.000
Square	4	1.39314	0.34828	408.35	0.000
Interaction	6	0.17839	0.02973	34.86	0.000
Residual Error	16	0.01365	0.00085		
Lack-of-Fit	10	0.00688	0.00069	0.61	0.767
Pure Error	6	0.00677	0.00113		
Total	30	7.75195			
R-Sq = 99.82%, R-Sq(adj) = 99.67%					

The R2 and adjusted-R2 for the Ra trimmed model are respectively 99.82% and 99.67% revealing sufficient adequacy in model predictive capabilities.

The student's t-test has also been done for determining the significance of each parameter. The results in Table 7 indicates that all linear and quadratic terms of parameters and the interaction between x_1 (voltage) and x_3 (flow rate), x_1 and x_4 (concentration), x_2 (tool feed rate) and x_4, and x_3 and x_4 are significant. The other model terms can be regard as insignificant terms. By removing these insignificant terms and applying the ANOVA, the proper quadratic model for Ra can be developed as follows:

$$Ra = 8.61964 - 0.303714x_1 - 6.6753x_2 - 0.87792x_3 - 0.0234x_4 + 0.0069x_1^2 + 7.74256x_2^2 + 0.05743x_3^2 + 5.79702E-05x_4^2 + 0.00338x_1x_3 + 0.00035x_1x_4 + 0.01013x_2x_4 + 0.00051x_3x_4 \quad (5)$$

Table 7: *The T-test results for Ra response including all parameters using the Minitab software*

All Term	**Coefficient**	**SE coefficient**	**T value**	**P-value**
x_1	0.239583	0.005961	40.190	0.000
x_2	0.103750	0.005961	17.404	0.000
x_3	0.070417	0.005961	11.812	0.000
x_4	0.428750	0.005961	71.922	0.000
$x_1 * x_1$	0.172426	0.005461	31.572	0.000
$x_2 * x_2$	0.077426	0.005461	14.177	0.000
$x_3 * x_3$	0.057426	0.005461	10.515	0.000
$x_4 * x_4$	0.144926	0.005461	26.537	0.000
$x_1 * x_2$	-0.005625	0.007301	-0.770	0.452
$x_1 * x_3$	0.016875	0.007301	2.311	0.034
$x_1 * x_4$	0.086875	0.007301	11.899	0.000
$x_2 * x_3$	0.008125	0.007301	1.113	0.282
$x_2 * x_4$	0.050625	0.007301	6.934	0.000
$x_3 * x_4$	0.025625	0.007301	3.510	0.003

Like before, a complete residual analysis has been done presented in the Figs. 6, 7 and 8. Similarly, the Ra model does not show any inadequacy.

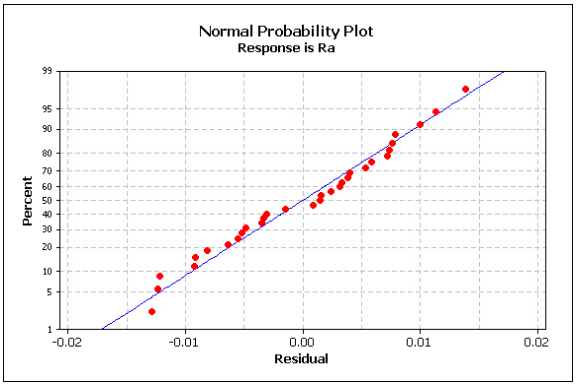

Fig. 6 *Normal probability plot of Residuals for Ra*

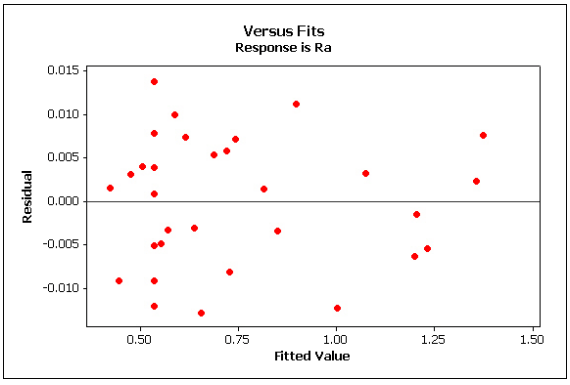

Fig. 7 *Residuals versus Fits for Ra*

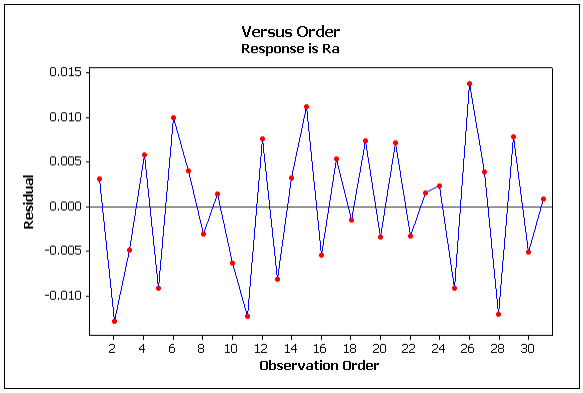

Fig. 8 *Residuals versus Observation Order for Ra*

5.3. Optimization by desirability functions

This desirability function approach developed by Derringer and Suich [16] is an attractive search-based optimization technique used to find the optimal parameters combination globally. This technique uses a desirability function as an objective function in which each response yi is transformed to an individual desirability function (di) between zero and one. That is, one indicates that the response is the completely desirable value (at its target), and zero shows that the response is the least desirable value (outside of its acceptable limits). Thus, the overall (composite) desirability (D) is determined by the geometric mean of the individual desirability functions as follows:

$$D = (d_1 d_2 ... d_n)^{1/n} = \left[\prod_{i=1}^{n} (d_i)\right]^{\frac{1}{n}} \qquad (6)$$

Where n is the number of responses. Also, the individual desirability function di will be defined depending on whether the response yi is to be maximized, minimized, or assigned a target value.

The goal of optimization in this article is to find maximum MRR (productivity) and minimum surface roughness (Ra). The optimization results were obtained by Minitab 16 software. According to the results of optimization, 30 V voltage, 0.6 mm/min tool feed rate, 7.34 l/min electrolyte flow rate, and 250 g/l concentration is the optimal machining parameters setting for achieving maximum MRR. Similarly, 18.28 V voltage, 0.38 mm/min tool feed rate, 6.74 l/min electrolyte flow rate, and 84.34 g/l concentration is the optimal machining parameters combination for achieving minimum Ra.

6. Conclusion

This study highlights that the electrochemical machining of 321 stainless steel criteria, i.e. MRR and Ra are greatly influenced by the different machining parameters. To sum up, the followings can be acquired from this investigation as main findings:

1. For gaining the model that covers all linear, quadratic and interaction terms, the RSM method has been appointed properly as the DOE method for solving curvature in ECM process responses.
2. Mathematical models have been developed through the RSM method for correlation the machining parameters, i.e. voltage, tool feed rate, electrolyte flow rate and concentration on the machining criteria, i.e. MRR and Ra, of 321stainless steel.
3. According to the ANOVA among the process parameters, the machining voltage and electrolyte concentration are the most effective factors on the machining criteria.
4. Increasing voltage and electrolyte concentration lead to increase in the MRR. Also, the proper flushing of electrolyte improves MRR which can be regulated by the electrolyte flow rate.
5. According to the optimization results, 30 V voltage, 0.6 mm/min tool feed rate, 7.34 l/min electrolyte flow rate, and 250 g/l concentration is the optimal machining parameters setting for maximum MRR, and 18.28 V voltage, 0.38 mm/min tool feed rate, 6.74 l/min electrolyte flow rate, and 84.34 g/l concentration is minimum Ra.

7. Acknowledgment

The authors would like to thank the Iran National Science Foundation (INSF) for financial support of this research.

8. References

1. Bhattacharyya, B., S.K. Sorkhel, Investigation for controlled electrochemical machining through response surface methodology-based approach. Journal of Materials Processing Technology, 86, 2009, 200-207.
2. Bhattacharyya, B., J. Munda, Experimental investigation on the influence of electrochemical machining parameters on machining rate and accuracy in micromachining domain. International Journal of Machine Tools & Manufacture, 43, 2003, 1301–1310.
3. El-Taweel, T.A., Modelling and analysis of hybrid electrochemical turning-magnetic abrasive finishing of 6061 Al/Al2O3 composite. The International Journal of Advanced Manufacturing Technology, 37, 2008, 705–714.
4. Haridy, S., S.A., Gouda, Z. Wu, An integrated framework of statistical process control and design of experiments for optimizing wire electrochemical turning process. The International Journal of Advanced Manufacturing Technology, 53, 2011, 191–207.
5. Hinduja, S., M. Kunieda, Modelling of ECM and EDM processes. CIRP Annals - Manufacturing Technology 62, 2013, 775–797.
6. Huang, S.F., Y. Liu, Electrochemical Micromachining of Complex Shapes on Nickel and Nickel-Based Superalloys. Materials and Manufacturing Processes, 29(11-12), 2014, 1483-1487.
7. Malapati, M., B. Bhattacharyya, Investigation into Electrochemical Micromachining Process during Micro-Channel Generation. Materials and Manufacturing Processes, 26(8), 2011 1019-1027.
8. Montgomery D.C., Design and analysis of experiments. New York: John Wiley, 2009.
9. Munda, J., B. Bhattacharyya, Investigation into electrochemical micromachining (EMM) through response surface methodology based approach. The International Journal of Advanced Manufacturing Technology, 35, 2008, 821–832.
10. Munda, J., M. Malapati, B. Bhattacharyya, Control of micro-spark and stray-current effect during EMM process. Journal of Materials Processing Technology, 194, 2007, 151–158.
11. Myers, R.H., D.C. Montgomery, Response surface methodology: process and product optimization using designed experiments. New York: Wiley, 1995.
12. Neto, J.C.S., E.M. Silva, M.B. Silva, Intervening variables in electrochemical machining. Journal of Materials Processing Technology, 179, 2006, 92–96.
13. Rajurkar, K.P., G. Levy, A. Malshe, M.M. Sundaram, J. McGeough, X. Hu, R. Rensnick, A. DeSilva, Micro and Nano Machining by Electro-Physical and Chemical Processes. CIRP Annals-Manufacturing Technology, 55(2), 2006, 643–666.
14. Rumyantsev, E., A. Davydov, Electrochemical machining of metals. MIR Publishers Moscow, Russia, 1989.
15. Venkata Rao, R., V.D. Kalyankar, Optimization of modern machining processes using advanced optimization techniques: a review. The International Journal of Advanced Manufacturing Technology, 73, 2014, 1159-1188.
16. Derringer, G., R. Suich, Simultaneous Optimization of Several Response Variables. *Journal of Quality Technology*, 12(4), 1980, 214-219.

THE ROLE OF METALLOGRAPHIC ANALYSIS FOR QUALITY EVALUATION OF WELDED STEEL PIPES

Prof. dr. Rrahim M.[1], Prof. dr. Mursel R.[2], Prof.dr.Hamit M.[1]
[1] Faculty of Applied Sciences, State University of Tetova, Republic of Macedonia[1]
[2]Faculty of Geosciences, University of Mitrovica, Republic of Kosova[2]

rrahimmaksuti@yahoo.com

Abstract: *Submerged arc welding is one of the most extensively used process for production of spiral welded steel pipes. Production process includes pipe forming by cold plastic deformation of hot rolled strips and double-sided submerged arc welding of the strip edges. The double-sided welded seam as an integral part of the final steel pipes must be carefully controlled because plays principal role on the quality of welded steel pipes. In this respect, optical metallographic analysis of the welded joint cross section were used as efficient and effective method to control the double-sided welded seam.*

The article presents a brief review of the role of optical metallographic analysis commonly used for quality evaluation of double-sided submerged arc welded steel pipes.

Keywords: METALLOGRAPHIC ANALYSIS, WELD JOINT, SUBMERGED ARC WELDING

1. Introduction

Submerged arc welding (SAW) is one of the most extensively used process for production of spiral welded carbon steel pipes suitable for pipelines [1]. Submerged arc welding (SAW) is traditionally considered as an efficient and highly productive joining technology for medium to high thickness steels. In Submerged arc welding (SAW) process, the welding arc is always covered with a layer of granular flux that protects the arc. The flux melts by arc heating forming a slag that protects the weld pool from the atmosphere, figure 1 [2, 3, 4].

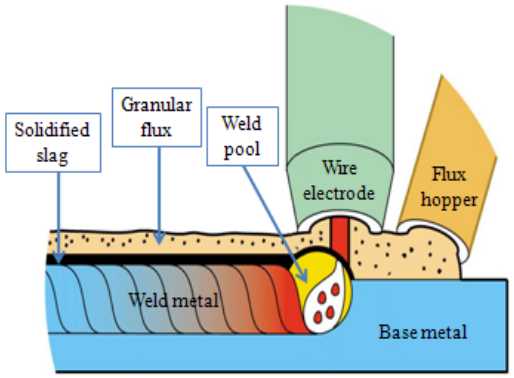

Fig.1 *Schematic representation of SAW*

Double sided spiral welded steel pipes produced from hot rolled strip which is gradually formed into round shape through three-roll-bending system, and its edges are joined inside and outside by submerged arc welding (SAW), figure 2.

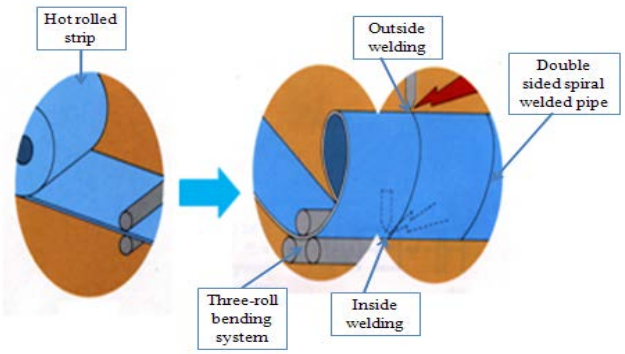

Fig.2 *Production of spiral welded steel pipes by SAW*

During pipe production, there is a need to precisely control all the processes with respect to the different operating parameters. There are several parameters which must be controlled during pipe production. Monitoring and control issues is of a great importance in SAW for the purpose of making pipes with consistent and defined quality at a high productivity. Monitoring the SAW process under industrial conditions is however not an easy task. Inspection and testing to ensure conformance to order requirements are integral parts of the production process and can be broadly classified into nondestructive and destructive testing /5/.

In steel pipe production by SAW, destructive testing within framework of quality assurance is widely used not for final inspection alone but also serves an important tool for efficient in-process control.

Metallography is the well known technique to reveal macrostructure and microstructure. Optical metallography, one of three general categories of metallography, entails examination of materials using visible light to provide a magnified image of the macro and microstructure [6].

Metallographic analysis also plays an important role to establish the causes of failures and the service condition of welded pipes as a constitutive parts of pipelines. These analysis provide the information regarding presence of defects and others metallurgical phenomena that manifest impact on the integrity of the welded pipes and pipelines. Metallographic examination is a key tool in the destructive examination of weldments, both as a process control tool and as a post-mortem examination of failed components [7].

Metallographic examination of weldments reveals macrostructural and microstructural features clearly when good metallographic preparation and the right etchant are used [7, 8].

Optical metallographic analysis of welded joint is a valuable analytical procedure widely used within the pipe industry. It is used for a variety of reasons including: set up of the production process, monitoring of the production process and finally, quality control activities for detecting fabricating defects and causes of the welded joint failures. In steel pipes production, metallographic analysis covers the range of pre-SAW, during-SAW and post-SAW activities. Metallographic analyses combined with others investigations can extract the most detailed information that can lead to a better understanding of the causes of the flaws and enabling to eliminate them.

Optical metallographic analysis can be carried out with little physical effort using apparently simple equipment and it is frequently regarded as easy operation but in the essence this is a

skilled operation. Proper training of metallographers in the methodology and interpretation of the results is very important. Optical metallographic analysis is essential in order to understand the relationship between microstructure and properties of welded joints of steel pipes.

This article presents a brief review of the role of optical metallographic analysis commonly used for quality evaluation of welded joint of spiral welded steel pipes by submerged arc welding (SAW).

2. Experimetal procedure

Double sided spiral line pipes Ø813x12mm, welded by submerged arc welding (SAW) were used to review the role of optical metallographic analysis for quality evaluation. For this purpose, pipe rings (20-30cm long) were cut out from the several produced pipes Ø813x12mm in the production line and from these rings were extracted specimens for optical metallographic analysis, transversal to the spiral weld, figure 3.

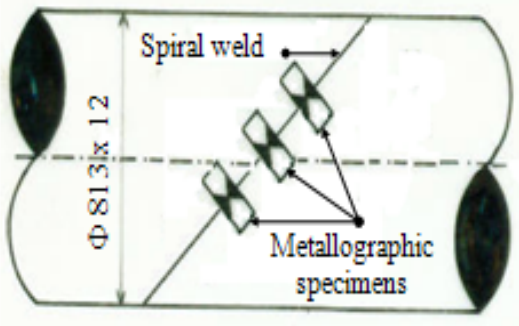

Fig.3 *Schematic illustrating of metallographic specimens*

In order to perform metallographic macro and micro analysis, the metallographic specimens were prepared by standard metallographic techniques that includes grinding, polishing and etching with suitable etchant, to reveal the macro and microstructure. Mechanical grinding is performed in successive steps using SiC abrasive papers of different grit sizes, usually 180, 220, 320, 600, 800 and 1000. Cooling is always necessary to avoid structural changes. Mechanical polishing is usually performed using diamond paste on a short nap cloth disc. After polishing, the specimens were etched with 3% natal (ethyl alcohol +3%HNO_3), followed by thorough washing and finally rinsed in alcohol and dried in a stream of warm air. It is important that care is taken at all stages of the preparation process to obtain a correct metallographic analysis of the welded joint.

Macro metallographic analysis is performed on etched cross section of the welded joint by standard visual examination with the naked eye and with optical microscope NEOPHOT 21 at low magnification.

Micro metallographic analysis is performed on etched cross section of the welded joint by optical microscope NEOPHOT 21 at high magnification.

3. Results and discussion

Figure 4 shows macrograph of the welded joint of double sided submerged arc welding (SAW) of spiral welded line pipes Ø813x12mm, after etching with 3% nital (ethyl alcohol +2%HNO_3) at room temperature. This technique is very useful and simple to use for revealing macrostructure of welded joint in pipe production.

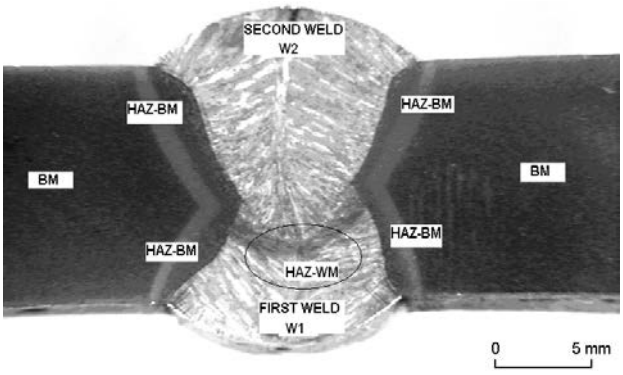

Fig.4 *Schematic illustrating of metallographic specimens*

The macrostructure of double sided submerged arc welding (SAW) of spiral welded line pipes Ø813x12mm generally shows two pass X-shape weld joint, being composed of areas of as deposited metal with columnar grains and areas that have been reheated by subsequent pass. Proper fusion has been achieved throughout the full thickness of the joint with good interpenetration and overlap between inside (W_1) and outside weld (W_2). No evidence of any weld defects such as undercut, lack of side wall fusion, gas porosity, etc. This macro-metallographic analysis is necessary at the beginning of the production process of welded pipes to determine the main parameters of welding. Without performing this analysis and without positive results arising from this analysis can not continue pipes production process.

It should be noted that macro-metallographic analysis is very important analysis in welded steel pipes production and also can be used for additional purposes, such as measuring of geometrical dimensions of welded joint, figure 5, hardness measuring, figure 6 as well as for milling of the V-notch in the constitutive parts of the welded joint for toughness testing, figure 7.

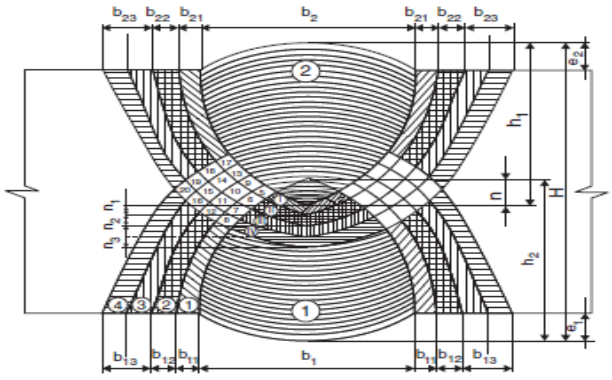

Fig.5 *Schematic illustrating of metallographic specimens for geometrical dimensions measuring*

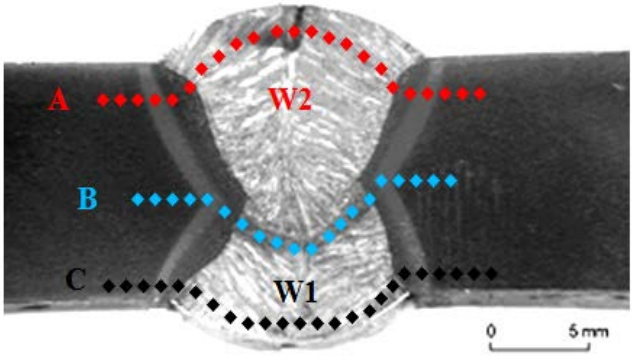

Fig.6 *Schematic illustrating of metallographic specimens for hardness measuring*

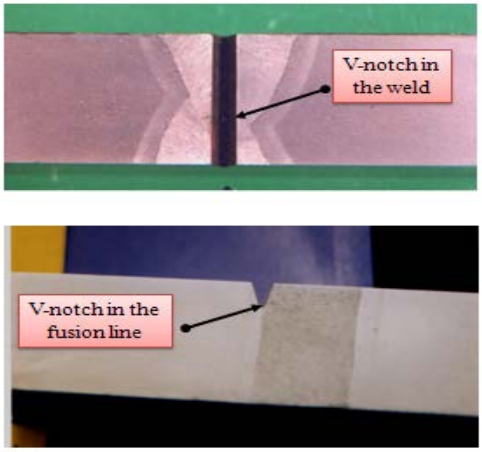

Fig.7 *Schematic illustrating of metallographic specimens for V-notch milling*

Micro-metallographic analysis is performed for a number of purposes, the most obvious of which is to assess the microstructure of the constitutive parts of welded joint (base metal-BM, heat affected zone-HAZ and weld metal-WM), figure 8. It is also common to analysis specific grain size, grain orientation, porosity, lack of fusion, lack of penetration, presence of inclusions, presence of cracks and others metallurgical phenomena such as local brittle zone, precipitation and reprecipitation of certain microparticles in the welded joint.

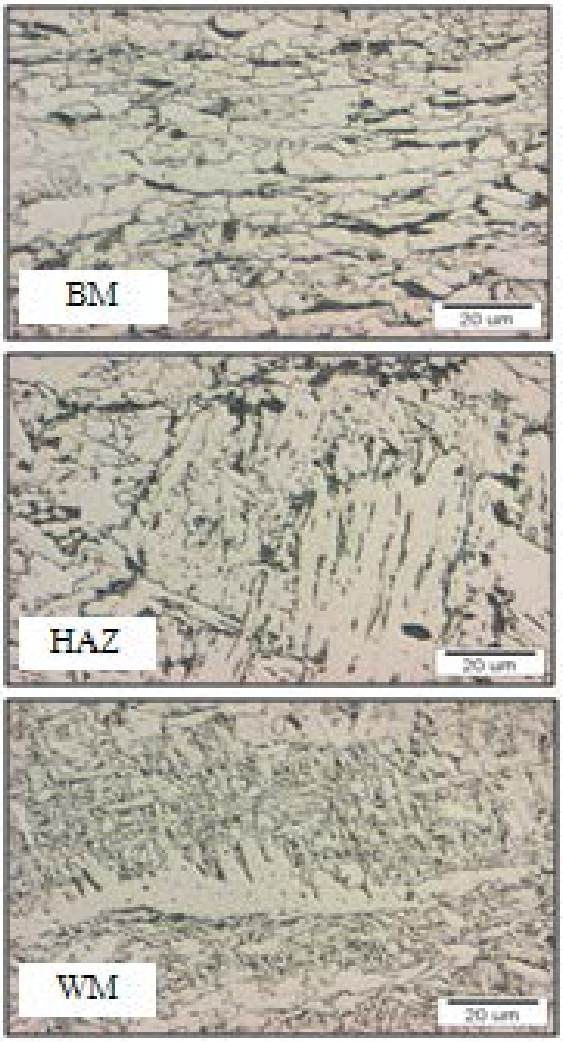

Fig.8 *Microstructure of welded joint*

4. Conclusion

From the results presented in this work, it is possible to draw the following conclusions:

Optical metallographic analysis of welded joint is a valuable analytical procedure widely used within the pipe industry and extremely important indispensable key tool for quality evaluation of the welded steel pipes. It is used for a variety of reasons, including evaluation of the production set up process, monitoring of the production process and quality evaluation of the welded steel pipes.

Macro-metallographic analysis is a fundamental step for evaluation of the quality of the welded joint of steel pipes and prelude to micro-metallographic analysis.

In conjunction with others equipment, metallographic analysis can extract the most detailed information about the assurance of a consistent top quality of the welded steel pipes and research and development (R&D) activities in the field of production of these pipes.

5. Literature

1. Komizo You-ichi, Overview of Recent Welding Technology Relating to Pipeline Construction, Transactions of JWRI, Vol.37(2008), No.1, 1-5.
2. Degala Ventaka Kiran and Suck-Joo Na, Experimental Studies on Submerged Arc Welding Process, Journal of Welding and Joining, Vol. 32, No. 3, 2014. 6, 215-223.
3. A. Bhatia, Fundamentals of Arc Welding, Continuing Education and Development, Inc. 9 Greyridge Farm Court Stony Point, NY 10980.
4. Ibrahim Khan, Welding Science and Technology, New Age International (P) Limited Publishers,New Delhi, 2007.
5. API-American Petroleum Institute, Specification for line pipe, Washington DC, USA, 2000.
6. M .R. Louthan, Optical Metallography, ASM Handbook, Volume 10, Material Characterizations, 1986, 299-308.
7. George F., Vander V., Metallography of Welds, Advanced Materials and Processes, June 2011, 19-23.
8. Donald C. Zipperian, Metallographyc Handbook, Pace Technologies, Tucson, Arizona USA, 2011.

DIMENSIONING OF LINEAR ROLLER BEARING

ОРАЗМЕРЯВАНЕ НА ЛИНЕЕН РОЛКОВ ЛАГЕР

Assoc. Prof. Pandev G., PhD., Eng.,
Faculty of Applied Mechanics – University of Chemical Technology and Metallurgy, Sofia, Bulgaria
gpep@uctm.edu

Abstract. *To the modern machines, especially those for the workflow automating, have been made more greater demands regarding the accuracy of their work under different conditions. In relation to this, in most constructions have been used linear bearings, which are especially suitable because of a number of their advantages.*

The present article aims to show the dimensioning of a linear roller bearing of specifically selected series, depending on the speed and acceleration at work, as forces and friction coefficients in different parts of the bearing have been previously specified and taken into account in the calculation.

As a result of the dimensioning it becomes possible to determine the duration of operation of the linear roller bearing of the so-set conditions, and the deformations in the various parts under load.

Keywords: LINEAR ROLLER BEARING, DIMENSIONING,

1. Introduction

Comparing the characteristics of different systems allows bearings to identify their advantages and disadvantages when operating in specific conditions and in certain construction of machinery.

The linear bearings are widely used in the precise mechanics, automation, and devices to measure and control because of their following advantages over the other types of bearings: sliding, hydrostatic and others :

- Absence of any kind of windage;
- A guaranteed interchangeability, based on the rapid development of their standardizing, resulting in minimizing the operating costs;
- Very low friction, depending on the speed of displacement.

In the present publication it will be considered a specific type of linear bearings [3,4], which are characterized by a very high precision of manufacturing and load capacity. This allows them to be put in constructions, requiring absence of windage, specified stiffness, low coefficient of friction. As a result, the construction of the machine is characterized by a long duration of operation. The load capacity, rigidity and duration of operation are highly dependent on the number and shape of the rolling elements constituting the construction of the linear bearing.

The friction coefficient μ while sliding, depends to a large extent on the nature of the material of the contacting elements, the state of their surfaces, load and speed. Its values are in the range 0.05 to 0.2 [1]. It increases very quickly when the sliding speed tends to 0 - then the value of μ can reach a maximum value of 0.3. Depending on the construction embodiment, the coefficient of friction μ in the linear bearings in question has a value from 0.0005 to 0.005, which is approximately 10 to 400 times smaller than that of a sliding bearing of the same dimensions.

The dynamic load (load capacity) C of a linear bearing corresponds to the duration of operation, equivalent to 100,000 m displacement, wherein the load of the elements remains constant – it does not change in value and in direction. At the same time, the static load must not be in any case greater than the dynamic one.

The duration of the exploitation (resource of work) of the linear bearing is defined as the distance in meters traveled by one of its guiding to the first signs of fatigue from one of the constituent elements.

The constructional varieties of linear bearings are the following:

- With a separator for pellets, rolls, or needles;
- With an insert for recirculation of the pellets or rolls;
- With a monorail (Fig. 1). This type of a linear bearing is characterized by a high rigidity, great dynamic and static load capacity, stable functioning, and a very good sealing of the support.

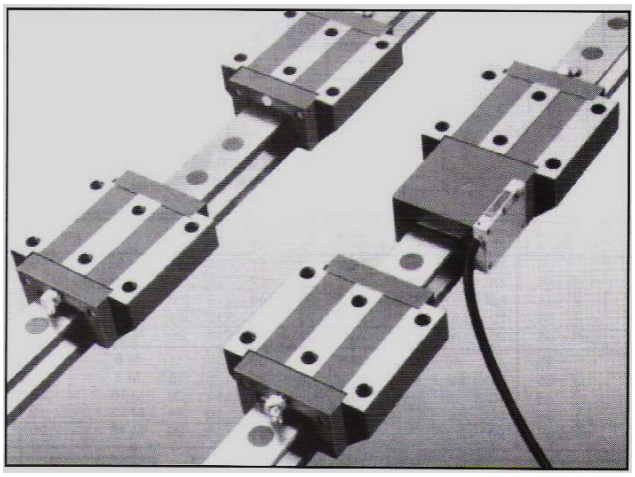

Fig. 1. *Linear roller bearing type monorail*

The objective of this article is to show the dimensioning of linear roller bearing and choosing a particular series, depending on the load, speed and acceleration at work, as the frictional forces in different parts of the bearing and the coefficient of friction have been specified in advance and taken into account when calculating.

2. Characteristics of linear roller bearing

They are the following (Fig. 2) [3]:

- Four classes of tolerances : from G0 to G3;
- Three classes of preloading: V1, V2 and V3, defined as a percentage of the load capacity C;
- Five type sizes (series) : 25, 35, 45, 55 and 65;

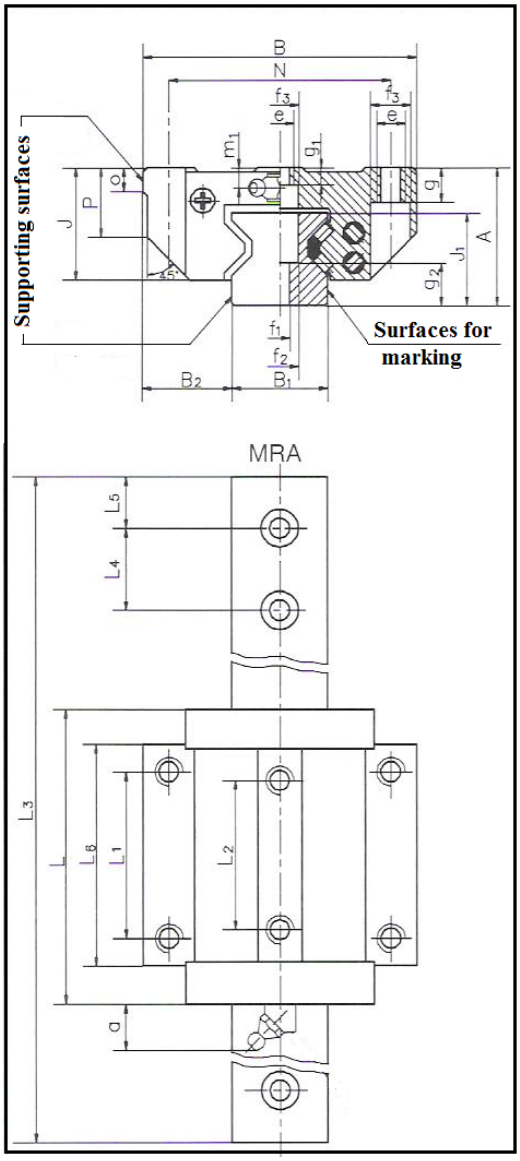

Fig. 2. *Construction of the linear roller bearing series MRA*

- Four series : Table 1.

Table 1. *Series of linear roller bearing*

Indication	MRA	MRB	MRC	MRD
Type of the support	standard	standard long	compact	Compact long

- The linear roller bearing operates in a temperature range from -**40°C** to **+80°C**, as for a short period can last up to +120°C.

- The standard length of the rail is calculated by the formula

(1) $L_3 = (n + k.p).L_4 + 2.L_5 (\pm 2\ mm)$, (Fig. 2) [3]

as the values of n, p and k are given in Table 2.

Table 2. *The value of the coefficients* ***n***, ***p*** *and* ***k***

Series	n	p	k
MR 25	9	6	1 to 16
MR 35	14	5	1 to 13
MR 45	10	4	1 to 11
MR 55	12	4	1 to 9
MR 65	7	4	1 to 7

- The loading and the types of variations of the support of the bearing are shown on Figure 3.

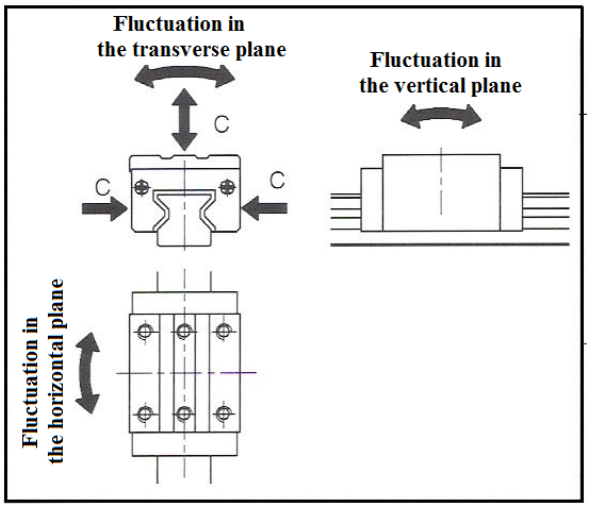

Fig. 3. *Loading C and fluctuations of the support*

The functioning of a linear roller bearing in normal conditions is performed at a speed up to 3 m/s (180 m/min) and acceleration up to 50 m/s^2 [2,3].

In cases where the lubrication of the bearing is carried out with oil, the power for moving F_R can be determined under dependency (2) for speeds lower than 30 m / min, as the coefficients of friction are shown in Table 3.

(2) $$F_R = F_{A,G} + v \cdot f_{A,v} + F_{w,G} + v \cdot f_{w,v} + F_j \cdot \mu,$$

where :

$\mathbf{F_R}$ – force for moving, N
v – speed, m/min
$\mathbf{F_{A,G}}$ – friction force of cleaner of lubricant at low speed, N
$\mathbf{f_{A,v}}$ – friction coefficient of cleaner of lubricant in a function of the speed, (N)/(m/min)
$\mathbf{F_{w,G}}$ – friction force of the the support at low speed, N
$\mathbf{f_{w,v}}$ – coefficient of friction of the support in a function of the speed, (N)/(m/min)
$\mathbf{F_j}$ – the sum of all external forces applied to the the support, N
μ – friction coefficient of the bearing.

When lubricating of the bearing with grease the friction force in the support $\mathbf{F_{w,G}}$ is initially the same as with the lubrication with an oil, but decreases after a few operation cycles outward - return.

Table 3. *Values of the coefficients and the forces of friction lubrication with oil for linear bearing with a class of pretension V2*

			MRA/MRC	MRB/MRD		
Series	$\mathbf{F_{A,G}}$ **(N)**	$\mathbf{f_{A,v}}$	$\mathbf{F_{w,G}}$ **(N)**	$\mathbf{F_{w,G}}$ **(N)**	$\mathbf{f_{w,v}}$	**μ**
25	7	0,15	5	6	0,25	0,001
35	9	0,20	8	10	0,35	0,001
45	11	0.25	12	15	0,50	0,001
55	13	0,30	16	20	0,70	0,001

3. An example for dimensioning a linear roller bearing

The presented example shows how to determine the limit of resistance against fatigue. It has not yet been developed a method for determining the limit of wear resistance.

The forces acting on the linear roller bearing, can be determined by approximation of the linearized characteristic curve of the deformations in all cases of its application.

As a result has always been obtained an approximate value, as the characteristic curve of the support can be linearized, while the elastic deformations of the rest of the structure of the bearing are overlooked.

3.1. Determination of the impacts on the support (Fig. 4)

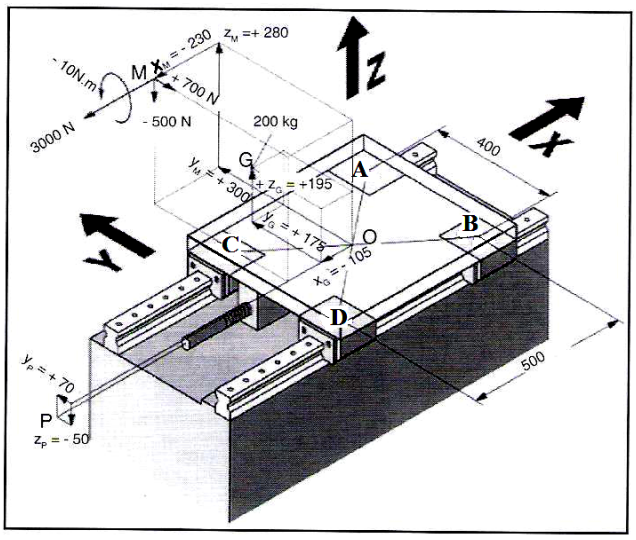

Fig. 4. *Coordinates and load applied on the the support*

The matrix of external influence on the bearing, seen in point **M** (-230, +300, +280), has the following form:

$$\tau_1 = \tau_{(\text{ext}\rightarrow\text{syst})} = {}_{M}\begin{Bmatrix} -3000, & -700, & -500 \\ -10, & 0, & 0 \end{Bmatrix}$$

This matrix is calculated for point O (0,0,0) by:

$$\tau_1 = {}_{O}\begin{Bmatrix} -3000, & -700, & -500 \\ -10 + (0{,}3x-500) - (0{,}28x-700), & 0 + (0{,}28x-3000) - (-0{,}23x-500), & 0 + (-0{,}23x-700) - (0{,}3x-3000) \end{Bmatrix}$$

The moment to point O is determined by the relationship

$\overrightarrow{M_O} = \overrightarrow{M_M} + \overrightarrow{OM} \wedge \overrightarrow{R}$ and then for $\boldsymbol{\tau_1}$, reduced in point O is obtained

$$\tau_1 = {}_{O}\begin{Bmatrix} -3000, & -700, & -500 \\ 36, & -955, & 1061 \end{Bmatrix}.$$

The impact of the transmission mechanism on the system of the linear bearing is applied in point **P** (0, +70, -50) and then the matrix has the form:

$$\tau_2 = \tau_{(\text{transm}\rightarrow\text{syst})} = {}_{P}\begin{Bmatrix} F, & 0, & 0 \\ 0, & 0, & 0 \end{Bmatrix} = {}_{O}\begin{Bmatrix} F, & 0, & 0 \\ 0, & -0{,}05.F, & -0{,}07.F \end{Bmatrix}$$

The interaction between of the bearing and the rail of the support is seen in the following four points – A, B, C и D (Fig. 4).

In point **A** (+K/2, +Q/2, 0) the rail of the bearing has an impact on the support A and the matrix τ_3 is:

$$\tau_3 = \tau_{(\text{rail}\rightarrow\text{supp.A})} {}_{A}\begin{Bmatrix} X_A, & Y_A, & Z_A \\ L_A, & M_A, & N_A \end{Bmatrix} = {}_{O}\begin{Bmatrix} 0, & Y_A, & Z_A \\ 0{,}5\,Q.Z_A, & -0{,}5\,K.Z_A, & 0{,}5\,K.Y_A \end{Bmatrix}$$

as $X_A = 0$, the friction forces are negligible, $L_A = 0$, $M_A = 0$ и $N_A = 0$ provided that the rigidity of the system is high enough and the geometry is sufficiently accurate to disregard the moments of the fluctuations of the support in the three planes as shown in Figure 3.

In an analogous manner is defined the impact of the rail and the support in the remaining three points – B, C and D.

In point **B** (+K/2, -Q/2, 0) the rail impacts on the support B :

$$\tau_4 = \tau_{(\text{rail}\rightarrow\text{supp.B})} = {}_{B}\begin{Bmatrix} 0, & Y_B, & Z_B \\ 0, & 0, & 0 \end{Bmatrix} = {}_{O}\begin{Bmatrix} 0, & Y_B, & Z_B \\ -0{,}5Q.Z_B, & -0{,}5K.Z_B, & 0{,}5K.Y_B \end{Bmatrix}$$

In point **C** (-K/2, +Q/2, 0) the rail impacts on support C :

$$\tau_5 = \tau_{(\text{rail}\rightarrow\text{supp.C})} = {}_{C}\begin{Bmatrix} 0, & Y_C, & Z_C \\ 0, & 0, & 0 \end{Bmatrix} = {}_{O}\begin{Bmatrix} 0, & Y_C, & Z_C \\ 0{,}5Q.Z_C, & 0{,}5K.Z_C, & -0{,}5K.Y_C \end{Bmatrix}$$

In point **D** (-K/2, -Q/2, 0) the rail impacts on support D :

$$\tau_6 = \tau_{(\text{rail}\rightarrow\text{supp.D})} = {}_{D}\begin{Bmatrix} 0, & Y_D, & Z_D \\ 0, & 0, & 0 \end{Bmatrix} = {}_{O}\begin{Bmatrix} 0, & Y_D, & Z_D \\ -0{,}5Q.Z_D, & 0{,}5K.Z_D, & -0{,}5K.Y_D \end{Bmatrix}$$

In point **G** (-105, +175, +195) the weight force acts on the system and then

$$\tau_7 = \tau_{(\text{weight}\rightarrow\text{syst})} = {}_{G}\begin{Bmatrix} 0, & 0, & -P \\ 0, & 0, & 0 \end{Bmatrix} = {}_{O}\begin{Bmatrix} 0, & 0, & -P \\ -0{,}175.P, & -0{,}105.P, & 0 \end{Bmatrix}$$

After bringing all matrices to point O, it can be applied the principle of the dynamics :

(3) $$\tau_1 + \tau_2 + \tau_3 + \tau_4 + \tau_5 + \tau_6 + \tau_7 = \delta$$

as

(4) $$\delta = {}_{G}\begin{Bmatrix} -m.\gamma, & 0, & 0 \\ 0, & 0, & 0 \end{Bmatrix} = {}_{O}\begin{Bmatrix} -m.\gamma, & 0, & 0 \\ 0, & 0{,}195.\,m.\gamma, & -0{,}175.m.\gamma \end{Bmatrix}$$

m = 200 kg, the mass of the system

$\gamma = 6$ m/s^2, the maximum acceleration.

As a result is obtained the following system of six equations

(5.1) $-3000 + F = -m.\gamma$
(5.2) $-700 + Y_A + Y_B + Y_C + Y_D = 0$
(5.3) $-500 + Z_A + Z_B + Z_C + Z_D - P = 0$
(5.4) $36 + 0{,}5Q(Z_A - Z_B + Z_C - Z_D) - 0{,}175P = 0$
(5.5) $-955 - 0{,}05F + 0{,}5K(-Z_A - Z_B + Z_C + Z_D) - 0{,}105P = 0{,}195m.\gamma$
(5.6) $1061 - 0{,}07F + 0{,}5K(Y_A + Y_B - Y_C - Y_D) = -0{,}175m.\gamma$

From equation (5.1) can be determined the force F :

(6) $\boldsymbol{F = 3000 - m.\gamma = 3000 - (200 \,.\, 6) = 3000 - 1200 = 1800\ N.}$

Equations (5.2) and (5.6) contain 4 unknowns. From the hypothesis that the geometry is perfect and rigidity of the system is infinite, it can be assumed that under the influence of moments around an axis z, we have $Y_A = Y_B$ и $Y_C = Y_D$.

These two equations can be presented as

$$700 + 2Y_A + 2Y_C = 0$$

$$1061 - 0{,}07.1800 + 0{,}5K.\,2(Y_A - Y_C) = -0{,}175\,.\,200\,.\,6$$

from where is obtained: $\mathbf{Y_A = Y_B = -550\ N}$, $\mathbf{Y_C = Y_D = +900\ N.}$

Equations (5.3), (5.4) and (5.5) contain four unknowns. The acceptance of the same hypothesis as above allows to make the following assumptions:

- $Z_{A/F} = Z_{B/F} = Z_{C/F} = Z_{D/F} = \mathbf{Z_F}$, where $Z_{A/F}$ is the vertical force, exerted by the rail on support A, and it represents the sum of the vertical forces (the same goes for $Z_{B/F}$, $Z_{C/F}$ and $Z_{D/F}$);
- $Z_{A/Mx} = -Z_{B/Mx} = Z_{C/Mx} = -Z_{D/Mx} = \mathbf{Z_{Mx}}$, where $Z_{A/Mx}$ is the vertical force, acting through the rail on the support A, and occurring a sum of the moments, relative to an axis x (the same goes for $Z_{B/Mx}$, $Z_{C/Mx}$ and $Z_{D/Mx}$);
- $Z_{A/My} = Z_{B/My} = -Z_{C/My} = -Z_{D/My} = \mathbf{Z_{My}}$, where $Z_{A/My}$ is a vertical force, acting through the rail on support A, and occurring a sum of the moments, relative to an axis y (the same definition goes for $Z_{B/My}$, $Z_{C/My}$ and $Z_{D/My}$).

Then from equation (5.3) is obtained

$$Z_A + Z_B + Z_C + Z_D = 4.Z_F = (m.g) + 500 = (200.9{,}81) + 500 = 1962 + 500 = 2462\ N.$$

Or $\mathbf{Z_F} = 2462/4 = Z_{A/F} = Z_{B/F} = Z_{C/F} = Z_{D/F} = 615{,}5\ N.$

From equation (5.4) follows

$Q/2 . (Z_A - Z_B + Z_C - Z_D) = Q/2 . (4 . \mathbf{Z_{Mx}}) = 0,175 P – 36$
$= (0,175 . 200 . 9,81) – 36 =$
$= 343,36 – 36 = 307,35 N.m$

Then $\mathbf{Z_{Mx}} = 307,35/2.Q = 307,35 /2.0,4 = 384 N =$
$= Z_{A/Mx} = - Z_{B/Mx} = Z_{C/Mx} = - Z_{D/Mx}$

From equation (5.5) is obtained

$K/2 . (- Z_A - Z_B + Z_C + Z_D) = K/2 . (4.Z_{My}) = - 2.K.Z_{My} =$
$= - 0,195 . m .\gamma + 0,105 . P + 0,05 . F + 955 =$
$= - 0,195.200.6 + 0,105.200.9,81 + 0,05.1800 + 955 = 1017 N.m$

Then $\mathbf{Z_{My}} = 1017/2.K = 1017/2.0,5 = 1017 N =$
$= Z_{A/My} = Z_{B/My} = - Z_{C/My} = - Z_{D/My}$

Then we receive

$Z_A = Z_{A/F} + Z_{A/Mx} + Z_{A/My} = 615,5 + 384 – 1017 = - 17 N$
$Z_B = Z_{B/F} + Z_{B/Mx} + Z_{B/My} = 615,5 – 384 – 1017 = - 786 N$
$Z_C = Z_{C/F} + Z_{C/Mx} + Z_{C/My} = 615,5 + 384 + 1017 = +2017 N$
$Z_D = Z_{D/F} + Z_{D/Mx} + Z_{D/My} = 615,5 – 384 + 1017 = +1248 N.$

From the obtained results it can be concluded that the vertical force impacting by the rail on the supports A and B shall be designed in a negative direction of z-axis and thus subjecting them to strength.

The vertical force acting through the rail respectively on the supports C and D, is designed in a positive direction of z-axis and subjecting them to pressure.

From the calculations made was established, that the linear roller bearings of the series **MRC 25 V1** may incur without a problem values obtained for the forces [4].

3.2. Resource of working of the bearing L

It is determined by the equivalent force P and a dynamic load C by the relationship:

(7) $L = a\,(C/P)^{10/3} . 10^5\ m,$

where a – safety coefficient.

The equivalent force P_i, which is used in formula (7) depends on the one hand on the calculated above forces in the four points of the the support, and on the other hand on the applied preloading :

(8) $P_i = F_P + 2/3 . F_i \rightarrow$ when $F_i \leq 3 . F_P$

(9) $P_i = F_i \rightarrow$ when $F_i > 3 . F_P$

where F_P – force of preloading,

and $F_i = |Y_i| + |Z_i|$.

For the selected in the above section linear roller bearing, the dynamic load C = 27 700 N [4], and the preloading is 3% for it. Then

$F_P = 27\,700 . 0,03 = 831 N,$

which allows to determine the following equivalent workloads :

$F_A = | - 550 | + | - 17 | = 567 N \quad or\ P_A = 831 + 2/3.567 = 1209 N.$

$F_B = | - 550 | + | - 786 | = 1336 N\ or\ P_B = 831+2/3.1336 = 1722 N.$

$F_C = | + 900 | + | - 2017| = 2917 N\ or\ P_C = 2917 N.$

$F_D = | + 900 | + | - 1248 | = 2148 N\ or\ P_D = 2263 N.$

From the above results it is established that the support is the busiest in p. C. Its resource of working L at a safety coefficient a = 1.0.

(10) $L = 1,0 . (27\,700/1980)^{10/3} . 10^5 = 660 . 10^6\ m.$

4. Conclusions

There have been analyzed the advantages of linear roller bearings relative to other constructions of bearings. It was found that the coefficient of friction in the linear roller bearing is for example 10 to 400 times smaller than that of the sliding bearing of the same size, which is beneficial to the bearing capacity and its operation.

There have been considered in detail the characteristics of the linear roller bearing – the classes of the tolerances, of the preloading, the series, the temperature range, and the conditions under which it can work - speed, acceleration, load. There have been determined the friction forces between different parts of the bearing at oil lubrication.

It has been solved an example with predefined specific output values, and has been chosen a corresponding series of a linear roller bearing, taking into account all impacts on the support, based on which has been solved a system of six equations. It allows to be identified the forces, acting in the four points of the support, as well as the type of tensions - tension and compression. It has been specified the resource of working on the linear roller bearing, according to the specified busiest point of the the support, as well as the deformations in those points.

References

1. АРНАУДОВ К., И.Димитров, П.Йорданов, Л.Лефтеров. Машинни елементи. Техника, София, 1980.
2. CHEVALIER A. Guide du dessinateur industriel. Edition HACHETTE *Technique*, 2004.
3. Corbet J.-Cl., A. Ducruet, L. Huchet. Le CODOTEC, 1996.
4. Prospect SCHNEEBERGER, 2012.

ANALYSIS OF WORKING OF NOVEL PUMPS

Sunny Narayan[1],

Faculty of Mechanical engineering ,Indus International University , India [1]

1. Introduction

Engines are common sources of power for many devices. many of these engines are very complex and need high levels of technological support for operation[1-6]. This paper focuses on the design, construction and operation of a simple device which can pump water and can be easily made without need for complex tools. these devices can be powered from simple combustion or directly from solar energy. The liquid piston fluidyne device which is simple form of a stirling engine uses the fluctuating pressure is to pump fluid . A simple proto type of this pump has been made and tested. basic theory of the device is also discussed and future recommendations made to improve current design.

2. Problem discussion

A liquid piston engine is a novel engine working on Stirling engine cycle.[7] A gas confined in a closed space expands when heated and contracts on cooling. This expansion and contraction can be used generate pressure Fluctuations which can be used to do useful mechanical work. The working of this pump is reviewed in next section of this work. Initially piston is at central and gauge is neutral indicating equal pressures on both sides. When gas present in hot end of arrangement expands, it pushes piston towards extreme left and moves towards cold end by means of connecting tube increasing pressure at cold end as indicated by gauge. As the gas comes in contact with cold end, it contracts and pressure falls hence pushing piston towards extreme leftend. Figures 1-3 indicate this operation.

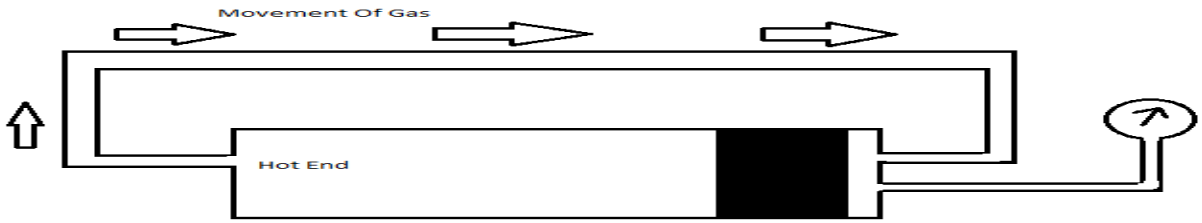

Figure 1-Neutral phase

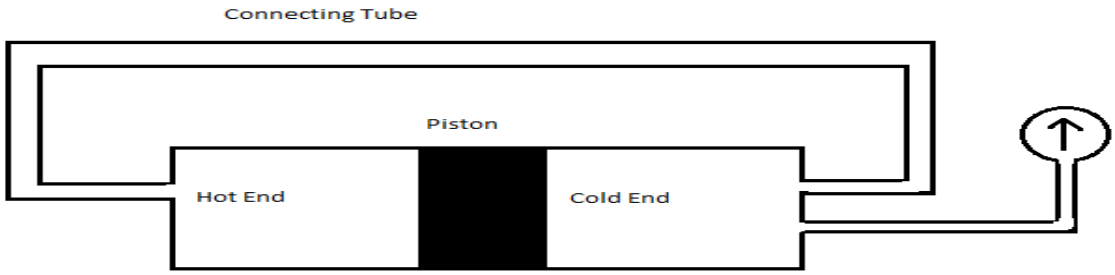

Figure 2-Expansion phase

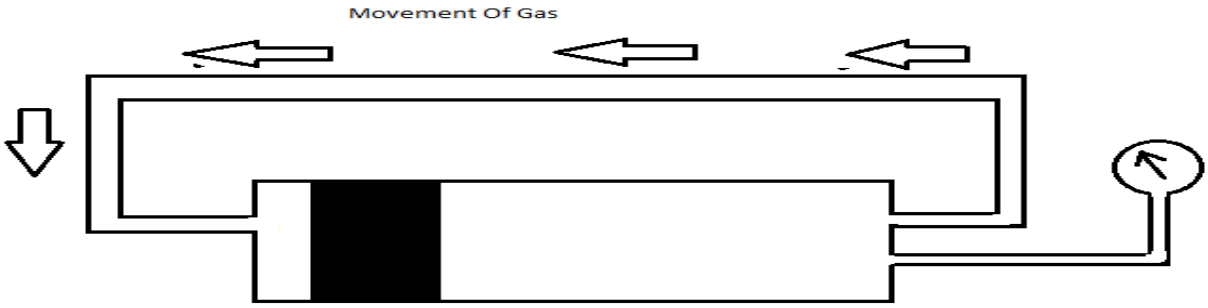

Figure 3-Contraction phase

3. Methodology

The main purpose of this work is to develop a competencies model for an effective performance of maintenance managers A test rig was designed and developed to gather more information about working of fluidyne engine. This setup used a displacer pipe of 45cm length(L) and 1.2 cm in diameter(D). Pumping line used had 15 cm height (H)& 0.78 cm in diameter(d). Methanol spirit was used as a fuel to heat up hot end. A typical lay out of system is shown in fig 4.

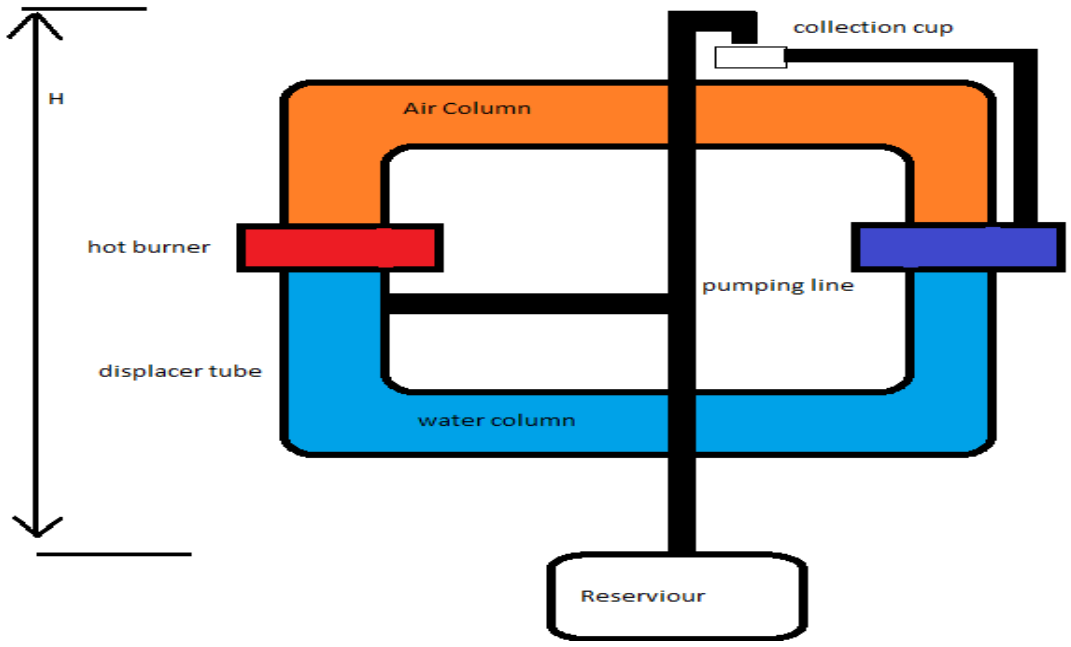

Figure 4-Experimantal setup

Frequency of oscillations was found to be 1.57Hz .Volume of water pumped from pumping column is given by Q:

$Q=A\sqrt{2gH}= 8.19cm^3/s = 8.19\times10^{-6}m^3/s$

Power needed to pump water $=\rho \times Q \times g \times H$

$=1000 \times 8.19\times10^{-6}\times 9.8 \times 0.15 = 0.012$ W

Further thermocouple and a manometer was used to record the temperatures and pressures in hot air column. Values of these can be seen in table no 1.

Table 1-Variations of pressure and temperature

Pressure (mm of Hg)	Temperature (K)	Time (s)
720	296	0
980	298	300
910	300	320

1210	302	340
910	305	360
1360	307	380
760	309	400
1440	311	420
740	313	440

3. Conclusion

Temperature & pressure in the air column rises with time as air gains more and more heat from the burning fuel as seen from values in table no 1,.Peak values of pressure was found to be around 1400 mm of mercury , whereas the peak temperature was found to be around 39°C indicating poor heat transfer to the air. In order to improve heat transfer the air column can be covered with an insulation material. Further in order to improve the heat transfer rate, bigger columns can be used so that more mass of air is able to gain heat from the burning fuel. Commercial form of such fluidyne engines can be developed by using solar energy as source of heat to create pressure oscillations, thus pumping ground water from a certain depth.

References

[1]http://www.saylor.org/site/wp-content/uploads/2011/01/Nervous-System.pdf

[2]http://soils.stanford.edu/classes/ges175items/lect-3_water_visual.pdf

[3] http://thevirtualheart.org/3dpdf/Heart_3d.pdf

[4] http://puretecwater.com/resources/basics-of-reverse-osmosis.pdf

[5] http://www.menet.umn.edu/~vandeven/ConfPaper-Developments%20Towards%20a%20LP%20Stirling%20Engine.pdf

[6]http://ftp.demec.ufpr.br/disciplinas/TM106/FK_AO_Final.pdf

[7] C. D. West, Liquid Piston Stirling Engine, Van Nostrand Reinhold, New York, 1983.

DEFECTS DETECTION IN GEAR USING DIRECT SPECTRUM ANALYSIS OF VIBRATION

ОБНАРУЖЕНИЕ ДЕФЕКТОВ В ЗУБЧАТОМ КОЛЕСЕ, ИСПОЛЬЗУЯ АНАЛИЗ ПРЯМОГО СПЕКТРА ВИБРАЦИИ

Dr.sc. ing. Litvinov D., Mg.sc. ing. Priževaitis A.,
Liepaja Affiliate – Riga Technical University, Latvia

Abstract: *This article provides a way to detect fatigue cracks in welded gearwheel at reinforcement dimensional cutting mechanism (flying shears) of rolling mill by analyzing the direct spectrum of vibration. This method is progressive and allows through regular vibration measurements to assess equipment condition and predict performance.*

Keywords: *FLYING SHEARS, ROLLING MILL, MONITORING, DIRECT SPECTRUM, SENSOR, VIBRATION DIAGNOSTICS.*

1. Introduction

Modern industry development produces the promoted requirements to reduction gearboxes reliability. Therefore on most industrial enterprises, possessing some park of gearboxes the vibration monitoring and diagnostics systems are implemented. Different firms can make these systems, which could have different configuration, but task for them one is looking after a working equipment, to expose the already present defects of gearing (basically gears, gearwheels, rolling bearings and journal bearings), and also to make the equipment capacity prediction.
Machines and equipment condition monitoring is one of the most effective methods to decline accident rate and increase technical systems reliability. For the reduction gearboxes vibration monitoring is very important, because in the process of condition irreversible change there always is a chain of defects and even one of them really changes the equipment vibration background.
The monitoring and diagnostics systems can be both stationary and portable. Functionally these systems do not differ practically. A difference is only in mobility. Application of these systems is gives another very important advantage: due to these systems, equipment repair conducted now on the real condition only.
Using the monitoring and diagnostics systems could easy to detect fatigue cracks in welded gearwheel at reinforcement dimensional cutting mechanism (flying shears) of rolling mill by analyzing the direct spectrum of vibration. This method is progressive and allows through regular vibration measurements to assess equipment condition and predict performance.

2. Nature of gear's vibration

The most frequently used diagnostic parameters of parallel-shaft reduction gearbox is shown in Table 1. [1] Table1.

Nr.	Type of defect	Diagnostic features	
		Vibration direct spectrum	Envelope spectrum of high frequency vibration
1	Pulsation of driving shaft	f_{rot1}, $kf_z \pm f_{rot1}$	kf_{rot1}, $k \leq 3$
2	Pulsation of driven shaft	f_{rot2}, $kf_z \pm f_{rot2}$	kf_{rot2}, $k \leq 3$
3	Distortion of driving gear	$2f_{rot1}$, $kf_z \pm 2f_{rot1}$	$2kf_{rot1}$, $k \leq 3$
4	Distortion of driven gear	$2f_{rot2}$, $kf_z \pm 2f_{rot2}$	$2kf_{rot2}$, $k \leq 3$
5	Teeth defect of driving gear	kf_{rot1}, $kf_z \pm kf_{rot1}$	kf_{rot1}, $k>5$
6	Teeth defect of driven gear	kf_{rot2}, $kf_z \pm kf_{rot2}$	kf_{rot2}, $k>5$
7	Toothing defect or toothing grease defect	kf_z	-
8	Defect of bearing	***RMS*** *increasing (medium frequency* ***MF****)*	*the appearance of shock pulses on* ***MF***
9	Bearing grease defect	*RMS increasing* ***(UHF)***	*the appearance of shock pulses on* ***UHF***

Note: f_{rot1} - rotating frequency of driving shaft, f_{rot2} - rotating frequency of driven shaft, f_z - tooth frequency, ***RMS*** - root mean square vibration, ***MF*** - medium frequency, ***UHF*** - ultra high frequency, $k=1,2,3,4,\ldots$ [1]

3. Industrial vibration monitoring and diagnostics systems.

In world industry is used the enormous amount the rotating equipment vibration monitoring and diagnostics systems of different firms.

2.1. Stationary systems.

The stationary monitoring system is needed above all things for a multimode strength equipment, guided an auxiliary personnel. Exactly personnel errors is more frequent than all are the defects multiplying reason of the guided equipment, which it must find out practically instantly (for a few turns of rotor) for failure timely prevention.
On Figure 1 the simplified structure of the vibration monitoring and diagnostics stationary system is shown.

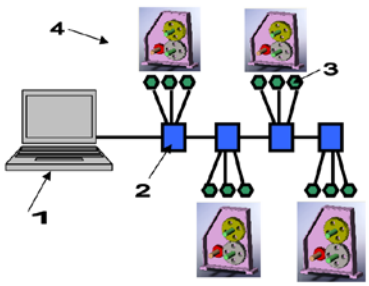

Figure1 *Structure of the vibration monitoring and diagnostics stationary system.*
1 - The computer with special software; **2** - The Signals transformation card in digital form; **3** - Vibration sensors; **4** – Supervising equipment.

2.2. Portable systems.

Equally with the stationary systems wide application is found the portable monitoring and diagnostics systems (Fig. 2), equipped by expert or automatic troubleshooting routines. These systems can be divided into two basic classes are the extended monitoring systems, including with the expert programs, it means, that diagnostics is executed by the prepared expert, and mass diagnostic systems with the standard rotating equipment automatic condition diagnostic and prediction programs. Such system consists of:

- A portable device (devices), providing vibration measuring and analysis in heavy industrial terms;
- Computer with the program of monitoring, containing a database and fulfilling operations row of signals analysis and processing of analysis results;
- Expert or automatic diagnostic program, processing obtained diagnostic information.

***Figure 2**. Vibration portable set on the vibration analyzer СД-21 base, produced by company BACT (Russia) [2]*

4. Description of the equipment which was under control.

Method of fatigue cracks detection in welded gears and gearwheels with the help of the direct spectrum of vibration analysis can be applied in the study of all gears. This method has been tested on flying shear of steel plant's rolling mill.

Flying shears is a machine for cutting the continuous length rolled product that does not require a stop rolling. These shears (Fig.3) are composed of housing, a drive shaft with a driving gear (4) and the working shafts with the driven gear wheels (5 and 6) on which are mounted blades for cutting the reinforcement. Positions 1, 2 and 3 are places for vibration sensors mounting.

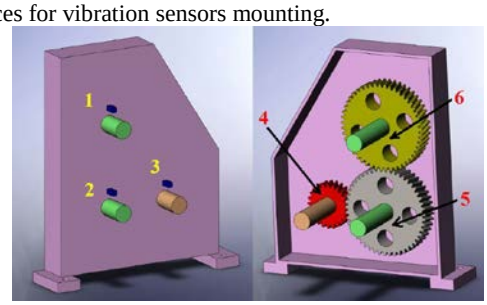

***Figure 3**. The scheme of flying shear under control.*

For a complete research on the state of flying shears, it is necessary to organize the 6 points of vibration control (Fig.4).

***Figure 4**. The scheme of the 6 points of vibration control.*

Reading data from the sensors is occurring remotely. To do this you must create a remote monitoring system (Fig.1)

The most effective way to monitor the status of welded gearwheels is direct spectra of vibration analysis, which is necessary to carry out about once a week.

5. The detection of a fatigue crack in a welded gear

Here is an example of the real detection of a fatigue crack in a welded gear. In comparison are given the spectrums: before appearance of cracks (black graph), when the crack has been formed (red graph) and after repair (blue graph) (Fig.5).

Since a crack formed in the top gearwheel, and the spectra are also obtained at the control point #5.

The direct spectrum (Fig.5), was obtained under the following conditions: measuring units: dB (A); cutoff frequency: $F_b = 800\,Hz$; spectrum lines - 1600 averages - 8.

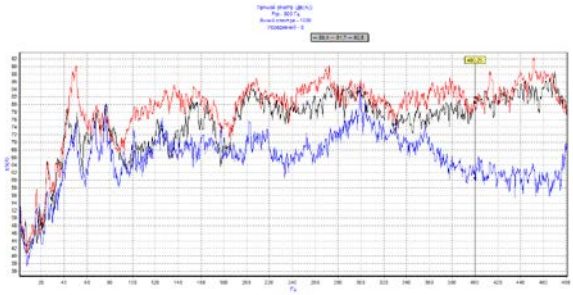

***Figure 5**. Direct spectrum – (dB(A)), $F_b = 800Hz$, Spectrum lines: 1600, Averages: 8.*

As seen from obtained direct spectrum, the red spectrum (corresponding to the already formed crack) has a clear excess of the level ranges from 40 to 180 Hz, from 240 to 280 Hz, from 330 to 390 Hz and so on.

In order to reduce the probability of error, it is necessary, after detecting a deviation in the spectrum, to conduct repeated measurements. And only on the basis of repeated measurements, to make conclusions about the state of the equipment.

One of the cracks, which was detected by analyzing the direct spectrum of vibration shown in Fig.6.

***Figure 6.** The photo of the real welded gearwheel, with the cracks. As can be seen, due to this method, was sufficiently prevented a serious accident and were spared a lot of resources.*

Conclusions

Vibration diagnostics of metallurgical or any rotating equipment is very important. This makes it possible to significantly reduce the costs of the equipment, to extend the term of its operation, as well as improve the quality of products. The company must have a diagnostic service that provides vibration monitoring and forecasting the state of the equipment. It is also necessary to establish the system of remote monitoring equipment. The cost of equipment and software for the diagnosis is usually recouped within a year at its regular use.

Literature

[1] Барков А.В., Баркова Н.А., Азовцев А.Ю., Мониторинг и диагностика роторных машин по вибрации. – Санкт Петербург: Изд. Центр СПбГМТУ, 2000. -159 с.

[2] http://www.vibrotek.ru/russian/

STUDYING ROTATIONAL MOTION OF LUFFING BOOM CRANES WITH MAXIMUM LOAD USING SIMULATIONS

Prof. Doci Ilir, PhD.[1], Prof. Hamidi Beqir. PhD.[1]
Faculty of Mechanical Engineering –University of Prishtina, Kosovo [1]

Ilir.doci@hotmail.com

Abstract: *Luffing Boom Cranes are type of cranes used for load carrying in building sites. They have complex structure with big dimensions and mechanisms. Their working usage is high. Main cycles of the work of Luffing Boom cranes are: lifting and lowering the working load, Boom luffing – upwards and downwards, rotation around vertical axes, and (if mobile type) translational movement forward and backwards. In this work, we are going to study the work of this crane while rotating with full loading. Study will be done using simulations with computer applications. The aim is to see the effects of dynamic forces and moments in the crane's main parts - metal construction, cables, and constraints during rotational work cycle, particularly at the start and end of the rotation. Also interest is to study the effects of load swinging in crane's stability. For this purpose, we modeled with software entire luffing boom crane. Crane is modeled from standard manufacturer, as a common model of luffing boom Crane.*

Keywords: LUFFING BOOM CRANE, ROTATIONAL MOTION, OSCILLATIONS, MODELING, SIMULATIONS

1. Introduction

The type of Crane taken for study is Liebherr 540 HC-l2 [2]. Properties of crane are: Length of the Boom - 60 m. Mass of the Boom – 140 t. Length of Mast – 53 m. Mass of mast – 160 t. Max carrying load Q_{max} = 6.6 t = 6600 kg . Crane rotation-angular speed: ω=0.6 rot/min. This is single rotational speed given by manufacturer [4].

During the rotation, crane's boom is in position at ψ = 15° with horizontal. There will be no luffing motion, nor lifting of load. Length of hoist cables is 20.5 m. Length of luffing cables is 20.7 m. Length of restraint cables is 28 m.

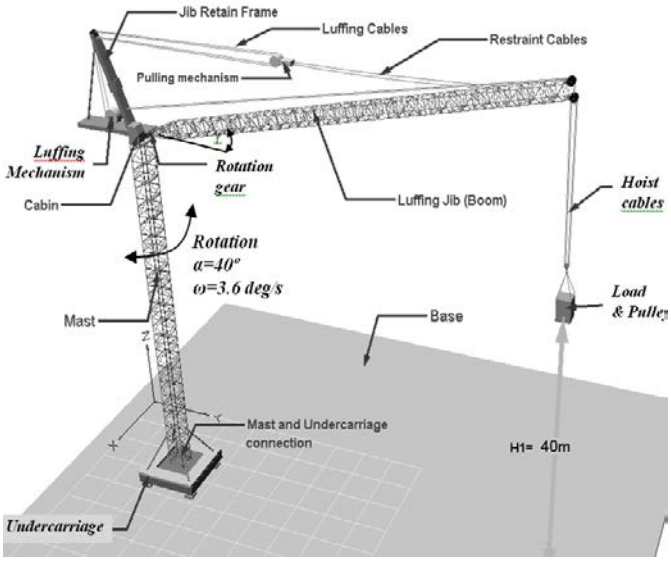

Fig.1. *Model of luffing boom crane*

Before simulations, weight Q (work load) is in the position of relative rest at the height H1=40 m (Fig.1). Simulation will be done for crane rotation with angular speed: ω=0.6 rot/min = 3.6 deg/s. Rotation will be simulated for angle of 40°. Simulation has three phases [3],[5]:

First phase – initial position of relative rest with no motion. Load hangs on hoist cables. Starts at time 0 s <t < 1s.

Second phase – process of active rotation with speed ω=0.6 rot/min = 3.6 deg/s. Starts after first phase, between time 1 s <t < 14s.

Third phase - rotation stoppage. Crane will stop rotating, but load, pulley and hoist cables will continue to swing. Starts after second phase, between time 14 s < t < 20 s.

This form of simulation scenario is close to real work of crane and best for achievement of reliable results. All the graphs in this paper have time in second on horizontal axes, and in vertical axes they have studied component in their basic units, depending on the parameter studied.

2. Results of force (tension) in restraint cables

This is the force acting on restraint cables resulting from weight of boom, load hanging and swinging during crane rotation. There are 4 cables. Restraing and luffing cables lifts up or lowers the Boom, but for the case of rotation they carry the boom, load and lifting mechanisms (Fig.1). They are considered most loaded part of crane [3]. Dynamic forces that appear on these cables come from load swinging, hoist cables and boom oscillations. The diagram of tension force in these cables is shown in Fig.2.

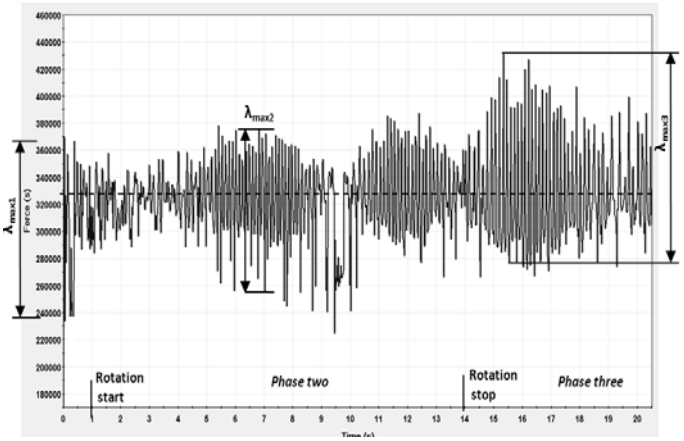

Fig 2. *Graph of Tension force on one of the Luffing cables – during Boom upwards motion*

Based on graph in Fig.2, medium value of tension force is F_{med} = 323000 N that is close to static value of force [3],[5], needed for calculation of dynamic coefficient [1],[2].

Phase one of the process – relative rest of Boom and load which is carried between times 0< t <1 s gives values of force that are dynamic in nature. Max value of force in this phase is F_{c1} = 362000 N. Value of amplitudes of force is high $\lambda_{max2} = (3.62\text{-}2.415)\cdot 10^5$ = 120500 N. Maximal frequency of oscillations is υ = 7 Hz. Phase one is usually called "load stabilization phase", before active motion.

Phase two – active rotation period - process of crane rotation is carried between times 1 s< t <14 s. Maximum value of the tension force is F_{c2} = 388000 N, in time t = 12.5 s. Value of max amplitude is $\lambda_{max2} = (3.888\text{-}2.765)\cdot 10^5$ = 112300 N. Maximal frequency of oscillations is υ = 9 Hz.

Phase three – rotation stoppage, between time 14 s< t <20 s. In this phase are achieved highest results of dynamic parameters for tension force. Maximum value is F_{c3} = 432000 N, in time t = 15.4 s. Value of max amplitude is λ_{max2} = (4.32-2.77)·10^5 = 155000 N. Maximal frequency of oscillations is υ = 9 Hz.

Based on comments above, and Fig.2, we can conclude that highest dynamic values of force are in phase three, after stoppage rotation. In this phase are received maximal values of oscillations, and amplitudes.

If we find the ratio between max value of dynamic force gained from results (fig.2) and medium value of force, we can calculate dynamic coefficient [1],[2],[4]:

$$\Psi = \frac{F_{dynamic}}{Fstatic} = \frac{432000}{323000} = 1.337$$

This concludes that value of dynamic force is higher that of static force for 33.7%. This needs to be taken in when calculating cables and selection of safety factors for cables that will be implemented on these cranes.

Based on literature [2], for cranes with boom and class H1, value of dynamic coefficient is Ψ = 1.3. This means that value of tension force should not exceed F_c < 323000*1.3 = 419900 N. This value is complied in most of rotation process until t < 14.5 s, from Fig.2. But after this time value of Ψ exceeds three times, in t1 =15.4s, t2 = 16.1 s and t3=16.2 s. This is a matter of concern that requires attention.

Conclusion is that restraint and luffing cables are heavily loaded with oscillations that results in high amplitudes and high number or frequencies.

3. *Force in the rotation gear between upper platform and boom*

This connection is important part of these cranes for determining dynamic effects in crane's metallic construction. The gear is the motion mechanism and connection between two main parts. In fig. 4 is shown the graph of resultant force for the case of rotation.

Dynamic occurrences that appear come from load swinging, cables and boom oscillations, and thereafter will be passed to mast and basement. Results that will be required are resultant force F_{rmax} = $\sqrt{F_x^2 + F_y^2 + F_z^2}$ in this connection which is a restraint (Fig.3).

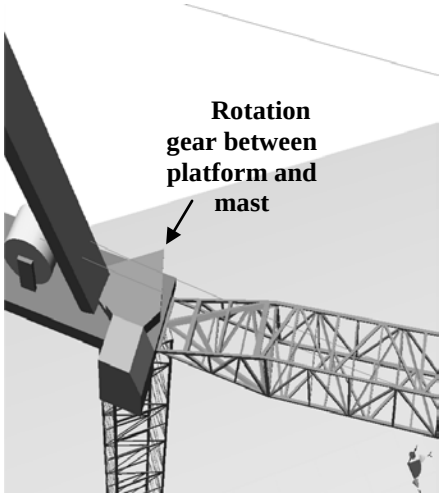

Fig.3. *Rotation gear between platform and mast*

Based on results in graph from Fig 4, we can conclude that curved line shows heavy dynamic nature of process that occurs in rotation gears. Value of max amplitudes are spread on entire graph (process), mainly during rotation period 8 s < t < 14 s, and after rotation stoppage 14 s < t < 15 s. Only after time t ≈ 17 s, oscillations have tendency of dropping down.

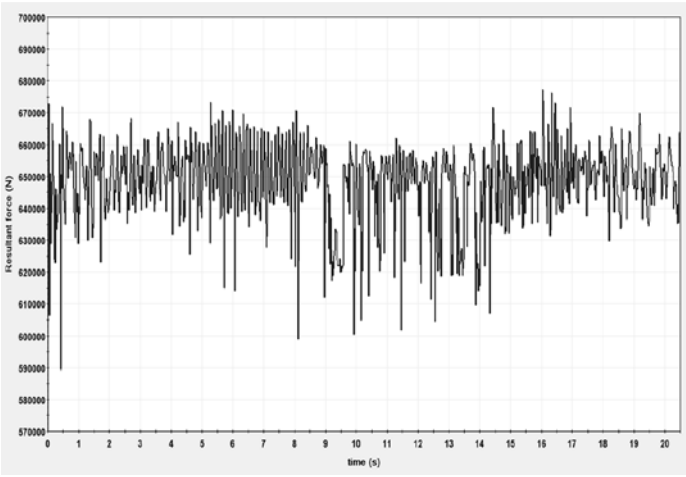

Fig.4. *Graph of Resultant force in the rotation gear of upper platform and mast during rotation*

Medium value of resultant force is F_{rmed} = 650000 N, which is close to static value. Maximum value of the resultant force is F_{rmax} = = 678000 N, in time t = 16.4 s. This value is gained after rotation stoppage. Compared to value of medium force, it is an increase of 4.3%. This is less than dynamic force - tension in restraint cables.

Max value of the frequency of oscillations is υ = 12 Hz, which occurs at time 6 s < t < 7 s. This is higher than frequency of restraint cables (υ = 9 Hz) for 33.3%.

4. *Force and momentum in the connection of mast and undercarriage*

These parameters are important for studying resultant force and momentum (torque) at the bottom of vertical mast and undercarriage and are important for studying stability of crane. This connection is a constraint that connects mast and basement of crane (fig. 5). Dynamic occurrences that appear here are passed from rotation gear and mast.

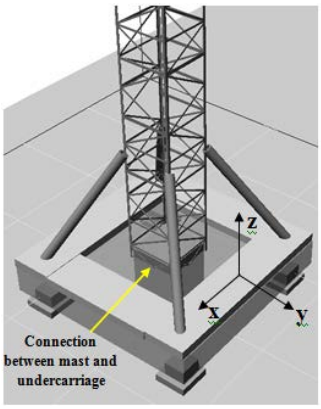

Fig.5. *Undercarriage and mast with local coordinative system*

In fig. 6 is shown the graph of resultant force for the case of rotation. Based on results from fig.6, we can conclude that graph shows heavy dynamic nature that occurs in bottom mast. Value of max amplitudes are spread on entire graph (process), mainly during active rotation between time 5 s<t<9 s, and after rotation stoppage 14 s<t<15 s. only after time t ≈ 18 s, oscillations have tendency of dropping down.

Medium value of resultant force is F_{rmed} = 806000 N, which is close to static value. Maximum value of the resultant force is F_{rmax} =

843000 N, in time t ≈ 17.2 s. this value is reached after rotation stoppage. Compared to value of medium force, it is an increase of 4.6%. This is close to dynamic force in rotation gear (paragraph 3). the curve of resultant force from fig.6 is similar to fig.4 of rotation gear. This proves that forces at bottom mast are directly passed from rotation gear through mast frame. max value of the frequency of oscillations is υ = 12 Hz, which occurs at time 6 s < t < 8 s.

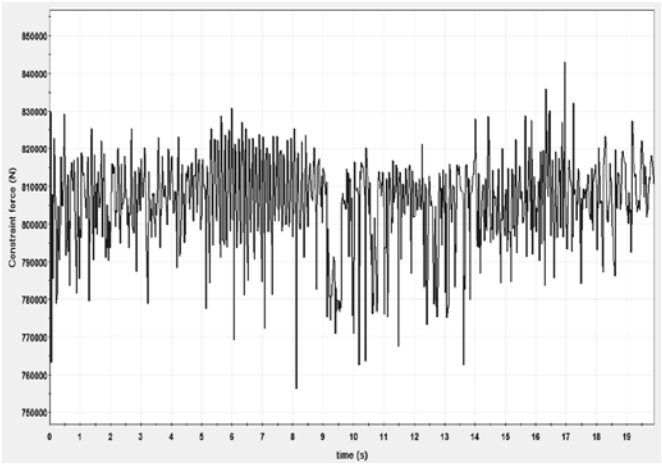

Fig.6. *Graph of resultant force in the constraint between mast and undercarriage*

In fig. 7 is shown the graph of momentum (torque) for the case of rotation. This is important parameter for calculating crane's stability from overturning. There are 4 curves shown in graph: three for each local axes of mast, and forth is resultant torque M.

Based on results from graph in fig.7 we can conclude that curved line shows heavy dynamic nature of moments-torque with high frequencies and oscillations that occurs in bottom mast, which are being passed to undercarriage and basement of crane. medium value of resultant torque is M_{rmed} = 8500000 Nm, which is close to static value.

Oscillations of torque around **y axes** are low at the beginning of rotation until t < 9 s, and almost with constant value close to static value. after time t > 9 s, values of torque increase (in negative value) due to rotation. oscillations also increase, with increasing amplitudes and frequencies that reach up to υ = 10 Hz. amplitudes of torque can reach up to $\lambda = -(6.2\text{-}4.2)\cdot 10^6 = -2\cdot 10^6$ Nm.

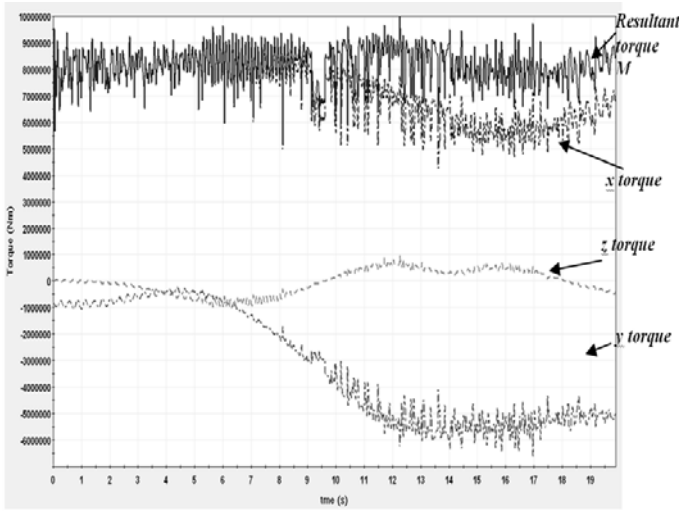

Fig.7. *Torque (momentum) in the constraint between mast and undercarriage*

Oscillations of torque around **x axes** are of high dynamic nature from start to the end of rotation process. Frequencies reach up to υ = 12 Hz (6 s<t<7 s). Amplitudes of torque can reach up to $\lambda = (9\text{-}5)\cdot 10^6 = 4\cdot 10^6$ Nm. This value is double higher than the value around **y axes**. This concludes that crane undergoes higher dynamic forces and moments around its **x axes,** compared to values around y axes and z axes. Oscillations of torque around **z axes** are of lower dynamic nature than other two previous cases. This means that moments around vertical z axes have little influence on crane.

Maximum value of the resultant torque $M=\sqrt{M_x^2+M_y^2+M_z^2}$ is M_{max} ≈ 10000000 Nm, in time t ≈ 12.5 s. This value is achieved during phase two, but it occurs only once. Most of extreme values of torque are around M_{max} ≈ 9200000 Nm. Compared to value of medium torque, it is an increase of 8.3%.

5. *Swinging of load and pulley*

Pulley system with load is main system that passes swinging and oscillations through cables on the metal construction of crane. Pulley with load and their according local coordinative system are shown on fig.8. On fig.9 are given swinging and oscillations of load based on local coordinate axes y (full line) and axes x (dotted line) from fig.8. Oscillations and swinging are measured in degrees (º). Based on figure 9, swinging of load reaches maximum values around **y axes** with max angle β_y ≈ -11.578º in time t≈12 s, and around **x axes**, with max angle of swinging β_x = 11.37º in time t ≈ 21 s.

Amplitude of swinging increases in time due to the swinging of load. Max amplitude of load swinging is $\lambda_{deg(max)}$ = 24º - (-24º) = 48º, between time 4 s< t <12 s. Swinging of load is best parameter for measuring influence carried from working load to the metal construction of crane. Simulation is carried until t = 26 s.

Based on literature [2], angle of load swinging should not exceed 15º. Maximum vale that we got is β ≈ -11.578º. If we consider wind on boom cranes, it should be added 3 % of load, or value of resultant force [2]. This concludes that crane will have no stability issues resulting from load swinging, even with a presence of wind.

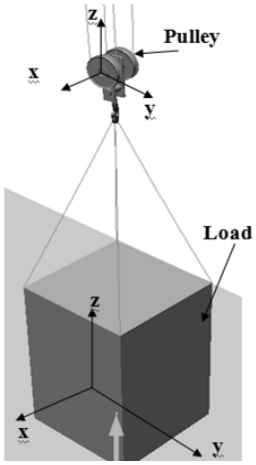

Fig.8. *Load and pulley. Local coordinate system of load*

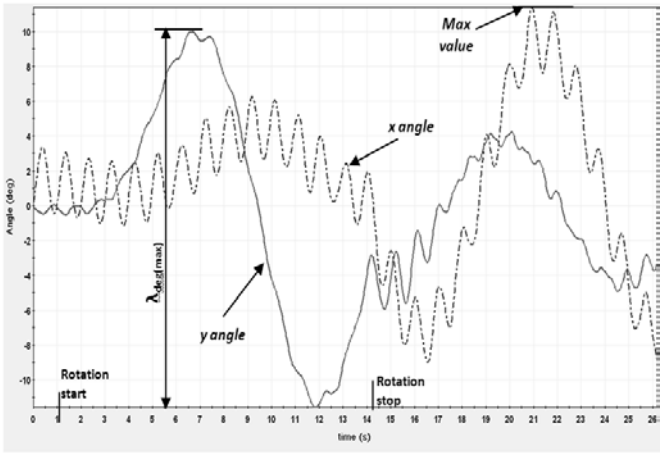

Fig.9. *Graph of Swinging of working load around **y axes** and **x axes***

6. *Conclusions*

Studying rotational motion of luffing boom cranes proved the dynamic nature of this process. Applying simulations with software [6] is a good method to find crane's acting dynamic forces, and determining dynamic stability. These forces and moments should be calculated for each major part and constraint, as it is done in this paper, in order to have best picture of occurrences in machine parts and components, in this case on luffing boom cranes. Main issues of crane rotation are intensive oscillations with high frequency and high amplitudes, mostly with irregular occurrence.

Results are shown for some crucial parts of these cranes, and they are commented for each case. Most complex work periods are motion start and stoppage. Most of crane metal parts can handle dynamic occurrences, based on their material and properties [4] and tables in literature [2],[1]. But in some cases, like tension force in restraint cables, the values gained exceeds the limitations, which are matter of concern. These oscillations, that might be difficult to measure with actual instruments can explain causes of stability problems, parts failure and materials fatigue. They are mainly induced by load swinging that produces forces in hoist cables, boom, mast and other parts. Influence in crane's stability have oscillations of other cables in crane, also oscillations of metallic construction and motion of mechanisms.

Based on these conclusions, proper restraints in crane basement should be done with high priority in order to prevent crane overturning. Speed of rotation should be kept as lower as possible, in order to minimize negative effects of load swinging, strain on parts of crane and problems with safety.

7. *References*

[1] Dresig, Hans, *Shwingungen mechanischer Antriebssysteme, Modellbildung, berechnung, analyse, synthese,* Sprenger Verlag, Berlin, 2001, p.66-68.

[2] DIN Taschenbuch 44, Krane und Hebezeuge 1, Beuth, 1995, DIN 15018 Teil 1, page 262-264.

[3] Ilir Doçi, Blerim Morina, *Studying luffing motion of boom on construction cranes while carrying load using simulations,* 18th International Research/Expert Conference,TMT 2014.

[4] https://www.morrow.com/sites/default/files/datasheets/540-HCL-12.pdf

[5] Ilir Doçi, Beqir Hamidi, Bujar Huruglica, *Analysis of translational motion of gantry crane with full loading using simulations,* 3rd International Scientific Conference on Engineering, MAT 2014, Mostar, Bosnia & Herzegovina.

[6] MSC VisualNastran 4D User Guide, MacNeal-Shwendler Corporation, Santa Ana, 2003.

ИЗСЛЕДВАНЕ НА ВЪЗМОЖНОСТТА ЗА МОДЕЛИРАНЕ И ИЗПОЛЗВАНЕ НА КОЕФИЦИЕНТ НА ПРЕДАВАНЕ НА УДАРНАТА СИЛА ПРИ УДАР НА ТВЪРДО ТЯЛО С ГУМЕН БУФЕР

INVESTIGATION OF THE POSSIBILITY FOR MODELING AND USING THE IMPACT FORCE TRANSMISSION COEFFICIENT AT AN IMPACT OF A RIGID BODY WITH A RUBBER BUFFER

Доц. д-р инж. Митев Н. Ал.
Технически университет – Габрово, България

E-mail: mitev_n@tugab.bg

Abstract: *On the basis of an experimental investigation of the impact of a rigid body with a rubber buffer, the experimental data obtained for the distribution of the impact force for the time of the impact (impact impulse) on the free front face, receiving the impact and the obtained reaction in the area of fixture of the buffer for the time of the impact and with the help of numerical investigation with them the possibility for modeling and using the impact force transmission coefficient has been investigated. The basic model's parameters have also been determined.*

Keywords: IMPACT, IMPACT FORCE, VISCOELASTIC IMPACT, RUBBER BUFFER, VISCOELASTIC BUFFER

1. Увод

Изследването на удара на твърдо тяло с гумен буфер и неговото моделиране е свързано с решаването на редица частни проблеми като: изследване и моделиране на материалните свойства на буферите, изследване и моделиране на вълновото движение на маса в буферите, изследване на процеса на дисипация на част от енергията на удара, изследване и моделиране на основните параметри на ударния процес и др. Един от основните въпроси за които често се търси решение е въпросът какво е силовото въздействие в мястото на закрепване при използване на гумени буфери за защита на крановите метални конструкции от недопустими по големина ударни сили, възникващи при аварийни ситуации. Сложността на проблема се състои в това, че вследствие на вълновото движение на маса в буфера, ефектът на наслагване на вълновия фронт на падащата и отразена вълна и в зависимост от съотношението на масите на удрящите се тела, реакцията в мястото на закрепване на буфера може съществено да се отличава от възникващата при удара сила върху свободната челна повърхнина от буфера (както като разпределение на ударната сила за времето на удара, така и като пикова стойност).

Моделирането на въздействието на ударната сила в мястото на закрепване на буфера при удар на твърдо тяло с гумен буфер с помощта на коефициент на предаване на ударната сила е един от най-преките пътища за практическо решаване на проблема, както за целите на анализа на ударния процес, така и при инженерни пресмятания.

Целта на настоящата работа е да се изследва възможността за използване на коефициент на предаване на ударната сила в мястото на закрепване при удар на твърдо тяло в гумен буфер и се определят основните моделни параметри.

2. Предпоставки и начин за решаване на проблема

Обект на изследване са 8 броя гумени буфери с цилиндрична форма с размери ф32х38, изработени от различни по вид каучукови смеси.

Въз основа на натурен експеримент на удар на твърдо тяло с гумен буфер са получените данни за разпределението на ударната сила въздействаща върху свободната челна повърхнина - $F_2(t)$, както и данни за разпределението на реакцията $F_1(t)$ в мястото на закрепване на буфера към тяло с коравина и маса приети за безкрайно големи .

Измерванията са направени с помощта на надлежно тарирана измервателна техника, а всички числени обработки и експерименти са проведени с помощта на потребителски програми на MathCAD с използване на потребителски и вградени функции на системата. Представените в доклада резултати са за един от изследваните буфери – S2, изработен от гума марка М531а. За останалите изследвани буфери се получават сходни резултати.

3. Числени експерименти. Резултати и дискусия

Получените данни за реакцията на силата в мястото на закрепване (запъване) $F_1(t)$ и ударното въздействие върху свободната челна повърхнина на буфера $F_2(t)$ са представени на фиг.1.

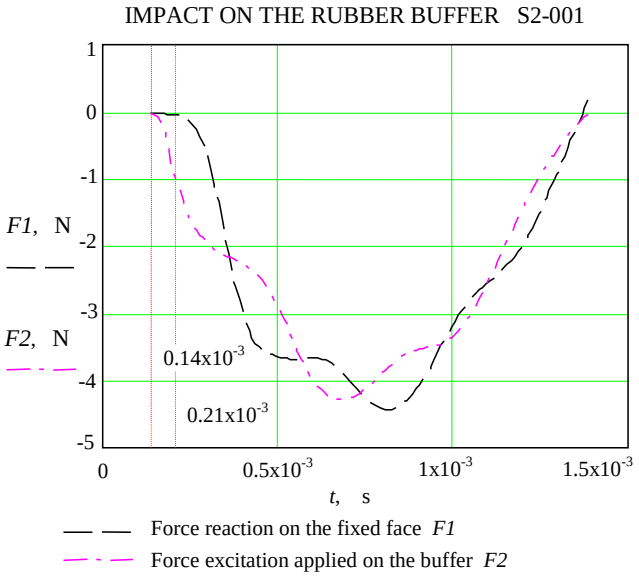

Фиг. 1. *Удар на твърдо тяло с гумен буфер. Ударна сила F2 върху свободната челна повърхнина на буфера и реакцията и в мястото на закрепване F1.*

За постигане на поставената цел използваме честотната област. Както за всяка реална механична система и в случая имаме пълна симетрия в спектъра, като използваме тази за реални положителни стойности на честотата. Прилагаме дискретна фуриерова трансформация (DFT) над масивите със стойности на ударната сила $F_2(t)$ и реакцията в мястото на закрепване $F_1(t)$. Сформираме нов масив представящ отношение на функцията на спектрална плътност (спектъра) на ударната сила $F_2(f)$ и функцията на спектрална плътност (спектъра) на реакцията в мястото на закрепване на буфера $F_1(f)$.

Съществува формална аналогия между отношението $F_2(f)/F_1(f)$ и механична система със съсредоточени параметри с една степен на свобода (SDOF) – елемент на Келвин. За дефинирането на параметрите на последната се използва най-често отношението на преместването на маса и силовото въздействие което го предизвиква в честотната област - $X(f)/F(f)$. И при двете функции (отношения) се наблюдават редуващи се зони на резонанс и антирезонанс. И въпреки, че аналогията е формална (зоните на резонанс при отношението на спектрите на двете сили съответства на зони на антирезонанс при отношението на спектрите на преместването и предизвикващото го силово въздействие) тя може да бъде използвана за дефиниране на коефициент (или функция) на предаване на ударната сила.

На фиг. 2 и фиг. 3 са представени графики на функциите на спектрална плътност на силите $|F_2(f)|$, $|F_1(f)|$ и $|F_2(f)|/|F_1(f)|$. На фигурите се наблюдават и двата резонанси пика, които са определящи за поведението на системата в наблюдаваната част от спектъра. Използвайки отляво и отдясно на всеки от резонансните пикове прозоречни функции “Hanning ги отделяме в самостоятелни информационни масиви. На фиг. 2 е показан и селектирания първи резонансен пик около резонансната честота – 1240.5 Hz, а на фиг. 3. селектирания втори резонансен пик за резонансната честота 1890.6 Hz.

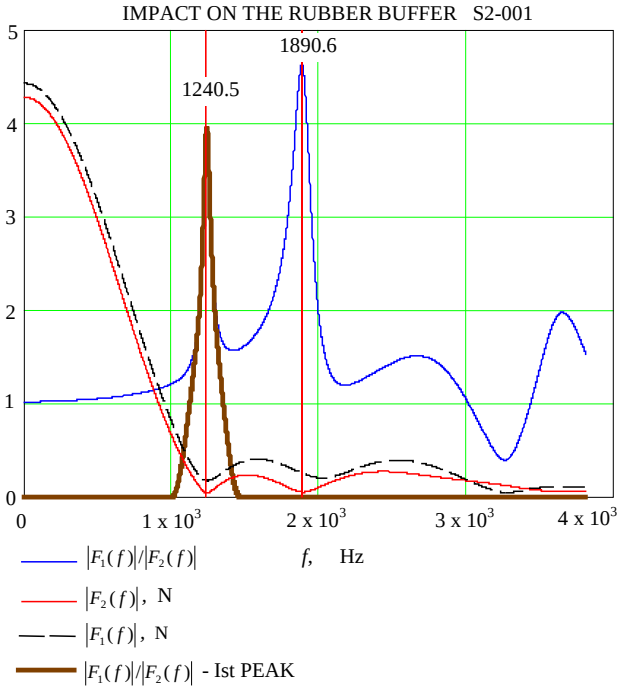

Фиг. 2. *Удар на твърдо тяло с гумен буфер. Функция на спектралната плътност на ударна сила -$|F_2(f)|$, функция на спектралната плътност на реакцията в мястото на закрепване $|F_1(f)|$, функция $|F_1(f)|/|F_2(f)|$ и селектирания с помощта на прозоречна функция “Hanning” I резонансен пик.*

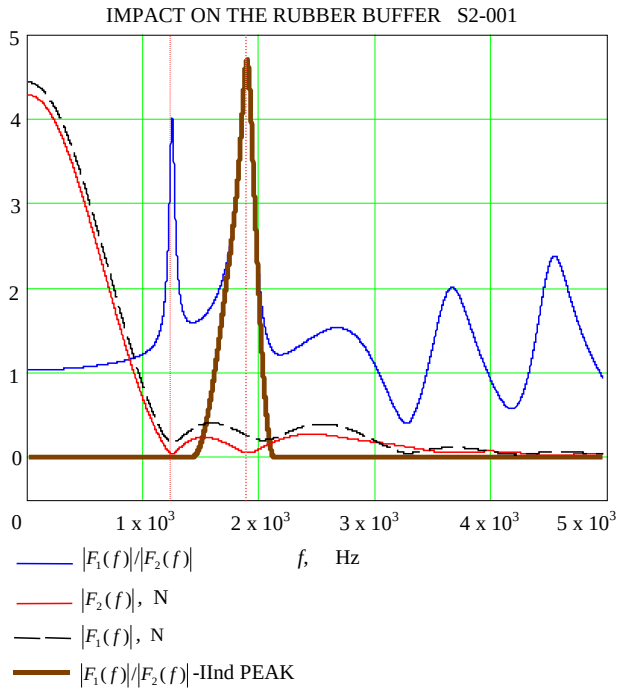

Фиг. 3. *Удар на твърдо тяло с гумен буфер. Функция на спектралната плътност на ударна сила -$|F_2(f)|$, функция на спектралната плътност на реакцията в мястото на закрепване $|F_1(f)|$, функция $|F_1(f)|/|F_2(f)|$ и селектирания с помощта на прозоречна функция “Hanning” II резонансен пик.*

Като първо приближение приемаме, че имаме система със слабо демпфиране, т.е., че демпфираната честота е приблизително равна на недемпфираната.

За пресмятане на коефициента на демпфиране по отношение на първия резонансен пик определяме честотната лента съответстваща на 3 dB от лентата на пропускане

За пресмятане на коефициента на демпфиране по отношение на първия пик определяме честотната лента съответстваща на 3dB от лентата на пропускане и първата резонансна честота f_1, непосредствено от фиг. 4, която за целта е преизчислена в dB, използвайки вградената функция “Trace”.

$f_1 = 1240.5\ Hz$ е демпфираната резонансна честота за I^{ви} пик.

$$\Delta f_{3dB} = 1270.3 - 1213.1$$

$$\Delta f_{3dB} = 57.2\ Hz$$

Скоростта на затихване с помощта на зависимостта

(1) $$\sigma_1 = \pi \,.\, \Delta f_{3dB}$$

$$\sigma_1 = 179.7\ \ rad/s$$

Коефициентът на демпфиране за първия резонансен пик се определя със зависимостта

(2) $$\zeta_1 = \frac{\Delta f_{3dB}}{2 f_1}$$, или също така

(3) $$\zeta_1 = \frac{\sigma_1}{2\pi \,.\, f_1}$$

$$\zeta_1 = 0.023055$$

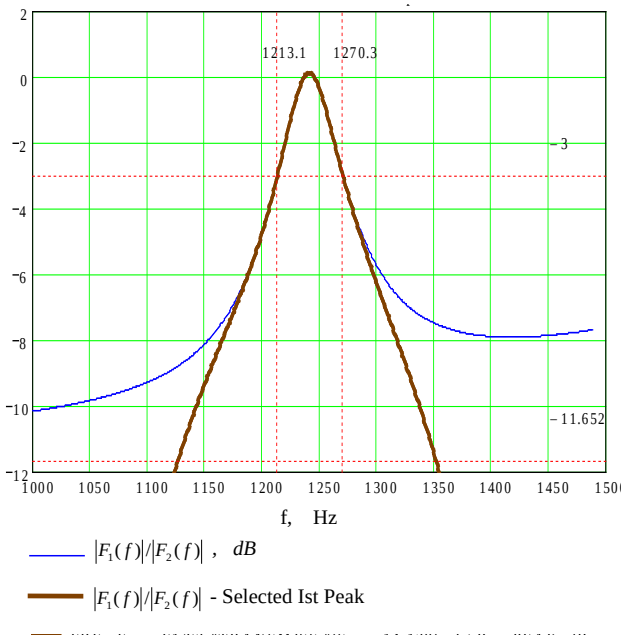

Фиг. 4. *Удар на твърдо тяло с гумен буфер. Определяне на граничните честоти и честотната лента съответстваща на ниво* Δf_{-3dB} *за първия резонансен пик.*

За пресмятане на коефициента на демпфиране за II[ри] резонансен пик използваме графиката показана на фиг. 5 и правим подобни пресмятания.

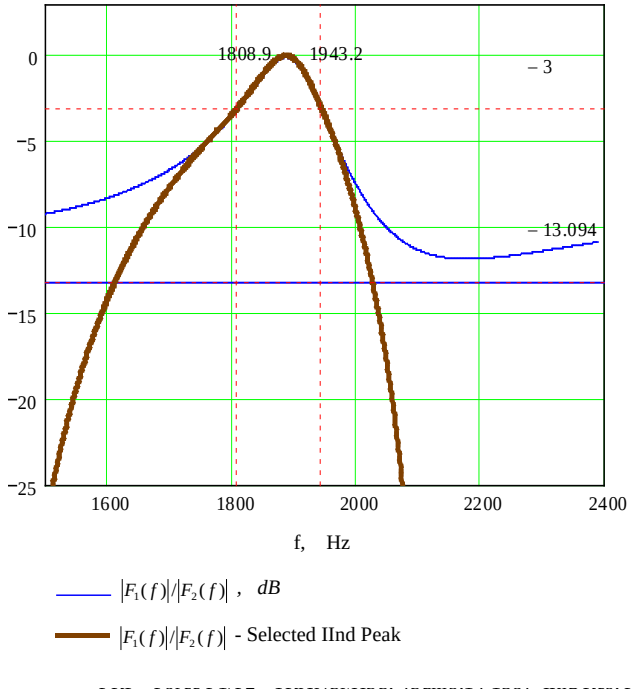

Фиг. 5. *Удар на твърдо тяло с гумен буфер. Определяне на граничните честоти и честотната лента съответстваща на ниво* Δf_{-3dB} *за втория резонансен пик.*

$f_2 = 1886.4\ Hz$ е демпфираната резонансна честота за II[ри] пик.

$$\Delta f_{3dB} = 1943.2 - 1808.9$$

$$\Delta f_{3dB} = 134.3\ Hz$$

Скоростта на затихване по отношение на втория резонансен пик съответно е

$$\sigma_2 = \pi \,.\, \Delta f_{3dB}$$

$$\sigma_2 = 421.92\ \ rad/s$$

Коефициентът на демпфиране

$$\zeta_2 = \frac{\Delta f_{3dB}}{2 f_2},$$

$$\zeta_2 = \frac{\sigma_1}{2\pi \,.\, f_2}$$

$$\zeta_2 = 0.035597$$

4. Заключение

Въз основа на проведените натурни експерименти при удар на твърдо тяло с гумен буфер S2 и числено експериментиране с тях, могат да бъдат направени следните изводи:

1. Изменението на ударната сила, приложена върху свободната челна повърхнина възприемаща удара $F_2(t)$ се различава съществено от реакцията в мястото на закрепване $F_1(t)$ на буфера, както по времето на възникване, така и като амплитудна стойност.

Закъснението при възникване на реакцията (при дадената дължина и плътност на буфера) е с около 7 ms. Закъснението при възникване на пиковата стойност за двете сили е около 13 ms;

2. Предложено е моделиране на коефициент на предаване на ударната сила (с помощта на каскадно свързани елементи на Келвин) и използвайки честотната област са определени основните моделни параметри.

5. Литература

[1] Гольдсмит В. Удар – теория и физические свойства соударяемых тел. М., Изд. Л-ры по строительству, 1965, 448с.

[2] Лавендел Э. Э., Абросимов Г. Э. Решение задачи об ударе абсолютно жестким телом по вякоупругому стержню конечной длины. Всесоюзная Н. Т. конференция по методы расчета вискоэластичных материалов. Рига, 1977, 156 с.

[3] Митев Н. Аналитично изследване поведението на образци от вискоеластични материали подложени на импулсно външно въздействие. trans & MOTAUTO' 06, Варна;

[4] Митев Н. Аналитично определяне на свободните надлъжни колебания на образци от вискоеластични материали вследствие от импулсно външно въздействие. trans & MOTAUTO' 06, Варна;

[5] Митев Н. Изследване удара на твърдо тяло с гумен буфер (Моделиране на материалните свойства и ударния импулс) Трета международна научно техническа конференция „Техника. Технологии. Образование. Сигурност", В. Търново, 2015 г.;

ЧИСЛЕНО ЕКСПЕРИМЕНТИРАНЕ ЗА МОДЕЛИРАНЕ НА НЯКОИ ЕНЕРГО-СИЛОВИ ПАРАМЕТРИ ПРИ УДАР НА ТВЪРДО ТЯЛО С ГУМЕН БУФЕР ПРИ СФЕРИЧНА ФОРМА НА СВОБОДНАТА ЧЕЛНА ПОВЪРХНИНА ВЪЗПРИЕМАЩА УДАРА

NUMERICAL INVESTIGATION FOR MODELING OF SOME ENERGY-FORCE PARAMETERS AT AN IMPACT OF A RIGID BODY WITH A RUBBER BUFFER WITH SPHERICAL SHAPE OF THE FREE FRONT FACE RECEIVING THE IMPACT

Доц. д-р инж. Митев Н. Ал.
Технически университет – Габрово, България

E-mail: mitev_n@tugab.bg

Abstract: *On the basis of the experimental data obtained from a natural experiment of an impact on a set of geometrically similar rubber buffers with different radii of the spherical front face receiving the impact and a numerical experimenting with them, basic energy-force dependences have been determined. Relevant conclusions have been made.*

Keywords: IMPACT, IMPACT FORCE, VISCOELASTIC IMPACT, RUBBER BUFFER, VISCOELASTIC BUFFER

1. Увод

Гумените буфери са елементи на безопасността използвани във всички области на машиностроенето за защита на елементи от конструкции от недопустими стойности на ударната сила. Характерна особеност на тяхното функциониране е, че между удрящите се тела за относително кратко време се извършва енергиен обмен с високи енергийни нива, като определена част от енергията на удара се разсейва в околната среда във вид на топлина. Вълновото движение на маса в буфера и дисипативните свойства на материалите, от които те се изработват спомагат за интензификацията на този процес. Буферите се изработват като прави тела с конична, цилиндрична, призматична или пирамидална форма, като челната повърхнина най-често е равнинна. Конструирането на буфери с не плоска челна повърхнина води до промяна на параметрите на ударния процес и трудности при тяхното изясняване и моделиране.

На буферите с не плоска челна повърхнина и техните характеристики са посветени ограничен брой публикации. Известно е, че буферите от изследвания в тази публикация вид са много по ефективни при най-ниски нива на енергийно натоварване, като при високи нива ефективността им намалява и е по-ниска от тази на буферите с плоска челна повърхнина.

Обект на изследване са шест броя гумени буфери с конична форма, с разлика в радиуса на сферичната челна повърхнина между двете гранични стойности - R=40 до R=∞ (т. е. плоска повърхнина).

Цел на настоящата работа е да се изследват основни параметри на гама геометрично подобни гумени буфери със сферична челна повърхнина, като се предложи апроксимация на зависимостта на максималната динамична сила от енергията на удара, зависимостта на максималната динамична сила от деформацията (динамичната коравина) и оцени влиянието на радиуса на челната повърхнина.

2. Предпоставки и начин за решаване на проблема

Представените в този доклад резултати са получени с помощта на числени експерименти над база данни, получена с помощта на натурен експеримент на удар при стъпално изменение на енергията на удара. Изследваните буфери са от гума марка M531A. Всички числени експерименти са проведени в среда на MathCAd с помощта на потребителски програми и при използване на някои вградени в ситемата функции.

3. Решаване на проблема. Резултати и дискусия

За апроксимация на зависимостта на максималната динамична сила $F_{din\_\max}$ от енергията на удара е експериментирано с различни по вид зависимости, като най-добри резултати са получени при използване на зависимостта:

$$F_{din\_\max} = AE^b, \quad (1)$$

където E е енергията на удара в J.

Стойностите на коефициентите A и b, както и достигнатите коефициенти на корелация са представени в табл.1, а резултатите от апроксимацията са показани на фиг. 1.

Табл. 1. Стойности на регресионните параметри при апроксимиране на $F_{din\_\max}(E)$ ***с помощта на зависимостта (1).***

ВИД БУФЕР	*A*	*b*	Коеф. на корелация *r*
RB_R040	406.75	0.6094	0.99996
RB_R060	439.17	0.6116	0.99993
RB_R080	452.91	0.6117	0.99993
RB_R100	486.64	0.6025	0.99999
RB_R120	530.01	0.5828	0.99993
RB_RINF	693.83	0.5248	0.99997

При гумени буфери със сферична челна повърхнина зависимостта на максималната динамична сила от деформацията (динамичната коравина) има ясно изразен нелинеен характер. Линейна апроксимация е възможна единствено за буфер RB_RINF с плоска челна повърхнина и то при значително отклонение от експерименталната крива.

Експерименталните криви представящи зависимостта на максималната динамична сила от деформацията и опитът за линеаризация при буфер с плоска челна повърхнина са

представени на фиг. 2. Коефициентът на корелация в този случай е $r = 09971$.

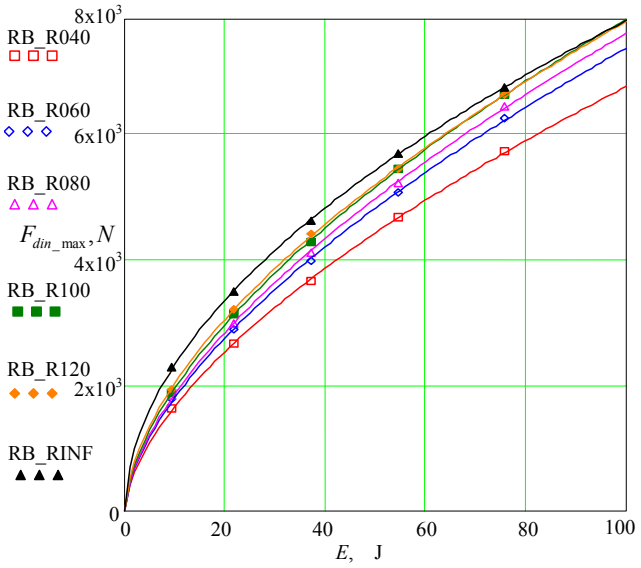

Фиг. 1. *Резултати от числен експеримент за апроксимация на зависимостта на максималната динамична сила F_{din_max} от енергията на удара със зависимостта (1) за конусни гумени буфери със сферична челна повърхнина с радиуси R=40, 60, 80, 100, 120 и R=INF (плоска челна повърхнина)*

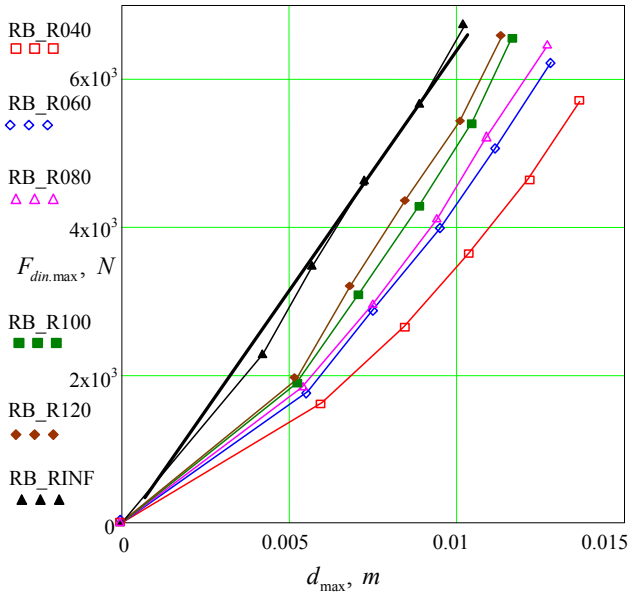

Фиг. 2. *Експериментални криви представящи зависимостта на максималната динамична сила F_{din_max} от деформацията (динамичната коравина) и резултът от опита за линеаризация на същата за гумен буфер с плоска челна повърхнина. Конусни гумени буфери със сферична челна повърхнина с радиуси R=40, 60, 80, 100, 120 и R=INF (плоска челна повърхнина).*

За апроксимиране на зависимостта на максималната динамична сила от деформацията (динамичната коравина) е използван полином от втора степен т.е. зависимостта (2), с която са постигнати много добри резултати. Резултатите от числените експерименти със зависимостта (2) са представени таблично в табл.2 и графично за всеки от изследваните буфери на фиг. 3...фиг.9.

(2) $F_{din\_max} = A_1 + A_2 . d_{max} + A_3 . d_{max}^2$.

Табл. 2. Стойности на регресионните параметри при апроксимиране на $F_{din\_max}(d_{max})$ с помощта на уравнение (2).

ВИД БУФЕР	A_1	A_2	A_3	Коеф. на корелация r
RB_R040	5.603	$1.528 . 10^5$	$1.920 . 10^7$	0.99995
RB_R060	-13.406	$2.214 . 10^5$	$2.087 . 10^7$	0.99979
RB_R080	-9.553	$2.258 . 10^5$	$2.260 . 10^7$	0.99981
RB_R100	-7.017	$2.231 . 10^5$	$2.912 . 10^7$	0.99964
RB_R120	-27.642	$2.624 . 10^5$	$2.832 . 10^7$	0.99884
RB_RINF	-30.439	$5.293 . 10^5$	$1.305 . 10^7$	0.99922

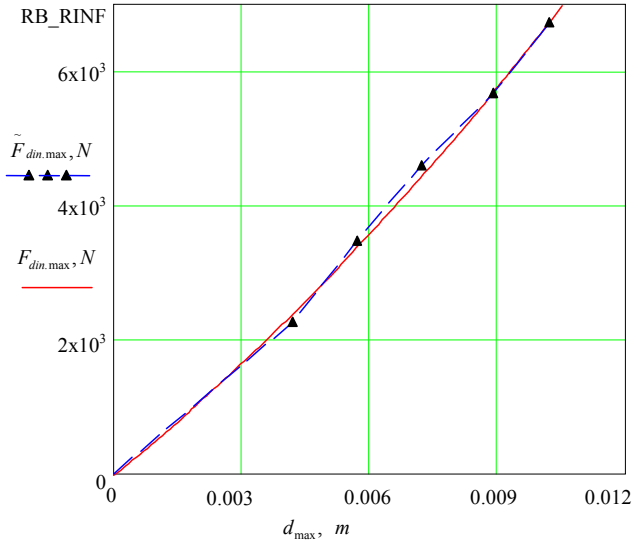

Фиг. 3. *Експериментална крива представяща зависимостта на максималната динамична сила от деформацията (динамичната коравина) $\tilde{F}_{din\_max}(d_{max})$ и апроксимиращата я със зависимостта (2) крива $F_{din\_max}(d_{max})$ при гумен буфер с плоска челна повърхнина (Буфер RB_RINF.)*

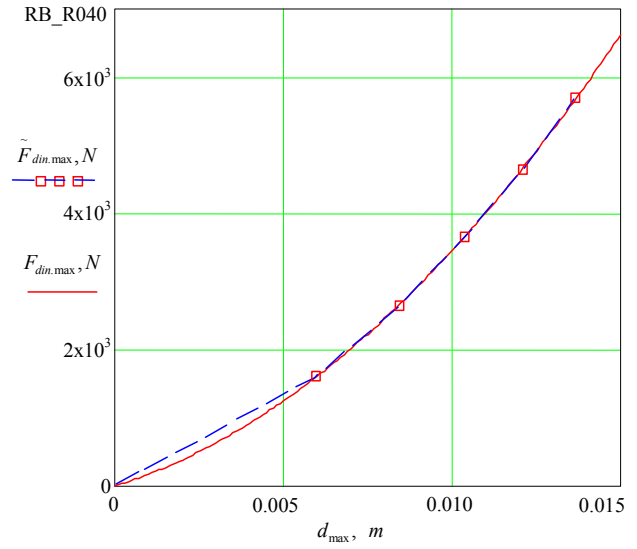

Фиг. 4. *Експериментална крива представяща зависимостта на максималната динамична сила от деформацията (динамичната коравина) $\tilde{F}_{din\_max}(d_{max})$ и апроксимиращата я със зависимостта (2) крива $F_{din\_max}(d_{max})$ при гумен буфер с радиус на сферичната челна повърхнина R=120mm (Буфер RB_R120).*

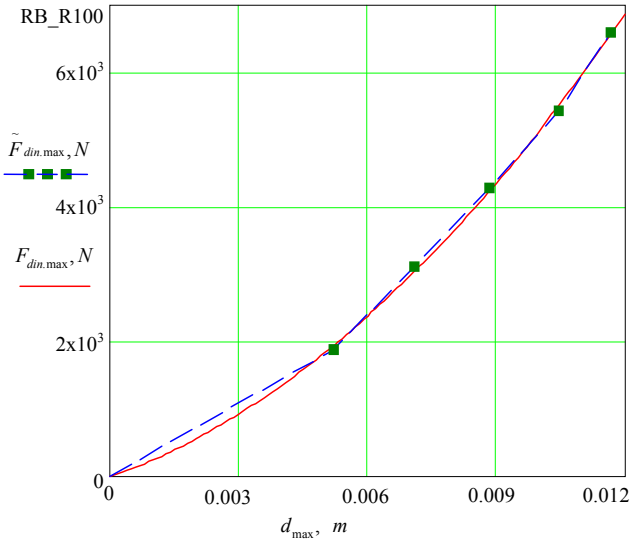

Фиг. 5. *Експериментална крива представяща зависимостта на максималната динамична сила от деформацията (динамичната коравина)* $\tilde{F}_{din\_max}(d_{max})$ *и апроксимиращата я със зависимостта (2) крива* $F_{din\_max}(d_{max})$ *при гумен буфер с радиус на сферичната челна повърхнина R=120mm (Буфер RB_R100).*

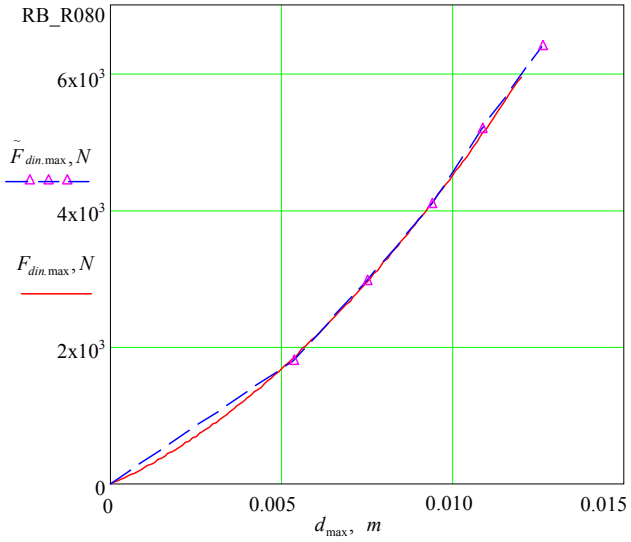

Фиг. 6. *Експериментална крива представяща зависимостта на максималната динамична сила от деформацията (динамичната коравина)* $\tilde{F}_{din\_max}(d_{max})$ *и апроксимиращата я със зависимостта (2) крива* $F_{din\_max}(d_{max})$ *при гумен буфер с радиус на сферичната челна повърхнина R=120mm (Буфер RB_R080).*

Експерименталните точки в графиките на фиг. 1 ... фиг. 8 са получени при начална скорост на удара съответно: 0; 0.612; 0.914; 1.211; 1.464 и 1.757 m/s, като стойностите са свързани с особеностите на използвания стенд.

Друга основна характеристика на изследваните буфери е зависимостта на продължителността на ударния импулс от радиуса на сферичната челна повърхнина, възприемаща удара при различни нива на енергийно натоварване. Резултатите от това изследване са показани в табличен вид в табл. 3. Графика на зависимостта на τ_{IMP} от R е показана на фиг. 9.

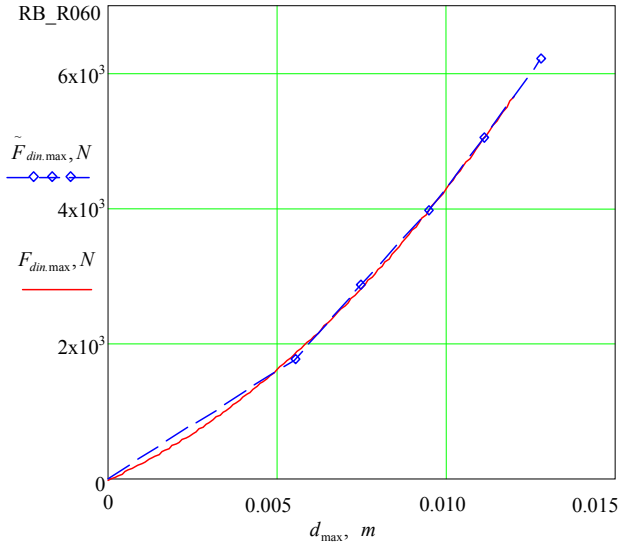

Фиг. 7. *Експериментална крива представяща зависимостта на максималната динамична сила от деформацията (динамичната коравина)* $\tilde{F}_{din\_max}(d_{max})$ *и апроксимиращата я със зависимостта (2) крива* $F_{din\_max}(d_{max})$ *при гумен буфер с радиус на сферичната челна повърхнина R=120mm (Буфер RB_R060).*

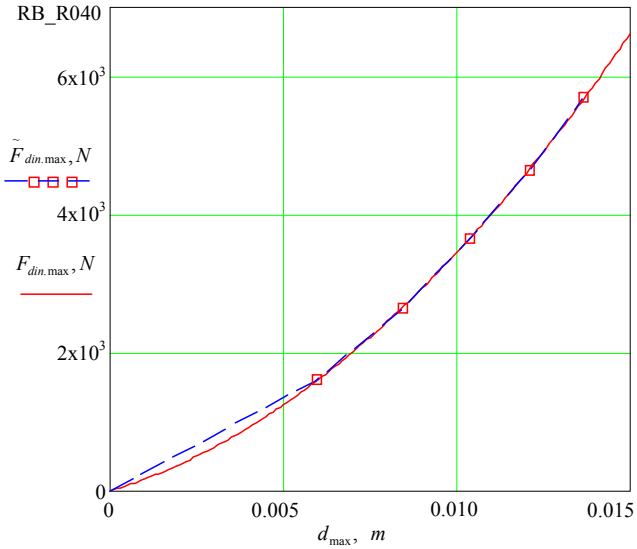

Фиг. 8. *Експериментална крива представяща зависимостта на максималната динамична сила от деформацията (динамичната коравина)* $\tilde{F}_{din\_max}(d_{max})$ *и апроксимиращата я със зависимостта (2) крива* $F_{din\_max}(d_{max})$ *при гумен буфер с радиус на сферичната челна повърхнина R=120mm (Буфер RB_R040).*

Табл. 3*. Числени стойности на продължителността на ударния импулс* τ_{IMP} *от радиуса* R *на челната повърхнина, възприемаща удара при различни стойности на енергията на удара:*
1. E1=9.42J, 2. E2=21.76J, 3. E3=37.07J, 4. E4=54.54J, 5. E5=75.80J

R	$\tau_{IMP\ E1}$	$\tau_{IMP\ E2}$	$\tau_{IMP\ E3}$	$\tau_{IMP\ E4}$	$\tau_{IMP\ E5}$
40	0.0311	0.0290	0.0274	0.0263	0.0253
60	0.0285	0.0260	0.0250	0.0241	0.0235
80	0.0278	0.0257	0.0246	0.0235	0.0228
100	0.0267	0.0244	0.0233	0.0226	0.0216
120	0.0260	0.0236	0.0225	0.0220	0.0209
200	0.0216	0.0201	0.0197	0.0198	0.0195

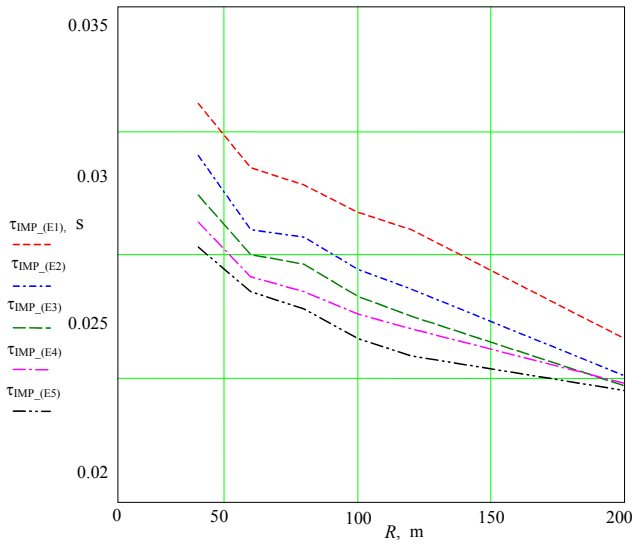

Фиг. 9. *Експериментални криви представящи зависимостта на продължителността на ударния импулс* τ_{IMP} *от радиуса* R *на челната повърхнина, възприемаща удара при различни стойности на енергията на удара:*
1. E1=9.42 J, 2. E2=21.76 J, 3. E3=37.07 J, 4. E4=54.54 J, 5. E5=75.80 J.

4. Заключение

Въз основа на данните, получени с натурен експеримент на удар на гумени буфери с конична форма и сферична челна повърхнина и числените експерименти проведени с тях могат да бъдат направени следните изводи:

1. Зависимостта на максималната динамична сила от енергийното натоварване $F_{din\_\max}(E)$ на буферите при удар на твърдо с гумен буфер има нелинеен характер за всички изследвани буфери. С намаляване на радиуса на сферичната челна повърхнина възприемаща удара зависимоста на $F_{din\_\max}(E)$ от енергията на удара намалява.

Зависимостта за всеки от изследваните буфери е апроксимирана с помощта на уравнение (1) с достатъчна за инженерната практика точност;

2. Зависимостта на максималната динамична сила от максималната деформация $F_{din\_\max}(d_{\max})$ за всички изследвани буфери има нелинеен характер. Възможна е линейна апроксимация на същата единствено за буферите с плоска челна повърхнина при относително ниски стойности на коефициента на корелация. За буферите със сферична челна повърхнина е възможна частична линеаризация на кривите за относително високите нива на енергийно натоварване.

Зависимостта на максималната динамична сила от максималната деформация $F_{din\_\max}(d_{\max})$ за всички изследвани буфери се апроксимира с достатъчно висока за инженерната практика точност с помощта на зависимостта (2).

3. Определена е и е представена графично зависимостта на продължителността на ударния импулс τ_{IMP} от радиуса R на сферичната челна повърхнина за различни нива на енергийно натоварване. С увеличаване на радиуса τ_{IMP} намалява по нелинеен закон. Получените стойности за продължитеността на ударния импус са за съотношение на масите на удрящите се тела $m_{rb} / m_{buffer} = 88.90$ (за буфер RB_R040).

4. Литература

[1] Гольдсмит В. Удар – теория и физические свойства соударяемых тел. М., Изд. Л-ры по строительству, 1965, 448с.

[2] Дымников С. И., Э. Э. Лавендел, М. А. Павловкис, М. И. Сниегс. Прикладны методы расчета изделй из выскоэластичных материалов. Рига, Зинатне, 1980, 238 с.;

[3] Митев Н., Б. Пенков, С. Петков. Вискоеластични буфери – установяване параметрите на ударния процес. Международна научна конференция UNITECH'05. Габрово, 2005 г., том II, с. II-57 II-62;

[4] Митев Н. Експериментално изследване поведението на образци от вискоеластични материали подложени на импулсно външно въздействие. Trans & MOTAUTO'06, Варна, 2006 г., том III, с. 06…09;

[5] Митев Н. Изследване влиянието на формата на свободната челна повърхнина възприемаща удара върху параметрите на ударния импулс при удар на твърдо тяло с гумен буфер. Trans & MOTAUTO'13, Варна, 2013 г., том II, с. 59…62;

[6] Митев Н. Изследване влиянието на формата на свободната челна повърхнина възприемаща удара при удар на твърдо тяло с гумен буфер върху енерго-силовите. Trans & MOTAUTO'14, Варна, 2014 г., том II, с. 93…95;

[7] Митев Н. Методика за пресмятане на вискоеластични буфери за подемно-транспортни машини. XVIII национална научно-техническа конференция с международно участие - АДП 2009. Созопол, 2009 г., с. 131…136;

[8] Пенков Б., Н. Митев. Определяне коефициентът на възстановяване на скоростите при удар върху буфер. VII Международна конференция по машиностроителна техника и технологии, AMTEX-2003. Варна, 2003 г., кн. №3, с. 202…206;

[9] Пенков Б., С. Петков, Н. Митев. Методика за изпитване на буфери. VII Международна конференция по машиностроителна техника и технологии, AMTEX-2003. Варна, 2003 г., кн. №3, с. 199…202;

[10] Пенков Б., С. Петков, Н. Митев. Стенд за изпитване на буфери. Известия на Технически университет – Габрово, том 28, 2003, с. 26…29;

RESEARCHES 0F THE INHIBITING PROPERTIES OF WATER AND ORGANIC EXTRACTS OF OIL SLIMES

ИССЛЕДОВАНИЕ ИНГИБИРУЮЩИХ СВОЙСТВ ВОДНЫХ И ОРГАНИЧЕСКИХ ВЫТЯЖЕК НЕФТЕШЛАМОВ.

Cand. of tech. science Assoc. prof. Chkhaidze D., Dr. of tech. science, Full prof. Megrelishvili Z., Academy doct. Assist. prof. Loria M.
Shota Rustaveli State University, Batumi, Georgia

Abstract: *Considered are inhibitor properties of the tank oil slime. Physical and chemical characteristics of oil and oil slime are given. Given are the data of tests on corrosive stability in atmospheric conditions and by accelerated anticorrosive method. It is shown that the aqueous and organic extract of the tank oil slime has obviously marked inhibitor properties that allow to recommend them for producing anticorrosive paint and varnish coatings.*
KEYWORDS*: OIL, SLIME, INHIBITORY QUALITIES, PAINT COATINGS.*

1. Introduction

In many enterprises of oil and gas industry the oil slime is multitonnage waste. A great amount of oil waste of various type and structure [1.2] is formed after the production, transportation and refining of oil and gas. Only according to the data of gas branch of "Gasprom" the oily waste constitute about 10.0 thousand tone in 2000 where the share of liquid waste is 70 % and paste like and hard ones – 30 %. The amount of formed waste in some enterprises varies from 578 tone a year to 2510 tone a year [3]. In spite of the variety of existing oil slime they could be divided into three general groups according to the conditions of their forming [1] :

-ground (formed as a result of the oil products spillage on the soil during industrial operations and emergency);

-benthonic (formed at subsidence of petrol floods at the bottom of the water reservoir);

-reservoir type (formed during the storage and transportation of oil products in tanks of various constructions)

The refining of such slimes for utilization generally provides the extraction of oil fraction [2] on the use of oil slime for slime concrete production in highway engineering [4]. All types of oily waste contain substances having inhibiting properties against corrosion. The research of slimes for using them in the production of corrosion-resistant paint coatings or for the improvement of their quality will allow to expand the material base of paint coatings products production and will assist the protection of environment.

2. The goal of the research.

To determine physical and chemical characteristics of tank oil slime of Batumi Oil Terminal and to define inhibitory quality of aqueous and organic extracts with the purpose of their use in a production and for the improvement of quality for corrosion-resistant paint coatings (aqueous, half oily, oily prime coating and enamel)

3. Object and research methods.

Tanks used during the processing and storage of oil products in course of time require scraping as the sedimentation (oil slime) appears at the bottom and on the walls reducing the actual space of a tank and affecting the quality of oil products. Systematic scraping of tanks is done at least once a year depending on the types of oil products. But in some cases the scrapping can be done earlier than the prescribed period because of changing the filled-in oil products in the tank or preparing the tank for systematic or extra repairing works. According to the results of most researches in scrapped oil slimes the oil products, water and mechanical impurities (particles of sand clay and corrosion etc.) relation vary in wide limits: carbons make up 5-9 %, water - 1-52 %, hard impurities - 068-65 %. Because of it, their physical and chemical indexes also vary in wide limits. The oil slime density varies in the limits of 830-1700 kg/m^3, the freezing point from 3^o C to +80^o C. The flash point is over the range from 35 to 120^o C. At ingress of water into oil products the true emulsion as water-oil is formed. The stabilization of this emulsion happens at the expense of natural stabilizers. In most cases the main part of tank slimes is made up of liquid-viscous products with a high content of organic substances, water and some additives of mechanical impurities [1].

Today Batumi Oil Terminal transfer oil from Azerbaijan (Azerilight Crude Oil) and Kazakhstan (Kumkol Crude Oil, Tengiz Grude Oil). In table 1 physical and chemical data of three types of crude oil determined for 6 months of 2011 year are given. The analyses have been carried out in Batumi Laboratory of Georgian branch C B(Intertek Cateb Brett) according to the standards of ASTM [5].

Table 1. Physical and chemical indexes of crude oil

Crude oil	Density at 20 ^{o}C, kg/m3	Water content, %	Mechanical impurities, %	Freezing point, ^{o}C	Sulphur content
Tengiz Grude Oil	790,3	0,05	0,009	-33,0	0,517
Azerilight Crude Oil	846,0	0,18	0,010	-9,0	0,143
Kumkol Crude Oil	827,0	0,27	0,022	+18,0	0,158

At the same period carried were the analyses of oil slime from the storage located on the terminal territory where the tank oil slime from above mentioned types of oil is collected The amount of accumulated slime of 200…2500 tone is the danger for environment. The accumulated oil slime is viscous mass of dark brown colour, with a density 933,1 kg/m^3 at 80^{o}C, water content 13,3 %, freezing point +3,0^o C ,mechanical impurities 0,443 % and sulphur structure 0,257 %.

For the definition of the possibilities for using such slime for the production of corrosion- resistant paint coatings the research of inhibitor quality of the given TOS is carried out. For this purpose the water extract TOS was prepared. (100 gr. of oil slime was being boiled in 1 litre of water for one hour)

After freezing the water extract was filtrated and used for performing accelerated corrosion - resistant tests [6]. For comparison the corrosive inhibitor "Malkor" (technical condition 2415-004-56478541-06) and distilled water were used. Corrosion of the plates was valued visually according to the size of the corroded surface of the plates.

The organic extract of the oil slime was got by the extraction of TOS (tank oil slime) with organic solvent (toluene, xylol). The weight 100 gr of TOS was taken and 1 L. of organic solvent was added. The mixture was allowed for 24 hours. The produced extract in various proportions was added into the known paint varnish enamel ГФ-927 (ТУ 6-10-662-95).

The samples covered with enamel were tested for corrosion-resistant both in atmospheric conditions and by accelerated corrosion-resistant method in 3 % sodium chloride solution. As an example the steel plates of mark CT 08 (steel 08) and size 100 x 150 mm were used. The plates were covered both by clean enamel ГФ-927 and enamel with added various amount of organic extract of TOS. The relationship for paint varnish compositions are given in table 2.

Table 2. *Paint varnish composition structure*

#	Enamel ГФ-927 mas. %	Organic extract TOS, mas. %
1	100	-
2	98,0	2
3	95,0	5
4	93,0	7
5	90,0	10

The duration of the test in atmospheric condition lasted 24 months but by the accelerated method - 60 days. Corrosive damage was defined according to the changes of mass of the samples (ГОСТ 17322-71).

4. Result and discussion

The received data given in figure 1 show that the water extract of TOS has obvious inhibitory quality against corrosion. From the researches [7] done earlier, the qualities of TOS could be used for the production and for the improvement of anticorrosive qualities of paint coatings.

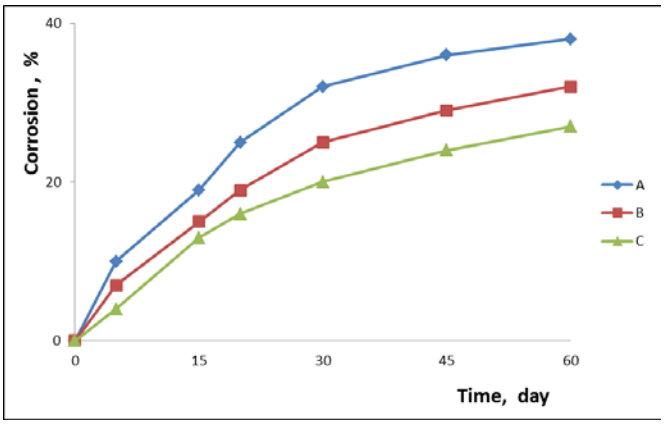

Fig.1 *The corrosion resistance of steel CT 08 (st.08) in distilled water (A), water extract of tank, slime (B) and in the solution of inhibitor corrosion (C).*

In oil refineries the waste is formed after contact cleaning of transformer oil by synthetic aluminosilicate adsorbent-adsorbent oil slime (AOS). It is the product of adsorbent regeneration caught by wet scrubbers.

The AOS consists of 90-94 % aluminosilicate and 5-8 % of petroleum coke consisting of the mix of high condensate aromatic hydrocarbon and naphthenes. Carried out was the work on researching AOS and on its base the technology for the production of anticorrosive ground compositions and underpaints [7] was developed. The inhibitory quality of water extract AOS is given in figure 2. In table 3 the developed ground compositions on the base of adsorbed oil slime are provided but in table 4, accordingly, the results of anticorrosive tests are provided. It is obvious from the tables that composition IV has the best corrosion-resistant qualities. The received primers with the use of AOS have improved characteristics in comparison with similar paint varnish materials [7].

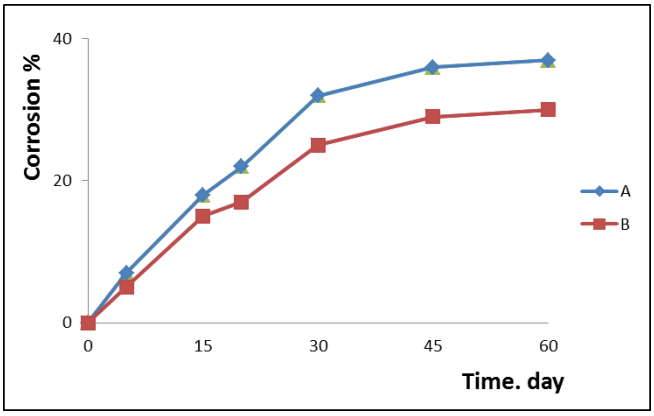

Fig.2 *Corrosion resistance of the steel G 08 (st.08) in distilled water (A) and in water extract of adsorbed oil slime (B).*

Table 3. *The structure of water-soluble primer on the base of dispersive polyvinylacetate (DPVA) [7]*

Primer components	Structure of components mas.%				
	I	II	III	IV	V
DPVA	25,0	20,0	15,0	10,0	5,0
AOS (adsorbed oil slime)	40,0	45,0	50,0	55,0	60,0
ZPS (zine phosphate slime)	4,0	4,5	5,0	5,5	6,0
SAS (surface active substances)	0,4	0,4	0,4	0,4	0,4
5 %-carboxyl methyl cellulose	2,0	2,0	2,0	2,0	2,0
Water	28,6	28,1	27,6	27,1	26,6

Table 4. *Data of anticorrosive tests of primer structure on the base of DPVA in 3 %. sodium chloride solution [7]*

#	Primer structure according to table 2	Share of steel surface under paint coating covered with corrosion after testing, %
1	Structure I	30,0
2	Structure II	20,0
3	Structure III	15,0
4	Structure IV	5,0
5	Structure V	12,0

The received results on corrosion resistance of paint-varnish compositions on the base of organic extract of TOS are given in table 5.

Table 5. *The data of tests on corrosion resistance in atmospheric condition and by accelerated corrosion-resistant method.*

#	Paint coatings structure table 1	Tests in atmospheric conditions	Tests by accelerated corrosion-resistant method
1	I structure	0,025	0,088
2	II structure	0,022	0,079
3	III structure	0,010	0,067
4	IV structure	0,015	0,075
5	V structure	0,018	0,080

Proceeding from the given data (tab 5) the paint coatings with the organic extract of TOS show the best anticorrosive qualities in all cases. The most effective structure is structure III.

5. Conclusion

Given researches show that the water and organic extracts of tank oil slime have obvious inhibitory qualities that allow to recommend them for using during the production of anticorrosive paint coatings. It not only serves the purposes of environmental protection but also allows to expand the material base of paint coatings production.

References

1. What is oil slime.26.09.2010 http/www.piligrim.selec.ru/news.php?act=news_id&news_id=6 (Russian);
2. Anchugova E.M,. Markarova M.K., Shemelinina T.H.. Efficiency and ecological aspects of using solutions of superficially active agents for dividing phases of mechanical impurities and oil from oil slimes. In the book “Izvestia” of Samara Scientific Centre of Russian Academi of Science, v.11, #1(2), 2009-pp 209-207 (Russian);
3. Problems of placement and utilization of waste in gas industry. “Materials of scientific and technical council ltd. “Gazprom”,Orenburg, 6-9 June 2001 Volume 1 and 2 (Russian)
4. Patent RF RU 2150546 C1, Slimeconcret/ T.I. Shein, S.F. Korenkova, O.M. Klimenkov,pub.06.10.2000, (Russian);
5. ASTM : D.5002, D 4928, D 4807, D 5853, D 4294
6. I.L. Rozenfeld, F.I. Rubinshtein, K.A. Zhigalova. Protection of metals from corrosion by paint coatings. M, “Khimia”,1986-p.222.(Russian);
7. D.T. Chkaidze, Z.N. Megrelishvili, M.D. Loria. Studying of inhibiting properties of tank oil slime for developing

LIGHT STEEL FRAMED CONSTRUCTION AND MODULAR HOMES

Beqir Hamidi, Lindita Hamidi
University of Pristina, Faculty of Mechanical Engineering
Bregu i Diellit, p.n., 10 000 Prishtine - Kosove

Abstract: *One of the greatest benefits when using these alternative building methods to construct affordable homes is the speed of erection. Delivery of units will be maximized while the quality will also be improved. At the moment one of the biggest problems with the RDP houses is the speed of delivery which causes the housing backlog in South Africa. This system has developed into a construction technology that addresses eight key challenges embodied in the low cost and affordable housing shortages facing developing and design tables to aid rapid selection of light steel sections, depending on the span, the loading and the steel grade used.*
KEY WORDS: MODULAR HOMES, FRAMED, TECHNOLOGY, DEVELOPING, DESIGN, CONSTRUCTION.

1. Introduction

These homes must be affordable for households with a median income. In South-Africa more than 60 % of the population falls within this definition. It is not a new realisation though. After the 1994 transition to democracy, it was very important to stabilise all housing provisioning. To overcome the fragmented housing regime with its skewed racial focus and to immediately start delivery. The all ANC's Reconstruction and Development Programme (RDP) stated that there was a lack of adequate housing and basic services in rural settlements and urban townships and that it had reached a point where severe changes had to be made. The ANC also endorsed 'Housing as a human right' and this made one of the RDP's priorities to provide for the homeless. In the last four years and average of 250 000 subsidised houses were built every year. The National Housing Finance Corporation (NHFC) and the banking sector's R42-billion Financial Service Charter commitment to the low income housing market has helped to provide houses through innovative access to housing finance. While a lot of houses where delivered, a problem became apparent between the competing demands of affordability and quality of the delivered houses. Corruption levels were also rising and became very serious. Little attention was given to the areas in which these homes were being built in respect to the supporting social and economic infrastructure. One very important aspect of this housing incentive is to increase its delivery over the next few years. "Reaching the target of 500 000 new housing opportunities requires funding of R345-billion by 2014, if we integrate the delivery of infrastructure and basic services. We are lobbying for a one-off injection to the budget to kick-start the process of boosting housing delivery," Housing Minister, reported (February 2008) [3]. The National Department of Housing (NDH) developed a plan called the Development of Sustainable human settlements, also known as Breaking New Ground (BNG), through which the government aims to ensure that every citizen has access to permanent housing that provides protection and access to basic services. One of the BNG's objectives is to get rid of all informal settlements by 2014.

2. Low moderate houses

RDP houses are at the lowest level of the affordable housing market, but the shortage also exists in more expensive, but still affordable houses (those costing less than R200 000). The Banking association reported that there is a shortage of 625 000 affordable houses in Kosovo. At the moment 17 000 units are being supplied a year, while 132 000 houses is needed to reduce the shortage by 60% in the next 5 years. The banks committed themselves to provide R42-billion worth of housing finance to low-moderate income households. If there aren't enough houses for households to buy, they won't need loans and the banks won't meet their targets. An analysis was done for the city of Johannesburg demonstrating the skewed housing delivery patterns that occurs notwithstanding the distribution of household affordability for housing. The table shows the number of units delivered per type in Johannesburg, versus the percentage of the population for whom such housing was affordable. The population is skewed towards the bottom of the income pyramid delivery is skewed towards the top end [5].

Table1: Housing delivery according to monthly income.

Monthly household Income category	**% population (Johannesburg)**		**Housing type affordability (indicative)**	**Number delivered in 2004**	**% of total delivery**
>R10 001	15%	15%	Mortgage >80m² Sectional title	6,217	**36%**
R7001-R10000	5%	18%	Mortgage <80m² Social housing	9,594	**56%**
R5001-R7000	6%				
R3501-R5000	7%				
R2501-R3500	9%	**68%**	Subsidised housing (RDP)	1,436	8%
R1501-R2500	10%				
R0-R1501	49%				
Total	**100%**			**17,247**	**100%**

This table also shows the high percentage of households earning less than R3500 a month and who qualify for RDP housing.

3. Quality of low income housing

The CSIR (March 2013) showed significant performance and sustainability enhancements for low income housing. Crucial planning is imperative to investigate how urban growth can be made more effective, especially regarding how urban growth can be developed cost effectively. The CSIR is researching solutions, through pilot projects, to some problems existing within the subsidy housing projects. The pilot project was started by the Department of Science and technology (DST), were the CSIR will assist in evaluating the efficacy of alternative technologies to improve the sustainability of the two housing projects in the Western and Eastern Cape. If one wants to look at the sustainability and self efficiency of the housing development, it has to include any environmental, technological and ecological issues. "To achieve this, certain basic research questions must be answered, such as what the thresholds/tipping points are of the approach (income, rainfall, wind speed, number of solar hours, number of units, size of land, access to jobs); and what technology is available to extend and maximise these thresholds", CSIR architect (April 2013) [4]. To assist research into innovative technologies in general, and their performance-enhancing capabilities in particular, the CSIR has built two pilot houses on its test site in Pretoria to investigate technology options. In recommending technologies to the DST, a fundamental component of the CSIR's research is addressing anticipated energy and water shortages facing the country. Certain technologies that are known to offer other benefits, such as job creation, are also being targeted. Similarly, the potential of the specific geographic conditions of the sites and the surrounding areas - for example local soils - must be investigated to see whether it could add value to the development. The location of the sites and the connections of these to existing and adjoining sites - such as public open space systems - must also be explored to ensure that these connections are maximised. "For our development proposal to serve as a model, it must not burden the financial sustainability of local authorities. One of the ways this can be done is to reduce the dependence of the development on municipal services, for example, use a range of technologies such as wind generators in conjunction with solar collectors. The introduction and implementation of sustainable urban drainage systems can also be considered together with a range of water treatment technologies."

4. Alternative for affordable housing

It is recognised that some contractors working in the low income market often do not lay foundations to standard. To eliminate cracked walls resulting from sub standard foundations, a CSIR - developed housing alternative technology - ultra-thin continuously - reinforced concrete used for roads - was adapted to form the foundation slab of the house. "Local labour can be used to construct such foundations (October 2008) [1]. One big difference to current houses is that the design of the bathroom/kitchen area was rationalised, and a waste outlet manifold used that is pre-manufactured, quality-tested and installed on site. This has reduced the extent of the plumbing installation substantially while ensuring that the installation is done to the required standard. Low income houses have no ceiling at present and thus no insulation, which results in incredible variations in temperatures. The thermal performance of the roof was improved dramatically with the addition of an insulation material that doubles up as a ceiling.

5. Prefabricated houses for low income housing

Prefabricated houses can be pre-assembled and delivered to site. A feature of prefabricated houses is:

- Low cost
- Convenient
- Durable

They are all made of standardized components, and connected by bolts. We can design;

- Make the prefab house according to the customer's is specific requirements.
- The houses can be assembled and disassembled for dozens of times and can be removed 10 times.
- All the steel components are painted and anti-rust which can be normally used for more than 20 years.

The steel structure makes the house resisting heavy wind of 100km/h and 7 grade earthquakes [2]. The wall system of colour steel sandwich panel has a good fire proof and heat insulation performance.

- Waterproof design of all steel structure.
- Environment - protection without any building rubbish.
- The transportation is convenient and one 40HQ container can load about 250 m^2.

Figure1. *Basic prefabricated house*

5. Conclusions

There is a housing problem in South Africa and the subsidized housing backlog is putting a lot of pressure on the government to deliver these types of housing. A study done by the CSIR shows those modular homes can be used for RDP houses and also to enlarge the existing houses. By using modular homes and light steel construction, the delivery would speed up, and better quality homes could be built for less.

Modular homes and light steel framed structures can both be used for low income housing and people would benefit from building or even renting these houses. The delivery of low income houses can be scaled up through the short construction periods and these construction methods also have the advantage of pre-assembly or factory assembly which would stop any unnecessary mistakes creeping in. The light steel construction industry is rapidly growing and SASFA already has 36 companies who are members who manufacture and erect these homes. The government has to do something about the housing backlog and these alternative building methods might just be the answer.

Literature:

[1] Hillier M., Lawson R.M. and Gorgolewski M., Over-roofing of Existing Buildings using Light Steel, The Steel Construction Institute P-246, 1999.

[2] Lawson R.M., Pedreschi R., Falkenfleth I. and Popo-Ola S.O., Over-cladding of Existing Buildings using Light Steel, The Steel Construction Institute P-247, 1999.

[3] The Steel Construction Institute P–271, 1999 Galjaard, H. C., Walraven, J. C., Static tests on various types of shear connectors for composite structures. University of Stuttgart, Germany, 2001.

[4] Lawson, R.M., Chung, K.F., Popo-Ola, S.O., Building Design Using Cold Formed Steel Sections - Section Properties and Load Tables, the Steel Construction Institute, 2002.

[5] Hamidi B., Light Steel Construction, University of Pristina, 2010.

SOME OPTIMIZATION METHODS FOR INCREASING THE ENERGY EFFICIENCY OF THE WATER SUPPLY SYSTEMS

Kostadinova S., M.Sc. Student, Panev A., M.Sc. Student, Prof. Dr Cingoski V.
Faculty of Electrical Engineering, "Goce Delcev" University - Štip, Republic of Macedonia

slavica.2254@student.ugd.edu.mk

Abstract: *We are witnessing the rapid growth of the energy prices and there are expectations that they will continue to grow in the future. Consequently, there is a constant need of energy efficiency improvements that could be achieved by decreasing of energy losses, smart and efficient energy utilization and conservation of energy resources.*

The water supply systems are large energy consumers. So, the investments in the increasing of their energy efficiency will not only have an economic dimension, but also they could have large positive effect on the environment protection. In this paper, an analysis of the degree of efficient usage of the energy and the appropriate techno-economic analysis of the energy consumption for a real water supply system is presented. Few methods for increasing the energy efficiency of water supply pump stations and an analysis of the potential benefits of this method are proposed and discussed too.

Keywords: WATER SUPPLY, ENERGY EFFICIENCY, OPTIMIZATION, ECONOMY

1. Introduction

The water supply systems consume electric power at each of the stages of the water production and supply chain: starting from pumping the water to the water treatment plant, along the water treatment process and during distribution of the water via the water supply network.

Energy losses in these systems are generally conditioned by a several reasons: inefficient pump stations, poor system design, installation and/or maintenance, old pipes with high network losses, bottlenecks in the supply network as well as inefficient operation strategies of the various supply facilities [1].

This paper proposes a few measures for increasing the energy efficiency of a typical water supply system, and a further analysis of a possible technical and economic benefits of these measures are defined. Several appropriate proposals for the modernization of this water supply system are given, with application of some contemporary computer techniques and procedures.

2. Analysis of a Typical Water Supply System

The investigated water supply system is the water supply system of the Municipality of Radovish, which operates through mixed gravitation/pumping mode, where gravitational system is used from three existing water catchments: "Ambari", "Stara Kaptaza" and "Filter Stanica", on one side, and water pumping system from the two pumping systems: "Industrija" and "Raklish", on the other side. Both pumping systems are connected with drawn pool which is filled with water from ten existing water wells [2].

The amount of water consumption is a time-variable function with the amounts that significantly varies annualy, monthly, daily and even hourly. These variations are generally implied from climate condition changes, the work of the major industrial plants, the number of inhabitants, the standard of the population, etc. However, usually there is larger water consumption during the summer period compared to the winter period [3].

The average daily water consumption during winter was 89 l/s, while in the summer the water consumption goes as high as 122 l/s [2]. This difference indicates a possibility of introducing two separate operational modes for the water supply system, the summer operational mode and the winter operational mode. This was the firstly suggested activity among the others for increasing the energy efficiency of the whole water supply system [2].

In order to analyze the characteristics of the water supply system of the Municipality of Radovish, a real simulation of the system was made using the LabView simulation package.

3. Annual Electricity Consumption

To determine the measures for energy efficiency improvement of the system, the analysis of the electricity costs for the last 6 years was done. The results of this analysis are shown on Fig. 1.

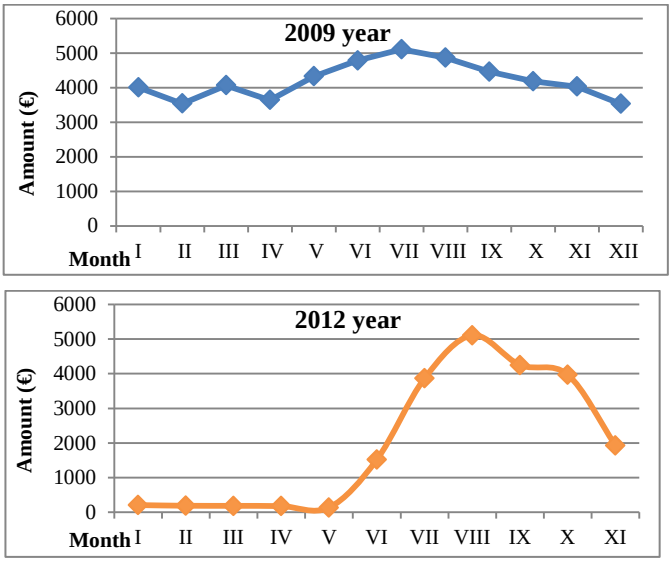

Fig. 1 *Cost paid for electricity consumption for 2009 and 2012 year*

It can be noticed that in 2009 the company had large electricity cost consistently all year around. Surging water consumption during the summer months is the main reason for larger cost in this period of the year. In 2012, the company significantly reduced electricity cost, mostly as a result of disconnection of the pumping stations during the winter i.e. the introduction of only the gravitational mode at the end of 2010 during the winter period.

Additionally, an analysis of the cost for the consumed reactive power for the period between 2008 and 2013 was made. The results are shown in Fig. 2, where it can be seen that in those 6 years the company had really high cost for consumed reactive power.

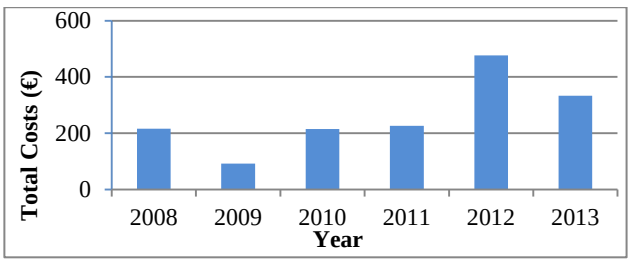

Fig. 2 *Reactive power cost paid for the period between 2008 and 2013.*

4. Problems and Weaknesses in the Water Supply System

From the analysis of the current state of the system and the reference annual consumption we realized that by the end of 2010, successful effort for increasing the energy efficiency in the system was made i.e. the introduction of the zonal water supply brought significant economic benefits for the company.

Additionally, from the analysis of the reactive power consumption we realized that this typical water supply system is using two types of electric motors which use excessive reactive power directly from the power grid, i.e. they have low power factor. This, so-called ***reactive power*** used by some power devices for creating an electromagnetic energy as a medium for conversion of the energy from one to another form, is not converted into useful work [4], therefore brings only additional energy cost to the company.

From the analysis of the pumps operation mode of the pump station "Industrija", we realized that except the turning off mode for the winter months, there is no other way to regulate its work during the summer months. According to received information, turning on and off is performed manually by the operator. This was considered as another subjective reason for increased electricity cost.

5. Research Results

During the research, beside reorganization of pump operation for winter and summer regimes, a set of additional measures to overcome the perceived weaknesses in the system were investigated and proposed, among which the most significant were the following two measures:

- the improvement of the power factor of the pumping systems, i.e. decrease the amount of reactive power taken from the grid and replace it with locally generated one, and
- the development of a system for automatic regulation of the three main parameters in the water supply system: pressure, water flow and the amount of water in the reservoir.

5.1. Measure #1: Reorganization of the Pumps Operation

This measure provided electricity cost reduction and some technical benefits:

- Reduced work of the motors and pumps,
- Increased motors and pumps efficiency,
- Extended “working life”,

The main disadvantages of this measure were low water supply quality or reduced pressure and water flow during the summer months, and consistently the same cost for water supply services for that period of the year. Because there were no additional investments for this measure and there was saving of around 67.5%, we could conclude that this measure was a highly cost-effective measure.

5.2. Measure #2: Reactive Power Compensation

With the application of adequate reactive power compensation generated locally by installed capacitor banks, additional increase of the energy efficiency of the whole system could be expected. In such case, the installed capacitor banks could provide only a part of the requested reactive power, leading to a reasonable increased value of the power factor at least to a level of 0.96. This is because only a power system that have power factor less than 0.95 are required to pay additional cost for taking the excessive reactive power from the electric power grid [5].

Calculation of the required reactive energy for compensation and selection of the type of compensation are two most important steps to achieve optimal cost-benefit of the proposed activity.

The amount of added reactive power could be calculated using well-known formula:

$$Q_c = Q_1 - Q_2 = P * (\tan\varphi 1 - \tan\varphi 2) \quad [VAr]$$

Based on the analyzed data, we made a calculation of the required reactive power used by both types of motors which are used in this particular water supply system. Thus, the calculated amount of reactive power that should be additionally provided by the capacitor banks was 4.9 [kVAr], and 12.9 [kVAr] for each type of the electric motor, respectively. Therefore, to achieved a full reactive power compensation for the whole electricity supply system (both pumping stations and all five motors) to the desired value for the power factor $\cos\varphi=0.96$, a total amount of 40.5 [kVAr] reactive power was required [6].

Because of the power supply stability and continuous load factor, as well as the short distance between the pumping stations and the supplying transformer substation *(less than 10 meters)*, the central compensation system was proposed. The capacitor banks should be installed at the same bus bar as the pumping stations next to the power transformer, to provide enough reactive power for the whole installation. Using the layout shown in Fig. 3, one could eliminate tariff penalties for excessive consumption of reactive power from the grid on one side, and on the other, relieve the supply transformer from unnecessary reactive load, increase its efficiency and prolong its operational life [4].

The main disadvantage of this central compensation mode is the fact that the reactive current generated by the capacitor banks would still flow through the supply cables towards the pumping stations, generating additional power losses. However, due to the very short distance between the power transformer and the pumping stations, increase of the power losses should be insignificant [6].

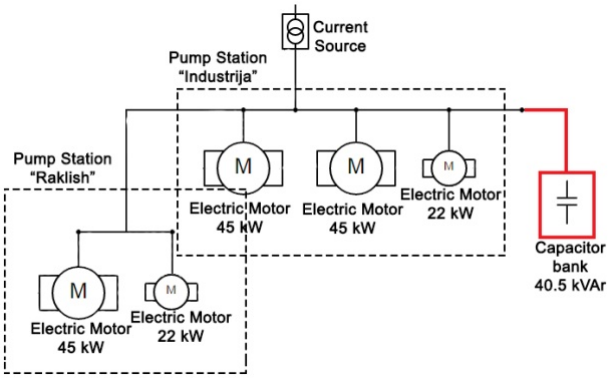

Fig. 3 *The pump stations with central reactive power compensation system [6]*

Speaking about the economic benefits of this measure, the total financial resources spent for procurement of the reactive power for the period between 2008 and 2013, (Fig. 2), were estimates at 1,559€, i.e. an average of 259.83€ per year, while the total investment for purchase and installation of the proposed compensation equipment and the realization of this improvement method was estimated at 326.5€. This investment could be also estimated as a cost-effective measure because the full investment in this kind of capacitor banks would be paid off for approximately 1 year and 3 months. To be precise, one could conclude that only with the implementation of the proposed measure this company could decrease the existing operational electricity cost for at least 1.7%.

5.3. Measure #3: Pumping System Operating Mode Optimization of the Depending on the Needs and Electricity Prices

The pumping system operating mode is a very complex process for large water supply systems. In our research the various operation modes of pumping system were investigated in order to find the one that will provide reduced power consumption and reduced cost for pump station maintenance. The increased electricity consumption during the months from May to November shows that it is necessary to activate both pumping stations.

To determine the electricity savings which can be achieved with the implementation of this measure, the real simulation of the system using the LabView simulation package was made. For this purpose, the data for the maximum hourly water consumption for the different parts of the city had to be known and used in the process simulation. For simulation purposes, the parts of the city which are water supplied using the pump station "Industrija" were only considered. Fig. 5 shows a graph with the values for the maximum hourly water consumption connected with this pump station.

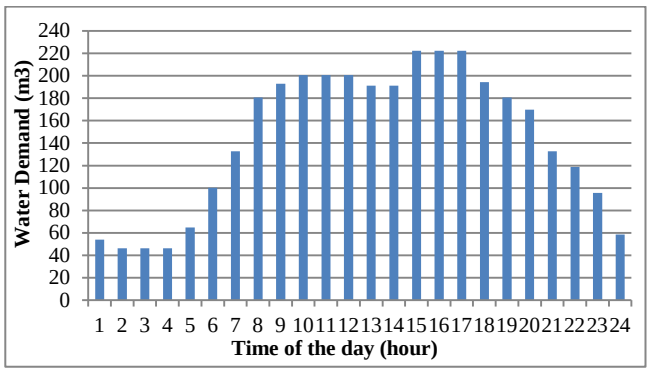

Fig. 4 *Maximum hourly water consumption*

Amount of Water Regulation

With the regulation of the amount of water in the reservoir, the costs optimization can be achieved only in respect of the company. The first step of the implementation of the proposed measure was to put into service the reservoir "Industrija". The optimization was achieved by determining the optimum upper and lower level of the water in the reservoir. Initially 900 m^3 for upper amount of water was considered i.e. the maximum capacity of the tank. Filling the reservoir to the maximum level through the night was planned.

The simulation is run for two periods: day-time and night-time.

- the period between 7:00 and 22:00, or the period of high tariff and accordingly, the high electricity prices, and
- the period between 22:00 and 7:00, or period of low tariff and accordingly, the low electricity prices.

Tab. 1 shows the results of the simulation when only one parameter is regulated (amount of water in the reservoir), i.e. the target function are total amount of money which the company would spend if the proposed measure is realized.

Table 1: *Costs of various optimization parameters*

Hysteresis		**7:00 h – 22:00 h**		
		200 m^3 & 300 m^3	200 m^3 & 500 m^3	200 m^3 & 900 m^3
7:00 h – 22:00 h	800 m^3 & 900 m^3	37.74 €	38.33 €	44.24 €
	500 m^3 & 900 m^3	41.45 €	39.90 €	47.32 €
	300 m^3 & 900 m^3	41.58 €	41.51 €	47.53 €

From the table can be seen that there is the lowest electricity consumption when the values of the upper and the lower level of the water during the period between 07:00 and 22:00, would be 200 m^3 and 300 m^3, and while for the period from 22:00 to 07:00 would be 800 m3 and 900 m3.

Water Pressure Regulation

The second set of optimization methods which use the same cost function - minimization of the company costs, is realized with the introduction of one additional optimization criteria: the amount of the water pressure in the water supply system. In this case, we "maintain" the pressure for the whole operational time to optimal value for water pressure in the water supply systems, at the value of 5 bar, without considering the amount of water in the reservoir. In this case, the optimal solution for 24 hour operation gives the following optimal values: consumption of 720 kWh during the high tariff period and 241 kWh during the low tariff period, or 44.24€ for whole operational period of 24 hours, or monthly (30 days period), the company could spend approximately 1327.32€ for pumping purposes.

Amount of Water and Water Pressure Regulation

Finally, optimization was realized using both optimization criteria jointly: (i) the amount of water in the reservoir, and (ii) the value of the water pressure in the water distribution system. The same optimization target function – the minimization of the energy cost was used. In this case, besides providing reduction of the operational cost for the water supply company, the obtained optimized operational mode results with rising of the quality of the water supply services for all customers connected to the system, mostly due to ensured minimum water pressure in the distribution network as requested by the water supply standards.

The optimization results for this two-parameter optimization procedure shows that for 24 hour operation the company will spend 685 kWh during the high tariff period (day-time) and 244 kWh during the low tariff period (night-time), or a total of 42.50€ per day, or monthly cost could be estimated at the amount of 1275.12€.

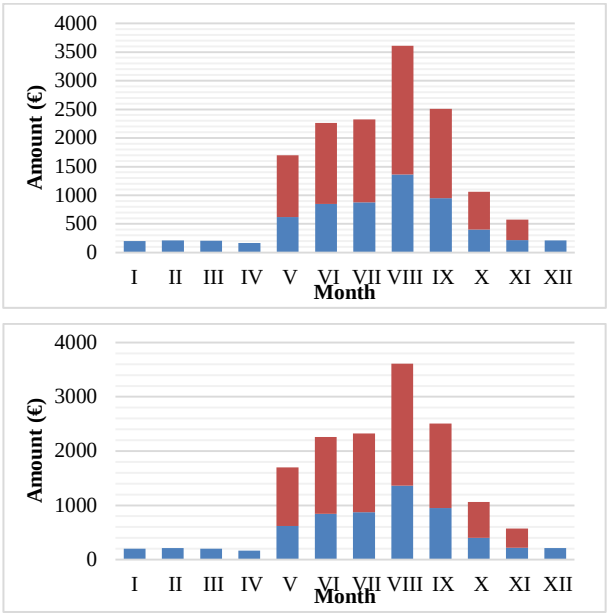

Fig. 5 *Monthly savings with optimization of the amount of water in the reservoir (above), and monthly savings with optimization of the amount of water in the reservoir and the water pressure (below)*

According to the simulations one could come to the conclusion that the largest energy savings could be obtained when the pumping station "Industrija" works in the optimization mode only for the amount of water in its reservoir. The savings per month that would be obtained with the implementation of this measure are given in Fig. 5, graph above. The amounts of money that the company will save only by the implementation of this measure are shown with red color on the above graph on Fig. 5. The results show that with usage of this optimization mode only, the company annually could save approximately 9 275€.

However, this optimization mode does not provide the improvement of the water quality supply services, i.e. sometimes, especially during the summer months the users are “receiving” the water with extremely low pressure (below 5 bar). Therefore, the optimization mode must include the quality of water supply services, i.e. one should definitely include the second optimization parameter, the value of the water pressure at the point of the last consumer in the water distribution system. This solution could be

optimal not only for the water supply company but also for all customers connected with this water supply system. The savings per month in such optimization mode, are presented in Fig. 5, graph below. The results show that with usage of this optimization mode only, the company annually could save approximately 8 681€.

This optimization mode could not be achieve without implementation of appropriate SCADA system for on-line monitoring and control of the whole water supply system. As part of our research, the investment cost for purchase and installation of such SCADA system was also analyzed. The investment cost according the regional prices for purchasing and installation of middle range SCADA system was estimated at about 21 700€.

Having into account the cost for additional SCADA investment and the annual savings that the company could achieve by implementation and utilization of that SCADA system, one could calculated that the pay-back period in the first case of the optimization (only the water level in the reservoir) could be approximately 2.3 years. In the second case of the optimization (water level and water pressure combined) the expected pay-back period could slightly increase, but even in that case it could be around 2.5 years. Both pay-back periods are acceptable and show very high cost effective measures that could be quickly and efficiently implemented in such water supply systems.

6. Conclusion

According to the aforementioned results, the type and the essence of the proposed measures for operational cost reductions and energy efficiency improvements, in Table 2 the economic benefits of each of the proposed measures are summarized:

Table 2: *Investment value and repayment time of the proposed measures*

Proposed Measures	**Investment value**	**Repayment time**
Reorganization of the Pumps Operation	/	/
Reactive Power Compensation	326.5 €	1 year & 3 months
Pumping System Operating Mode Optimization	21 700 €	2 years & 4 months or 2 years & 6 months

According to the summarized results shown in Tab. 2, for this typical water supply system, we suggest:

1) Further improvements of zone-based water supplying method in order to improve the quality and the quantity of the water supply services.

2) Procurement and installation of adequate equipment for reactive power compensation for elimination of the unnecessary financial costs due to excessive reactive power consumption.

3) Activation of "Industrija" water reservoir for optimization of the water supply mode for the whole city.

4) Investment in the adequate SCADA system for monitoring and management of the water supply system, especially for the amount in the water level in the reservoir, optimization of the pumps operating mode with the respect of the water needs and electricity prices.

This ranking list of measures is proposed to the responsible persons in the company in order to decide which of the proposed measures are technically and economically viable for implementation by the company.

7. References

[1] M. Feldman, Aspects of Energy Efficiency in Water Supply, Proceedings of the 5th IWA Water Loss Reduction Specialist Conference 26-30 April Cape Town South Africa pp. 85-89, 2009

[2] ЈП "Плаваја, Снабдување со вода за пиење и одведување на урбани и отпадни води во Општина Радовиш 2010 година", April, 2011

[3] L.K Reynolds, S. Bunn. Integrating Water Systems - Boxall && Maksimovic (eds): Improving energy efficiency of pumping systems through real-time scheduling systems, Taylor & Francis Group, London 2010

[4] Schneider Electric. Reactive Energy Management – Low Voltage components, January 2013

[5] Свет на енциклопедиски знаења. Реактивна моќност, 21 April 2015 г. http://mk.swewe.net/

[6] S. Kostadinova, V. Cingoski, S. Gelev, R. Golubovski, Increasing Energy Efficiency of Water Supply Systems with Pump Systems Power Factor Improvement, Zbornik radova sa XX međunarodnog naučno - stručnog skupa INFORMACIONE TEHNOLOGIJE - sadašnjost i budućnost, Žabljak, Crna Gora, 23 - 28 februari 2015.

MODELING AND STUDY OF THE PROCESS OF BILLETS EXTRUSION WITH ADDITIONAL BACK-PRESSURE IN EQUAL CHANNEL STEP MATRIX

МОДЕЛИРОВАНИЕ И ИССЛЕДОВАНИЕ ПРОЦЕССА ПРЕССОВАНИЯ ЗАГОТОВОК С ДОПОЛНИТЕЛЬНЫМ ПРОТИВОДАВЛЕНИЕМ В РАВНОКАНАЛЬНОЙ СТУПЕНЧАТОЙ МАТРИЦЕ

S.N. Lezhnev, As.R.Toleuova, E.A. Panin
Karaganda state industrial University, Kazakhstan, Temirtau

Abstract: *This work is devoted to the study of stress-strain state and power parameters in the simulation of the process of extrusion billets with additional back-pressure in equal channel step matrix. Analyzing the obtained results we can conclude that the matrix without backpressure cannot achieve complete closing of internal defects of a deformable metal. The backpressure created by the increase of the roughness of the output channel of the matrix, has a beneficial effect on the stress-strain state of the metal, which in turn allows you to provide the best structured deformable metal*

KEY WORDS: *EXTRUSION, EQUAL CHANNEL STEP MATRIX, STRESS-STRAIN STATE, POWER PARAMETERS, SIMULATION.*

Introduction

One of the promising methods of obtaining metal from sub-ultrafine grained structure is equal channel pressing in angular and step matrices. Thus it is proved that if the compression of the metal to be implemented in equal channel angular matrix with backpressure, it creates a more favorable stress-strain state to produce the metal with sub-ultrafine grained structure in comparison with the pressing in this matrix without backpressure. In works [1-4] were studied various investigations of this kind of deformation.

One of the options to create a backpressure in the pressing process of the metal in equal channel angular matrix is the narrowing of the output channel of the matrix. During compaction of metal in equal-channel step matrix, unlike in the angular matrix, the pressure already created by the presence of the second junction of the channels of the matrix. The additional backpressure during equal channel pressing in step matrix can be achieved, as with angular pressing by narrowing the output channel of the matrix, or through the use of this matrix with the output channel roughness higher than the surface roughness of the input and intermediate channels of the matrix.

This work is devoted to the study of stress-strain state and the power parameters in the simulation of the process of extrusion billets with additional backpressure in equal channel step matrix in the software package DEFORM to determine optimum conditions to create a more favourable stress-strain state for obtaining a metal from sub-ultrafine grained structure with little energy consumption..

Study of stress-strain state

The stress-strain state during compaction in equal-channel step matrix with the backpressure was analyzed according to the results of stress distribution, strain intensity and force of deformation.

The presence of internal compressive stresses positive effect on the brewing internal defects and the quality of the metal (fig. 1). Comparative analysis of the stress distribution over the cross section of the workpiece shows that mainly dominated by compressive stresses. The overall compression scheme provided in the most part of the cross section, guarantees the absence of macro - and microcracks in the metal and conducive to the maximum degree of plasticity of a deformable workpiece.

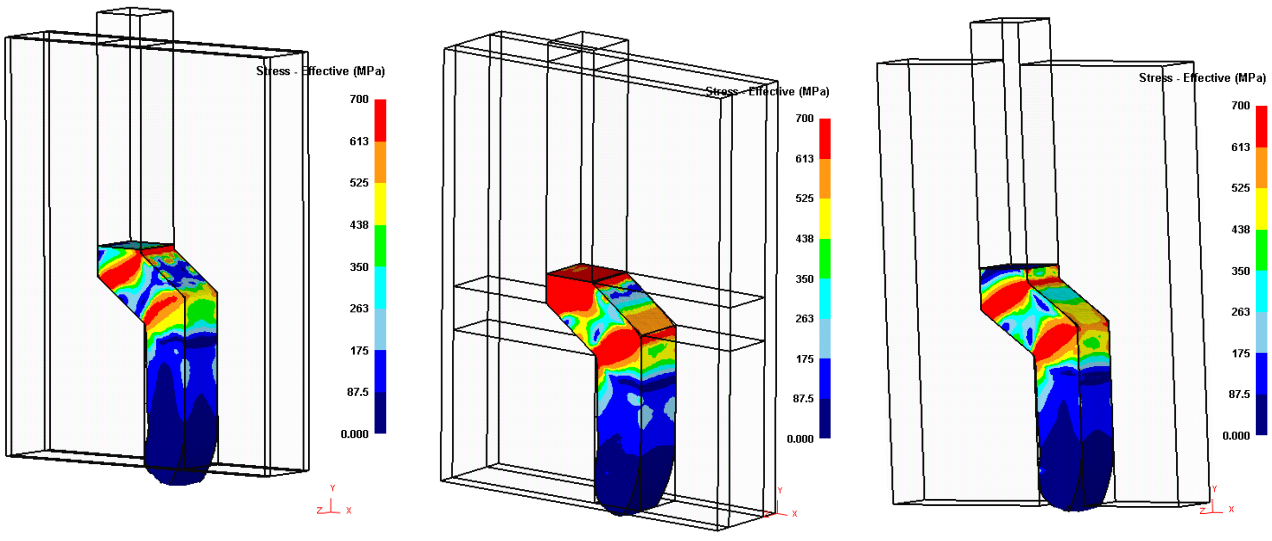

a b c

Fig. 1 *- Stress distribution: a) with narrowing output channel, b) with different degree of roughness, c) without backpressure*

The distribution of equivalent stress shows that the maximum value reaches at the junction of channels. In the matrix with a narrowing output channel maximum value of equivalent stress reaches 700 MPa at the junction of channels; in an inclined channel prevails to 280 MPa, in the third channel equivalent stress is reduced from 175 to 0 MPa (fig. 1a). In the matrix with different roughness maximum value of equivalent stress reaches 700 MPa, after the first junction of channels it is 263 – 350 MPa, and after the second is reduced to 0 MPa (fig. 1b). However, equivalent stress in the third channel different from the previous example: here the area is exposed to tension, much more. In the matrix without back pressure maximum value of equivalent stress equal to the value of the previous matrices and after the second junction channels in the matrix, value is reduced to zero (fig. 1c).

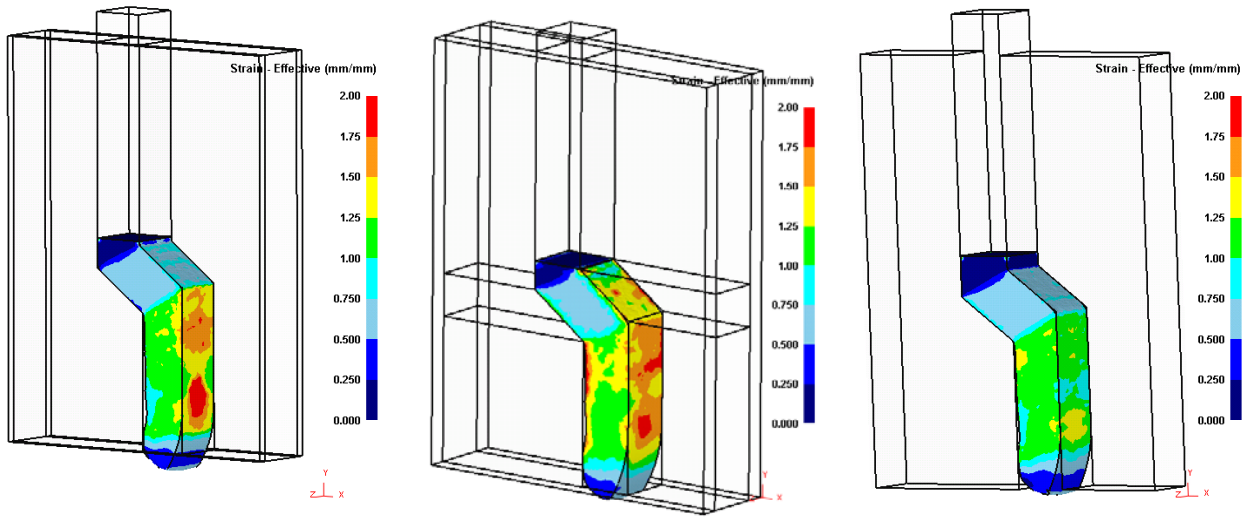

a b c

Fig. 2 *- Strain distribution: a) with narrowing output channel, b) with different degree of roughness, c) without backpressure*

Analyzing the strain distribution we can say that the increase in the coefficient of friction between the workpiece and the tool leads to increased efforts of deformation (fig. 2).

In the first two cases, the largest equivalent strain is achieved when workpiece is moving from the second channel in the third and its value is 0.75 to 1.0. In the matrix with narrowing output channel, the average value of equivalent strain is in the range from 1.0 to 1.25 (fig. 2a). In the matrix with different roughness with the increase of the coefficient of friction is significantly increased and the accumulated deformation, which averages 1,0 – 1,50; sometimes, on the inner surface of the third channel, reaches 2.0 (fig. 2b). In the matrix without backpressure the value of equivalent strain is in the range 0,75 - 1,25 (fig. 2c). The figures show that the matrix with different degrees of roughness can increase the value of equivalent strain.

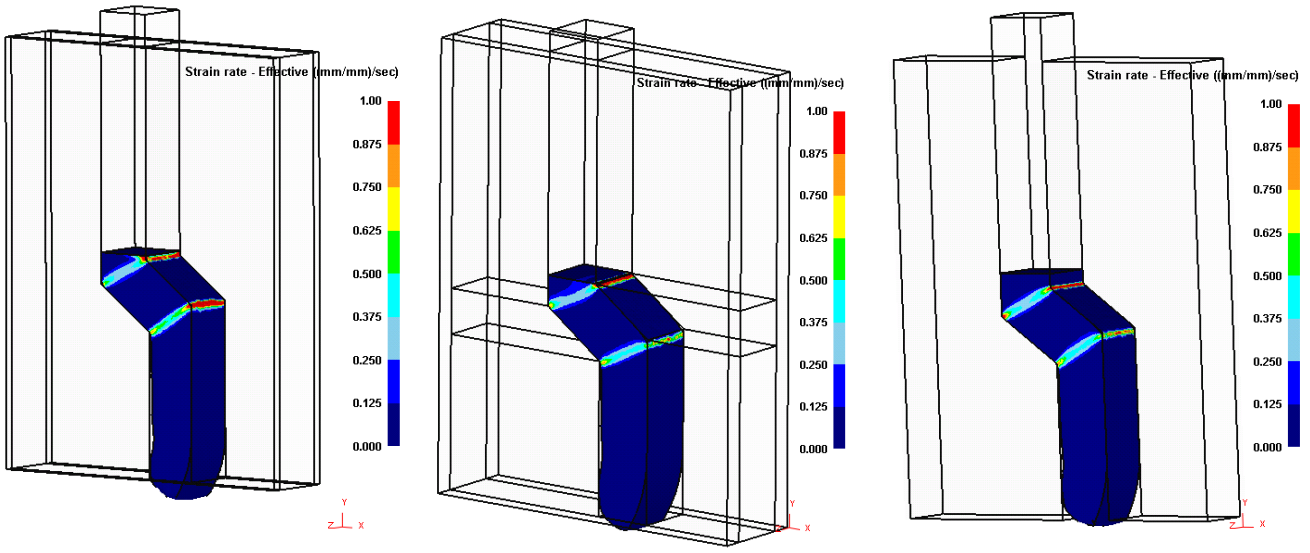

a b c

Fig. 3 *– Shear strain distribution: a) with narrowing output channel, b) with different degree of roughness, c) without backpressure*

The analysis of the distribution of shear strain shows significant strain localization at the zone of intersection of the channels and near the borders of the fracture profile of the matrix, hence, the workpiece passes through the localization zone of intense shear deformation.

Study of extrusion force

Then was examined the effect of narrowing channel and increasing of roughness degree of the channels on the force of deformation. This dependence will be determined from the graphs that have been constructed according to the simulation results.

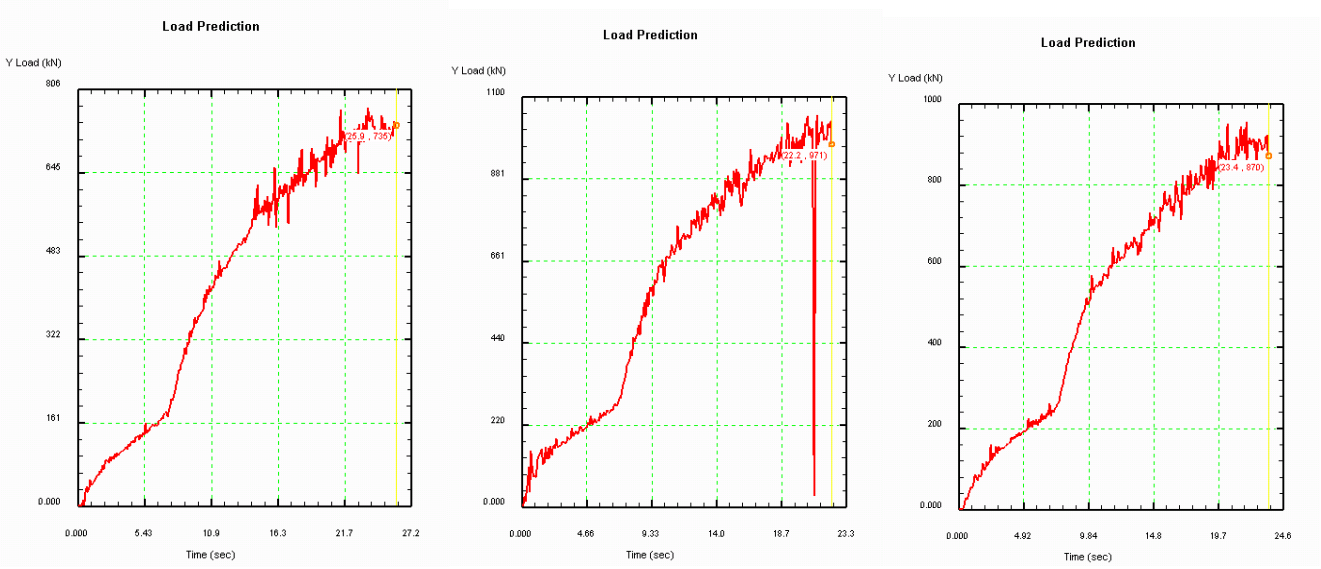

a *b* *c*

Fig. 4 *– Force of deformation: a) with narrowing output channel, b) with different degree of roughness, c) without backpressure*

Fig. 4 shows that the force is zero until the moment when the workpiece stops on the first joint in the matrix. The variation of these dependences shows that during the compression in the step matrix occurs in a two-step increase in force. At the initial stage the increasing force related to overcoming resistance in the first joint of channel in matrix. The second joint of the channel leads to the next stage of force increasing. Further, the force increases uniformly due to the fact that the volume of deformed metal.

The use of equal-channel step matrix with narrowing output channel the maximum force is 735 kN, while the curve increases smoothly (fig. 4a). In the matrix with different degrees of roughness, due to the increase of the friction coefficient in the output channel, the value of force increases to 971 kN, the curve is on a steeper trajectory, since a higher coefficient of friction increases the deformation resistance (fig. 4b), but this value is not significantly different from the value of the force when using a matrix with narrowing the output channel. In the matrix without backpressure the maximum force is 870 kN (fig. 4c).

Conclusions

Analyzing the obtained results we can conclude that the matrix without backpressure cannot achieve complete brewing internal defects of a deformable metal, unlike matrices, which uses the backpressure. The application of the narrowing channel, as a way of additional backpressure in the forming process is not quite acceptable, as is a reduction of the original size of the workpiece, and this leads to the fact that after each cycle of deformation it is necessary to change the tooling. The backpressure created by the increase of the roughness of the output channel of the matrix, has a beneficial effect on the stress-strain state of the metal, which in turn allows you to provide the best structured deformable metal.

References

1. O. Krivtsova et al., 2014, Advanced Materials Research, 1030-1032, 1337.
2. S.N. Lezhnev et al., 2015, Advanced Materials Research, 1095, 722.
3. S. Lezhnev, A. Naizabekov, I. Volokitina, O. Chalaya, 22nd International Conference on Metallurgy and Materials, Metal 2013, May 15-17.2013, Brno, Czech Republic, 329-334.
4. Naizabekov, A.B., Ashkeev, Zh.A., Lezhnev, S.N., Toleuova, A.R. Billet deformation in uniform-channel stepped die (2005). Steel in Translation, 35 (2), pp. 37-39.

НЯКОИ АСПЕКТИ ОТНОСНО ЛАЗЕРНОТО ПОВЪРХНОСТНО УЯКЧАВАНЕ В ЗАВИСИМОСТ ОТ ТОПЛОФИЗИЧНИТЕ СВОЙСТВА НА ОБРАБОТВАНИЯ МАТЕРИАЛ

PhD. Vladimir Shtarbakov[1], PhD. Maik Shtreblau[2]

"Metal"PLC, Varna, Bulgaria [1], 9000 ZPZ, v_shtarbakov@yahoo.com
Technical university – Varna, Bulgaria [2], Studentska 1, streblau@yahoo.com

Abstract: *In the present paper changing of technological parameter, such as depth and shape of hardened layer, hardening in depth possibilities and hardness on the surface in depend of therophysical properties of materials used in an laser surface hardening process were investigated. Analysis was based on distribution of thermal field in depth of samples treated by different energy density of laser influence. Thermal field was determinate by using of finite element method (FEM). FEM was realized in COMSOL Multhyphysics software.*

Key words: LASER SURFACE HARDENING; CONCENTRATED ENERGY FLUX; FEM ANALYSIS;

1. Въведение

Обработката на материалите с концентрирани енергийни потоци (лазер, плазма електронен лъч) е перспективно технологично направление в машиностроенето. Възможността за определяне на необходимите параметри на въздействие е от първостепенно значение за постигане на желаната форма, грапавост и в някои случаи твърдост, зададени по конструктивни изисквания. Основните фактори влияещи на процеса са: състоянието на въздействаната повърхност, вида на материала, неговите топло-физични характеристики, зависещи най-вече от химическият състав.

Въздействието с концентриран енергиен поток върху повърхността на различни класове стомани е изследвано от редица автори. В [1] е представен модел за предвиждане степента на аустенизация, т.е достигане на температури над A_{c3} при обработка на подевтектоидни въглеродни стомани, а в [2] що се отнася за нисколегирани такива. Числена симулация и експериментална проверка на висикоскоростния цикъл на обработка с лазерно въздействие на повърхността на стомана мартензитен клас е представен в [3].

Ефекта от процесните параметри на въздействие на концентриран енергиен поток и дебелината на обработвания детайл върху разпределението на вътрешните напрежения и възможните фазови промени на ниско и средно въглеродни подевтектоидни стомани е представено в [4, 5]. Особено важно е последното при рязане с лазерно въздействие на дебелостенни детайли, от порядъка 5-25 mm и повече, но същото не е изследвано в представените работи.

Така целта на настоящата работа е разработването на методика за оценка влиянието на процесните параметри на лазерно въздействие при рязане на дебелостенни детайли (10mm) от стомани, притежаващи възможност за фазови превръщания при въпросната обработка.

2. Методика

За реализиране на поставената цел, на изследване е подложена стомана 66Mn4 (DIN). Като най-ефективно средство за пределяне разпределението на топлина в изследваните образци и като следствие съответните фазово-структурните промени, до които това води е използван на FEM анализ.

Термо-физичните свойства на изследвания материал са взети от [6], и са представени в таблица.1, химическият и състав в таблица.2.

Таблица 1: *Топло-физични свойства на стомана 66Mn4 (DIN)*

Топлопроводност ,W/m K	50.7
Температура на топене, ^{0}C	1470
A_{C1}, ^{0}C	721
A_{C3}, ^{0}C	745

На лазерно повърхностно въздействие е подложена метална плоча с размери 10x100x100 mm. Изрязан е образец с размери (фиг.1) Ø32x10 mm. Обработката е извършена с помощта на система MAZAK 48 SUPERTURBO с импулсен CO_2 резонатор осигуряващ лъч с дължина на вълната 1064 nm. Средната мощност на импулса на въздействие е 1000W, а максимална пикова съответно 10 kW. Работната честота е 200Hz. Диаметърът на фокусираният върху повърхността на образеца лазерен лъч е 0.6 mm, а скоростта на преместване 4 mm/s. За определяне дълбочината на въздействие на лазерното излъчване върху представената на фиг.1 проба са извършени стандартни металографски изследвания включващи светлинна микроскопия и измерване на микротвърдост, натоварване 1 N в посока към вътрешността на образеца по диаметър Ø32.

Таблица 2: *Химически състав на стомана 66Mn4 (DIN)*

Съдържание на елементи			
C, %	Si, %	Mn, %	Cr, %
0,62-0,70	0,17-0,37	0,90-1,20	<0,30

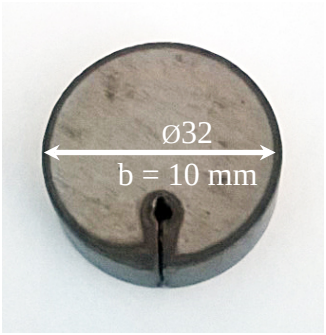

Фиг.1 *Форма и размери на изрязания образец.*

За определяне на влиянието на лазерното въздействие в коя да е точка от изследваната проба е необходимо да се реши числено диференциалното уравнение на топлопроводността (1) за представените начални и гранични условия в този случай:

$$\frac{\delta T}{\delta t} = a\left(\frac{\delta^2 T}{\delta r^2} + \frac{1}{r}\frac{\delta T}{\delta r} + \frac{1}{r^2}\frac{\delta^2 T}{\delta \varphi^2} + \frac{\delta^2 T}{\delta z^2}\right) + h(T_s - T) + q_0 \qquad (1)$$

където:

r - радиус вектор; T – температура; h – коефициент на топлообмен; q_0 – топлинен поток; t - време.

Като начално условие приемаме равномерно разпределение на топлината в изследваното тяло (2):

$$T(r,\tau) = T_0 = const \qquad (2)$$

Граничните условия са според уравнение (3):

$$\lambda_c\left(\frac{\delta T}{\delta n}\right)_s = \alpha\left(T_s - T\right) \qquad (3)$$

представящо равенство между конвективния топлообмен и топлопроводността на повърхността на топлинно въздействие

Уравнение(4) дава решение на диференциално уравнение (1) при начални условия (2) и гранични (3):

$$\theta = \theta_0 f\left(F_0; B_i; \frac{x}{l}\right) \qquad (4)$$

където:

$\theta = T_s - T$

$\theta_0 = T_{0,s} - T$

$F_0 = \frac{at^2}{l}$ - критерий на Фурие;

$B_i = \alpha \frac{\delta}{\lambda}$ - Критерий на Био;

$\frac{x}{l}$ - бездимисионна стойност.

Резултати и анализ

На фиг.2 са представени металографските изследвания извършени на повърхността на изследвания образец. Микротвърдостта (фиг.2а) в зоните в непосредствена близост до въздействието на концентрирания енергиен поток са от порядъка на 840-870 $HV_{0,1}$. Това говори за възможността за разстояние до 0,2-0,25 mm от въздействието се състои от мартензит (фиг.2б), отговаряща на представените твърдости. Същото се отнася и за преходната зона в дълбочина до 0,4-0,6 mm. Твърдостта се понижава плавно до стойности 400 $HV_{0,1}$. Структурата е смесена, състояща се от мартензит, остатъчен аустенит и останала неразтворена изходна карбидна фаза (фиг.2в). Над 0,6 mm от зоната на лазерно въздействие структурата е ферито-перлитна, с твърдост 220-250 $HV_{0,1}$ (фиг.2г).

Резултатите от фиг.2 се потвърждават от тези получени в резултат на числения симулационен анализ (фиг.3). На дълбочина до 0,2 mm температурата се запазва постоянна над необходимата (730-750^{0}C) за фазови промени при нагряване. Тя е в рамките на 950-1150^{0}C за целия период на въздействие при движение на лазерния лъч със скорост 4 mm/s върху повърхността на образеца представен на фиг.1. Това осигурява възможността при високоскоростен режим на охлаждане да се осъществи бездифузинното полиморфно мартензитно превръщане, водещо до представените на фиг.2а,б твърдости от порядъка на 840-870 $HV_{0,1}$.

Необходимата скорост на охлаждане за извършване на описаните фазови промени се постига чрез топлоотвеждане в дълбочина на материала. Това се осигурява от локалността на лазерното въздействие, концентрирано в област с диаметър 0,6 mm. В дълбочина от 1 mm под зоната на въздействие (Z-1) положението се променя съществено. На 0 mm е равна на температаурата на топене, което осигурява отрязването на образеца (фиг.3г), така както е на повърхността му (фиг.3а). В радиално направление от зоната на въздействие (фиг.3д) на

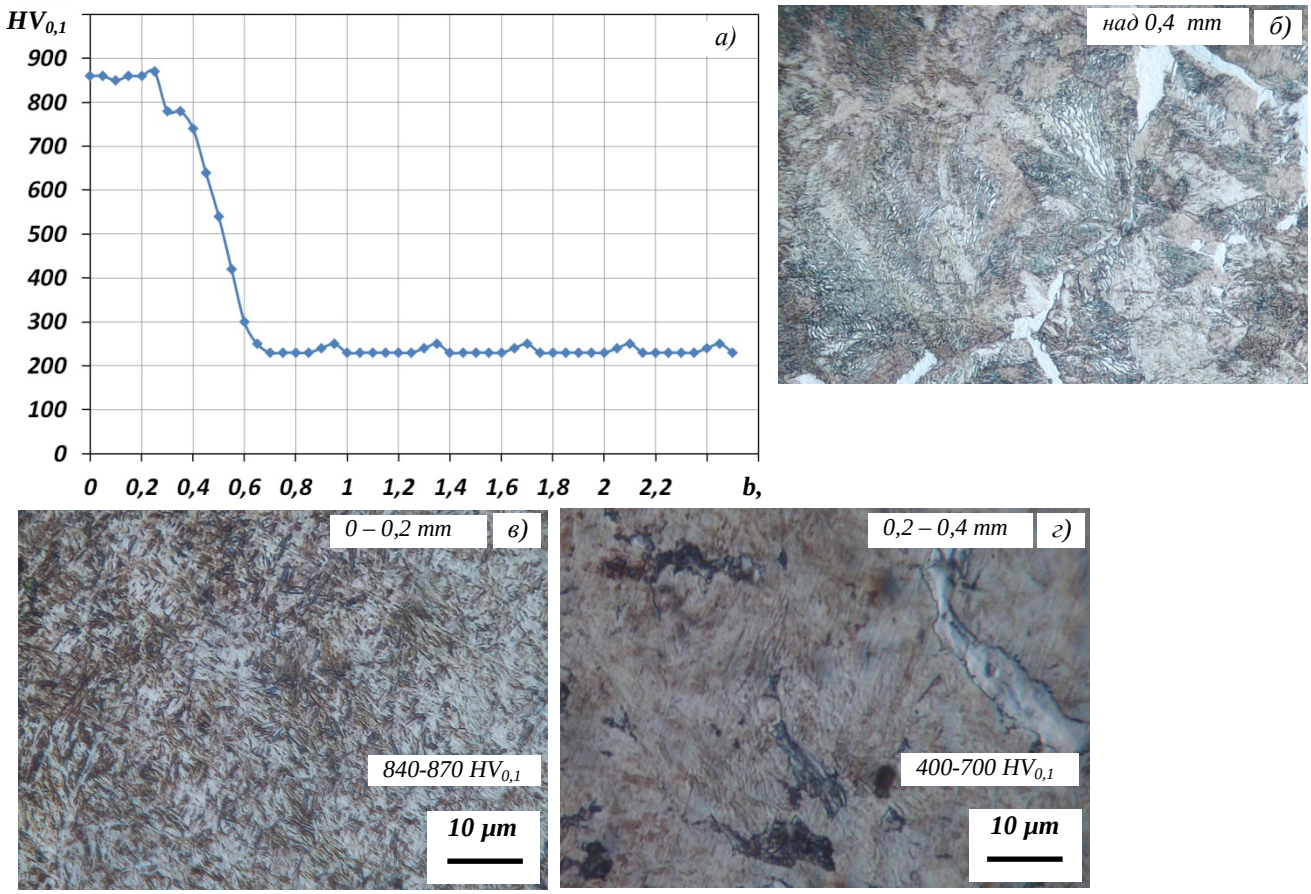

Фиг.2 *Изменение на микротвърдостта на повърхността радиално от зоната на въздействие в дълбочина на изследваната проба - (а) и на микроструктурата (б, в, г).*

протичане на мартензитно превръщане. Същото е обусловено от възможността както за нагряване до температурата осигуряваща фазовите промени „ферит + перлит → аустенит“ в твърдо състояние, така и за охлаждане с необходимата за протичане на въпросното безфифузионно полиморфно превръщане скорост. Микроструктурата в зоната на разстояние от 0,2 mm температурата е чувствително по-ниска в сравнение със същата на ниво Z0. Това е предопределено от Гаусовия характер в разпределението на топлинния поток в зоната на лазерно въздействие в място с диаметър 0,6 mm. Стойности от порядъка до 500^{0}C не са достатъчни за реализиране на необходимия термичен цикъл и осъществяване

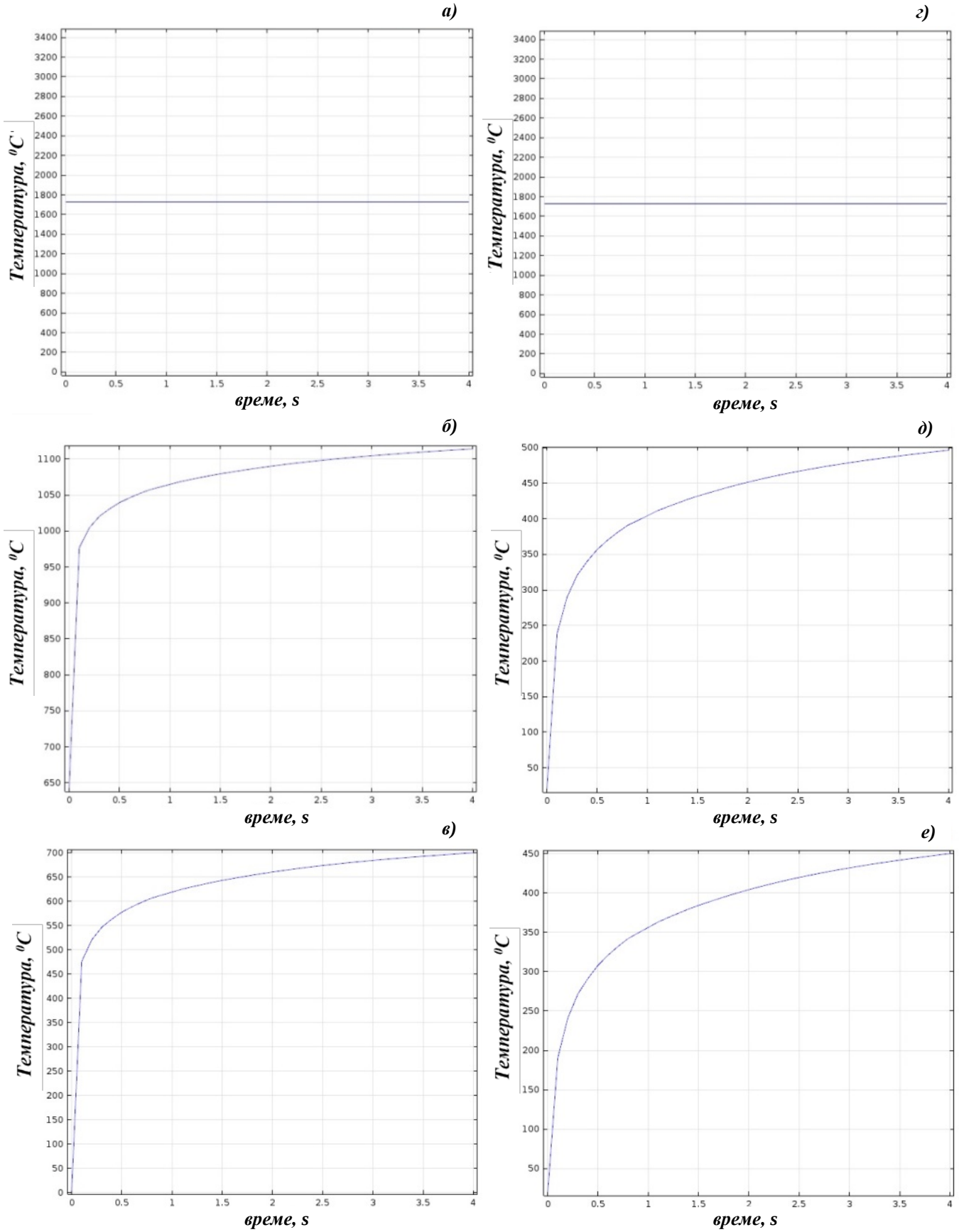

Фиг.3 *Изменение на температурата на повърхността радиално от зоната на въздействие при нагряване (а,б,в) и в дълбочина на 1 мм (г,д,е) на разстояние 0 mm-(а,г) 0,2 mm -(б,д) и 0,4 mm -(в,е).*

на полиморфни промени при нагряване и съответно при охлаждане. Логично още по-ниска е температурата на разстояние от 0,4 mm в радиално направление.

Резултатите от структурния металографски анализ (фиг.2) и числения симулационен анализ (фиг.3) позволяват да се потвърди коректността на представената методична постановка. Същата е възможно да се използва за определяне на оптималните параметри на режима на рязане чрез лазерно въздействие на въглеродни и нисколегирани стомани ферит-перлитен клас с дебелина на материала до 10 mm и дължина на вълната на лазерното въздействие от 1064 nm. Последното предполага използването на квантов резонатор с активна CO_2 или Nd:YAG среда за генериране на режещия лъч.

Като недостатък на представената методика е необходимо да се отчете факта, че трябва да е известна точната стойност на коефициента на поглъщане на лазерното въздействие на повърхността. Той представлява в случая и коефициент на топлообмен на повърхността на образеца. Може да се приеме, че загубите от конвективен топлообмен в резултат на твърде краткото време за въздействие на лазерния лъч е пренебрежимо малко.

Изводи

На базата на проведените изследвания може да се направи заключение, че представената методика за числено моделиране на процеса на разпределение на температурата при лазерно въздействие върху повърхността на изследваната стомана 65Г / 66Mn4 (ГОСТ / DIN) съответства на реалните резултати. Това дава основание да се приложи при избора на технологични параметри на въздействие на лазерна повърхностна обработка (рязане, уякчаване). Необходимо е разширяване на номенклатурата на реално изследвани материали с цел оптимизация на методиката за подбор на параметрите на въздействие.

Литература

[1] Orazi L., Fortunato A., Cuccolini G., Tani G. - An efficient model for laser surface hardening of hypo-eutectoid steels, Applied Surface Science, 256, 2010, p.1913–1919

[2] Lakhkar R.S., Shin Y.C., M.Krane J.M. - Predictive modeling of multi-track laser hardening of AISI 4140 steel, Materials Science and Engineering A, 480, 2008, p.209–217

[3] Tani G., Fortunato A., Ascari A., Campana G.- Laser surface hardening of martensitic stainless steel hollow parts, CIRP Annals - Manufacturing Technology, 59, 2010, p.207–210

[4] Yilbas B.S., Arif A.F.M., AbdulAleem B.J.- Laser cutting of holes in thick sheet metals: Development of stress field, Optics and Lasers in Engineering, 47, 2009, p.909–916

[5] So S., Ki H. - Effect of specimen thickness on heat treatability in laser transformation hardening, International Journal of Heat and Mass Transfer, 61, 2013, p.266–276

[6] http://www.matweb.com/, (on line)

HOOP TENSILE PROPERTIES OF FILAMENT WOUND PIPES

Prof. d-r Srebrenkoska V.[1], MSc. Zhezhova S.[1] and Naseva S. [1]
Faculty of Technology, University Goce Delchev - Shtip[1], R. Macedonia
E-mail: vineta.srebrenkoska@ugd.edu.mk

Abstract: *In this study hoop tensile properties of continuous fiber reinforced composites pipes are investigated. The test pipes were manufactured of glass fiber and epoxy resin by filament winding method with three different winding angle configurations (10°, 45° and 90°). Three specimens from each model of filament wound pipes with help of split-disk tests were tested and the hoop tensile strengths and modulus of elasticity were determined. From received results it is concluded that, mechanical properties of composite specimens are depended from winding angles in filament winding technology, whereas that bigger winding angle lead to higher hoop tensile properties of filament-wound tubular samples. The optimal values for the hoop tensile strength are obtained for the samples winded with 45° winding angle.*

KEYWORDS: COMPOSITE PIPES, FILAMENT WINDING, SPLIT-DISK TEST, GLASS FIBERS, EPOXY RESIN

1. Introduction

Many of the modern industrial applications and technologies require materials with superior properties that cannot be met by conventional monolithic materials, such as metal alloys, ceramics and polymers. Because of their heterogeneous nature composite materials have several advantages over traditional engineering materials, which make them attractive for many industrial applications. Properties of composites arise as a function of its constituent materials, their distribution, and the interaction among them and as a result an unusual combination of material properties can be obtained. Composite materials have superior mechanical properties like high specific stiffness, high specific strength, high fatigue strength and good impact properties.

From the wide family of composites, fiber reinforced composites have taken much attention due to their better mechanical properties. Composites produced by long fibers with high aspect ratio are called continuous fiber reinforced composites. Fibers are the materials with very high aspect ratios; i.e. they have one very long dimension compared to the others. They have significantly more strength in the long direction than the other directions. These composites have found a wide range of application area due to their anisotropic nature, the direction dependence of their properties results in much better design flexibility that cannot be obtained by monolithic materials or particle reinforced composites.

Filament winding technique can be accepted as one of the most common production techniques, for the synthesis of polymer matrix composites (PMC).

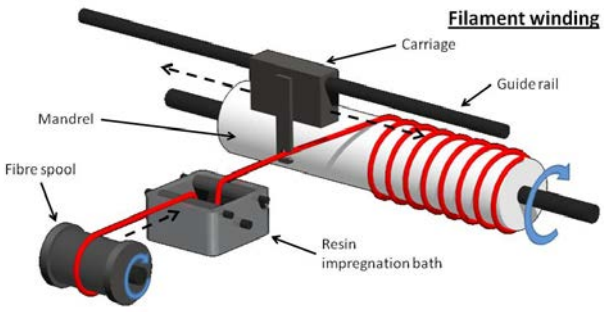

Figure 1. *Schematic presentation of the filament winding technology*

Filament winding is a process where the reinforcing agent in the form of continuous fibers (glass, carbon, aramid, etc.) is accurately positioned in the impregnation agent in the form of liquid resin (polyester, epoxy, etc.) to form a cylindrical shape. Figure 1 shows a filament winding process. A number of fiber rovings are pulled from a series of creels and tensioners that control the tension of the fibers into a liquid resin bath that contains the resin itself, the hardeners and the accelerators. At the end of the resin tank, the rovings are pulled through a wiping device where the excess resin is removed from the rovings. Once the rovings are thoroughly impregnated and wiped, they are collected together in a flat band, pass through the carriage and located on the mandrel. The traversing speed of carriage and the winding speed of the mandrel are controlled to generate the desired winding angle patterns. After the appropriate number of layers has been applied, curing is carried out in an oven or at room temperature, after which the mandrel is removed.

The filament winding method in general, has several advantages over other methods.

- It is highly repetitive and precise in fiber placement.
- It can use continuous fibers to cover the whole component area, which simplifies the fabrication process of many components and increases reliability and lowers the cost by reducing the number of joints.
- It is less labor intensive, which reduces the costs significantly.
- Large and thick walled structures can be built.

Based on that, it is clear that the filament winding technology is used for creating new materials with distinct anisotropy according to the direction in which the fiber is placed. In other words, different directions result in a material with different mechanical properties.

Three types of testing geometry are commonly used in testing of filament-wound composite structures, namely; flat specimens (coupon specimens), ring specimens, and tubular specimens. Axial (tension/compression), shear, and bending response of each testing geometry can be determined by applying a suitable loading to the specimen. For evaluation of the tensile properties of filament wound composite structures split-disk test is usually used.

Proposed ring shape of samples may be applied in axial tension test, internal pressure test, etc., as well as their combinations. Hoop tensile strength of specimens can be determined with help of split-disk test. Split-disk tests are very efficient in determine the performance of tubular structures which are usually used under internal pressure developing high hoop.

This research will present the hoop tensile properties of different models of specimens based on the different winding angle, manufactured with conventional filament winding equipment.

2. *Preconditions and means for resolving the problem*

a. Experimental stand

Samples with different winding designs were winded on iron mandrel with help of laboratory filament winding machine MAW FB 6/1 with six axes, roller type resin bath manufactured from Mikrosam A.D. The filament winding machine is given in Figure 2.

Figure 2. *Filament winding machine MAW FB 6/1*

The resin system employed in the fabrication of the pipes is Araldite LY564/Aradur 917/Accelerator 960-1 from Huntsman. This polymer system is suitable for filament winding, wet laminating, and pultrusion processes and it was recommended by the producer. The reinforcements employed in the fabrication of the pipes are 10 bobbins of E- glass fiber roving 185P with 1200 tex from Owens Corning. Glass fibers with constant fiber tension 110 N pass through a resin bath and gets wet before winding operation. The velocity of the filament winding was 21 m/min. During the manufacturing of the test pipes, three different winding angles are used, 10°, 45° and 90° (table 1).

Table 1: *Designation of models of samples*

Number of samples	**Characteristics (conditions of the experiment)**		
	X_1 (m/min) *velocity of the filament winding*	**X_2 (N)** *fiber tension*	**X3 (^{0})** *winding angle*
1	21	110	**10**
2	21	110	**45**
3	21	110	**90**

Winding angle is the angle between fiber and the line on surface of the mandrel, which is parallel to mandrel axis. Coupled helical winding of layers (± θ) are usually preferred, whereas hoop winding - winding angle, very close to 90° and winding with very low winding angle can also be used. By varying the winding angle with respect to the mandrel axis, directional strength can be obtained by considering the loads, which will operate on the finished product.

low winding angle (θ = 10^0)

helical winding (θ=45^0)

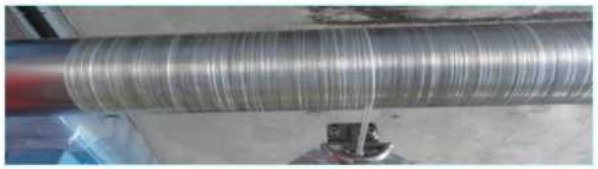

hoop winding(θ=90^0)

Figure 3. Winding of impregnated glass fibers

Calculated mass ratio between fiber and resin of the produced composite pipes was 75:25 wt. %. After winding samples were cured with industrial heater at 80°C and at 140°C, for four hours. After the curing operation, the removal of the mandrel from the specimens was performed. In this experimental study the investigation of the effect of winding angles on hoop tensile strength of glass fiber reinforced filament wound ring specimens was performed.

3. *Results and discussion*

For tensile tests three split-disk test specimens from each model of filament wound pipes was cut according to ASTM D2290. Tensile tests of split-disk samples were carried out at room temperature using universal testing machine Schenck with max load of 250 kN and loading speed of 5 mm/min. Width and thickness of each split-disk samples was measured with help of micrometer with reading to at least 0.0254mm. In this way prepared specimens were elongated till rupture with help of test fixture, made according to standard (Fig. 4).

Figure 4. *Split-disk test specimen and test fixture with specimen for hopp tensile testing*

Based on the obtained results, the general behavior of the specimens were determined. The results of the testing method of the split-ring specimens for determination of the hoop tensile strength are presented in Table 2.

Table 2: *Hoop tensile strength results of split-disk tests*

	Sample Designation	Weight (g)	Width (mm)	Thickness (mm)	F_{max} (N)	Tensile strength (MPa)	Winding angle (^{0})
1	1 -1	42,2	13,97	3,18	1600	18,00	10
	1-2	43,0	13,85	3,14	1250	14,34	
	1-3	43,7	14,00	3,14	1759	20,00	
2	2-1	53,6	14,01	3,18	25000	280,57	45
	2-2	53,8	13,9	3,16	24225	275,76	
	2-3	53,8	14,01	3,16	24400	275,57	
3	3-1	52,8	14,06	3,64	94500	923,24	90
	3-2	52,8	14,12	3,64	90250	877,97	
	3-3	53,8	14,12	3,65	93000	902,25	

The hoop tensile strength of the specimens were calculated by using the following equation:

$$\sigma = \frac{F_{max}}{2 \cdot A_m} \quad (1)$$

In equation (1) σ is ultimate hoop tensile strength, MPa, F_{max} is maximum load prior to failure recorded in Newton (N), whereas A_m is minimum cross-sectional area of the two reduced sections, d x b, mm^2 (Fig. 5).

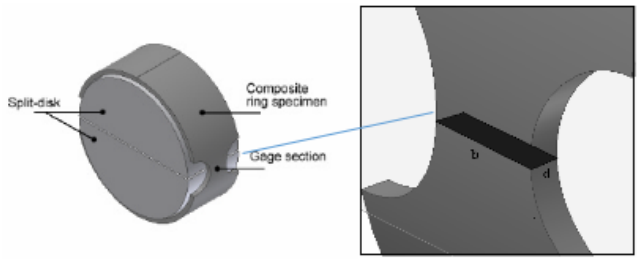

Figure 5. *Cross-sectional area on which hoop tensile stress is applied*

From the results shown in table 2 can be observed, that split-disk specimen 3 with tensile strength with average value of 901,15MPa had shown the best results and it was winded with angle 90^0. The specimen designated with 1 winded with angle 10^0 had shown much lower value up to 10 times lower than tensile strength from sample 3. From received results it can be concluded that mechanical properties of composite specimens depended from winding angles in filament winding technology, namely, the bigger winding angle lead to higher hoop tensile properties of filament-wound tubular samples. The optimal values for the hoop tensile strength are obtained for the samples winded with 45° winding angle.

4. Conclusion

Advantages of filament winding technique are high specific strength, specific modulus and fiber volume percentage of the finished products and high repeatability of the process. Production can be repeated successively, to obtain the same properties of the finished products.

The main limitation of filament winding technique is the difficulty in production of complex shapes due to the requirement of very complex mandrel designs. From results of the mechanical testing can be concluded, that the best results in tensile strength and break force were obtained from composite pipes winding with angle 90°. Change of winding angle will cause variation in the final mechanical results, whereas that bigger winding angle lead to higher hoop tensile properties of filament-wound tubular samples.

5. Literature

1. M. Hastak, A. Mirmiran, D.Richard, J. Reinf. Plast. Compos. 2003, 22, 1409-1430.
2. S. K. Mazumdar, Composites Manufacturing: Materials, Product, and Process Engineering, CRC Press, 2002.
3. P. Mertiny, F. Ellyin, and A. Hothan, An Experimental Investigation on the Effect of Multi-Angle Filament Winding on the Strength of Tubular Composite Structures, Composites Science and Technology, Vol 64, pp. 1-9, 2004.
4. E. Sideridis, G. A. Papadopoulos, Short-Beam and Three-Point-Bending Tests for the Study of Shear and Flexural Properties in Unidirectional- Fiber-Reinforced Epoxy Composites, Journal of Applied Polymer Science, 93, pp. 63-74, 2004.
5. S. Putic, M.Stamenovic, M. Zrlic, M. Bajaceta, Bending properties of Glass - Polyester Composite Pipes, 3th International Conference on Deformation Processing and Structure of Materials, 2007, Belgrade.
6. ASTM Standards D 2290-00, "Standard Test Method for Apparent Hoop Tensile Strength of Plastic or Reinforced Plastic Pipe by Split Disk Method", ASTM International, West Conshohocken, PA, 2013, www.astm.org.
7. G. Belingardi, M. P. Cavatorta, C. Frasca, Compos. Sci. Techol. 66, pp. 222-232, 2006.
8. S. Risteska, B. Samakoski, M. Stefanovska, Int. J. Eng. Res. Technol. 3, pp. 250-255, 2014.
9. A. Dorigato, A. Pegoretti, J. Compos. Mat., 48, pp. 1121-1130, 2014.
10. C. Dong, J. Duong, I. J. Davies, Flexural Properties of S-2 Glass and TR 30S Carbon Fiber - Reinforced Epoxy Hybrid Composites, Polym. Compos. 33, pp. 773-781, 2014.
11. I. J. Davies, H. Hamada, Adv. Composite Maters. 10, pp. 77-96, 2001.

Three-dimensional S-N curve method to estimate fatigue life of EN AW 6063.T66 aluminium alloy during combined loading under in-and-out of phase shift 0° and 90° and comparing with fatigue criteria

Ing. Uhríčik M., PhD.[1]; Ing. Kopas P., PhD.[1]; Prof. Ing. Palček P., PhD.[1]; Ing. Hurtalová L., PhD.[1]

[1]Faculty of Mechanical Engineering, University of Žilina, Slovak Republic
E-mail: milan.uhricik@fstroj.uniza.sk, peter.kopas@fstroj.uniza.sk, peter.palcek@fstroj.uniza.sk, lenka.hurtalova@fstroj.uniza.sk

Abstract: *The article deals with determining of fatigue lifetime of structural materials during by multiaxial cyclic loading. The theoretical part deals with the fatigue and with criteria for evaluation of multiaxial fatigue lifetime, especially Fatemi-Socie, Smith-Watson-Topper, Brown-Miller and Liu. The experimental part deals with testing of specimens for identification of the strain-life behaviour of material and determining the number of cycles to fracture of aluminium alloy for phase shift 0° and 90°. Extensive fatigue experiments were conducted using 6063.T66 aluminium alloy under multiaxial bending-torsion loading.*

KEYWORDS: ALUMINIUM ALLOY, MULTIAXIAL FATIGUE, FATIGUE LIFETIME, CRITERIA, CYCLIC LOADING

1. Introduction

Aluminium is the world's most abundant metal and is the third most common element, comprising 8% of the earth's crust. The versatility of aluminium makes it the most widely used metal after steel. Pure aluminium is soft, ductile, corrosion resistant and has a high electrical conductivity. It is widely used for foil and conductor cables, but alloying with other elements is necessary to provide the higher strengths needed for other applications. Aluminium is one of the lightest engineering metals, having strength to weight ratio superior to steel. By utilising various combinations of its advantageous properties such as strength, lightness, corrosion resistance, recyclability and formability, aluminium is being employed in an ever-increasing number of applications. This array of products ranges from structural materials through to thin packaging foils [1, 2, 3].

Fatigue failures in metallic structures are a well-known technical problem. In a specimen subjected to a cyclic load, a fatigue crack nucleus can be initiated on a microscopically small scale, followed by crack grows to a macroscopic size, and finally to specimen failure in the last cycle of the fatigue life. Understanding of the fatigue mechanism is essential for considering various technical conditions which affect fatigue life and fatigue crack growth, such as the material surface quality, residual stress, and environmental influence. This knowledge is essential for the analysis of fatigue properties of an engineering structure [4, 5].

Fatigue under combined loading is a complex problem. A rational approach might be considered again for fatigue crack nucleation at the material surface. The state of stress at the surface is two-dimensional because the third principal stress perpendicular to the material surface is zero [6]. Another relatively simple combination of different loads is offered by an axle loaded under combined bending and torsion. This loading combination was tested in our and also in many others experiments [7, 8]. In spite of this fact, fatigue mechanisms are still not fully understood. This is partly due to the complex geometrical shapes and also complex loadings of engineering components and structures which result in multiaxial cyclic stress-strain states rather than uniaxial.

2. Fatigue criteria

There are plenty of hypotheses used for evaluating a degree of damage caused by variable load [9, 10]. Life prediction methods which presume homogeneous material (free from cracks, inclusions or defects) at the outset of the investigation can be divided into strain-based (low-cycle fatigue) and stress-based (high-cycle fatigue) methods. Low-cycle fatigue is characterized by repeated plastic strains during cyclic loading conditions where fatigue failure occurs after relative low number of load cycles (in the order of 10^4 cycles). This design approach is normally used in fatigue assessment of local areas where high stress concentrations exist and the material response locally is repeated plastic deformation. In addition, stress-based approaches use the elastic stress range (or amplitude) as the governing load parameter. There were chosen four fatigue criteria: Fatemi-Socie, SWT, Brown-Miller and Liu fatigue criterion.

Fatemi and Socie [11] observed that the Brown and Miller's idea could be successfully employed even by using the maximum stress normal to the critical plane, because the growth rate mainly depends on the stress component normal to the fatigue crack. Starting from this assumption, he proposed two different formulations according to the crack growth mechanism: when the crack propagation is mainly MODE I dominated, then the critical plane is the one that experiences the maximum normal stress amplitude and the fatigue lifetime can be calculated by means of the uniaxial Manson-Coffin curve; on the other hand, when the growth is mainly MODE II governed, the critical plane is that of maximum shear stress amplitude and the fatigue life can be estimated by using the torsion Manson-Coffin curve [9]. Criterion has the following form:

$$\frac{\Delta\gamma}{2}\times\left(1+k\times\frac{\sigma_{n,max}}{\sigma_y}\right)=\frac{\tau_f^{'}}{G}\times\left(2\times N_f\right)^{b_\gamma}+\gamma_f^{'}\times\left(2\times N_f\right)^{c_\gamma} \qquad (1)$$

Smith, Watson and Topper (SWT) created a parameter for multiaxial load, which is based on the main deformation range $\Delta\varepsilon_1$ and maximum stress $\sigma_{n,max}$ to the main plane. Criterion has the following form:

$$\sigma_{n,max}\times\frac{\Delta\varepsilon_1}{2}=\frac{\sigma_f^{'2}}{E}\times\left(2\times N_f\right)^{2b}+\sigma_f^{'}\times\varepsilon_f^{'}\times\left(2\times N_f\right)^{b+c} \qquad (2)$$

Brown and Miller [12] observed that the fatigue life prediction could be performed by considering the strain components normal and tangential to the crack initiation plane. Moreover, the multiaxial fatigue damage depends on the crack growth direction. Different criteria are required if the crack grows on the component surface or inside the material. In the first case they proposed a relationship based on a combined use of a critical plane approach and a modified Manson-Coffin equation, where the critical plane is the one of maximum shear strain amplitude. Criterion, which was created, has the following form:

$$\frac{\Delta\gamma_{max}}{2} + S \times \Delta\varepsilon_n = A \times \frac{\sigma_f - 2 \times \sigma_{n,mean}}{E} \times \left(2 \times N_f\right)^b + B \times \varepsilon_f' \times \times \left(2 \times N_f\right)^c \quad (3)$$

Liu created a virtual model of the deformation energy, which is a generalization of the axial energy on the basis of prediction of fatigue life. Criterion has the following form:

$$\Delta W = 4 \times \sigma_f' \times \varepsilon_f' \times \left(2 \times N_f\right)^{b+c} + \frac{4 \times \sigma_f'^2}{E} \times \left(2 \times N_f\right)^{2b} \quad (4)$$

Where: γ_f' is the fatigue ductility coefficient in torsion; ε_f' is the fatigue ductility coefficient; σ_f' is the fatigue strength coefficient; $\sigma_{n,max}$ is the maximum stress; $\sigma_{n,mean}$ is the mean stress; σ_y is the stress in the direction of the axis y; τ_f' is the fatigue strength coefficient in torsion; $\Delta\gamma_{max}$ is the maximum shear strain range; $\Delta\varepsilon_n$ is the normal strain range; ΔW is the virtual strain energy; b is the fatigue strength exponent; b_γ is the fatigue strength exponent in torsion; c is the fatigue ductility exponent; c_γ is the fatigue ductility exponent in torsion; N_f is the number of cycles to fracture; A, B, S, k, α are material parameters; E is the elasticity modulus in tension; G is the elasticity modulus in torsion.

3. Test material

The research was conducted on an AlMgSi07.F25 aluminium alloy: the EN AW 6063.T66 aluminium alloy. The EN AW 6063.T66 is a medium strength alloy, suitable for applications where no special strength properties are required. The T66 treatment corresponds to solution heat-treated and then artificially aged (precipitation hardened) to a higher level of mechanical properties through special control of a manufacturing process. The material used in this research was delivered in the form of a cylindrical shape with a diameter 10 mm. The length of cylindrical bars was 150 mm. The material was in a rolled state. The shape of test bar is shown in Fig.1. This test bar had a defined section, in which was expected an increased concentration of stress and creation a fatigue fracture.

Fig.1 *The shape of a test bar*

4. Experimental strain-life data results

One hundred and ninety-five smooth specimens for phase shift 0° and one hundred and ninety-five smooth specimens for phase shift 90°, were tested under strain controlled conditions in order to identify the strain-life behaviour of the experimental material. After machining, the specimen surfaces were mechanically polished. The experiments were carried out in an electro mechanic fatigue test machine developed on University of Žilina (Fig.2 and Fig. 3).

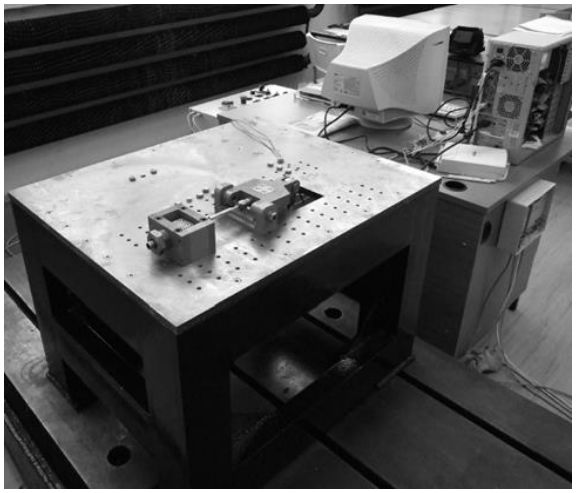

Fig.2 *Electro mechanic fatigue test machine*

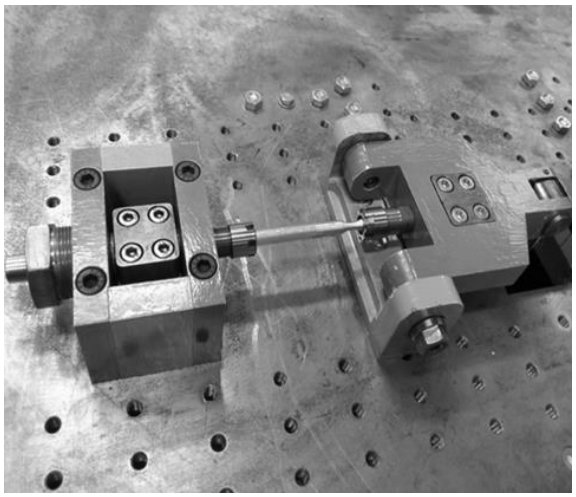

Fig.3 *A gripping attachment of test machine*

For evaluation of fatigue curves it needs to know stress and strain conditions on individual loading levels. A sinusoidal waveform was used as command signal. The fatigue tests were conducted with constant strain amplitudes, at room temperature, in air. The specimens were cyclic loaded under strain control with symmetrical proportional bending- torsion loading, with a nominal strain ratio, R_ε = -1.

The computational fatigue tests were performed under in-phase cyclic loading with the zero mean value. All tests were performed under controlled bending and torsion moments. Frequency of each analysis was equal to 30 Hz.

This research was conducted on an EN AW 6063.T66 aluminium alloy. This material is a medium strength alloy, suitable for applications where no special strength properties are required.

From experimentally measured values of number of cycles to failure was created three-dimensional fatigue curve $\varepsilon_{xx} - \gamma_{xy} - N_f$ for phase shift 0°, which is shown in Fig. 4.

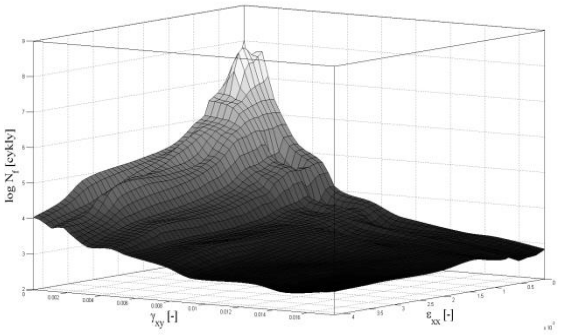

Fig.4 *Three-dimensional fatigue curve ε_{xx} - γ_{xy} - N_f for multiaxial fatigue with phase shift 0°*

For another analysis was used a Fatigue Calculator software [13]. This program can quickly calculate fatigue lifetime of selected material. In our calculation we considered with four multiaxial criteria described above.

From those calculated values of number of cycles to failure were created three-dimensional fatigue curves for phase shift 0°. In Fig. 5 is shown a three- dimensional fatigue curve for Fatemi-Socie criterion, in Fig. 6 is for SWT criterion, in Fig. 7 is for Brown-Miller criterion and in Fig. 8 is for Liu criterion.

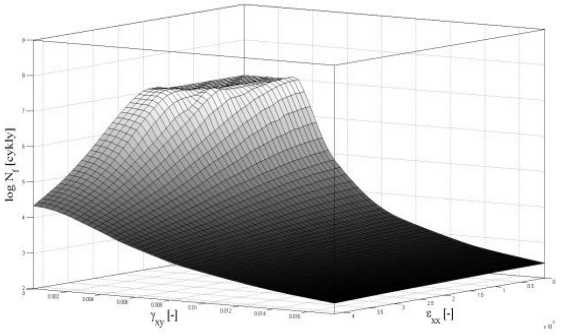

Fig.5 *Three-dimensional fatigue curve ε_{xx} - γ_{xy} - N_f for multiaxial Fatemi-Socie criterion with phase shift 0°*

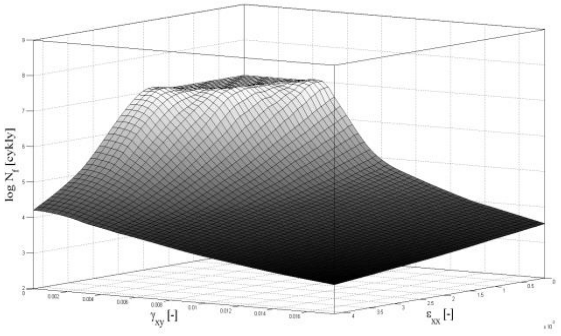

Fig.6 *Three-dimensional fatigue curve ε_{xx} - γ_{xy} - N_f for multiaxial SWT criterion with phase shift 0°*

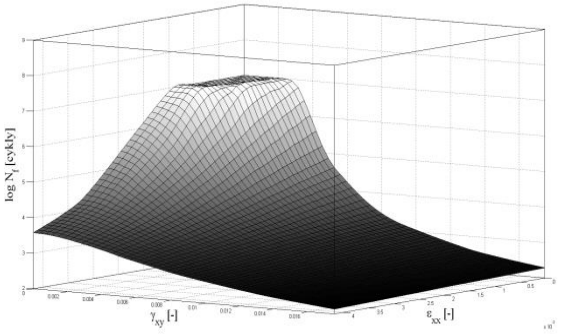

Fig.7 *Three-dimensional fatigue curve ε_{xx} - γ_{xy} - N_f for multiaxial Brown-Miller criterion with phase shift 0°*

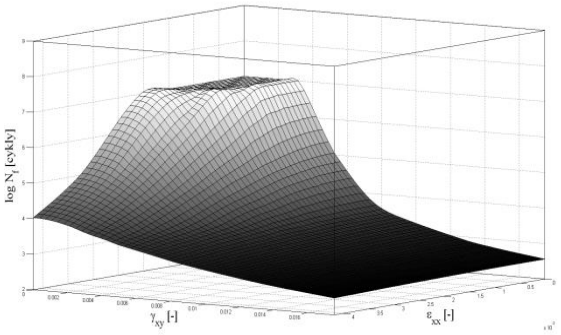

Fig.8 *Three-dimensional fatigue curve ε_{xx} - γ_{xy} - N_f for multiaxial Liu criterion with phase shift 0°*

From the experimentally measured fatigue values there was created three-dimensional fatigue curve $\varepsilon_{xx} - \gamma_{xy} - N_f$ for phase shift 90°, which is shown in Fig. 9.

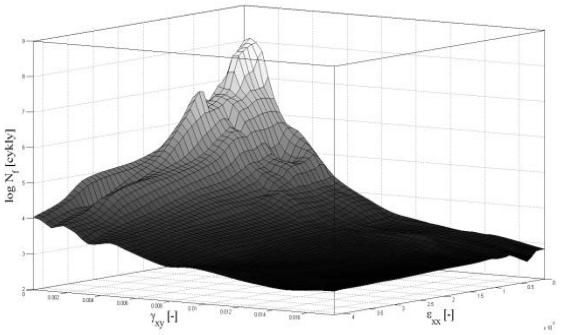

Fig.9 *Three-dimensional fatigue curve ε_{xx} - γ_{xy} - N_f for multiaxial fatigue with phase shift 90°*

Using by Fatigue Calculator software there were calculated values of number of cycles to failure of three-dimensional fatigue curves for phase shift 90°. From the Fig. 10 it can be seen a three-dimensional fatigue curve for Fatemi-Socie criterion, in Fig. 11 can be seen fatigue results for SWT criterion, in Fig. 12 can be seen fatigue results for Brown-Miller criterion and in Fig. 13 can be seen fatigue results for Liu criterion.

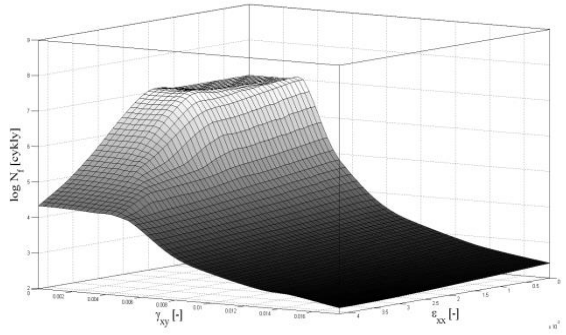

Fig.10 *Three-dimensional fatigue curve ε_{xx} - γ_{xy} - N_f for multiaxial Fatemi-Socie criterion with phase shift 90°*

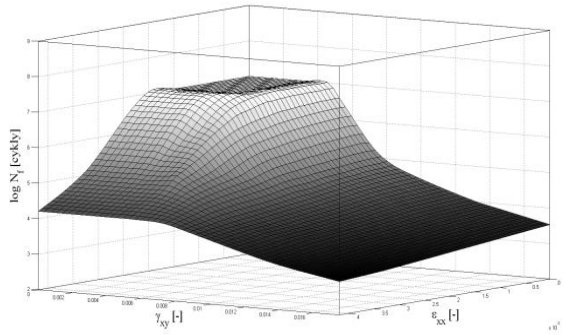

Fig.11 *Three-dimensional fatigue curve ε_{xx} - γ_{xy} - N_f for multiaxial SWT criterion with phase shift 90°*

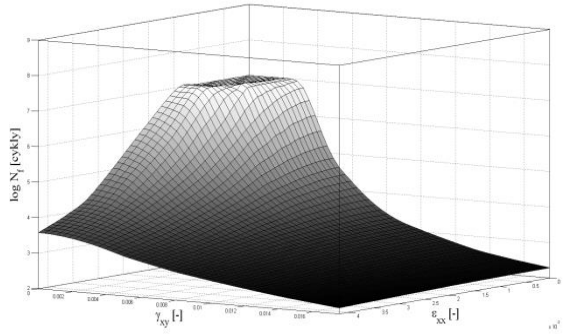

Fig.12 *Three-dimensional fatigue curve ε_{xx} - γ_{xy} - N_f for multiaxial Brown-Miller criterion with phase shift 90°*

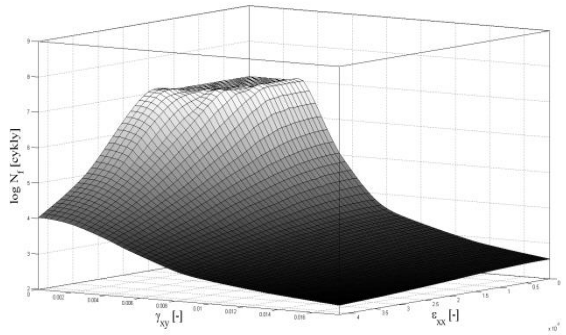

Fig.13 *Three-dimensional fatigue curve ε_{xx} - γ_{xy} - N_f for multiaxial Liu criterion with phase shift 90°*

5. Conclusion

Every multiaxial criteria applied to fatigue lifetime calculation and also values of number of cycles to failure from experiment for specimens of aluminium alloy EN AW 6063.T66 increases with decreasing strain amplitude continuously in the cycles of number region. Comparing three-dimensional curves is evident that criteria from Fatigue Calculator give higher lifetime than experiment in the whole area of the number of cycles at the same load amplitudes. This may be caused by different material parameters, which were used for each models of damage. They probably do not include all real parameters and properties of the comparison of the experimental material that probably affected the sensitivity of the numerical calculation.

6. Acknowledgements

This work has been supported by Scientific Grant Agency of Ministry of Education of Slovak Republic and Slovak Academy of Science, No.1/0797/12, No.1/0533/15 and project EU ITMS 26110230117.

7. References

[1] www.aalco.co.uk

[2] HURTALOVÁ, L., TILLOVÁ, E. (2013). *Elimination of the negative effect of FE-rich intermetallic phases in secondary (recycled) aluminium cast alloy*, pp.44-50. Manufacturing Technology, Vol.13, Num.1, ISSN 1213-2489.

[3] UHRÍČIK, M., PALČEK, P., SOVIAROVÁ, A., SNOPIŃSKI, P., (2014). *Change of internal friction on aluminium alloy with 10,1% Mg dependence on the temperature*, pp.467-470. Manufacturing Technology, Vol.14, Num.3, ISSN 1213-2489.

[4] BOKŮVKA, O., NICOLETTO, G., KUNZ, L., PALČEK, P., CHALUPOVÁ, M. (2002). *Low & high frequency fatigue testing.* CETRA and University of Žilina, Žilina.

[5] BATHIAS, C. (2001) *Fatigue in the very high cycle regime*. Vienna, Austria.

[6] BANNANTINE, J. A., SOCIE, D. F. (1992). *A multiaxial fatigue life estimation technique.* In: Advances in Fatigue Lifetime Predictive Techniques, ASTM STP 1122. Eds: M. R. Mitchell a R. W. Landgraf. Philadelphia, American Society for Testing and Materials, pp. 249-275.

[7] GOUGH, H.J. AND POLLARD, H.V., (1951). *Some experiments of the resistance of metals to fatigue under combined stresses.* Min. of Supply, Aero Res. Council, RSM 2522, Part I.

[8] LEGER, J. (1989) *Fatigue life testing of crane drive shafts under crane-typical torsional and rotary bending loads*. Schenck Hydropuls Mag., Issue 1/89, pp.8–11.

[9] BALDA, M., SVOBODA, J., FRÖHLICH, V., (2003). *Using hypotheses for calculating fatigue lives of parts exposed to combined random loads*, Engineering Mechanics, Vol. 10, Issues 5, pp. 12-15.

[10] CHUNG, Y. S., ABEL, A.. *Low cycle fatigue of some aluminium alloys*. In: Low Cycle Fatigue, ASTM STP 942, H., American Society for Testing and Materials, Philadelphia, PA, pp. 94-106

[11] FATEMI, A. , SOCIE, D. F. (1988). *A critical plane approach to multiaxial fatigue damage including out-of-phase loading.* Fatigue Fract. Engng. Mater. Struct , pp.149-166.

[12] BROWN, M. W., MILLER, K. J. (1973). *A theory for fatigue under multiaxial stress-strain conditions.* In: Proc. Inst. Mech. Engrs, Vol. 187, 1973, pp.745-755.

[13] www.efatigue.com

ОПТИМИЗАЦИЯ НА ПРОЦЕС ОБЕЗВОДНЯВАНЕ ПО ИКОНОМИЧЕСКИ КРИТЕРИЙ

OPTIMIZATION OF DEWATERING PROCESS BY ECONOMICAL CRITERIA

доц. д-р Парашкевова Д. Д. МГУ „Св. Иван Рилски”, София, РБългария, dani.parashkevova@gmail.com
инж. Стойкова Л. С. МГУ „Св. Иван Рилски”, София, РБългария, lachezara.stoykova@gmail.com

Abstract: *The purpose of the dewatering is reducing the water content to a specified value and this allows better preservation, storage and transport of products. It is known that depending on the water content, the products are divided by the liquid, wet, humid, air dry and dry. There are three stages in most dressing plants for the removal of humidity in flotation concentrate: thickening, filtration and drying. In one way or another each of these processes are automated. But local automation does not exhaust the potential of technological units, full use of which is possible only in a concerted work. The shared use of production equipment, combined into a consistent technological circuit must be performed primarily at productivity, but as a general criterion for efficiency of the system is necessary to take qualitative and economic indicators.*

For the operational control of dewatering process, of great importance are: selected criterion for optimization and development of advanced computer systems.

Keywords: PROCESS, DEWATERING, THICKENING, FILTRATION, DRYING, OPTIMIZATION CRITERIA, CONTROL, AUTOMATION

1. Увод

Отделянето на влагата от флотационния концентрат в повечето обогатителни производства преминава през три етапа: сгъстяване, филтрация и сушене. Повечето системи за управление на процес обезводняване са локални. Но локалната автоматизация не изчерпва потенциалните възможности на технологичните агрегати, пълното използване на които е възможно само при тяхната съгласувана работа. Съгласуването на свързаните апарати, обединени в последователна технологична верига, трябва да се осъществява преди всичко по производителност, а в качеството на общ критерий за ефективна работа на системата могат да се приемат качествените и икономически показатели на процес обезводняване.

Най-разпространените съоръжения и машини за разделяне на течната от твърдата фаза са сгъстителите, филтрите и барабанните сушилни.

2. Предпоставки и начини за решаване на проблема

Параметрите, характеризиращи крайната влажност на продукта при определени производства не могат да бъдат постигнати само с процесите сгъстяване и филтрация, изключвайки процес сушене. От друга страна, изключването на операциите на филтриране на сгъстения продукт от общия процес за отделяне на влагата води до съществено увеличаване на разходите, свързани с необходимостта от изпарение на голямо количество течност в сушилните.

В редица процеси на обезводняване филтрацията заема важно място. От работата на това звено зависи сушенето и затова е необходимо много от параметрите на процес филтрация да се стабилизират или регулират. Управлявайки изходните параметри на вакуум-филтрите лесно могат да се постигнат минимални разходи за обезводняване при зададена влажност на готовия продукт.

При автоматично управление на процес обезводняване от голямо значение има изборът на критерий за оптимизация и създаването на съвременни системи, чрез които да се осигури оперативното му управление.

Като общ икономически критерий за оптимизация в целия цикъл на обезводняване може да се приеме сумата от разходите, изчислени за единица продукция. Общите разходи за обезводняване се формират от отделните разходи за сгъстяване, филтрация и сушене. Тези разходи могат да се намалят при правилно изчислено разпределение на натоварването, т.е разпределение на количеството отделена течност между тези процеси.

3. Решение на проучения проблем

На фиг.1 са показани изменението на диференциалните стойности в различните етапи на обезводняване. Под диференциална стойност се разбира разходите, направени за единица отделена влага при различна влажност на продукта. Например, разходите за 1 [gr] отделена влага в работния участък от кривата на диференциалните стойности при сгъстяване са еднакви.

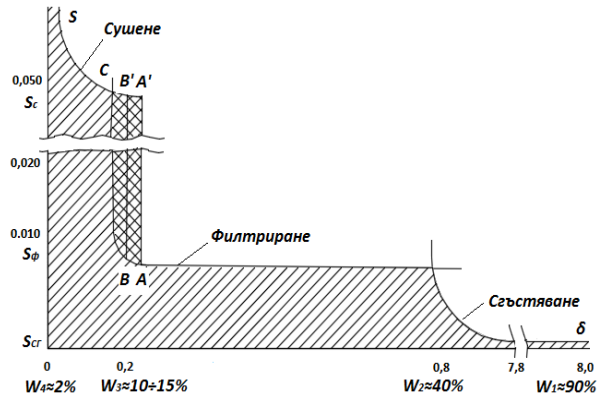

Фиг. 1. *Криви на диференциалните стойности при отделните стадии на процес обезводняване*

Всички процеси на обезводняване се характеризират с увеличаване на времето, необходимо за отделяне на едно и също количество влага. При сгъстяване изменението на концентрацията на сгъстения продукт се описва с диференциалното уравнение:

$$(1) \quad \frac{\partial C}{\partial t} = M\frac{\partial^2 C}{\partial x^2} - L.g\left(\gamma_T - \gamma_{TB}\right)(1-2C)\frac{\partial C}{\partial x},$$

където g е земното ускорение, C - концентрация на твърдата фаза в продукта, M - коефициент на дифузия, L - константа, свързана със съпротивлението на средата, γ_T - относително тегло на течната фаза в продукта, γ_{TB} - относително тегло на твърдата фаза в продукта.

$$(2)\quad dr_{об} = \frac{\varepsilon.\mu.r_0.h^2}{\Delta p}\left[\frac{1-m_0}{1-m_0 m_e}\right]\frac{dm_e}{m_e^y},$$

където m_e е ефективно насищане, равно на отношението на обема на движещата се течност към общия обем течност и въздух, ε - порьозност.

Функцията за който и да е стадий на обезводняване S_i може да се запише в следния вид:

$$(3)\quad S_i = S_{0i} + \frac{a_i}{W - W_{кр.i}},$$

където S_{0i} е начална диференциална стойност на обезводняване в стадий i, W - текуща стойност на влажността, a_i - коефициент на пропорционалност, $W_{кр.i}$ - най-малката възможна стойност на влажността, която може да се достигне в стадий i.

Намаляването на разходите за доизсушаване на концентрата при филтриране е илюстрирано на фиг.1. Ако филтрацията завършва при влажност, съответстваща на точка B вместо точка A, то намаляването на разходите за процес сушене са пропорционални на площта на фигурата $ABB'A'$. Разходите ще бъдат най-малки, ако процес филтрация завършва при влажност, съответстваща в точка C. В съответствие с функцията (3) и фиг.1, изразът за общата стойност $S_{об}$ за целия процес обезводняване има вида:

$$(4)\ S_{об} = S_1 + S_2 + S_3 = \int_{W_2}^{W_1}\left(S_{сг} + \frac{a_{сг}}{W - W_{кр.сг}}\right)dW + \int_{W_3}^{W_2}\left(S_ф + \frac{a_ф}{W - W_{кр.ф}}\right)dW + \int_{W_4}^{W_3}\left(S_c + \frac{a_c}{W - W_{кр.c}}\right)dW$$

Ако се приеме, че $W_{кр.с} = 0$, тъй като практически в сушилната може да се отдели цялата влага, а най-малките стойности на сгъстения $W_{кр.сг}$ и филтриран $W_{кр.ф}$ продукт имат максимални величини, определящи се от основните свойства на пулпа, характеристиките на оборудването и от много други фактори, влияещи върху цялостния процес. Например, $W_{кр.ф}$ не може да бъде равно на нула, тъй като при филтриране чрез вакуум-филтър налягането е недостатъчно за отделяне на цялата капилярна влага. Величината на началната влажност на концентрата W_1 може да се счита за постоянна, тъй като малките й изменения не могат да доведат до значителен ръст на разходите за сгъстяване.

4. *Резултати и дискусия*

Задачата на оптимизацията за процес обезводняване, която е свързана с достигане на минимални разходи за единица продукция, може да се представи във вида:

$$(5)\quad S_{об} = S_{\min},$$

където $S_{\min}$ са минимално възможните разходи за единица продукция при дадени условия.

На величината обща стойност на разходите за процес обезводняване най-силно влияе филтрирането. Ако този процес започва при малка плътност на продукта, то увеличаването на общите разходи за обезводняване ще са за сметка на филтрирането. При малка плътност на сгъстения продукт по-изгодно ще бъде да се продължи процеса на сгъстяване, а не да започне филтриране. Ако филтрирането завършва при достатъчно висока влажност, то сумарните разходи за обезводняване ще нараснат и от увеличените разходи за стадий сушене.

Основните изходни параметри на процес филтриране са производителността и влажността. Повишаването на производителността е свързано с увеличаване броя на оборотите на вакуум-филтъра в определени граници, което води до повишаване на влажността. И обратно, намаляването на производителността води както до промяна в началната диференциална стойност на обезводняване $S_ф$, така и до промяна на крайната влажност на кека W_3.

Както е известно, производителността на вакуум-филтъра нараства при увеличаване плътността на изходния продукт, постъпващ от сгъстителя.

Зависимостта между началното значение на диференциалната стойност на обезводняване на филтъра $S_ф$ и неговата производителност Q има вида:

$$(6)\quad S_ф = \frac{K}{Q}$$

Стойността на влажността на концентрата след филтриране може да се опише със следващия израз, показващ връзката между влажността на пулпа след сгъстителя W_2 и производителността на вакуум-филтъра Q:

$$(7)\quad W_3 = W_2 = \frac{b}{\sqrt{Q}}$$

Като се заместят зависимости (6) и (7) в израз (4), се получава:

$$(8)\quad S_{об} = \int_{W_2}^{W_1}\left(S_{сг} + \frac{a_{сг}}{W - W_{кр.сг}}\right)dW + \int_{W_2 - \frac{b}{\sqrt{Q}}}^{W_2}\left(\frac{K}{Q} + \frac{a_ф}{W - W_{кр.ф}}\right)dW + \int_{W_4}^{W_2 - \frac{b}{\sqrt{Q}}}\left(S_c + \frac{a_c}{W_2}\right)dW;$$

$$(9)\quad S_{об} = -S_{сг} - \frac{a_{сг}}{W_2 - W_{кр.сг}} + \frac{a_ф}{W_2 - \frac{b}{\sqrt{Q}} - W_{кр.ф}} + S_c + \frac{a_c}{W_2}$$

Ако $S_{об} = 0$, то сумарните разходи ще са минимални. Представяйки израз (9) в друг вид и като се приравни към нула, се получава:

$$(10)\quad W_2^3 + \left(\frac{b}{\sqrt{Q}} + t_1\right)W_2^2 + \left(\frac{b}{\sqrt{Q}} + K_1\right)W_2 + c_1\frac{b}{\sqrt{Q}} + d_1 = 0,$$

където:

$$(11)\quad t_1 = W_{кр.ф} + W_{кр.сг} + \frac{a_{сг} - a_ф + a_c}{S_c - S_{сг}};$$

$$(12)\quad K_1 = W_{кр.ф} + W_{кр.с} - \frac{a_{сг}W_{кр.ф} + a_ф W_{кр.сг} - a_c\left(W_{кр.ф} + W_{кр.сг}\right)}{S_c - S_{сг}};$$

$$(13)\quad c_1 = \frac{a_c W_{кр.сг}}{S_c - S_{сг}};$$

$$(14)\quad d_1 = \frac{a_c W_{кр.сг} - W_{кр.ф}}{S_c - S_{сг}}$$

Корените на уравнението (10) отговарят на изискването $S_{об} = S_{\min}$. С алгебричните уравнения (9) и (10) се определя връзката между желаната производителност Q на вакуум-

филтъра и влажността на продукта, постъпващ за филтриране при минимални разходи. Заместваики в уравнение (10) текущата стойност на влажността на изходния продукт и решавайки неговата относителна Q, може да се намери оптималната производителност $Q_{опт}$, отговаряща на желаните най-добри стойности в общия цикъл. И обратно, ако се променя производителността на филтъра, то по уравнение (10) може да се съди за това, каква плътност на продукта е необходимо да се достигне в сгъстителя.

Може да се направи извода, че чрез получените изрази могат да се изберат стойности на производителността на вакуум-филтъра при различна влажност на пулпа W_2, отговарящи на изискването за минимални общи разходи на обезводнителния процес.

Ако изменението на производителността се постига чрез изменение броя на оборотите на вакуум-филтъра, то влажността на кека след продухването също ще се промени, а оттам и съотношението на разходите за филтриране и сушене (фиг.1).

Системата за автоматично управление на целия процес обезводняване трябва да включва:

- регулиране плътността на продукта от сгъстителя;
- регулиране разхода на пулп и неговото ниво във ваната на вакуум-филтъра;
- стабилизация на вакуума;
- регулиране влажността на кека;
- регулиране влажността на концентрата след сушене.

На фиг.2 е дадена блокова схема за оптимално управление на цикъла на обезводняване, включващо контрол и регулиране на влажността на продукта след всяка операция въз основа на икономически критерий по каналите за управление.

В блоковата схема количеството течност и твърдо вещество са обозначени съответно с M_i и m_i, а всеки обект е представен чрез две звена, първото от които е за течност, а второто – за твърд продукт. Това условно разделяне на обекта е необходимо, за да се разкрият специфичните особености за протичащите процеси. Предавателните функции на звената на обектите по влажност $W_{1в}(p)$, $W_{2в}(p)$, $W_{3в}(p)$ и по твърдо вещество $W_{1т}(p)$, $W_{2т}(p)$, $W_{3т}(p)$ съответстват на периодична функция с инерционно звено със закъснение:

$$(15)\quad W(p)=\frac{k}{1-pT}e^{-\tau}$$

При смущение на входа на системата, например при увеличаване или намаляване количеството на влагата с ΔM в сгъстителя (при това количеството твърдо вещество може да е постоянно)се променя съотношението течно-твърдо в пулпа в разтоварването на сгъстителя. Това обстоятелство променя производителността на вакуум-филтъра и влажността на изходния кек, което изисква промяна в работния режим на сушилната така, че съотношението M_c / m_c на изхода на системата да не се променя.

При работа в автоматичен режим отчетите за производителността на всички агрегати и текущите стойности на влажността $W_1 \div W_4$ постъпват в операторска станция. Въз основа на приведените по-горе изрази за изчисляване на оптималните стойности на производителността на вакуум-филтъра и в съответствие с тях от системата се изработват управляващи въздействия, постъпващи към изпълнителните устройства на I - сгъстителя, II - филтъра и III - сушилната.

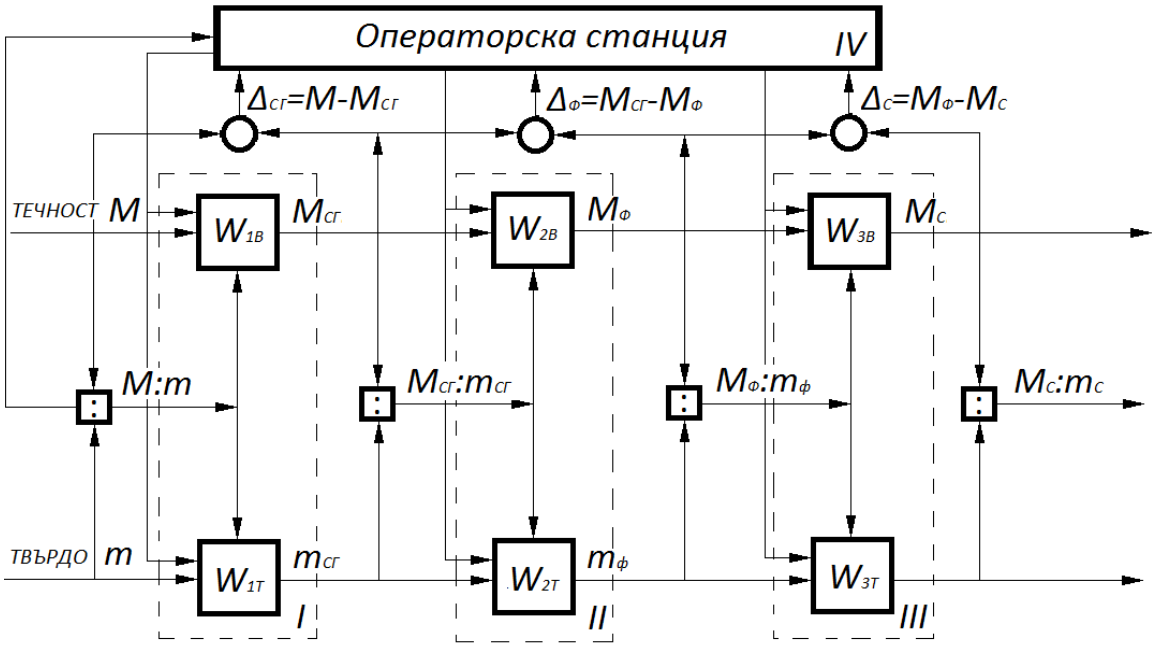

Фиг.2 . *Блокова схема за оптимално регулиране цикъла на обезводняване*

5. Заключение

За получаване на високо качествена готова продукция в обогатителните фабрики е необходима автоматична стабилизация на влажността на концентрата в зададени регламентирани граници. Основна задача на системата за управление на процес обезводняване е чрез осигуряване на минимални загуби на твърдо да се постигне максимален икономически ефект. Автоматизацията на технологичните процеси сгъстяване, филтрация и сушене включва контрол на състоянието на технологичното оборудване, контрол на технологичните параметри, регулиране и оптимизация по икономически критерий.

6. Литература

1. Ковачев К., Г. Клисуранов. Обогатяване на полезни изкопаеми. София, Изд. „Техника”, 1987

2. Тихонов О. Автоматизация производственных процессов на обогатительных фабриках. Москва, Изд. „Недра”, 1985

3. Троп А., В. Козин, Е. Прокофьев. Автоматическое управление технологическими процессами обогатительных фабрик. Москва, Изд. „Недра”, 1986

4. Sougy Jacques, Guillaneau Jean-Claude. *Les capteurs innovants dans I`industrie minėrale.* [Congrės SIM ”Minėral et massif central”, Clermont-Ferrand, 9-12 oct., 2001]. Mines et carrières. 2001. 83, sept., с. 121. Фр.

5. Engineering and Mining Journal, 2013

BOUSINESQ'S PROBLAM IN THEORY OF ELASTICITY AND ULTRASONIC

Alexander POPOV
Bulgarian Academy of Science, Institute of Mechanics, Sofia, Bulgaria

Abstract : *The evaluation of yield stress - σ_S is frequently encounter in material testing. In this method there is necessity of manufacture of test-tube from tested material or detail and made tension test. There is destructive method. For many details there is not acceptable. In material testing there is interest to non-destructive evaluation of yield stress σ_S for the materials and details. In this paper is lock at possibility for non-destructive evaluation of yield stress σ_S by means measure Brinel,s hardness – HB or velocities of propagation of longitudinal and transversal ultrasonic waves - V_L and V_T in tested materials and details.*

KEY WORDS: *NON-DESTRUCTIVE EVALUATION OF YIELD STRESS, VELOCITIES OF PROPAGATION OF ULTRASONIC WAVES*

1. INTRODUCTION

The evaluation of the technological characteristics yield stress - σ_S is frequently encounter in material testing [1]. In this method there is necessity of manufacture of test-tube from tested material or detail and made tension test. There is destructive method. For many details there is not acceptable.

In material testing there is interest to non-destructive evaluation of yield stress σ_S for the materials and details.

In this paper is lock at possibility for non-destructive evaluation of yield stress σ_S by means measure Brinel,s hardness – *HB* or velocities of propagation of longitudinal and transversal ultrasonic waves - V_L and V_T in tested materials and details.

2. CONTACT BOUSSINESQ'S PROBLEM

The contact Boussinesq's problem in theory of elasticity [2,3,4] in follow. Let the surface $x_1\ x_2$ is loaded with force *F* by sphere with diameter D (figr.1). The stresses $\{\sigma_{ij}; i, j = 1,2,3\}$ and displacements $\{u_i; i = 1,2,3\}$ is necessity to determined.

In particular, displacement $u_3(0)$, in contact point, is $u_3(0) = \frac{1}{4.\pi}\left(\frac{1}{\mu}.\frac{\lambda+2.\mu}{\lambda+\mu}\right)\frac{F}{d/2}$ [1], where λ, μ - Lame's coefficients [1,6].

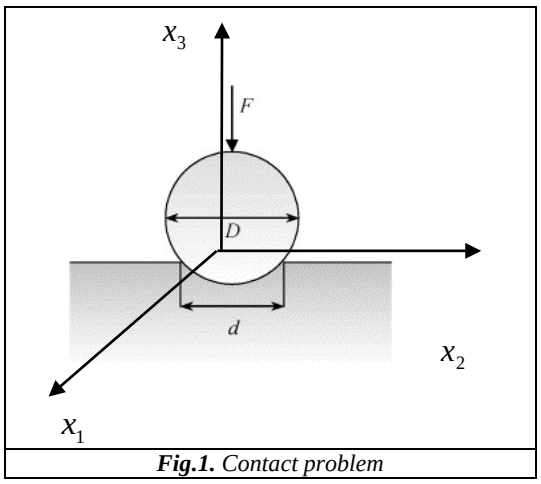

Fig.1. *Contact problem*

In Brinel's testing [4] the conditions there are [1]:

$\frac{P}{D^2}$ = 30; D = 10mm; $\frac{d}{D} = \frac{2}{5}$. Therefore

$u_3(0) = \frac{375}{\pi}\left(\frac{1}{\mu}.\frac{\lambda+2.\mu}{\lambda+\mu}\right)$.

From the stresses $\{\sigma_{ij}; i, j = 1,2,3\}$, there is the [2,3]

$$\tau_{\max} = \frac{1}{2}\,\varphi(\nu)\ HM,(\ Bousinesq) \qquad (1)$$

$$\varphi(\nu) = \frac{1}{2}(1-2.\nu) + \frac{2}{9}(1+\nu).[2.(1+\nu)]^{1/2}$$

HM is Maier's hardness. $HM = \frac{F}{S}$, where *F* – load, *S* – area of circle of impress in area ($x_1\ x_2$), $S = \frac{\pi.d^2}{4}$. The relationship between *HM* and Brinel's hardness *HB* is $\frac{HB}{HM} = 1 - \Psi$, where Ψ - steppe of deformation in impress [4]. In general $\Psi = \Psi\left(\frac{d}{D}\right)$ and therefore *HB* < *HM*. If $\frac{d}{D} < \frac{2}{5}$ (Ψ < 3 %)q then deferent between *HB* and *HM* is ~ 3 %. Therefore

$$HM \approx HB \qquad (2)$$

If introduce the sphere in area ($x_1\ x_2$) there is elastic-plastic contact (fig.1). There is Treska's condition [5]

$$\tau_{\max} = \tau_S = \frac{1}{2}\,\sigma_S \qquad (3)$$

In this case the relationship (1) reduce to

$$\sigma_S \approx \varphi(\nu)\ HB,(\ Bousinesq) \qquad (4)$$

In experimental verification he yield stress σ_S calculated by (2) is not acceptable. There is necessity from condition for agreement of

experimental data with (2). To introduce coefficient K_{AGR}. In this case the (2) reduce to

$$\sigma_S \approx K_{AGR}\ \varphi(\nu)\ HB,(\ Bousinesq) \qquad (5)$$

For steel with %C ~ 0.15 the data from mechanical test are: HB^{MT} = 1430 *MPa*, σ_S^{MT} = 255 *MPa*, ν = 0.28 [7] т.е. $\varphi(0.28)$ = 0.67. Therefore

$$K_{AGR} = \frac{1}{3.75} \approx \frac{1}{4}.$$

3. BRINEL'S HARDNESS

In material science Brinel's hardness *HB* is define by [1,4]

$$HB = \frac{P}{\pi.D.u_3(0)} \qquad (6)$$

Put the test condition and the displacement $u_3(0)$ in (6) and Brinel's hardness is

$$HB \approx \frac{4}{5}\left(\mu.\frac{\lambda+\mu}{\lambda+2\mu}\right) \qquad (7)$$

Relationship between Lame's coefficients - λ, μ and velocities of propagation of longitudinal and transversal ultrasonic waves - V_L and V_T [ASTM E 494-92] is [6]

$$\lambda + 2.\mu = \rho V_L^2\ ;\ \mu = \rho V_T^2 \qquad (8)$$

There is relationship between Lame's coefficients – λ, μ and Young's modulus – E and Poisson's ratio - ν

$$\lambda = a_\lambda(\nu)\,E\ ;\ \mu = a_\mu(\nu)\,E \qquad (9)$$

where $a_\lambda(\nu) = \frac{\nu}{(1+\nu)(1-2.\nu)}$, $a_\mu(\nu) = \frac{1}{2.(1+\nu)}$. As for carbon steels the Poisson's ratio is written in a relatively narrow range, namely $0.23 \le \nu \le 0.32$, it can be considered an average value of υ ≈ 0.28. In this sense, in the parameters $a_\lambda(\nu)$ and $a_\mu(\nu)$ from (9) are constants, i.e. $a_\lambda(\nu) \equiv a_\lambda$ and $a_\mu(\nu) \equiv a_\mu$.

Density distributions p(λ) and p(μ) of the random values λ and μ are obtained from the theorem of density functional distribution of dependent random value (Probability Theory) and applied to the dependencies:

$$p(\lambda) = \frac{1}{a_\lambda}\ p\left(E\right)\ ;\ p(\mu) = \frac{1}{a_\mu}\ p\left(E\right) \qquad (10)$$

where $p(E) = \frac{1}{\sigma\sqrt{2\pi}}\ exp\left(-\frac{(E-a)^2}{2\sigma^2}\right)$

The mathematical expectation and the dispersion of the random values λ and μ are given in:

$$\mathbf{M}(\lambda) = a_\lambda\ \mathbf{M}(E)\ ;\ \mathbf{M}(\mu) = a_\mu\ \mathbf{M}(E) \qquad (11)$$

$$\mathbf{D}(\lambda) = a_\lambda^2\ \mathbf{D}(E)\ ;\ \mathbf{D}(\mu) = a_\mu^2\ \mathbf{D}(E) \qquad (12)$$

Density distribution $p_{HB}(HB)$ is calculated by

$$p_{HB}(HB) = \frac{1}{2}\ (HB)^{-1/2}\ p_\mu\left((HB)^{1/2}\right) \qquad (13)$$

4. EQUIPMENT AND MEASURING IN NDE

The following technical tools (SONATEST, England, PANAMETRICS, USA) are used for measurements velocities of ultrasonic wave propagation through investigated materials and details:

- Digital ultrasonic flaw detector SITESCAN 150S (SONATEST, England). The measurements are carried out by means option "measurement of time propagation of ultrasonic wave" with accuracy 0.01 μs.
- Calibration block – CBV with V_L= 5.93 mm/μs (SONATEST, England).
- Transducers with X-cut of piezo-electric element (for longitudinal waves, fig.4. and Y-cut of piezo-electric element (for transversal waves, fig.5. and frequency 5 MHz.

Fig.4. *Transducers with X-cut of piezo-electric element*

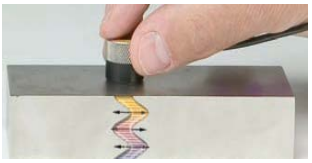

Fig.5. *Transducers with Y-cut of piezo-electric element*

A digital micrometer for thickness measure (Digimatic Micrometer, Range 0-30 mm, Accuracy 0.0001 mm (f. Mitutoyo – Japan) is used also.

The values of the "unknown" velocity of longitudinal end transversal ultrasonic wave $V_X \equiv \left(V_L; V_T\right)$ in $mm/\mu s$ is calculate by

$$V_X = \frac{l_X}{T_X/2} \qquad (14)$$

where $T_X \equiv \left(T_L; T_T\right), \mu s$ are the values of the "unknown" time of propagation of longitudinal and transversal ultrasonic wave, l_X - is the thickness of the studied specimen in mm.

Presentation of velocity measurement of V_L and V_T. The relative error for velocity $\frac{\Delta V_{L,T}}{V_{L,T}}$ is

$$\frac{\Delta V_{L,T}}{V_{L,T}} = 2.\left(\frac{\Delta l}{l} + \frac{\Delta t_{L,T}}{t_{L,T}} \right) \qquad (15)$$

where $\Delta V_{L,T}; \Delta l; \Delta t_{L,T}$ - absolute errors respectively for velocity, thickness, time. Confidence interval for measure velocity is

$$\overline{V_{L,T}} \pm \left(1 + \frac{1}{n} \right) T(n;\alpha) S_{V_{L,T}} \qquad (16)$$

where $\overline{V_{L,T}}$ и $S_{V_{L,T}}$ are respectively mean and standard deviation for measure velocity, n – number of readings, $T(n;\alpha)$ - Student's distribution in probability $\Pr = 1 - \alpha$.

5. CONCLUSION

The solution of Boussinesq's problem in theory of elasticity is analyzing and obtained the relationship $\sigma_S \approx \frac{1}{4} \varphi(\nu)\, HB$, who is agreement with experimental data. The functions $\nu(V_L; V_T)$ and $HB(V_L; V_T)$ are known.

For non-destructive evaluation of yield stress σ_S by means measure of velocities of propagation of longitudinal and transversal ultrasonic waves - V_L and V_T in testing materials and details is derivate.

REFERENCE

1. ZOLOTOREVSKII *V.S.*, *Mechanical properties of metals*, Misis, Moscow, 1998 (in Russian).
2. NOWACKI *W.*, *Teoria sprezystosci*, Panstwowe Wydawnictwo Naukowe, Warszawa, 1970 (in Poland).
3.TIMOSHNKO, *S. P., and* GOODIER, *J. N.*, Theory of Elasticity, 3rd edition, McGraw- Hill, Inc., New York, 1970.
4. MARKOVEC *M.P.*, *Non-specimen methods for evaluation of mechanical properties of metals*, MEI, Moscow, 1983 (in Russian).
5 KOLAROV *D., A.* BALTOV, *N.* BONCHEVA, *Mechanics of plastic media*, Publishing House of the BAS, Sofia, 1975 (in Bulgarian).
6. SOKOLNIKOV *I.S.*, *Mathematical theory of elasticity*, Second edition, McGraw- Hill, Inc., New York, 1956.
7. DIMOV *D. and &* , *Tables and formulas in mechanics of materials*, Tehnika, Sofia, 1972 (in Bulgarian).
8. POPOV AL., POPOV A.P., K.M.MINCHEV, *NDE of Yield stress for low-carbon steels*, 10th National Congress on Theoretical and Applied Mechanics, v. I I, p.268, Varna, 2005.
9 POPOV AL., *Non-Destructive evaluation of mechanical properties of steels*, Monograph "MASHIN DESIGN", University of Novi Sad, Faculty of Technical Sciences, may 18th 2007, 47th anniversary of the faculty, p.461-468.
10. POPOV A.P., *Measuring of velocity of ultrasonic with one-sided accessibility*, National Conference "Acoustics'2007", Sofia, november 2007, pp.85-87, 2007.
11. POPOV AL., *Ultrasonic testing of mechanical properties of cast iron*, Conference "NDT'2008", Scientific letters of Union of mechanical engineering, Year XV, Number 2(105),June 2008,pp.104-109.
12. POPOV AL., *NDE of stress-strain diagram characteristics for cast iron*, XII Int. Conf. on Mechanical Engineering,, Bratislava, 13 - 14.11.2008, ISBN 978-80-227-2982-6, Paper No 14 on CD.

CREATING NANOSTRUCTURED SUPERHARD AND HEAT-RESISTANT SURFACE LAYERS ON CARBON TOOL STEEL AT INFLUENCE TO INTENSE ELECTRON BEAMS

СОЗДАНИЕ НАНОСТРУКТУРИРОВАННЫХ СВЕРХТВЕРДЫХ И ЖАРОПРОЧНЫХ ПОВЕРХНОСТНЫХ СЛОЕВ НА УГЛЕРОДИСТЫХ ИНСТРУМЕНТАЛЬНЫХ СТАЛЯХ ПРИ ВОЗДЕЙСТВИИ ИНТЕНСИВНЫХ ЭЛЕКТРОННЫХ ПУЧКОВ

Senior Researcher, Candidate of Engineering Sciences Milonov A.S., Postgraduate Danzheev B.A., Research Officer Dasheev D.E., Main Scientist Researcher, Doctor of Engineering Sciences, Assoc. Prof. Smirnyagina N.N.
Institute of Physical Materials Science SB RAS, 670047, Ulan-Ude, Russia,
e-mail: terwer81@mail.ru, bel.tunka@mail.ru, fokter@mail.ru, smirnyagina09@mail.ru

Absract: *The saturation of the surface layers of metals and alloys boron is conducted with the purpose of increase of their surface hardness, wear resistance, etc. Multicomponent layers containing in its composition borides of refractory metals, as a rule, formed by the methods of chemical-thermal processing in the interaction boriding component with refractory or by saturation boron refractory impurities metal or alloy.*

In this work, we studied the features of formation of vanadium and iron borides on the surface of instrumental steels U8A and R18 under the influence of intense electron beams in continuous and pulse modes.

KEYWORDS: ELECTRON BEAM, BORIDES, ALLOYS, MICROHARDNESS, X-RAY DIFFRACTION, STRUCTURE, THE SELF-PROPAGATING HIGH-TEMPERATURE SYNTHESIS (SHS)

1. Introduction

The surface layers saturation of metals and alloys from boron spend with the purpose of increase of their surface hardness, wear resistance, etc. Application of electronic heating with high (> 10^9 W/m^2) specific capacity in vacuum owing to fast not inertial achievement of limiting heats and ease of regulation of heating in a wide range of temperatures opens sample opportunities for creation of boride layers.

In [1] it was informed about formation of strengthening coating of TiB_2, CrB_2, VB_2, W_2B_5 on carbonaceous steels under influence of an electron beam on boron compound reactionary daub in vacuum. The assumption of an active role of a surface metal has been made at electron beam alloying of self-heating synthesis products which initiated by an electron beam and proceeding in reactionary daub of steochemetric mixtures.

In this work, we studied the features of formation of vanadium and iron borides on the surface of instrumental steels U8A and R18 under the influence of intense electron beams in continuous and pulse modes.

2. Layers based on the boride VB_2 on steel U8A

Vanadium boride layers VB_2 (and forth, and borides of iron Fe_2B and FeB) at the same time synthesized and formed on the surface of cutting plates size 12×12×5 mm with roughness Rz = 4.41 ÷ 4.02 microns of instrumental steels U8A and R18. Samples were prepared by applying the reactionary daubs on the pre-prepared (well-fat) surface of the steel. In the composition of the daubs consisted of 1:1 by volume stoichiometric mixture oxide, boron containing and carbon component and organic binder - solution 1:10 glue BF-6 in acetone. As initial substances used amorphous boron, charcoal (birch) and oxides V_2O_3, Fe_2O_3. Processing of samples was conducted within 2-5 minutes with the power of electron beam 150-300 watts. The pressure in the vacuum chamber did not exceed 2×10^{-3} Pa [2, 3].

X-ray diffraction revealed that in the boride layer on steel U8A observed prevalence of carbide phases (cementite). This can be explained only by the deviation from stoichiometry by evaporation of the intermediate boron oxide. Application of the protective layer of amorphous oxide B_2O_3 (1:1 by volume reactionary daub: daub based B_2O_3) allowed to form a more uniform boride layers. It was found that the weight of the crystalline phases in the samples is 92.3%, and the amorphous phases – 7.7%, while the crystallite size ranges from 15 to 70 nm.

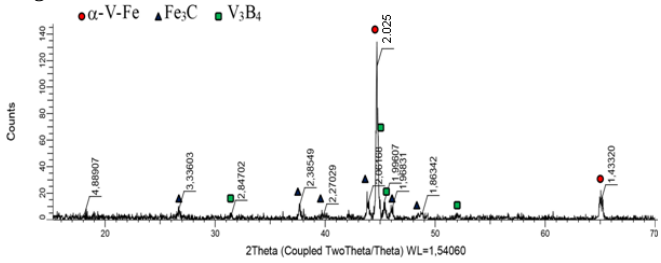

Figure 1. *X-ray pattern of layer based VB_2, formed on steel U8A*

On X-ray patterns of all investigated vanadium boride layers can be observed reflections of refractions belonging vanadium ferrite α-Fe-V, the corresponding phase α-Fe_9V space group *Im3m*, with a cubic lattice parameter a = 0.2878 nm and cementite Fe_3C (PDF 00-003-0989), space group *Pbnm* with rhombic elementary cell with parameters a = 0.4518, b = 0.5069 and c = 0.6736nm, z = 4 (Figure 1).

On X-ray patterns of vanadium diboride layers found boride V_3B_4 (PDF 03-065-2551, space group *Immm*, with elemental rhombic cell with parameters a = 0.303, b = 1.318 and c = 0.2986 nm, z = 2). Education vanadium diboride VB_2 radiographically not detected, although there are reflexes, light intensity related to the interplanar distances of this phase. In this regard, more research is needed.

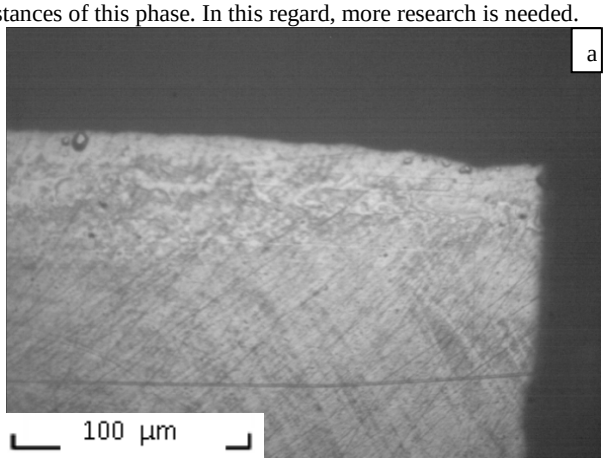

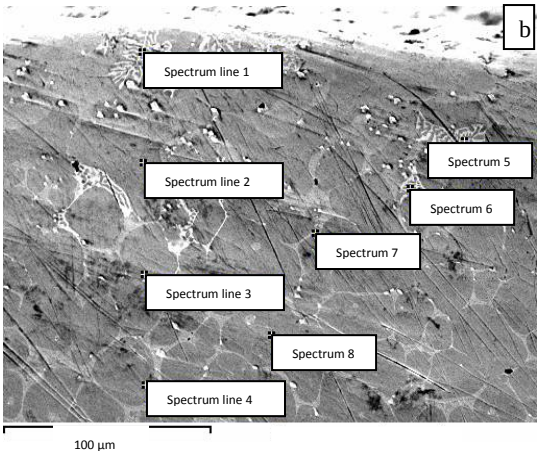

Figure 2. *General view (etched layer) (a) and structure (b) layer VB_2 on steel U8A*

Figure 2 shows a general view (Figure 2.a) and the structure of the boride layer VB_2 on the surface of cutter plate steel U8A (Figure 2.b). Layer thickness reaches up to 500 µm.
Microhardness testing showed uneven distribution of its thickness in the cross-section. Separate very rare inclusions have microhardness HV≈ 24000 MPa and are located in the surface layers. Next we will see two areas: in the first area microhardness reaches 2500 MPa, and in second - 1500 MPa. The metal base is microhardness 200 MPa.

3. Layers of iron borides Fe_2B and FeB at high-cutting steel R18.

X-ray diffraction (XRD) revealed that in the samples of cutter plate steel R18 after electron beam treatment reflexes following phases are present: the metal substrate - α-Fe and carbide W_3Fe_3C. It was found that the weight of the crystalline phase is 92.7% and the amorphous phase – 7.3%.
Boride FeB located near the surface of the coating. This is evidenced by the results of the investigation of the end surface of the cutter plate steel R18 and X-ray analysis data (scanning electron microscope JSM-6510LV JEOL with microanalysis system INCA (Figure 3).
Application of the protective layer of amorphous oxide B_2O_3 contributed obtaining equilibrium boride layers Fe_2B and FeB.

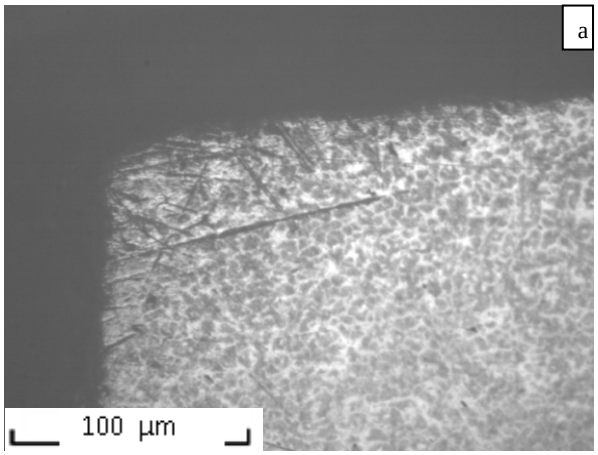

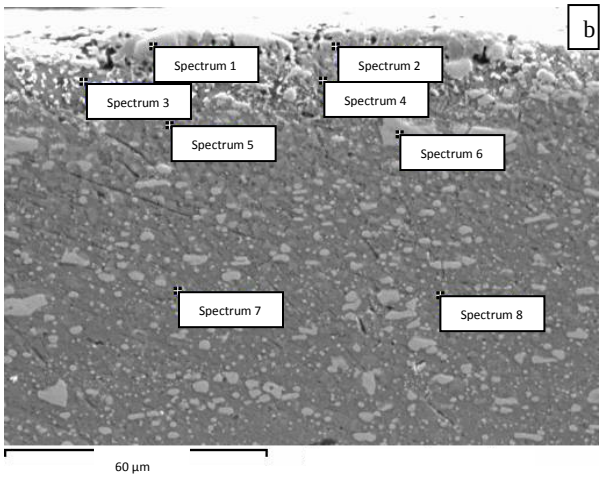

Figure 3. *General view (a) and structure (b) boride layer FeB on steel P18*

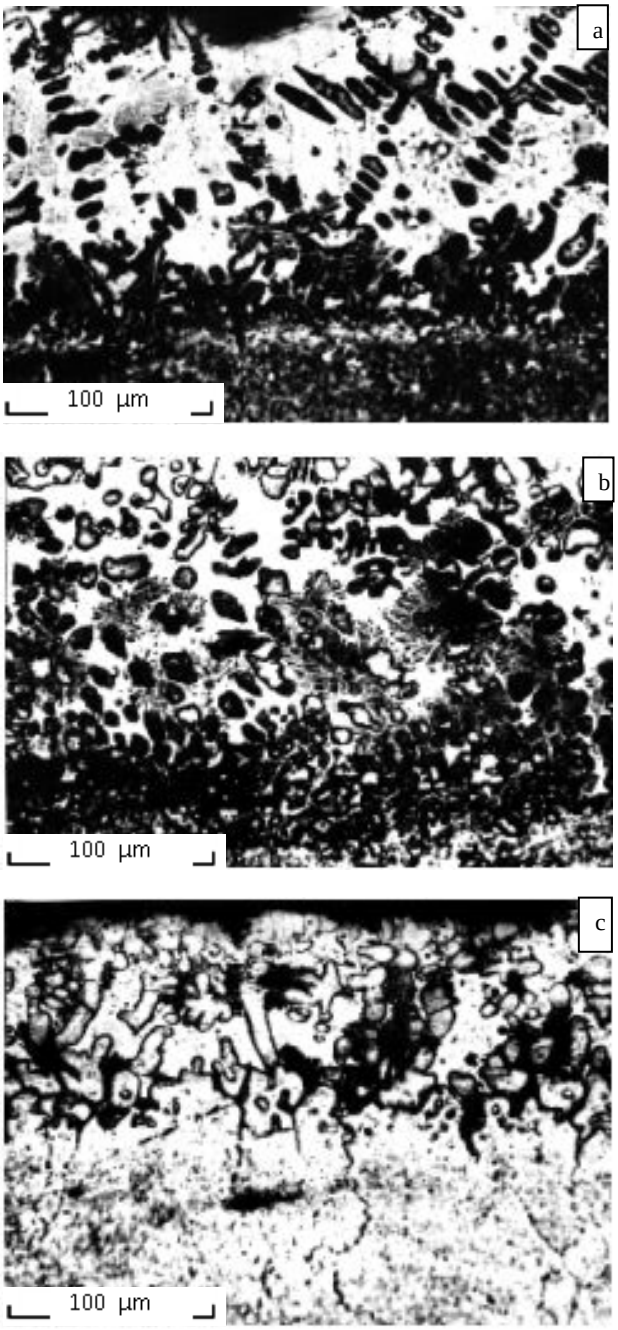

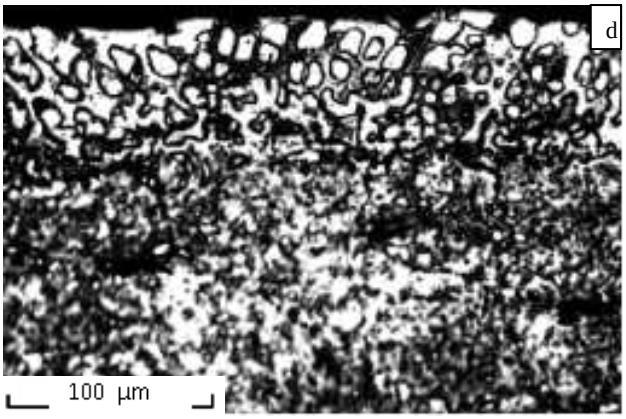

Figure 4. *Structure of the surface layer on the steel R18 after electron beam boriding, a – at the power density of the electron beam J =2.8×10^4 W/cm^2, b – at the power density of the electron beam J=2.5×10^4 W/cm^2, c,d – at the power density of the electron beam up to J =2.2×10^4 W/cm^2*

4. Wear resistance of boride layers on high-cutting steel R18

When the electron beam boriding steel R18 with the power density of the electron beam J =2.8× 10^4 (W/cm^2) layer was formed as a result of deep weld penetration, which determined its structure. Figure 4a shows that when directed crystallization main axis line dendrites oriented in the direction of heat removal. The structure of dendrites (chain separate globules) indicates of the intermittent nature of their education. When power density of the electron beam J=2.5×10^4 (W/cm^2) layer consists predominantly of stellate dendrites (Figure 4b). When reducing the power density up to J =2.2×10^4 (W/cm^2), surface layer also contains stellate dendrites, but their number is not dominant (Figure 4c,d). Microhardness layer is 1100-1860 kg/mm^2. The thickness of layer is 25-100 μm.

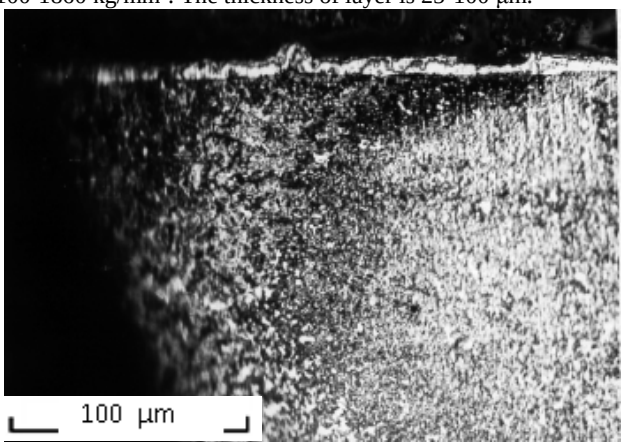

Figure 5. *The microstructure of cutters from steel R18 after electron beam treatment*

After treatment by the electron beam of cutter plate with boron-containing daubs, on the surface formed layer with thickness 8-10 μm (Figure 5). The resulting layer have a specified thickness practically over its entire length. With increasing × 500 shows that the layer contains particles which are located not only within the layer, but also at the boundary layer - base. This suggests that these particles are carbides of alloying elements (tungsten, chromium, molybdenum and vanadium). Layer was firmly held on the metal base. Microhardness layer slightly higher microhardness is 550 bases and HV and 410 HV, respectively.

To assess the tribological properties of the resulting layer tests conducted strength incisors. Tests were performed on lathes 1A616 on the following modes: feed - 0.1 mm / rev, rate speed - 224 rev / min, depth of cut - 1.0 mm. Processed material - steel 45 and sus321. Wear incisors determined by the rear surface with a magnifying glass Brinell. Geometric parameters of incisors: rake angle γ= 15^o, the main rear angle α = 8^o, plan approach angle φ = 45°. Criterion for stability incisors taken the time to reach the limit flank wear of 0.6 mm.

The results are given in figure 6. The figure shows that formation boride layers thickness of 8-10 μm on the front surface, allows to increase the resistance of incisors almost 1.5 times (for processed steel sus321).

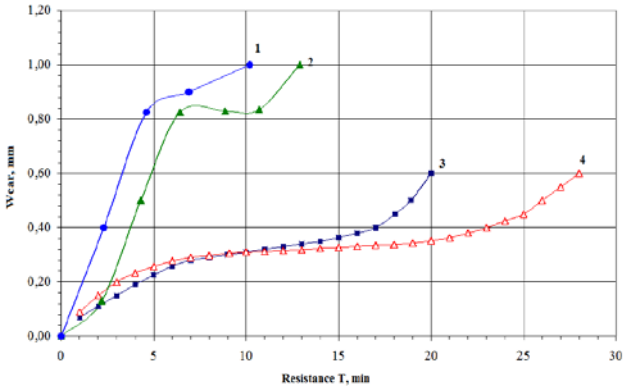

Figure 6. *Kinetics of wear cutters from steel R18 1-R18 hard. (steel sus321), 2-R18 thermochemical treatment (steel 45), 3-R18 electron-beam boriding (steel sus321), 4-R18 hard. (steel 45)*

5. Conclusion

Conditions for the formation, structure and properties boride layers on the surface cutting plates of carbon steel U8A formed during electron beam processing in vacuum were investigated and discussed.It found that at the directional crystallization the main axis of line dendrites is focused in the direction of heat removal. The structure of dendrites (a chain separate globuly) speaks about intermittent nature of their education. Microhardness layer constitutes 1100-1860 HV. The thickness of 25-100 μm.

The formation boride layers thickness of 8-10 microns on the front surface, allows to increase the resistance of incisors almost 1.5 times (for processed steel sus321).

A more significant increase of resistance incisors are associated with increased thickness boride layers. When electron beam boriding thickness of boriding layer can be up to 300 microns, but the temperature processing is 1100-1200^{o}C. The processing time is 2-3 minutes. On this basis, electron-beam boriding cannot be recommended as a final, but as an intermediate processing operation of the cutting tool, for example, before hardening. It should be noted that to achieve the same thickness of a layer when diffusion borating (for example, when borating in sealed containers with safety valve) is required not less than 3 hours.

6. Acknowledgments

This work was supported by the Russian Foundation for Basic Research, project 15-48-04217 r_sibir_a.

7. Literature

1. N.N. Smirnyagina, I.G. Sizov, A.P. Semenov, Neorgan. Materials. 2002. - vol. 138. - № 1. - pp 48-54.
2. Dasheev D.E., Smirnyagina N.N. Features of the process of self-propagating high-temperature synthesis, a structure and strong properties of borides iron layers on the carbonaceous steel 3, generated under a powerful electron beam in vacuum. // News of higher educational institutions. Physics. - 2012. - V. 55. - № 12/2. - pp. 51-54.
3. Dasheev D.E., Smirnyagina N.N. Features of the process of self-propagating high-temperature synthesis, a structure and strong properties of borides iron layers on the carbon steels, generated under a powerful electron beam in vacuum //J. Chem. Chem. Eng. 2013.- V.7.- № 4.- pp 319-325.

MODELING AND OPTIMIZATION OF THE COMPOSITION OF TITANIUM -BASED ALLOYS BY APPROXIMATION WITH REGRESSION MODELS

Nikolay Tontchev[1], Martin Ivanov[2] Emil Yankov[3]

[1]University of Transport, 158 Geo Milev str.,1574 Sofia, Bulgaria, e-mail: tontchev@vtu.bg

[2] New Bulgarian University – Sofia, [3] "Angel Kanchev" University of Ruse

Abstract: *The article is dedicated to an approach optimizing a task of statistical modeling of the mechanical properties of products in real production metallurgy design. The approach is designed for the benefit of producers-metallurgists aimed at providing panels of Ti - alloys of a specific set of eventual industrial properties. This is accomplished by a procedure of composition optimizing based on existing certificates of brands Ti - alloys. The article presents an approach using mathematical models of optimization problem following the implementation of approach the classical methodology capable of decision-making in the production practice.*

Keywords: METALLURGICAL DESIGN, TENSILE PROPERTIES, COMPOSITION-PROCESSING-PROPERTY CORRELATION, OPTIMIZATION OF THE COMPOSITION

1. Introduction

An effective approach at metallurgical design is to use data from previous experience, processed up to a statistical model, based on a large amount of data related by composition, processing and properties. The design of the alloy composition and the optimization of the technological-process parameters are directly related to the resolution of the compromise between the measured values related to certain selected indicators of the quality of a set of materials for a test group or a class [1]. The most characteristic for these approaches is that they do not use the principles of metallurgy and metal physics. It is relied mainly only on an a priori information about the relation "composition and processing and their influence on the properties." Compared with physical models, the advantage of statistical models is their ability to explore a complex of properties and to obtain information in a timely and effective manner, even when there are no well-established physical theories and models.

The aim of this study is to present a robust approach for determining the influence of alloying elements on the properties of Ti - alloys that ensures better results than the input ones used to obtain a mathematical model.The formulated optimization models are used at the stage of modeling the mechanical properties of the composition of Ti - alloys during the production metallurgy process.

The multidimensional regression analysis is one of the most popular data-mining methods. It has been applied successfully to the study of multiple relationships in metallurgical industry, [2] – [4]. Due to the nature of each statistical analysis, the coefficients of limitations imposed by the regression analysis are known only approximately. That should be reflected in the mathematical model of the optimization problem.

2. General description of the approach

The analysis presented in this paper is related to the analysis of mechanical properties of Ti - specimens described by the following parameters: yield strength, Rp 02 [MPa], tensile strength and relative elongation (A [%]). The limitations connected with these

parameters are due to Ti grade characteristics and customer's specifications. However, the main problem is that these parameters cannot be under direct observation during the manufacturing process, so any limitations associated with them cannot be clearly defined in the optimization model. That means that we must develop models linking the final mechanical properties of the specimen/sample of the steel chemical composition as well as the parameters of the production process.

The regression analysis allows describing the relation between the variables of input and output, without going into the phenomenon nature during the process.

The regression models presented below have been created based on the data collected during the industrial production process.

The statistical analysis described in this section is based on a data set of 300 records extracted from the whole database.

The Pareto front was built based on this initial information related to the couple of parameters yield strength, Rp_{02} [MPa] and relative elongation (A [%]). The chemical composition of the various compositions is given in an implicit form in the case. From the list of compositions in the full range of variations there have been selected Pareto compositions for which the sum of the basic elements had a relatively small value. The selection is focused on compositions for which the relatively small price of their expensive elements does not affect the values of the explored parameters for optimization. The obtained regression models are related to this information. In respect to the problem under examination, nonlinear regression dependencies have been identified for each of the mechanical properties of alloys. The regression dependencies are of the following kind:

Here bij are the regression model parameters. The coefficients in equations are defined in Table 1. The models can be used for prediction if the check-up F > F (0.5, ν1,ν2) described in details has been made.

The relationship between the derived coefficients in Table 1 and the specific chemical elements is described in the regression elements.

Rp_{02} = 1211.88 + 51.5221 Al - 24.9734 Mo - 80.7796 Sn + 96.9246 Zr + 209.828 Cr + 80.3385 Fe + 72.0976 V - 21.4625 Si + 40.3190 O - 6.81555 Al^2 - 106.347 Al Mo - 69.9600 Al Sn - 43.6439 Al Zr + 15.4261 Al Cr -61.9896 Al Fe -81.5665 Al V + 10.3925 Al Si + 47.3631 Al O + 31.7825 Mo^2 - 24.5042 Mo Sn - 19.5766 Mo Zr - 43.8777 Mo Cr - 34.0499 Mo Fe - 70.3951 Mo V - 51.3807 Mo Si + 60.8373 Mo O + 6.35824 Sn^2 - 62.3299 Sn Zr - 49.0562 Sn Cr + 47.2030 Sn Fe - 84.9186 Sn V + 7.34492 Sn Si + 47.5112 Sn O + 44.0214 Zr^2 -39.5834 Zr Cr - 34.9639 Zr Fe + 19.4983 Zr V + 34.0014 Zr Si + 1.40613 Zr O + 109.626 Cr^2 - 26.3554 C Fe + 12.6771 Cr V + 0.829980 Cr SI - 24.8476 Cr O - 75.0358 Fe^2 + 3.91375 Fe V + 25.5956 Fe Si - 67.2523 Fe O - 6.09390 V^2 + 19.2299 V Si + 17.1889 V O -51.7804 Si^2 +19.0743 Si O -38.5409 O^2

Table 1. *Coefficients of regression modelds of the examined target parameters.*

№	designation	Rp_{02}	A	№	designation	Rp_{02}	A
1	b(0 0)	1211.88	43.4377	29	b(3 4)	-62.3299	7.48801
2	b(1 0)	51.5221	-12.4873	30	b(3 5)	-49.0562	3.57374
3	b(2 0)	-24.9734	5.83605	31	b(3 6)	47.2030	-13.2362
4	b(3 0)	-80.7796	16.1346	32	b(3 7)	-84.9186	18.1995
5	b(4 0)	96.9246	-26.5634	33	b(3 8	7.34492	2.45297
6	b(5 0)	209.828	-41.6628	34	b(3 9)	47.5112	-7.84135
7	b(6 0)	80.3385	-11.3614	35	b(4 4)	44.0214	-12.5869
8	b(7 0)	72.0976	-12.2634	36	b(4 5)	-39.5834	11.2109
9	b(8 0)	-21.4625	9.45284	37	b(4 6)	-34.9639	11.6078
10	b(9 0)	40.3190	-7.32094	38	b(4 7)	19.4983	-1.06720
11	b(1 1)	-6.81555	4.99262	39	b(4 8)	34.0014	-5.39692
12	b(1 2)	-106.347	32.8537	40	b(4 9)	1.40613	3.89560
13	b(1 3)	-69.9600	13.9749	41	b(5 5)	109.626	-11.8927
14	b(1 4)	-43.6439	6.60931	42	b(5 6)	-26.3554	18.2370
15	b(1 5)	15.4261	2.81458	43	b(5 7)	12.6771	12.9706
16	b(1 6)	-61.9896	24.7026	44	b(5 8)	0.829980	0.427527
17	b(1 7)	-81.5665	26.9275	45	b(5 9)	-24.8476	8.14636
18	b(1 8)	10.3925	-4.94533	46	b(6 6)	-75.0358	22.7628
19	b(1 9)	47.3631	-7.11438	47	b(6 7)	3.91375	14.6460
20	b(2 2)	31.7825	-8.72509	48	b(6 8)	25.5956	-10.9786
21	b(2 3)	-24.5042	3.37836	49	b(6 9)	-67.2523	18.1532
22	b(2 4)	-19.5766	1.36551	50	b(7 7)	-6.09390	1.46032
23	b(2 5)	-43.8777	13.8703	51	b(7 8)	19.2299	-4.26022
24	b(2 6)	-34.0499	13.3358	52	b(7 9)	17.1889	-6.80520
25	b(2 7)	-70.3951	18.9816	53	b(8 8)	-51.7804	14.9821
26	b(2 8)	-51.3807	9.02304	54	b(8 9)	19.0743	-5.02353
27	b(2 9)	60.8373	-3.70434	55	b(9 9)	-38.5409	1.21278
28	b(3 3)	6.35824	2.60378				
Rp_{02}		R = 0.9880		F cal. = 18.8637 $_{(a=0.05,54,25)}$ > 1.8367 = F tabl			
A		R = 0.9906		F cal. = 24.2416 $_{(a=0.05,54,25)}$ > 1.8367= F tabl			

A = 43.4377- 12.4873 Al + 5.83605 Mo + 16.1346 Sn - 26.5634 Zr - 41.6628 Cr -11.3614 Fe - 12.2634 V + 9.45284 Si - 7.32094 O + 4.99262 Al^2 + 32.8537 Al Mo + 13.9749 Al Sn + 6.60931 Al Zr + 2.81458 Al Cr + 24.7026 Al Fe + 26.9275 Al V- 4.94533 Al Si - 7.11438 Al O - 8.72509 Mo^2 +3.37836 Mo Si + 1.36551 Mo Zr + 13.8703 Mo Cr + 13.3358 Mo Fe + 18.9816 Mo V + 9.02304 Mo Si -3.70434 Mo O + 2.60378 Sn^2 +7.48801 Sn Zr + 3.57374 Sn Cr- 13.2362 Sn Fe + 18.1995 Sn V +2.45297 Sn Si-7.84135 Sn O - 12.5869 Zr^2 + 11.2109 Zr Cr + 11.6078 Zr Fe - 1.06720 Zr V - 5.39692 Zr Si + 3.89560 Zr O - 11.8927 Cr^2 + 18.2370 Cr Fe + 12.9706 Cr V + 0.427527 Cr Si + 8.14636 Cr O + 22.7628 Fe^2 + 14.6460 Fe V - 10.9786 Fe Si + 18.1532 Fe O + 1.46032 V^2 - 4.26022 V Si - 6.8052 V O + 14.9821 Si^2 - 5.02353 Si O + 1.21278 O^2

The numerical experiment [6] has proved the ability to improve the quality of Ti alloy of a certain class. Mathematical models suitable for forecasting and optimization have been derived. The approach of Taguchi applied has lead to a desired result, to separate variables Xi for the examined parameters that do not influence significantly on the final result. With this limit, the numerical optimization for maximum search has been conducted with each chemical composition. That allows improving it. Relative elongation A turned to be less variable index and yield strength Re requires caution with extreme selecting. The decision of bi-criteria problem set has been defined thus proving that the Taguchi approach is applicable to a similar class of problems.Following the applied optimization procedure and based on the derived models, a solution was formulated. According to it, the content of aluminum and molybdenum is about 8-9 percent, and the values of vanadium, chromium and silicon are negligible. Fig. from 1-8 visualizes an interpretation of the main alloying elements and their effect on the investigated variables at fixed values of the rest of the elements that are equal to the determined optimal

Conclusion

It has been proven that during the design of the properties of the materials it is possible to determine effective solutions via defining a multicriteria problem. It has been proven that during modeling process costs for the different Ti - alloys grades in aggregate, it is possible to evaluate equally possible for realization technological routes.Optimal compositions of a Ti-alloys have been determined grade by Pareto-front in terms of strength and ductility that are experimentally verified for a particular application. The number and the amount of alloying elements in low-alloy steels are determined. For Ti - alloys with economic alloying there are constructed models defining the relationship.

References

1. **Tontchev N**. Materials Science, Effective solutions and Technological variants, 2014/3/3, LAMBERT Academic Publishing
2. **Malinov, S, Sha, McKeown, J.J.**: Modelling and Correlation between Processing Parameters and Properties of Titanium Alloys using Artificial Neural Network. Computational Material Science 21, 375—394 (2001)
3. **Potemkin V.K.,O.S. Khlybov, V.A. Peshkov**, Complex mathematical model for predicting mechanical properties and structure of steel sheets, Metal Science and Heat Treatment 42, 11-12 (2000).
4. **Palanisamy P., I. Rajendran, S. Shanmugasundaram**, Prediction of tool wear using regression and ANN models in end-milling operation, International Journal of Advanced Manufacturing Technology 37, 29-41 (2008).
5. **Rodrigues P.C.M., E.V. Pereloma, D.B. Santos,** Mechanical properties of an HSLA bainitic steel subjected to controlled rolling with accelerated cooling, Materials Science and Engineering A283, 136-143 (2000).
6. **Tontchev N., Y. Kalev,** (2013): Determing Influence of Alloying Elements on Properties of Alloys by Robust Experiment, MEST Journal, July, pp. 31 – 39.

Yield strength, Rp $_{02}$ [MPa]

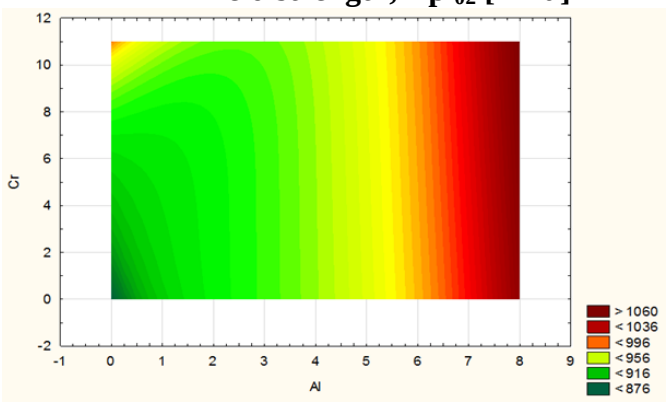

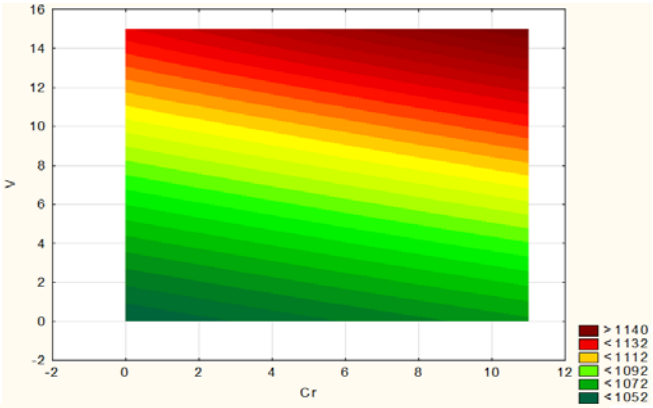

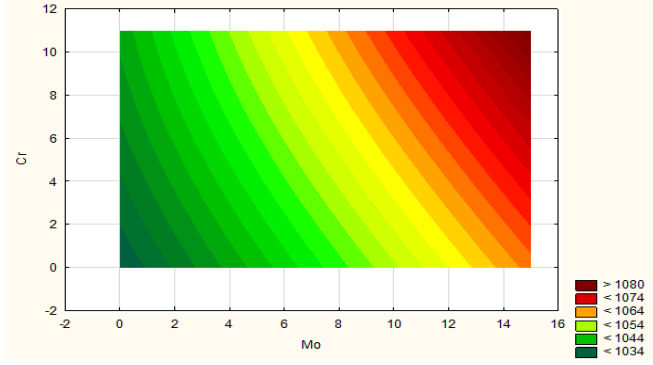

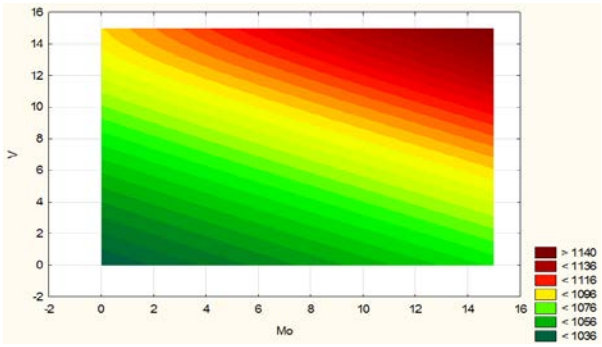

Relative elongation (A [%])

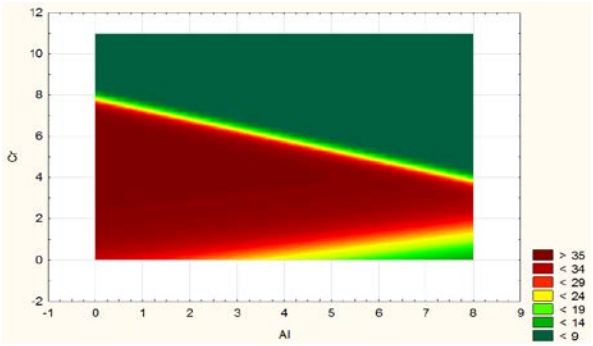

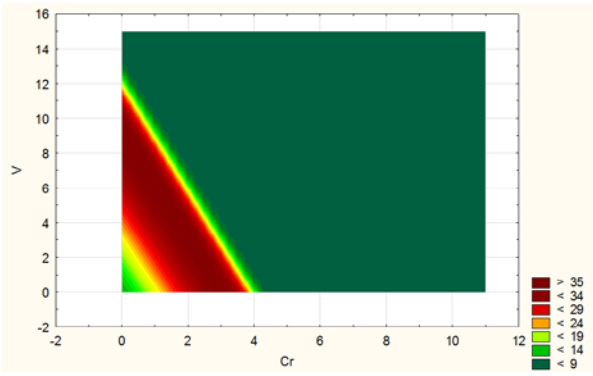

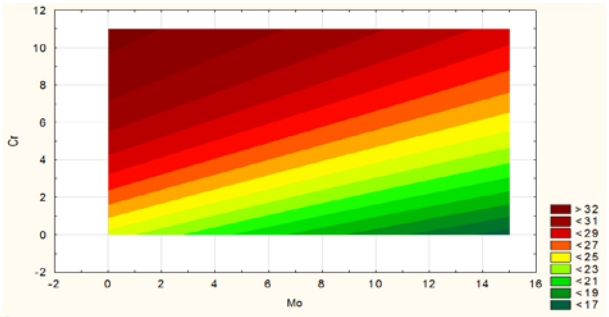

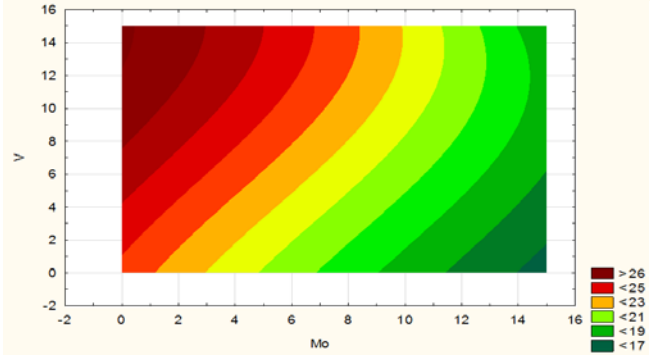

DESIGN OF POLYMER COMPOSITE PIPES PRODUCED BY FILAMENT WINDING TECHNOLOGY

Pop Metodieva[1] B., MSc. Zhezhova S.[1], Srebrenkoska S. [2], Naseva S. [1], Prof. Dr Srebrenkoska V.[1]
[1]*Faculty of Technology, University Goce Delchev – Shtip, R.Macedonia*
[2]*Faculty of Technology and Metallurgy, Ss.Cyril & Methodius University, Skopje, R.Macedonia*
E-mail: vineta.srebrenkoska@ugd.edu.mk

Abstract: *The aim of this study is to investigate the design of continuous fiber reinforced composite pipes, produced by filament winding technique. For this purpose, the full factorial experimental design was implemented. When designing filament winding composites three major factors are the most important: fiber orientation, fiber tension and velocity of the filament winding. The ultimate target is to achieve the composite pipes with good characteristics as bearing material for construction with the lowest possible weight. Preparation of the composites was done by applying the 2^3 full factorial experimental design. For the purposes of these investigation, eight test specimen configurations are made and on the basis that, test results should provide material properties useful in the design stage. The velocity of the filament winding was taken to be the first factor, the second – fiber tension and the third – winding angle. The first factor low and high levels were chosen to be 525 m/min and 21 m/min, respectively, for the second factor – 64 N and 110 N, respectively and for the third factor – 100 and 900, respectively.*
KEYWORDS: \ FILAMENT WINDING, GLASS FIBERS, EPOXY RESIN, COMPOSITE PIPES.

1. *Introduction*

Development of new composites and new applications of composites is accelerating due to the requirement of materials with unusual combination of properties that cannot be met by the conventional monolithic materials. Actually, composite materials are capable of covering this requirement in all means because of their heterogeneous nature (Krivokuća, M. et. al., 1999).

Properties of composites are strongly influenced by the properties of their constituent material, their distribution, and the interaction among them. The composite properties may be the volume fraction sum of the properties of the constituents, or the constituents may interact in a synergistic way so as to provide properties in the composite that are not accounted for by a simple volume –fraction sum of the properties of the constituents (Roux, M, 2010).

Fiber – reinforced composite materials consist of fibers of high strength and modulus embedded in or bonded to a matrix with distinct interfaces between them. In this form, both fibers and matrix retain their physical and chemical identities, yet they produce a combination of properties that cannot be achieved with either of the constituents acting alone. In general, fibers are the principal load-carrying members, while the surrounding matrix keeps them in the desired location and orientation, acts as a load transfer medium between them and protects them from environmental damages due to elevated temperatures and humidity, for example (Dorigato A., Pegoretti A., 2014).

Many fiber-reinforced composites often a combination of strength and modulus that are either comparable to or better than many traditional metallic materials. Because of their low density, the strength-weight ratios and modulus weight ratios of these composite materials are markedly superior to those of metallic materials. In addition, fatigue strength as well as fatigue damage tolerance of many composite materials are excellent. For these reasons, fiber reinforced composites have emerged as a major class of structural materials and are either used or being considered for use as substitution for metals in many weight-critical components in aerospace, automotive, and other industries. Filament winding technique is a very important and widely used technique for production of fiber reinforced composites (Mallick, P.K, 2007).

For the production of composite materials by the filament winding technology, a reinforcing agent in the form of continuous fibers (glass, carbon, aramid, etc.) and an impregnation agent in the form of liquid resin (polyester, epoxy, etc.) are used.

The basis of this technology includes winding of resin-impregnated fibers into a tool and hardening of the wound structure (Figure 1).

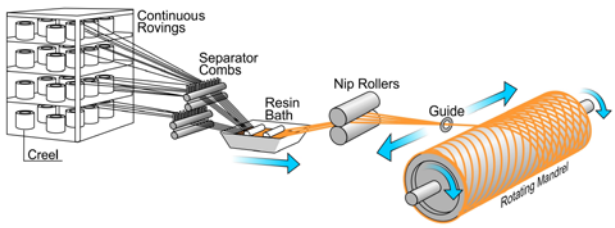

Figure 1. *Schematic presentation of the filament winding technology*

This technology enables the fiber to be placed into the direction of the load that may be expected during exploitation of construction elements. Owing to this unique capability, the mechanical properties of fibers in the longitudinal direction can be maximally exploited (Belingardi, G. et al., 2006).

Based on that, it is clear that the filament winding technology is used for creating new materials with distinct anisotropy according to the direction in which the fiber is placed. In other words, different directions result in a material with different mechanical properties.

Thus produced composite materials have the highest percent of fibers of all composite materials and small density. This fact is important for loaded elements of construction, which also need to have small mass.

2. *Preconditions and means for resolving the problem*

a. Experimental stand

For the production of the composites 10 bobbins of E-glass fiber roving 185P with 1200tex from Owens Corning were used. The glass fibers were impregnated into epoxy resin system Araldite LY564/Aradur 917/Accelerator 960-1

from Huntsman.
The preparation of the composites was done by applying the 2^3 full factorial experimental design. For the purposes of these investigation, eight test specimen configurations are made and on the basis that, test results should provide material properties useful in the design stage. The velocity of the filament winding was taken to be the first factor, the second – fiber tension and the third – winding angle. The first factor low and high levels were chosen to be 5,25 m/min and 21 m/min, respectively, for the second factor – 64 N and 110 N, respectively and for the third factor – 100 and 900, respectively (Table 1).
Samples with different winding designs were winded on iron mandrel with pins on the both sides with help of laboratory filament winding machine MAW FB 6/1 with six axes, roller type resin bath manufactured from Mikrosam A.D. Fibers pass through a resin bath after tensioning system and gets wet before winding operation.
After winding samples were cured with industrial heater at 80oC and at 140°C, for four hours.

Table 1. *Full factorial experimental design - 2^3*

No. exp.	Matrix of full factorial experimental design							Characteristics (conditions of the experiment)		
	X_1	X_2	X_3	X_1 X_2	X_1 X_3	X_2 X_3	X_1 X_2 X_3	**X_1 (m/min)** *velocity of the filament winding*	**X_2 (N)** *fiber tension*	**X_3 (°)** *winding angle*
1	-1	-1	-1	+1	+1	+1	-1	5,25	64	10
2	+1	-1	-1	-1	-1	+1	+1	21	64	10
3	-1	+1	-1	-1	+1	-1	+1	5,25	110	10
4	+1	+1	-1	+1	-1	-1	-1	21	110	10
5	-1	-1	+1	+1	-1	-1	+1	5,25	64	90
6	+1	-1	+1	-1	+1	-1	-1	21	64	90
7	-1	+1	+1	-1	-1	+1	-1	5,25	110	90
8	+1	+1	+1	+1	+1	+1	+1	21	110	90

Primary level	X_1 = 13,125	X_2 = 87	X_3 = 50
Interval of variation	7,875	23	40
Lower level	5,25	64	10
Upper level	21	110	90

3. Results and discussion

Tensioning system is an important part of filament winding. This importance gets critical when winding at high angles. Since tension changes the friction force between fiber and the mandrel, it should be kept at a certain value during winding operation (Jones, R. M., 1998).

Fiber tension also affects the volumetric ratio of composite at a given point. Excessive resin, due to a low tension, can result in decreased mechanical properties (Putic, S., et. al., 2007). Therefore, tensioning systems should be capable of rewinding a certain value of fiber. This condition occurs when fiber band reverses at the end of tube, while winding at low angles.

Wetting can be done by two commonly used bathing type: drum bath and dip bath.

Drum bath provide: less fiber damage than dip bath, this is especially important when using carbon fibers, drum baths can be heated for a better wetting action, lowering resin viscosity, reducing fiber speed, increasing fiber path on the drum are other methods used for better wetting action.

Dip bath provides: a better wetting action, resin can be heated during the travel of fiber through a dip bath, non-rotating surfaces are used for guidance, non-rotating surfaces provide good wetting, dip baths are used with aramid or glass fibers. Each layer of reinforcement can vary in winding tension, winding angle, or resin content.

In filament winding, one can vary winding tension, winding angle and/or resin content in each layer of reinforcement until desired thickness and strength of the composite are achieved. The properties of the finished composite can be varied by the type of winding pattern selected (Babu, M., et al., 2009). Three basic filament winding patterns are:

1) Hoop Winding: It is known as girth or circumferential winding. Strictly speaking, hoop winding is a high angle helical winding that approaches an angle of 90 degrees. Each full rotation of the mandrel advances the band delivery by one full bandwidth (Figure 2).

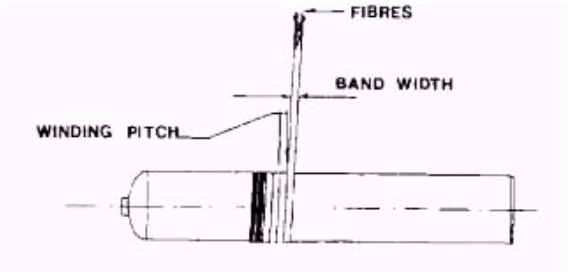

Figure 2. *Presentation of hoop winding of layers*

2) Helical Winding: In helical winding, mandrel rotates at a constant speed while the fiber feed carriage transverses back and forth at a speed regulated to generate the desired helical angles (Figure 3).

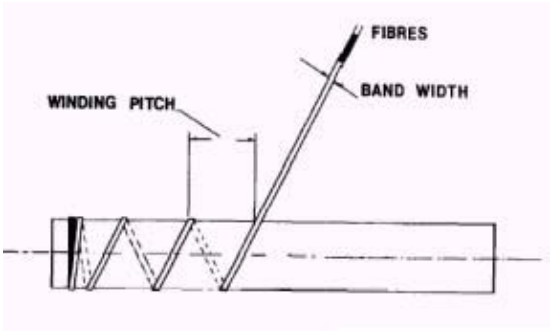

Figure 3. Presentation of coupled helical winding of layers

3) Polar Winding: In polar winding, the fiber passes tangentially to the polar opening at one end of the chamber, reverses direction, and passes tangentially to the opposite side of the polar opening at the other end (Figure

4).

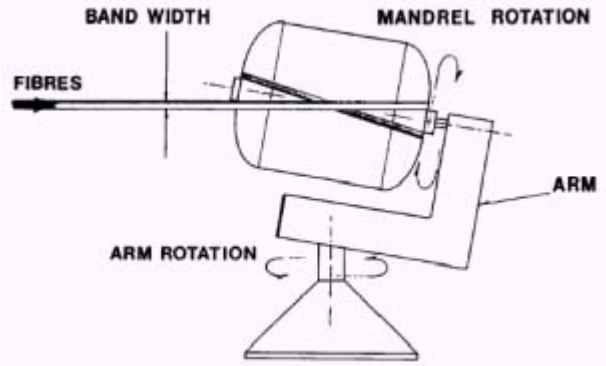

Figure 4. Presentation of polar winding of layers

In other words, fibers are wrapped from pole to pole, as the mandrel arm rotates about the longitudinal axis as shown in Figure 2. It is used to wind almost axial fibers on domed end type of pressure vessels. On vessels with parallel sides, a subsequent circumferential winding would be done.

In the above three, helical winding has great versatility. Coupled helical winding of layers (±Θ) are usually preferred, whereas hoop winding - winding angle, very close to 90° can also be used. Very low winding angle values need some arrangements at the ends of the mandrel, such as pins, etc. By varying the winding angle with respect to the mandrel axis, directional strength can be obtained by considering the loads, which will operate on the finished product. Almost any combination of diameter and length may be wound by trading off wind angle and circuits to close the patterns. Usually, all composite tubes and pressure vessels are produced by means of helical winding.

Filament winding is a manufacturing process which can offer:

• A high degree of automation;

• Relatively high processing speeds (> 50 m/min winding speed);

• An ability to fabricate composites with relatively high fibre volume fractions (~ 70%).

The main limitation of filament winding technique is the difficulty in production of complex shapes due to the requirement of very complex mandrel designs. In addition, production of reverse curvature parts is not possible by using this technique.

Figure 5. Produced glass fiber/epoxy resin filament wound composite pipes

4. Conclusion

The glass fiber/epoxy resin composite pipes were produced by using of filament winding technology. For the designing of the filament winding composite pipes the full factorial experimental design - 2^3 was applied. Base on that eight test specimen configurations were made. Three major factors were taken and two levels of variation. The first factor low and high levels were chosen to be 5,25 m/min and 21 m/min, respectively, for the second factor – 64 N and 110 N, respectively and for the third factor – 10^0 and 90^0, respectively. The effect of a filament-winding processing variables on longitudinal and hoop tensile and bending properties of the prepared composites further will be investigated. The produced filament wound composite pipes are shown on figure 5.

5. References

1. Babu, M. S., Srikanth G. & Biswas, S. Composite Fabrication by Filament Winding - An Insight. AEC/MECH/2009.
2. Belingardi, G., Cavatorta, M. P., Frasca C., Compos. Sci. Techol. 66, pp. 222-232, 2006.
3. Dorigato A., Pegoretti A., J. Compos. Mat., 48, pp. 1121-1130, 2014.
4. Jones, R. M., Mechanics Of Composite Materials (Materials Science & Engineering Series) Hardcover – July 1, 1998
5. Krivokuća, M., Putić, S., Uskoković, P. Aleksić. R., Uticaj strukture na savojna svojstva laminarnog kompozitnog materijala, III Jugoslovenska Konferencija o Novim Materijalima YUCOMAT 99, Herceg-Novi, Zbornik izvoda, (1999), p.228.
6. Mallick, P.K., Fiber-Reinforced Composites: Materials, Manufacturing, and Design, Third Edition (Mechanical Engineering), 2007.
7. Putic, S., Stamenovic, M., Zrlic,M., Bajaceta, B, Bending properties of Glass – Polyester Composite Pipes, 3th International Conference on Deformation Processing and Structure of Materials, Belgrade, 2007.
8. Roux, M., Reinforced Nanocomposites for electrical Applications, Master thesis, European School of Material Sciences and Engineering, France, 2010.

ПОВЕРХНОСТНЫЕ ВОЛНЫ ТИПА РЭЛЕЯ В СИСТЕМЕ СЛОЙ-ПОЛУПРОСТРАНСТВЕ ПРИ ОТНОСИТЕЛЬНОМ СКОЛЬЖЕНИИ

THE SURFACE WAVES OF THE RAYLEIGH ON THE SYSTEM OF LAYER AND SEMI-SPACE BY UNDER THE RELATIVE SLIDING

Давтян Артем Александович - магистрант института механики, НАН Армения, специалист конструкторского отделении <<Прогресстех Армения >> ООО, (+37477)732734
E-mail artyom.davtyan@yahoo.com

Davtyan A. A.

Abstracr: *Start the investigation of surface waves is related to the work of Rayleigh [1], in which the existence of elastic waves propagating along the free boundary of the semi-space, with an amplitude decaying exponentially in depth semi-space. Obviously, the energy of Rayleigh waves localized near the free boundary of the semi-space. This work Rayleigh proved the existence of seismic waves reduce to earthquakes.*

It is assumed that on the surfaces of bounding layers the conditions of splitting contact take place. The layer and the semi- space are moving relative to each other with constant velocity V. The dispersion equation which define the phase velocity of surface waves has been received. The conditions of existence of the surface wave, in the particular in the case of the same material of the layer and the semi-space have been occurred. It has been investigated short wave and long wave approximations, for which it has been determined phase velocity depending on the elastic properties of the material layer and the semi-space.

Начало исследования поверхностных волн связано с работой Рэлея [1], в которой установлено существование упругих волн, распространяющихся вдоль свободной границы полупространства, с амплитудой, экспоненциально затухающей по глубине полупространства. Очевидно, энергия волн Рэлея локализована у свободной границы полупространства. Этой работой Рэлей обосновал существования сейсмических волн приводящих к землетрясениям.

Предполагается, что на поверхностях ограничивающих слой имеют место условия Навье и скользящего контакта. Слой и полупространство движутся относительно друг друга с постоянной скоростью V. Получено дисперсионное уравнение, определяющее фазовую скорость поверхностной волны. Установлено условие существования поверхностной волны в частном случае одинаковых материалов слоя и полупространства. Исследованы коротковолновые и длинно волновые приближения, для которых определены фазовые скорости в зависимости от упругих свойства материалов слоя и полупространства.

1. В прямоугольной декартовой системе координат (x, y, z) упругое полупространство занимает область $-\infty < x < \infty, 0 < y < \infty, -\infty < z < \infty$,упругий слой-область $-\infty < x < \infty, 0 \le y < -h, -\infty < z < \infty$. Слой и полупространство двигаются относительно друг друга параллельно плоскости раздела $y = 0$ с постоянной скоростью V .Рассматривается задача плоской деформации. Величины относящиеся к слою отмечаются индексом (1), а величины относящиеся к полупространству – индексом (2).

Уравнения движения слоя и полупространства имеют вид [1]

$$c_{t1}^2 \Delta u_1 + \left(c_{l1}^2 - c_{t1}^2\right)\frac{d}{dx}\left(\frac{\partial u_1}{\partial x} + \frac{\partial v_1}{\partial y}\right) = \frac{\partial^2 u_1}{\partial t^2} + 2\frac{\partial^2 u_1}{\partial x \partial t} + V^2\frac{\partial^2 u_1}{\partial x^2},$$

$$c_{t1}^2 \Delta v_1 + \left(c_{l1}^2 - c_{t1}^2\right)\frac{d}{dy}\left(\frac{\partial u_1}{\partial x} + \frac{\partial v_1}{\partial y}\right) = \frac{\partial^2 v_1}{\partial t^2} + 2\frac{\partial^2 v_1}{\partial x \partial t} + V^2\frac{\partial^2 v_1}{\partial x^2}. \quad (1.1)$$

$$c_{t2}^2 \Delta u_2 + \left(c_{l2}^2 - c_{t2}^2\right)\frac{d}{dx}\left(\frac{\partial u_2}{\partial x} + \frac{\partial v_2}{\partial y}\right) = \frac{\partial^2 u2}{\partial t^2},$$

$$c_{t2}^2 \Delta v_2 + \left(c_{l2}^2 - c_{t2}^2\right)\frac{d}{dy}\left(\frac{\partial u_2}{\partial x} + \frac{\partial v_2}{\partial y}\right) = \frac{\partial^2 v_2}{\partial t^2}. \quad (1.2)$$

Где приняты обозначения

$$c_{ti}^2 = \frac{\mu_i}{\rho_i}, c_{li}^2 = \frac{\lambda_i + 2\mu_i}{\rho_i} \; i = 1, 2. \quad (1.3)$$

Здесь u_i, v_i - компоненты вектора упругих перемещений в плоскости (x, y), λ_i, μ_i - коэффициенты Ламе, ρ_i - плотности материалов слоя и полупространства соответственно.

Предполагается, что на плоскостях ограничивающих слой осуществляются условия Навье. На внешней границе слоя [2]

$$u_1 = 0, \sigma_{22}^{(1)} = 0 \text{ при } y = -h, \quad (1.4)$$

а на стыке слоя и полупространства

$$v_1 = v_2, \sigma_{21}^{(1)} = 0, \sigma_{21}^{(2)} = 0, \sigma_{22}^{(1)} = \sigma_{22}^{(2)} \text{ при } y = 0. \quad (1.5)$$

Требуется найти решения систем уравнений (1.1) и (1.2), удовлетворяющих граничным условиям (1.4),(1.5) и условиям затухания

$$\lim_{y\to\infty} u_2 = 0, \lim_{y\to\infty} v_2 = 0. \quad (1.6)$$

Для решения представленной задачи удобно использовать преобразование Ламе [1,2]

$$u_i = \frac{\partial \phi_i}{\partial x} + \frac{\partial \psi_i}{\partial y}, v_i = \frac{\partial \phi_i}{\partial y} - \frac{\partial \psi_i}{\partial x}. \quad (1.7)$$

С помощью (1.7)системы уравнений(1.1),(1.2)преобразуются к виду

$$c_{l1}^2 \Delta\varphi_1 = \frac{\partial^2 \varphi_1}{\partial t^2} + 2V \frac{\partial^2 \varphi_1}{\partial x \partial t} + V^2 \frac{\partial^2 \varphi_1}{\partial x^2}, \quad (1.8)$$

$$c_{t1}^2 \Delta\psi_1 = \frac{\partial^2 \psi_1}{\partial t^2} + 2V \frac{\partial^2 \psi_1}{\partial x \partial t} + V^2 \frac{\partial^2 \psi_1}{\partial x^2}.$$

$$c_{l2}^2 \Delta\varphi_2 = \frac{\partial^2 \varphi_2}{\partial t^2}, c_{t2}^2 \Delta\psi_2 = \frac{\partial^2 \psi_2}{\partial t^2}. \quad (1.9)$$

Граничные условия(1.4),(1.5) заменяются следующими условиями

$$\frac{\partial \psi_1}{\partial y} = 0, \varphi_1 = 0 \text{ при } y = -h, \quad (1.10)$$

$$\begin{cases} \dfrac{\partial \varphi_1}{\partial y} - \dfrac{\partial \psi_1}{\partial x} = \dfrac{\partial \varphi_2}{\partial y} - \dfrac{\partial \psi_2}{\partial x} \\ 2\dfrac{\partial^2 \psi i}{\partial x \partial y} + \dfrac{\partial^2 \psi_i}{\partial y^2} - \dfrac{\partial^2 \psi_i}{\partial x^2} = 0, (i = 1, 2) \\ \left(\lambda_1 + 2\mu_1\right)\dfrac{\partial^2 \varphi_1}{\partial y^2} + \lambda_1 \dfrac{\partial^2 \varphi_1}{\partial x^2} - 2\mu_1 \dfrac{\partial^2 \psi_1}{\partial x \partial y} = \left(\lambda_2 + 2\mu_2\right)\dfrac{\partial^2 \varphi_2}{\partial y^2} + \lambda_2 \dfrac{\partial^2 \varphi_2}{\partial x^2} - 2\mu_2 \dfrac{\partial^2 \psi_2}{\partial x \partial y} \end{cases} \text{ при } y = 0 \quad (1.11)$$

Условия затухания, вместо(1.6), будут

$$\lim_{y\to\infty} \varphi_2 = 0, \lim_{y\to\infty} \psi_2 = 0. \quad (1.12)$$

2. Искомые функции задачи представляются в виде гармоническими функциями для волн распространяющихся вдоль координатной линии x. Решение системы уравнений (1.9), удовлетворяющее условиям затухания(1.12) получается в виде

$$\varphi_2 = A_2 e^{-V_2 ky} \exp i\left(\omega t - kx\right), \quad (2.1)$$

$$\psi_2 = C_2 e^{-S_2 ky} \exp i\left(\omega t - kx\right).$$

В(2.1) A_2, C_2 - произвольные постоянные

$$V_2 = \sqrt{1 - \theta_2 \eta^2}, S_2 = \sqrt{1 - \eta^2}, \eta = \frac{\omega}{k c_{t2}}, \theta_2 = \frac{c_{t2}^2}{c_{l2}^2}. \quad (2.2)$$

Отсюда также следует, что безразмерная характеристика искомой фазовой скорости поверхностной волны η должна удовлетворять условию

$$|\eta| < 1. \quad (2.3)$$

Для системы уравнений(1.8)решение удовлетворяющее условиям(1.4)будет иметь вид

$$\varphi_1 = A_1 \operatorname{sh}\left[V_1 k\left(h + y\right)\right] \exp i\left(\omega t - kx\right), \quad (2.4)$$

$$\psi_1 = C_1 \operatorname{ch}\left[S_1 k\left(h + y\right)\right] \exp i\left(\omega t - kx\right).$$

где

$$V_1 = \sqrt{1 - \theta_1 \theta\left(\eta - \chi\right)^2}, S_1 = \sqrt{1 - \theta\left(\eta - \chi\right)^2}, \chi = \frac{V}{c_{t2}}, \theta_1 = \frac{c_{t1}^2}{c_{l1}^2}, \theta = \frac{c_{t2}^2}{c_{t1}^2}. \quad (2.5)$$

Подстановка(2.4) во второе граничное условие из системы четырех условий(1.11) и (2.1) в третьею граничное условие из (1.11) дает

$$C_1 = \frac{2i\nu_1}{2-\theta(\eta-\chi)^2}\frac{\operatorname{ch}\nu_1 kh}{\operatorname{ch} s_1 kh}A_1, C_2 = -\frac{2i\nu_2}{2-\eta^2}A_2. \tag{2.6}$$

Удовлетворение первому и четвертому из граничных условий (1.11) приводит к уравнениям

$$\nu_1 A_1 \operatorname{ch}\nu_1 kh + iC_1 \operatorname{ch} s_1 kh = -\nu_2 A_2 + iC_2, \tag{2.7}$$

$$\left(2-\theta(\eta-\chi)^2\right)A_1 \operatorname{sh}\nu_1 kh + 2is_1 C_1 \operatorname{sh} s_1 kh = \gamma\left(\left(2-\eta^2\right)A_2 - 2is_2 C_2\right).$$

где принято новое обозначение

$$\gamma = \frac{\mu_2}{\mu_1}. \tag{2.8}$$

С помощью(2.6)задача приводится к решению системы двух однородных алгебраических решений относительно произвольных постоянных A_1, A_2

$$\frac{\nu_1\theta(\eta-\chi)^2}{2-\theta(\eta-\chi)^2}A_1 \operatorname{ch}\nu_1 kh + \frac{\nu_2\eta^2}{2-\eta^2}A_2 = 0,$$

$$\frac{\left(2-\theta(\eta-\chi)^2\right)^2 \operatorname{ch}\nu_1 kh - 4s_1\nu_1 \operatorname{ch}\nu_1 kh \operatorname{th} s_1 kh}{2-\theta(\eta-\chi)^2}A_1 + \gamma\frac{\left(2-\eta^2\right)^2 - 4\nu_2 s_2}{2-\eta^2}A_2 = 0. \tag{2.9}$$

Равенство нулю детерминанта системы (2.9) приводит к следующему уравнению, определяющему безразмерный параметр η, характеризующий фазовую скорость поверхностной волны

$$\left(2-\eta^2\right)\operatorname{ch}[\nu_1 kh]\left(\gamma\nu_1\theta(\eta-\chi)^2\left(\left(2-\eta^2\right)^2 - 4\nu_2 s_2\right) + \nu_2\eta^2\left(\left(2-\theta(\eta-\chi)^2\right)^2 - 4\nu_1 s_1 \operatorname{th}[s_1 kh]\right)\right) = 0 \tag{2.10}$$

В предельном случае $kh \to \infty$, т. е. для двух встречно движущихся полупространств, из (2.10) получается уравнении

$$\eta = \chi + \sqrt{1/\theta\theta_1}$$

$$\gamma\nu_1\theta(\eta-\chi)^2\left(\left(2-\eta^2\right)^2 - 4\nu_2 s_2\right) + \nu_2\eta^2\left(\left(2-\theta(\eta-\chi)^2\right)^2 - 4\nu_1 s_1\right) = 0. \tag{2.11}$$

которое исследовано в статьях [3,4]. Вопрос существования поверхностных волн в системе слой-полупространство при отсутствии скольжения $(V=0)$ рассмотрен в статье [5].

Уравнение (2.10) имеет корень $\eta = \chi$. Нетрудно проверить, что этому корню соответствует тривиальное решение $u_i \equiv 0, v_i \equiv 0$.Действительно, согласно (2.9) при $\eta = \chi$ следует $A_2 = 0$, а из (2.6) следует $C_2 = 0, C_1 = iA_1$. Затем из(2.1) следует $\varphi_2 = 0, \psi_2 = 0$ и согласно (1.7) при $i = 2$ получается $u_2 \equiv 0, v_2 \equiv 0$. Согласно (2.5) $\nu_1 = s_1 = 1$, откуда из (2.4) получается

$$\varphi_1 = A_1 \operatorname{sh} k(h+y)\exp i(\omega t - kx),$$

$$\psi_1 = C_1 \operatorname{ch} k(h+y)\exp i(\omega t - kx). \tag{2.12}$$

Подстановка (2.12) в (1.7) дает $\varphi_1 \equiv 0, \psi_1 \equiv 0$.

Уравнение (2.10) имеет также корень $\eta = 0$. Аналогичным образом можно показать что и этому корню соответствует тривиальное решение.

3. В частном случае, когда материалы слоя и полупространства одинаковы

$$\mu_1 = \mu_2 = \mu, \lambda_1 = \lambda_2 = \lambda, \rho_1 = \rho_2 = \rho, \tag{3.1}$$

в уравнении (2.10) следует принять $\gamma = 1, \theta = 1$, а в выражениях для ν_i, s_i

$$\theta_1 = \theta_2 = \frac{\mu}{(\lambda+2\mu)} = \theta_*. \tag{3.2}$$

Если в приведенном примере рассматривать коротковолновое приближение

$$k^2 h^2 \gg 1, \tag{3.3}$$

то уравнение (2.10) приведется к виду

$$P_2\left(\left(2-(\eta-\chi)^2\right)^2-4P_1^2\right)=0, \tag{3.4}$$

где

$$P_1=\sqrt{1-\theta_*(\eta-\chi)^2},\ P_2=\sqrt{1-\theta_*\eta}. \tag{3.5}$$

Из равенства $P_2=0$ получается корень $\eta=\theta_*^{-1}$, который не удовлетворяет условию затухания (2.3). Равенство нулю второго сомножителя из (3.4) приводит к уравнению

$$(\eta-\chi)^2\left((\eta-\chi)^2-4(1-\theta_*)\right)=0. \tag{3.6}$$

Так как $\eta=\chi$ является тривиальным корнем, то решение уравнения (3.6) при $\chi>0$ и ограничении (2.3) имеет вид

$$\eta=\chi-2\sqrt{1-\theta_*} \tag{3.7}$$

если имеет место условия

$$2\sqrt{1-\theta_*}-1<\chi<2\sqrt{1-\theta_*}+1. \tag{3.8}$$

В частности, если $\theta_*=0$, то поверхностная волна существует при $1<\chi<3$ (скорость движения слоя больше скорости сдвиговой объемной волны). Если же $\theta_*=1/3$, то поверхностная волна существует при $\chi>2\sqrt{\frac{2}{3}}-1\approx 0.63$.

Из (3.7) и (3.9) следует, что поверхностная волна может распространяться в противоположенном направлении по сравнению с направлением движения слоя.

Необходимо отметить, что в случае отсутствия движения $(\chi=0)$ для тонкого слоя (или в длинноволновом приближении) поверхностная волна не существует.

Если в приведенном примере рассматривать длинноволновое приближение

$$k^2h^2 \ll 1, \tag{3.9}$$

то уравнение (2.10) приведется к виду

$$P_2\left(\left(2-(\eta-\chi)^2\right)^2-4P_1^3kh\right)=0, \tag{3.10}$$

4. Уравнение (3.10) имеет корень при случи $\chi=0$, при произвольных значениях kh и η.

$$\sqrt{1-\theta_*\eta}\left(\left(2-\eta^2\right)^2-4\sqrt[3]{1-\theta_*\eta^2}\,kh\right)=0, \tag{3.11}$$

В таблице 1 приводятся некоторые значения η в зависимости от безразмерного параметра kh, характеризующего длину волны при $\theta_*=0.25(\nu=1/3)$.

Табл. 1 $\theta_*=0.25$

kh	*0*	*1.0*	*1.5*	*2.0*	*3.0*	*4.0*
η	*1.41*	*1.68*	*1,71*	*1,73*	*1,77*	*1,78*

Из таблицы видно, что поверхностная волна при $kh\to\infty$ получается значение фазовой скорости волны Рэлея.

5. Если допустить, что материал слоя не обладает жесткостью на сдвиг $\eta_1=0$, то вместо уравнения (2.10), для определения безразмерного параметра фазовой скорости η получается следующее уравнение

$$\mu_2\left[\left(2-\eta^2\right)^2-4V_2S_2\right]+\lambda_1V_2\theta_*(\eta-\chi)^2\eta^2\,\mathrm{th}\,\alpha kh=0, \tag{4.1}$$

где

$$\theta_*=\frac{c_{t2}^2}{c_{l1}^2},\ \alpha=\sqrt{1-\theta_*(\eta-\chi)^2}. \tag{4.2}$$

Уравнение (4.1) имеет решение $\eta=\chi$, если χ есть решение известного уравнения Релея

$$\left(2-\chi^2\right)^2-4\sqrt{1-\theta_2\chi^2}\sqrt{1-\chi^2}=0 \tag{4.3}$$

при условии $\chi^2<1$. В частности, при $\theta_2=1/3$ следует $\eta=\chi\approx 0,919$.

В предельном случае $kh \to \infty$ уравнение (4.1) приводится к виду

$$L(\eta) \equiv \left(2-\eta^2\right)^2 - 4\nu_2 S_2 - \rho_1\rho_2^{-1}\left(\eta - x\right)^2 \eta^2 = 0. \tag{4.4}$$

Исключая из уравнения (4.4) тривиальный корень $\eta = 0$ [6] получим

$$L(\eta) \equiv \eta^2 - \frac{4\sqrt{1-\eta^2}}{\sqrt{1-\eta^2}+\sqrt{1-\theta_2\eta^2}} - \frac{\rho_1}{\rho_2}\left(\eta - x\right)^2 = 0. \tag{4.5}$$

Уравнение (4.5) имеет следующие свойства

$$L(-1) = 1 - \frac{\rho_1}{\rho_2}\left(1+x\right)^2 = 0, L(1) = 1 - \frac{\rho_1}{\rho_2}\left(1-x\right)^2 = 0, \tag{4.6}$$

$$L_1(0) = -2\left(1-\theta_2\right) - \rho_1\rho_2^{-1}x^2 < 0.$$

Из (4.6) следует, что для того чтобы уравнение (4.4) имело корни в интервалах $-1 < \eta < 0$ и $0 < \eta < 1$, достаточно наличие условий

$$\rho_1\left(1+x\right)^2 < \rho_2 \text{ и } \rho_1\left(1-x\right)^2 < \rho_2. \tag{4.7}$$

Так как в случае $x = 0\left(\nu = 0\right)$ из (4.7) следует, что поверхностная волна существует, то движение слоя может привести к устранению поверхностной волны.

Нетрудно показать, что в длинноволновом приближении $\left(k^2h^2 \square\ 1\right)$,согласно (4.1) поверхностная волна не существует.

ЛИТЕРАТУРА

1. Новацкий В. Теория упругости М.: Мир, 1975, 872 с.
2. Miklowitz J. The theory of elastic wave and waveguides-Amsterdam: North-Holland, 1978, 648 p.
3. Заславский Ю.М. Дисперсия поверхностных волн, бегущих вдоль плоской границы встречно-скользящих полупространства и слоя. Акуст. журн. 1994, т40, №6, с. 950-952.
4. Белубекян М. В. Особенности распространения поверхностных волн вдоль границы встречно скользящих полупространств. Акуст. журнал, т45, №3, с. 418-419.
5. Белубекян М. В., Давтян А. А., Упругие волны в системе слой-полупространство при условии скользящего контакта на плоскостях ограничивающих слой. В сб. "Актуальные проблемы механики сплошной среды"(посв.Н. Х. Арутюняну). Ереван, Изд. ЕГУАС, 2012, т1. с. 116-120.
6. Белубекян М. В. Поверхностные волны в упругих средах. В сб. "Проблемы механики деформированного твердого тела". Ереван Ин-т механики НАН Армении 1997, с 79-96.
7, Белубекян М. В., Давтян А. А., Мгерян Д. Э.,Поверхностныеволнывсистемевстречно скользящихслояиполупространства, Механика 2013, Ереван, Изд. ЕГУАС, 2013, с. 101-105.

NANOSTRUCTURED ALUMINUM-MATRIX COMPOSITE MATERIAL REINFORCED WITH FULLERENES C_{60}

НАНОСТРУКТУРНЫЙ АЛЮМОМАТРИЧНЫЙ КОМПОЗИЦИОННЫЙ МАТЕРИАЛ, УПРОЧНЕННЫЙ ФУЛЛЕРЕНАМИ C_{60}

Dr. Perfilov S., Dr. Evdokimov I., Dr. Pozdnjakov A., Dr. Blank V.
FSBI TECHNOLOGICAL INSTITUTE FOR SUPERHARD AND NOVEL CARBON MATERIALS, Moscow, Troitsk, Russia
E-mail: nhoots@mail.ru, ivan_911@mail.ru, pozdnjkov@yandex.ru, vblank@tisnum.ru, bagramov@mail.ru

Abstract: *The effect of nanostructuring and reinforcement of aluminum alloy AMg6, with fullerenes C_{60}, produced by mechanical activation and hot extrusion, has been investigated. The specific features of obtained nanostructured aluminum-matrix composite materials have been studied by X-ray analysis, differential scanning calorimetry and electron microscopy. Structure, phase composition and its relation with mechanical properties had been studied as a function of consolidation temperature.*
KEYWORDS: NANOCOMPOSITE, FULLERENE, ALUMINIUM, MECHANICAL ACTIVATION, CARBON NANOMATERIALS

1. Introduction

Aluminum and its alloys are the most widely used materials in modern science and industry. Unfortunately such materials produced by traditional technologies of casting, forging, liquid punching etc., mostly reached the limit of their mechanical, physical and technological properties. Nowadays, nanostructuring and modifying with high modulus nanoparticles, whiskers or fibers are one of the promising ways to improve the complex of material's properties.
Discovered in last decades such carbon nanostructures as fullerenes, carbon nanotubes, nanodiamonds, graphenes ets., are considered as one of most promising reinforcements for modern composites, due to their unique outstanding physical and mechanical properties.
In this work structure, phase composition and its relation with mechanical properties of nanostructured composite materials based on aluminum-magnesium alloy, modified with fullerenes C_{60}, are studied.

2. Experimental

Commercial aluminum-magnesium alloy AMg6 (1560, Al – 6 Mg – 0.6 Mn (wt.%)) and fullerenes C_{60} (99.9 %) were used as initial materials. Components (AMg6+0.3 wt.% C_{60}) were mechanically activated in planetary ball mill AGO-2U for 45 minutes. To prevent oxidation and other unwanted chemical reactions all manipulations with initial materials and nanostructured powders were carried out in glovebox with argon atmosphere (O_2 < 0.1 ppm, H_2O < 0.1 ppm). Nanostructured powders were consolidated via hot extrusion at temperature 300-400 °C and deformation ratio > 6.
Structure and phase composition were studied with X-Ray diffraction (XRD), transmitting (TEM) and scanning (SEM) electron microscopy. Thermal stability was studied on Perkin Elmer differential scanning calorimeter (DSC).

3. Results and discussion

According to XRD data, average aluminum crystallite size after 45 minutes of mechanical activation is 45-55 nm. It is well known that nanomaterials often exist in metastable condition. Under heating, deformation or other external stresses, nanomaterials demonstrate fast transitions to more energetically favorable state. For metallic nanomaterials this transitions usually occur in recrystallization and other structural transformations. DSC measurements show that obtained nanostructured composite materials are stable up to 350 °C. At higher temperatures irreversible transformations of structure and phase composition appear. Using XRD and Raman spectroscopy it was found, that DSC thermal effect corresponds to grain growth and aluminum carbide (Al_4C_3) formation. Thus, to prevent it extrusion temperature has been chosen at 300°C. After extrusion average crystallite size has not changed, it was confirmed with TEM (fig. 1a) and SEM (fig. 1b) investigations.

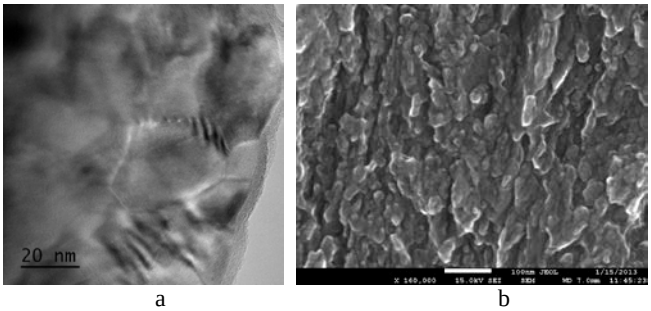

a b

Figure 1 *– TEM (a) and SEM (b) images of nanostructured aluminum-matrix composite material, reinforced with C_{60}*

It should be noted, that the structure doesn't change at elevated temperatures. Average crystallite size and phase composition in the extruded samples, exposed to heating up to 190 °C for 170 hours, remain unchanged. Treated in such a way samples demonstrate 5-10% increase of strength and plasticity in comparison with non-treated ones. This can be explained by the aging effect combined with internal stress relaxation.
Mechanical tests show that the samples of nanostructured aluminum-matrix composite materials, reinforced with fullerenes C_{60}, demonstrate significant increase of physical and mechanical properties (table 1).

Table 1 *– Physical and mechanical properties of nanostructured aluminum-matrix composite materials, reinforced with fullerene C_{60} (Along extrusion axis)*

Material	Extrusion temp. °C	Ultimate strain, MPa	Elongation, %	Micro-hardness, HV	Specific strength, km
Initial alloy	-	350	15	65	13
AMg6+C_{60}	300	800	2	220	31
AMg6+C_{60}	350	560	7	205	21
AMg6+C_{60}	400	520	20	200	20

4. Summary

Obtained nanostructured aluminum-matrix composites demonstrate high thermal stability, good machinability and significantly increased mechanical properties. Such composites could be used in varies brunches of science and industry as constructional or functional material.